The University Of Sheffield.

Pressure Drop and Forced Convective Heat Transfer in Porous Media

Ahmed Faraj Abuserwal

Supervisor: Dr Robert Woolley

Co-Supervisor: Professor Shuisheng He

Dissertation Submitted to the Department of Mechanical Engineering, University of Sheffield in partial fulfilment of the requirements for the

Degree of Doctor of Philosophy

May 2017

Acknowledgments

First and foremost, I would like to express my gratitude to my supervisor and tutor, Dr Robert Woolley, for his expert guidance which has been invaluable. The continual encouragement I have received from him has allowed me to persevere even when difficulties arose. His excellent comments and suggestions have improved my research capabilities and supported my efforts to publish a number of papers, including this dissertation.

I owe a similar debt of gratitude to a lab technician, Mr Malcolm Nettleship, for his continuous support in the lab. His willingness to share his time, experience and knowledge for the construction the test rigs has been a tremendous help. Without this support, I frankly could not have achieved the aims and objectives of this thesis.

In addition, acknowledgment and gratitude for Dr Russell Goodall is due for his enormous level of support and encouragement in giving me permission to use equipment and the required materials to produce the metal sponges. During various meetings, his comments and suggestions were invaluable to the success of my work and publications.

Furthermore, I would like to offer thanks to Dr. Farzad Barari and Dr. Erardo Elizondo Luna for their support and help, and a special thank you to Mr. Wameedh Al-Tameemi, who supported me by sharing his instruments. I would also like to extend my thanks to my colleagues in the lab; Mr. Basim A Al-Bakri**,** Mr. Ahmed Al-Rubaiy and Mr. Abdulaziz Gheit**.**

Finally, it is impossible to express with words the love and appreciation I have for my wife for the support she has given me to achieve my dreams and targets. Her patience and encouragement were the source my success. Without her taking on family responsibilities during my studies, I would not have been able to complete my thesis.

I dedicate this work to my late and dear parents who were the source of tenderness, love and encouragement throughout my life. This work is also dedicated to my delicate and precious daughter, Arwa, to the rest of my children; Faraj, Abdalmohiemen and Abdalmalek and to my darling wife.

Abstract

Metal foams, a new class of porous material with highly permeable structure and higher porosity (>0.60) compared with classical porous granular beds, are a viable solution to enlarge the thermal exchange area and provide a high heat capacity and high specific area. These metal foams are available in a number of solid materials with different porosities and pore size.

There is a current lack of understanding regarding metal foam microstructure parameters' effects on hydraulic and thermal parameters. This is a barrier to the design and implementation of various industrial applications. The current study aims to discover the effects of the pore shape and morphological parameters in terms of pore size and porosity at relatively low ranges of porosity (0.57-0.77) on fluid flow and conductive and convective thermal transport phenomena.

Sixty nine aluminium metal sponges were produced with a replication manufacturing technique (porosities 0.57-0.77, pore diameters 0.7-2.4 mm) with different irregular and spherical pore shape. The porosity was controlled by infiltration pressure and the pore size by preform salt diameter.

Two test rigs were designed and built to measure pressure drop at low and high flow rates. The frontal air velocity varied from 0.01 m/s to 8 m/s and the permeability based Reynolds number changed between 0.003 and 80. The four flow regimes; Pre-Darcy, Darcy, Forchheimer and Turbulent were identified in all samples. The transition points between the flow regimes were found to change gradually with the porosity and pore diameter. The permeability was measured in the Darcy flow regime while inertia and drag coefficients were measured in the Forchheimer regime. The pressure drop increased with frontal fluid velocity in linear and quadratic typical relations at low and high flow rates, respectively, and with decreases in both porosity and pore size.

The permeability increased with both porosity and pore size whilst inertia and drag coefficients decreased. The permeability normalised with pore diameter and correlated well with porosity. The irregular pore shape samples induced lower pressure and inertia coefficient and higher permeability more than those with

spherical pore shape. Permeability based friction factor was also expressed as function of permeability based Reynolds numbers and was found to tend towards inertia coefficient at turbulent regime.

The comparative steady state technique was used to measure the effective thermal conductivity (ETC). The ETC was found to decrease with increase of porosity, and no measurable influence of pore size and shape was observed. ETC was normalised by solid phase material thermal conductivity and correlated well with porosity for a broad range of porosity from 0.5 to 1.0.

The convective heat transport phenomenon was also studied experimentally using the single blow transient technique and a purpose built test rig. The outlet fluid temperature was modelled and matched with the recorded experimental history. The direct matching and maximum gradient approaches were used to obtain the number of transfer units (NTU_m) by using an iterative approach. The convective and volumetric heat transfer coefficients were also determined over the range of permeability based Reynolds numbers between 10 and 80. The NTU_m decreased with Reynolds number whilst the convective and volumetric heat transfer coefficients and Nusselt number increased. The thermal performance in terms of the above parameters increased with a decrease of both pore size and porosity. The thermal performance of irregular pore shape samples is lower than that of the spherical pore shape samples.

In order to improve the thermal performance, three samples with different pore diameter were sliced and examined. The thermal performance in terms of NTU_m and volumetric heat transfer coefficient were found to increase by 34% and 38%, respectively. The increase in both these parameters was more significant at lower Reynolds numbers. This is because the thermal conductivity effect reduced with an increase of flow rate.

The manufacturing defects were tracked using the image processing technique for scanned surfaces samples. Missing or damaged cells, inclusions and closed cells defects were identified in some studied samples. The effect of these imperfections resulted in scattering of the experimental results.

Table of Contents

List of Figures

List of Tables

Nomenclature

A	Empirical constant in Ergun Equation
A	Cross sectional area of the sample (m^2)
a	Empirical constant
A_h	Sample heat transfer area (m^2)
A_{hw}	Cross sectional area of the holder (m^2)
A_{min}	Free flow cross sectional area (m^2)
A_R	Free flow area ratio
a_s	Specific area per unit volume (m^{-1})
A_w	Heat transfer area of the holder (m^2)
B	Empirical constant
b	Empirical constant
b	The perimeter of flow passage through the porous matrix (m)
c	Empirical constant
C_1	Constant
C_2	Constant
C_E	Drag form coefficient (m^{-1})
C_f	Specific heat of fluid (J/Kg.K)
D	Aluminium block diameter (m)
D	Pipe diameter (m)
D_f	Ligament or fibre thickness (m)
D_i	Inner diameter of insulation material (m)
d_{lu}	Node thickness (m)
D_o	Outer diameter of insulation material (m)
d_p	Particle or pore diameter (m)
D_{st}	Struts thickness (m)
d_w	Average windows cell size (m)
dx	Unit length of element (m)
F	Constant
f	Inertia coefficient
f_k	Friction factor

G	Shape function
h	Convective heat transfer coefficient ($W/m^2.K$)
h_v	Volumetric heat transfer coefficient ($W/m^3.K$)
K	Permeability (m^2)
K_{effc}	The effective thermal conductivity of the complex (W/m.K)
K_{effe}	Effective thermal conductivity (W/m.K)
K_f	Fluid thermal conductivity (W/m.K)
K_{in}	Insulation material thermal conductivity (W/m.K)
K_{sol}	Thermal conductivity of the flux-meter material solid (W/m.K)
K_w	Thermal conductivity of wall material (W/m.K)
L, L_S	Sample thickness (m)
L_1	Upper aluminium block thickness (m)
L_2	Lower aluminium block thickness (m)
L_e	Entrance length (m)
m_s	Mass of the sample (Kg)
$\dot{m}_f$	Fluid mass flow rate (Kg/s)
n	Empirical constant
N	Number of slices
NTU_m	Number of transfer units of the matrix
NTU_w	Number of transfer units of the holder wall
Nu_{vdp}	Nusselt number
Por	Bed porosity
P_t	Pitch size (m)
Q_C	Power dissipated (W)
Q_I	Upper block heat transfer rate (W)
Q_{II}	Lower block heat transfer rate (W)
Q_{Loss}	Heat loss to outside (W)
Q_S	Sample heat transfer rate (W)
r	Particle or pore radius (m)
R	Radius of flux-meter (m)
R_a	Air gap thermal resistance (K/W)

Re	Reynolds number
Re_{dp}	Reynolds number based particle or pore diameter
Re_K	Reynolds number based permeability
R_{NTU}	Number of transfer units ratio
R_s	Slice thermal resistance (K/W)
R_t	Total thermal resistance (K/W)
R_{tc}	Total heat capacity ratio
S_m	Control volume total area of solid phase material (m^2)
S_w	Control volume total area of wall material (m^2)
t	Non-dimensional time
T	Temperature (°C)
t^*	System time (s)
T_{av}	Average temperature (°C)
T_f	Dimensionless fluid temperature
t_f	Air gap thickness (m)
T_f^*	Dimensional fluid temperature (°C)
T_{fb}	Average fluid temperature (°C)
T_{fexp}	Experimental out let fluid temperature
T_{fi}	Inlet fluid temperature (°C)
T_{fmax}	Dimensional maximum fluid temperature (°C)
T_{fo}	Outlet fluid temperature (°C)
T_{fpred}	Predicted outlet fluid temperature
T_i	Inner side insulation material (°C)
T_o	Dimensional initial temperature for the system (°C)
T_m^*	Dimensional matrix temperature (°C)
t_s	Slice thickness (m)
t_T	Total thickness of the complex (m)
T_w	Average wall temperature (°C)
T_w	Dimensionless wall temperature
T_w^*	Dimensional wall temperature (°C)
V	Frontal fluid (Darcy or seepage) velocity (m/s)

V	Sample volume (m^3)
X	Dimensionless location
X	Tortuosity
z	The perimeter of flow passage through holder wall (m)
$\frac{\Delta P}{L}, \frac{\partial P}{\partial X}$	Pressure gradient (Pa/m)
ΔP	Pressure drop (Pa)
ΔT	Temperature difference (°C)

Greek symbols

ε_0	Initial packing porosity
λ_m	Dimensionless effective thermal conductivity of matrix
λ_w	Dimensionless effective thermal conductivity of holder wall
μ_f	Fluid dynamic viscosity (Pa.s)
ρ_f	Fluid density (Kg/m^3)
ε	Porosity
λ	Nondimensional thermal conductivity
μ	Fluid dynamic viscosity
ρ	Fluid density
τ	Real time

Abbreviations

LPM	Litre per minute
PPI	Pores per inch
V.S	Very small pore diameter samples
S	Small pore diameter samples
M	Medium pore diameter samples
L	Large pore diameter samples
ETC	Effective thermal conductivity
TPS	Transient plan source
NaCl	Sodium chloride

NTU	Number of transfer units
EDM	Electrical discharge machining
PDE	Partial differential equation
LTE	Local Thermal Equilibrium
LTNE	Local Thermal Non Equilibrium

Subscript

a	Air
Al	Aluminium
Av	Average
eff	Effective
f	Fluid/fibre
i	Inner/inlet
in	Insulation
m	Matrix
max	Maximum
min	Minimum
o	Outer/outlet
P	Pore or particle
R	Ratio
S	Sample/slice
sol	Solid
t	Total
v	Volumetric
w	Wall/window

Chapter 1

1. Introduction

1.1 Background

The world is facing the twin challenges of increasing energy demand and also increasing greenhouse emissions which contribute to global warming [1, 2]. Fossil fuels are a major energy resource and the main cause of the global warming [3-5]. These emissions were found to increase by 49% between 1984 and 2004 due to the rapid growth of energy consumption [1]. Energy demand is still steeply increasing leading to increased CO_2 levels and more pollution concerns [4, 5].

There is a substantial amount of thermal energy generated in different kinds of industrial applications. There are numerous proposals for capturing this energy, a number of which utilise porous media. The wasted energy might be reused in thermal regenerators [5-10] or converted directly to electricity by solid-state energy converting devices [7]. The use of stored solar energy obtained by using the packed beds of porous media to minimise the consumption of fossil fuels is also a promising solution [5, 11]. In electronic applications, the heat flux dissipated from electronic components is also in high demand due to the rapid development of this technology [12]. In integrated circuits the dissipated heat flux was 0.1 kW/cm^2 in 2008 [13] and is expected to increase up to 1 kW/cm^2 in the near future [14]. Therefore, to manage these increased heat fluxes, components with more efficient cooling sinks are required [13].

Porous materials are of interest in a number of engineering applications and have received a great deal of attention in scientific research and industry. This is because they provide both a large surface area and high heat capacity in a small volume [6, 15, 16]. They also have variable design geometries to make into different shapes and sizes as packed beds. This is suitable for a variety of applications such as in chemical reactors [17]. These beds can be produced in the form of wire mesh screens, ball bearings, and metal foams. The earliest porous media were packed beds consisting of particles and pellets which had low porosity (0.3-0.6) resulting in high pressure drop [17-20]. These were typically used in thermal storage devices, and

chemical reactors [5, 16, 17, 21-24]. A new material called open cell metal sponges have attracted attention due to their large specific area, light weight, high porosity and relative strength [25]. These metal sponges have been the alternative material used in oscillating thermal regenerators [15, 25, 26], in the thermal regenerators of Stirling engines [8, 27, 28] and heat exchangers [25, 29-31].

The metal foams are a type of porous media those voids are typically filled with fluid. The structure of the foam is a network of struts and ligaments that form a matrix. The void volume is made up of pores which can be closed (closed-cell foams) or interconnected by fibres (open-cell foams) [32-37]. Open celled metal foams consist of a reticulated cellular structure similar to sponges. That is why they are often referred to as metal sponges [38]. Metal foams are classified based upon their microstructure into several categories: open-cell, closed cell, semi open and fibre arrangement [32-36]. The open celled sponges' morphology provides a high specific surface area and creating tortuous form offering enhanced mixing to improve heat exchange. Both types are also thermally and electrically conductive based on solid phase material, and are also strong, stiff and light weight [33, 34]. The typical structure of open and closed cell metal sponges is shown in Figure 1-1. The cellular metallic materials are available in a number of solid phase materials: aluminium, nickel, copper, ceramic, steel, silicon carbide and other metal alloys [17, 39-41].

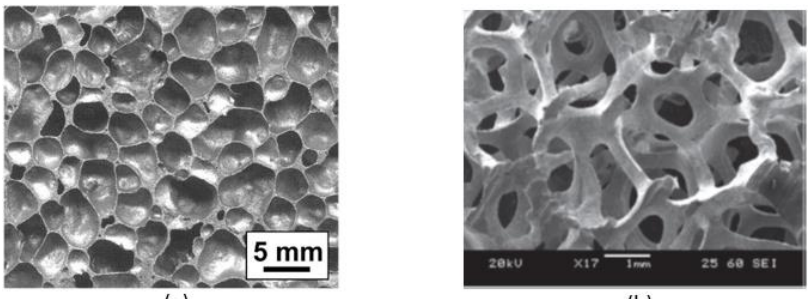

(a) (b)

Figure 1-1 The typical structure of closed and open cell metal sponges: (a) closed cell, reproducing from [42] with permission of Elsevier; (b) open cell, reproducing from [43] with permission of Elsevier

1.2 Thermal regenerator

The thermal regenerator is a temporary thermal energy storage device that absorbs the thermal energy from the hot working fluid in first stage. In the second stage the heat is picked up from the solid prism by a blown cold fluid. The prism of

regenerators take the form of the compact heat exchangers and composed of particles [15], mesh wire screens [22] and porous materials [8, 15]. There are two types of thermal regenerators; rotary and fixed bed. In the former one as illustrated in Figure 1-2, the bed (rotor) rotates periodically to face the hot and cold streams those flow through fixed channels [15].

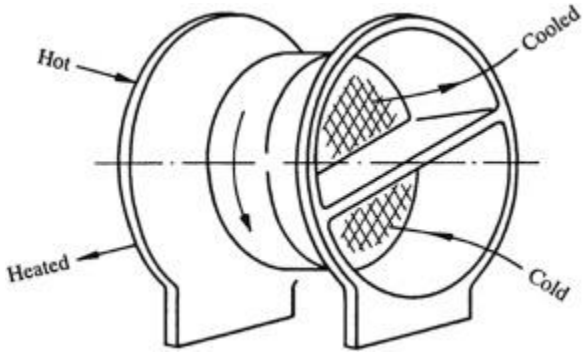

Figure 1-2 The rotary thermal regenerator, reproducing from [44] with permission of Elsevier

In the fixed thermal regenerator, the bed is fixed and the hot and cold fluid streams are passed through the storage prism as shown in Figure 1-3.

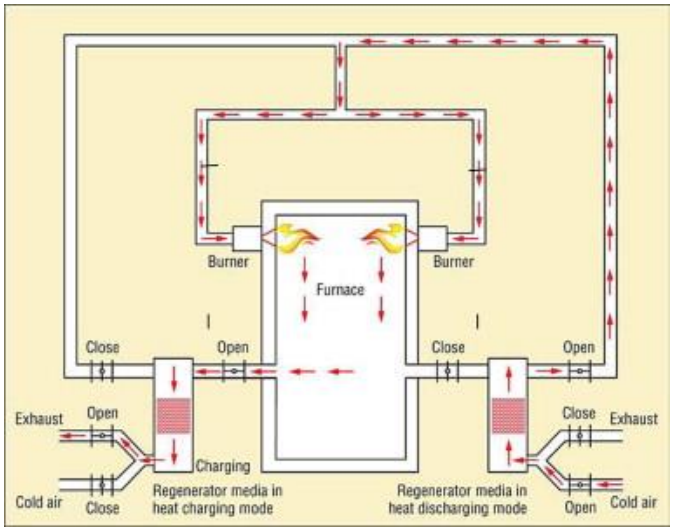

Figure 1-3 The fixed bed thermal regenerator, reproducing from [6] with permission of Elsevier

Both types of thermal regenerators are used in cooling gas systems, chemical industrial processes, and sterling engines in order to improve heat recovery. One of the important design factors is a high specific area (heat transfer area per unit volume) of the packed materials (compactness) [6, 15]. The volumetric heat capacity and the thermal conductivity of the storage materials were also found to have a

significant effect on the storage energy. For example, the use of stainless steel in the structure of a regenerator results in higher thermal energy storage compared with the same volume of aluminium as a result of the high density of the stainless steel. The increase in the thermal conductivity of the phase materials causes a reduction of temperature gradient between the fluid and solid wall.

1.3 Aims and Motivation

Metal sponges are multipurpose and multifunctional materials [45, 46] that have wide range of engineering and industrial applications. Their unique structure results in enhanced heat transfer mechanisms [47, 48]. The tortuosity of the pore structure results in more turbulent flow [47, 49]. They also have an extended heat transfer area [47, 48]. Typical applications are thermal energy storage devices, gas turbines, electronic cooling, chemical reactors and solar collectors [8, 11, 19, 34, 48, 50-52]. Metal sponges are also used as extended heat transfer surfaces in heat exchangers, dehumidification techniques and refrigeration systems [29, 47, 53-56].

Information about heat and fluid transport in low porosity replicated cellular materials is scarce in open literature. Thermal characteristics, in terms of the convective heat transfer coefficient, has been shown to increase as the porosity decreases [51, 57-59]. This project aims to study relatively low porosity cellular materials experimentally. The number of transfer units and volumetric heat transfer coefficient (applicable to thermal regenerators) and the convective heat transfer coefficient and Nusselt Number (applicable to extended heat transfer surfaces) will be measured.

A number of replicated aluminium sponges with different pore sizes and low relative porosity with spherical and irregular pore shapes were produced. The single blow technique was adopted to measure the number of transfer units and interstitial and volumetric heat transfer coefficients.

The effective thermal conductivity was measured separately as it is a key parameter in heat transfer evaluation. Measurements of effective thermal conductivity at relatively low porosity are rare for the open cell metal sponges. A comparative steady state method was implemented.

Determination of the pumping power in terms of pressure drop across the porous materials sponges is one main objectives of this study. The pressure drop was measured to obtain the hydraulic parameters in terms of permeability and inertia coefficient. The effect of material properties (e.g. porosity and pore size) on the transition bounds of flow regimes in metal sponges at low porosity has not been investigated. In turn the identification of flow regimes is of importance to measure the hydraulic parameters such as the permeability and inertia and drag form coefficients. Four flow regimes in porous media were identified and the permeability will be measured at Darcy flow regime.

To study repeatability a large number of samples will be examined. Manufacturing defects have been found to have a measurable influence on the mechanical properties of metal foams [60-62]. Understanding of their effect on pressure drop and convective heat transfer is uncommon. Therefore, tracking the defects and determining their impact is essential to obtain reliable conclusions about the material properties. The fluid free flow area is the only open path available for fluid to pass through the matrix. The free area was identified by an image processing technique to quantify its effect on the thermal and hydraulic characteristics for some selected samples.

Based on this the following Aims and Objectives are listed below:

- Determine the steady state pressure drop and hydraulic parameters of porous media.
  - Identify the flow regimes, primarily Darcy and Forchheimer, for each sample.
  - Measure how the pressure drop changes with flowrate. Examine the impact of the porous media properties (e.g. porosity and pore diameter) on the pressure drop.
  - Determine the flow properties associated porous media for each sample such as the permeability, drag coefficients and friction factor. Examine the impact of the porous media properties on the flow properties.

- Provide empirical corrections of the experimental results and compare the performance of the porous media studied here with other porous media reported in the literature.

- Measure the effective thermal conductivity

  - Manufacture and characterise an experimental apparatus to determine the thermal conductivity of the samples.
  - Use the comparative steady state method to measure the effective thermal conductivity.
  - Determine the significance of the porous media properties on the effective thermal conductivity.
  - Obtain an empirical correlation for the measurements from this study. Compare the performance of the porous media manufactured in this study with those reported in the literature.

- Convective heat transfer

  - Perform single blow measurements where the sample is subjected to a step change in temperature.
  - Derive an appropriate mathematical model with which to model the experimental results. Include the effects of axial and longitudinal conduction
  - Implement a matching technique to match the predicted and measured outlet fluid temperatures.
  - Determine both the number of transfer units (*NTU*) convective and volumetric heat transfer coefficients.
  - Study how the heat transfer parameters change with flow rate for varying porous media parameters.
  - Compare the metal foam results with those of mesh wire screens and spherical balls.
  - Experimentally investigate the impact of changing the longitudinal conduction by slicing a sample.

- Manufacturing defects

Characterise the different types of manufacturing defect that occurred and determine their impact on the flow and heat transfer results.

1.4 Organization

This thesis structure is organised based in the topics in nine chapters and two appendices. In Chapter 1, the background, motivation and aims of this study are presented. In Chapter 2, the critical literature review of previous studies based on different topics are addressed. The methodology and experimental work are documented in Chapter 3. The replication manufacturing technique to produce the aluminium sponges is described in Chapter 4. The fluid flow results in terms of pressure drop and hydraulic parameters are documented in Chapter 5. In this chapter the effect of porosity and pore size on the fluid flow in terms of pressure drop and flow regimes in porous media is clarified. In Chapter 6, the measurements of effective thermal conductivity and the comparison with available analytical models and empirical correlations are provided. In Chapter 7, the convective heat transfer measurements results obtained by the single blow method are presented. This chapter also assesses the impact of the geometrical parameters on convective heat transfer characteristics. The tracking technique of manufacturing defects and their effect on thermal and hydraulic characteristics are also addressed in Chapter 8. In appendices A and B the calibration techniques of thermocouples and mass flow meters are documented respectively.

1.5 Publications

- Ahmed F. Abuserwal , Erardo Mario Elizondo Luna, Russell Goodall, Robert Woolley, *The effective thermal conductivity of open cell replicated aluminium metal sponges.* International Journal of Heat and Mass Transfer, 2017. **108, Part B**: p. 1439-1448.
- Ahmed F. Abuserwal , Farzad Barari, Erardo Mario Elizondo Luna, Russell Goodall, Robert Woolley, flow in replicated aluminium sponges: permeability determination and pressure characterization measurements (under preparation).

- Ahmed F. Abuserwal , Farzad Barari, Erardo Mario Elizondo Luna, Russell Goodall, Robert Woolley, Convective heat transfer characterisations in replicated aluminium sponges (under preparation).

Chapter 2

2. Literature review

The structural characterizations of open cell metal foams make them promising materials for a number of engineering applications [63-65]. This has resulted in significant research in the field of thermal and hydraulic transport phenomena in porous materials. Studies also focus on the development of manufacturing techniques to improve the microstructure parameters for new applications. The unique structural form of metal sponges has attracted much attention in the fields of heat transfer and fluid flow [63-65]. However, there are still a number of aspects that are poorly understood due to the complexity of the material.

The thermal and hydraulic characterisations of metal foams; such as the convective heat transfer coefficient, effective thermal conductivity, permeability and form and inertia coefficients, can be determined experimentally and numerically [52]. Experiments have been widely performed to measure these parameters, e.g. for pressure and convective heat transfer [39, 59, 64, 66-69], and for thermal conductivity [18, 19, 34, 70, 71]. However, they depend on obtaining samples of sufficient size and it is difficult to ascertain what is happening inside the material. Numerical simulations are typically performed by CFD. The matrix is obtained by 3D topographical scans of actual samples [32, 36, 52, 71, 72] or representative unit cells for example cubic or 3D tetrakaidecahedron cell [18, 53, 73, 74]. Shown in Figure 2-1 and Figure 2-2 are examples of the 3D CT-Scan and representative unit cells used in the literature respectively.

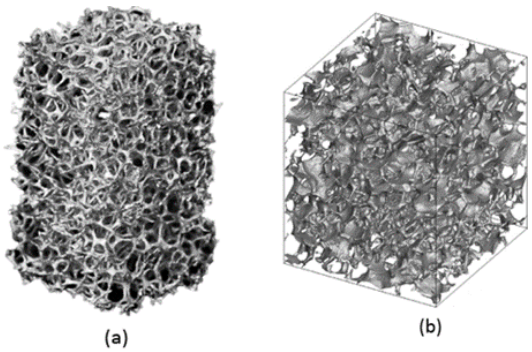

Figure 2-1 Samples of 3D CT-scan images: (a) Aluminium foam PPI=30, reproducing from [32] with permission of Elsevier; (b) FeCrAl foam Por=0.89, reproducing from [36] with permission of Elsevier

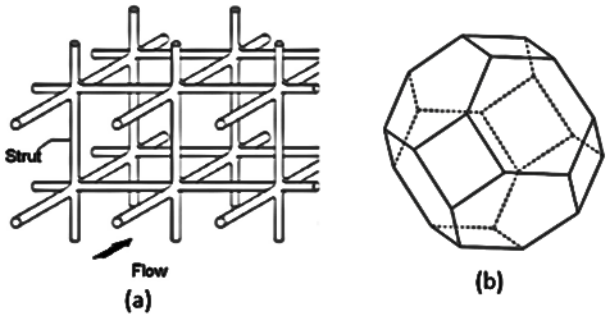

Figure 2-2 Samples of representative unit cell: (a) cubic cell, reproducing from [65] with permission of Elsevier; (b) tetrakaidecahedron cell, reproducing from [75] with permission of Elsevier

2.1 Fluid flow through porous media

Fluid flow in porous media is treated in a similar manner to that in pipes. The flow is characterised in terms of Reynolds number and different flow regimes have been identified and are associated with changes in the friction factor and pressure drop. However, the large surface area, complex internal shapes and natural variation in the media mean there is considerable experimental scatter and differences in the definition of the characteristic length. This means it is difficult to compare the flow properties of different porous media. Here the results for granular beds and then metal foams will be surveyed.

2.1.1 Fluid flow in granular beds

Granular beds were one of the first engineering applications of porous materials for application such as, ground water management, distillation, filtration, chemical reactors and thermal energy storage [9, 76]. It was quickly realised that understanding the effects of microstructure parameters (e.g. porosity and pore size) on pressure losses in flowing fluid was essential for designing enhanced systems [17, 39, 77]. The subject of fluid flow through a porous media has been a topic of research for more than 150 years [18, 78]. The majority of the investigations have dealt with low porosity granular mediums. These permeable materials are composed of granular particles, pellets, and mesh wire screens. The porosity for these materials typically varies from 0.3 to 0.6 and they are known to have high pressure drop [18-20]. It is generally acknowledged that the first contribution in this subject was in 1856 by Darcy [79]. He conducted experiments of the flow of water through packed beds of sand of different thickness (L), and found the superficial average velocity (V) as

directly proportional with pressure drop ($\frac{\Delta P}{L}$) across the packed bed. The proportional coefficient (now called permeability) was defined as the hydraulic conductivity (K) [17, 80, 81].

$$\frac{\Delta P}{L} = \frac{\mu}{K} V \qquad 2.1$$

The average Darcy or seepage (frontal) fluid velocity was found by using the cross section area of the holder and volume flow rate [80] and μ is the viscosity of the flowing fluid.

The distribution of particles and their packaging influences the pressure drop [82, 83]. Measurements are only given for simple cases and the studies tend to rely on experimental work [77]. In 1952 Ergun [84] presented a pioneering empirical correlation for a pressure drop as a relation of bed porosity (ε), the diameter of granular particle (d_p), the frontal fluid velocity and fluid properties.

$$\frac{\Delta P}{L} = A \frac{(1-\varepsilon)^2}{\varepsilon^3 d_p^2} \mu V + B \frac{(1-\varepsilon)}{\varepsilon^3 d_p} \rho V^2 \qquad 2.2$$

The empirical coefficients A and B were given as 150 and 1.75 respectively. This correlation has been widely used to predict the pressure drop in porous media. However, the values of coefficients A and B have been found to vary with different packed beds [83, 85-87]. The coefficient A was found to vary between 174 and 184 and coefficient B from 1.81 to 1.94 in complex and simple structure of porous media depending on particle diameter [87]. The replacement of ε^3 by $\varepsilon^{3.6}$ with coefficient B=1.8 - 4.0 and coefficient A=180 was also recommended depending on the roughness of particles composed porous matrix [88]. In contrast, these values were found to have close agreement with the universal values in correlation for 1 mm and 3 mm spheres [77]. The correlation with the universal coefficients was also validated well with the experimental results for water and air with different particles diameter (1.5 - 6.0 mm) [89].

In this topic, a number of experimental investigations have been conducted in order to study the effect of geometrical parameters and fluid flow on the pressure

drop. With increasing the frontal fluid velocity the pressure drop increased in the typical linear relationship at low flow rates and quadratic ally at relatively high flow rates in different kinds of porous media [19, 39, 41, 77, 78, 82, 86, 90-97].

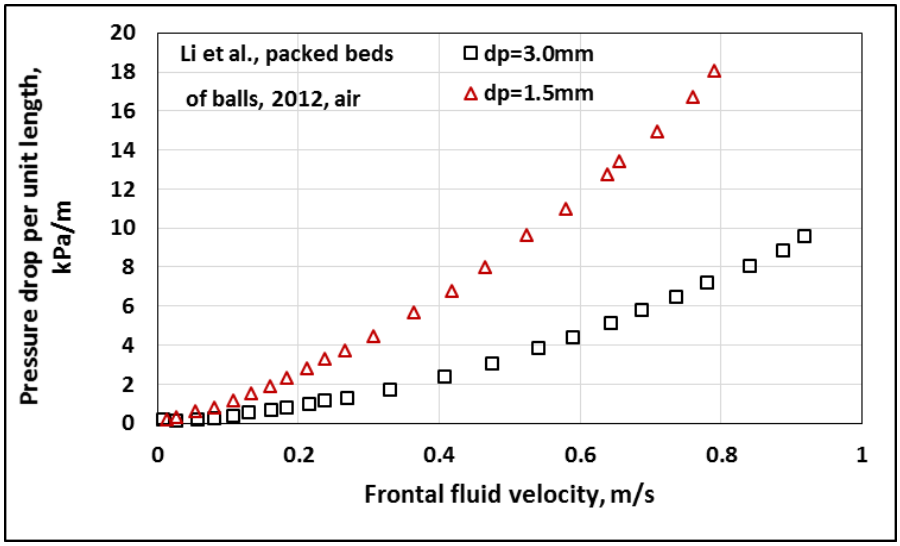

Figure 2-3 The effect of particle diameter on pressure drop [89]

The effect of geometrical parameters (porosity and particle diameter) on pressure drop in granular packed beds was also studied. The pressure drop was found to increase with decrease of particle diameter and bed porosity [77, 82, 83, 86, 87, 89, 98-101]. Shown in Figure 2-3 is the effect of particle diameter on pressure drop in packed beds of spherical particles [89]. This increase in pressure loss is due to the decrease of particle diameter, causing a closely packed arrangement and results in smaller passages for the flow.

The flow in porous media is complex due to the random internal structure in the path of flowing fluid. This complex morphological network is the cause of sudden changes of the flow direction, disrupting boundary layers and creating continuous throttling through the tortuous open paths. These obstacles result in high pressure drop compared with flow in open areas [77, 82, 100].

Reynolds number is a common criterion to define the transition points of flow regimes [99], but there is no agreement for the appropriate characteristic length in porous media [67, 77, 78]. The average particle diameter for granular beds has been

used as the characteristics length in the Reynolds number [5, 66, 76, 78, 82, 86, 87, 92, 98, 100, 102, 103].

$$Re_{dp} = \frac{\rho V d_p}{\mu} \qquad 2.3$$

However, the particle diameter is not representative of the space that the fluid inhabits. There is also considerable variation in the shapes of the spaces between the particles. For this reason the permeability has been proposed as the characteristic length. It depends on the space between the solid and accounts for the whole volume of the porous media [19, 39, 41, 77, 78, 82, 86, 90-92, 96, 97, 104, 105]. The disadvantage of this approach is that flow measurements must be made in order to find K

$$Re_K = \frac{\rho V \sqrt{K}}{\mu} \qquad 2.4$$

The fluid flow regimes in granular packed beds of porous media has also received significant attention in a number of studies due to its importance [77]. In porous media, the existence of four flow regimes is generally acknowledged; Pre-Darcy, Darcy, Forchheimer and turbulent [76, 77, 86, 87, 104].

The pre-Darcy regime occurs at very low flow rates. There is little information on this regime in the literature due to difficulties in measuring low flow rates and pressure drops [77, 82, 99]. The flow in this regime shows non-Newtonian behaviour and the pressure drop across the bed is inversely proportional with flow rate and nonlinearly increases with flow rate [77, 82, 86]. Small counter currents have been observed caused by the flow streaming along the cell walls in the opposite to direction to the main flow [87, 106].

In the Darcy regime, the relationship between the flow velocity and pressure drop is linear [77, 82, 86, 87, 104, 106]. Viscous forces are dominant [76, 82, 86, 87, 106]. This regime was found to occur at Reynolds number based particle diameters less than unity for the packed beds of spheres. The nature of the velocity profile has been shown to be determined by the local geometry [106] as the flow passes over the surface and the pressure loss is solely due to viscous forces [76, 77, 86, 106]. In

contrast, the contradictions of the lower and upper bounds of this regime have been reported with regard to the different structural parameters of granular packed beds such as, porosity, particle diameter and matrix type, whether spherical or pellets [77, 82, 86, 87, 99].

Shown in Figure 2-4 is the typical linear and quadratic realtionships between the pressure gradient and frontal fluid velocity in Darcy and Forchheimer regimes respectively [99]. The effect of the particle diameter on the transition point from Darcy regime is also clear, where the transition fluid velocity increased gradually with granular diameter [99].

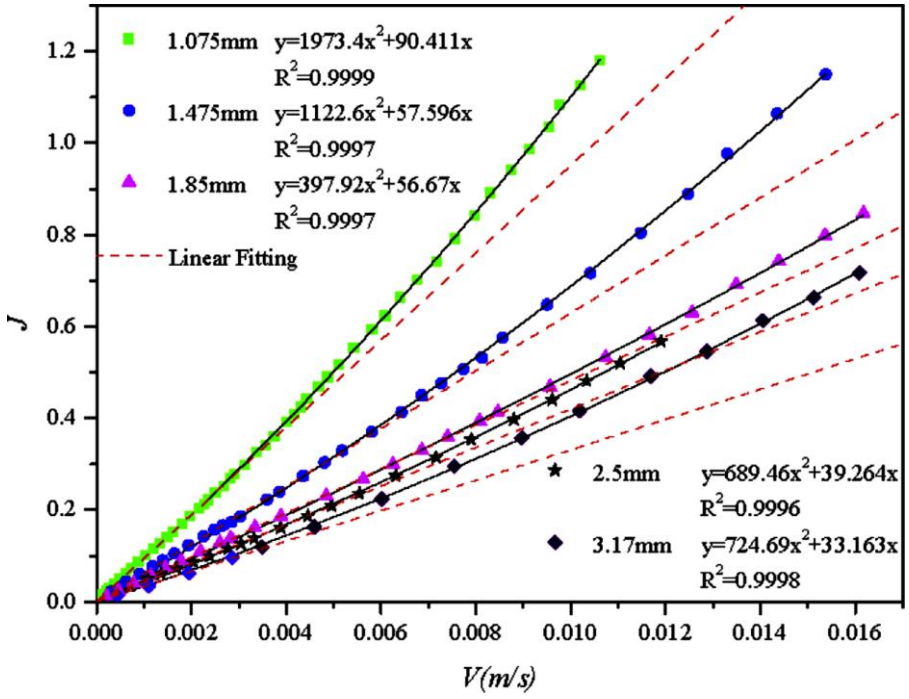

Figure 2-4 The effect of particle diameter on pressure drop. Reproducing from [99] with permission of Elsevier

The Forchheimer regime occurs at higher flow velocities and is characterized by a nonlinear relationship between pressure drop and velocity as shown in Figure 2-5. This has been explained to be the result of inertia forces (separation and wake effects) [76, 77, 92, 104, 106]. To achieve a good fit to the experimental data, quadratic and cubic relationships between the pressure drop and flow velocity were demonstrated in 1901 and 1930 respectively by Forchheimer and both used to obtain the hydraulic parameters [87, 107, 108].

$$\frac{\Delta P}{L} = aV + bV^2 \qquad 2.5$$

$$\frac{\Delta P}{L} = aV + bV^2 + cV^3 \qquad 2.6$$

The Darcy and Forchheimer regimes are both considered to be steady and laminar in nature [104]. The final regime which occurs after a further increase in flow velocity is the turbulent regime. In this regimethe drag form forces are completely prevalent [39, 76, 80, 86, 87, 107, 109]. The flow in this regime is unsteady and highly chaotic [91, 106]. The typical quadratic relationship of pressure gradient with frontal fluid velocity has been also observed at relative high flow rates.

The first term of the right-hand side in Equation 2.5 is the Darcy equation which accounts the viscous force effect and has a linear dependence on velocity. The second term describes the effect of inertia and drag forces in the second order dependence on fluid velocity. Both the inertia and drag coefficients values have been shown to be influenced by the roughness of the foam, the cell and ligament shape, the base material and the manufacturing method [18, 19, 39, 52, 97, 110-114]. The study by Beavers and Sparrow [92], who measured the pressure loss in high porosity cellular nickel materials, suggested a universal value of inertia coefficient of 0.074. Subsequent studies have demonstrated that the inertia coefficient differs depending on the microstructure of the porous media [19, 39, 96, 107, 115, 116].

There is no agreement about the demarcations of the flow regimes [104]. This is likely to be partly due to difficulties in the definition of the Reynolds number as the particle diameter is ambiguous and changes and Re is defined with different characteristic lengths [77, 82, 86, 87, 99].

The common methodological technique to identify the flow regimes is the change in slope of reduced pressure gradient data against the frontal fluid velocity [77, 86, 87, 90, 104]. As shown in Figure 2-5, the relationship changes depending on the flow regime present in porous media [86]. At the Darcy flow regime, the slope of reduced pressure gradient is zero and it increases to linearity at the Forchheimer regime. By increasing the flow, the gradient increases again at the turbulent regime.

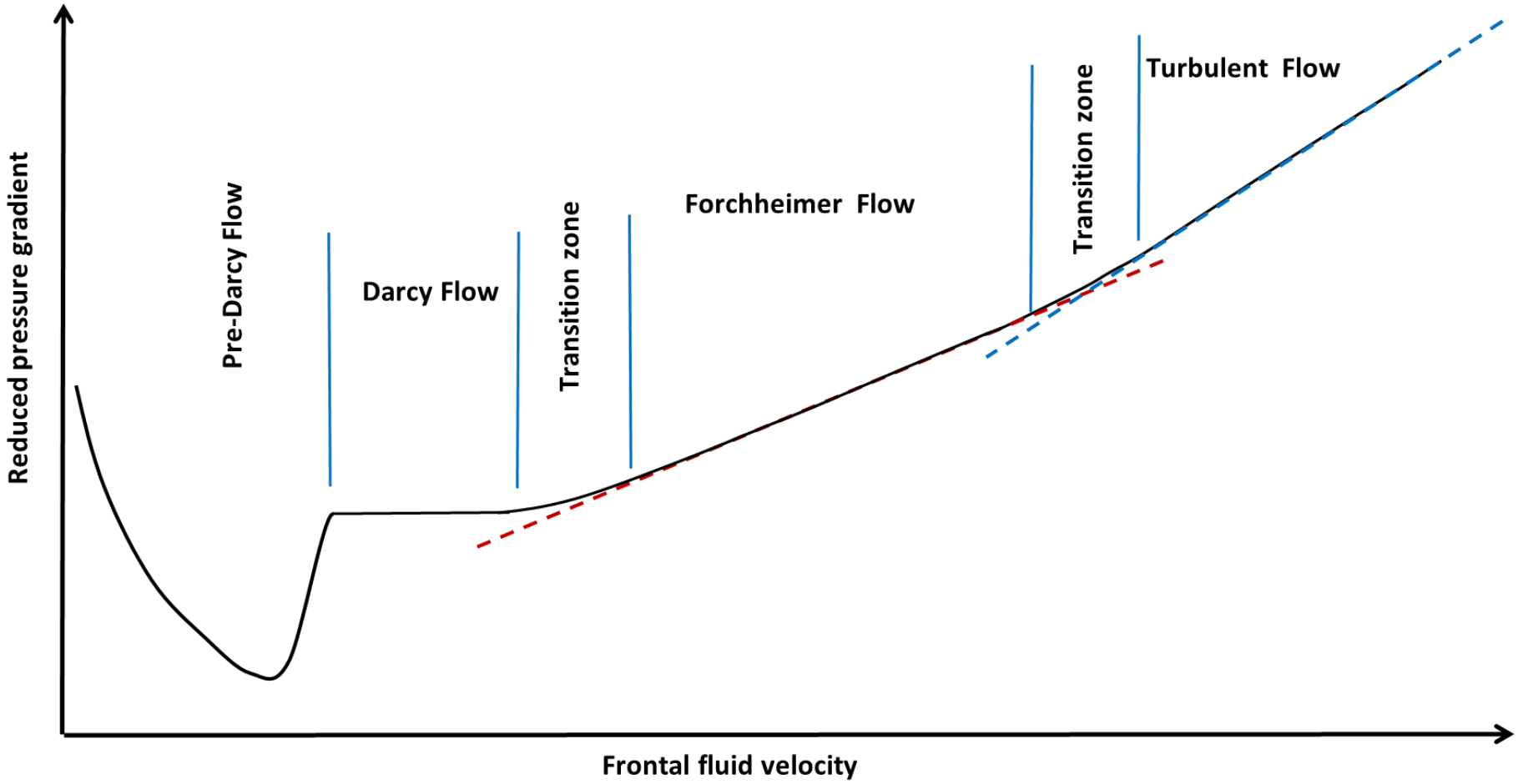

Figure 2-5 The flow regimes in porous media

2.1.2 Fluid flow in metal foams

Metal foams are form a solid structure, composed of struts connecting lumps or nodes surrounding random, open celled pores. They are characterized by their porosity (or relative density), pore size (or number of pores per inch, PPI) [17, 39]. The use of the metal foams in different applications has grown due to their induced pressure drops compared with old fashion types of porous media. As catalytic reactors and thermal regenerators, metal foams were found to induce lower pressure drops, between 2.5 and 10 times than that induced by packed beds of spheres with the same exchange area [8, 117, 118].

A significant number of pressure measurements have been performed with both air and water as working fluids at different flow rates across different types of metal foams. Additionally, the hydraulic loss is commonly presented in terms of pressure gradient against frontal fluid velocity and friction factor against the Reynolds number [39, 77, 90, 92].

In the reported studies for pressure measurements through metal foams, the relationship of porosity and pore diameter (or PPI) with pressure drop and hydraulic parameters is non-monotonical [103]. This means the same pressure drop is induced with different combinations of pore size and porosity.

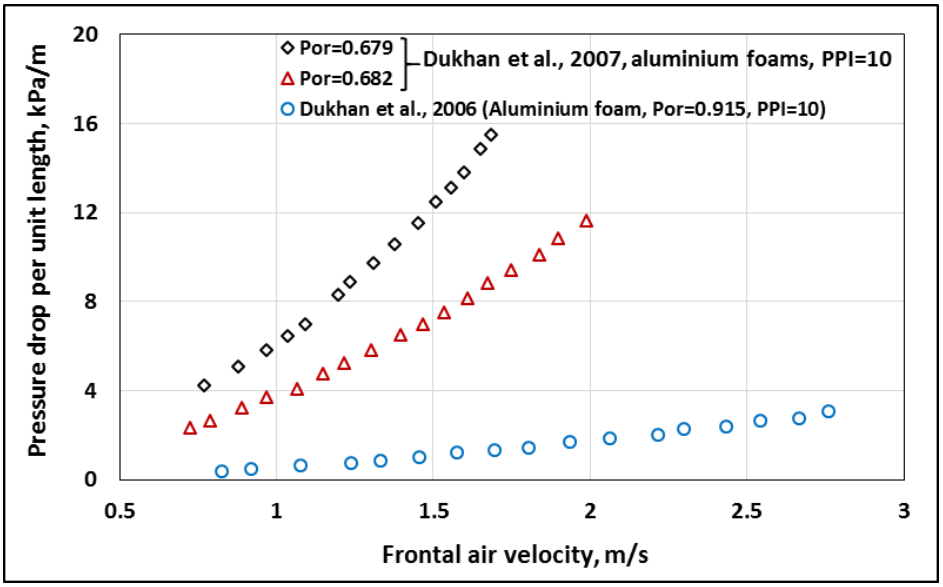

Figure 2-6 The effect of porosity on pressure drop

The porosity has a measurable effect on pressure drop, as clear from Figure 2-6. Decreasing the porosity from 0.915 to 0.682 increases the pressure drop by 7 times in the same class of metal foams. The pressure drop also increases by 1.7 times when the porosity decreases by only 0.3%.

Decreasing the porosity increases the pressure drop and inertia and drag coefficients while the permeability decreases in different base material metal foams with porosities between 0.68 and 0.97 and different pore sizes [17, 19, 39, 67, 68, 90, 103, 109, 112, 117-130]. The same authors found that the pressure gradient and inertia and form drag coefficients increase with decrease of pore size and permeability decreases. Whereas, Bhattacharya et al. [18] found the inertia coefficient depends only on porosity for aluminium foams with porosities ranged from 0.906 to 0.97 and pore densities from 5 to 40 PPI.

The increase of pressure drop and inertia and drag coefficients with PPI (or decrease pore diameter) was reported and the permeability was found to decrease with increase of PPI [39, 90, 120, 127, 131]. The effect of pore size on pressure drop is also significant. As clear from Figure 2-7, the increase in pore diameter by two times decreases the pressure gradient by 1.5 at fixed porosity in aluminium foams.

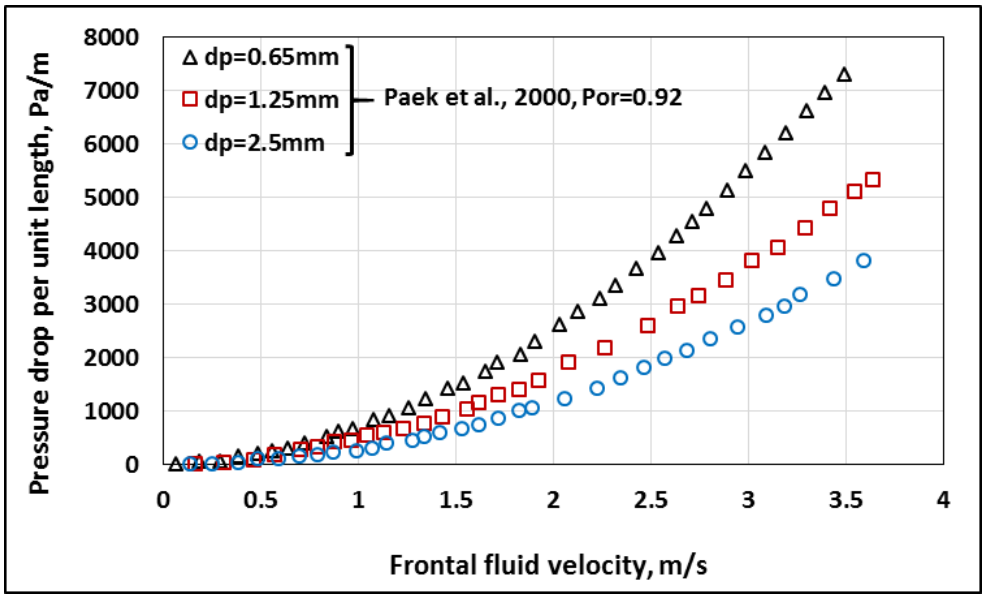

Figure 2-7 The effect of pore diameter on pressure drop

This is because the decrease in pore size and porosity results in an increase of surface area and blockage path of the flow , creating higher resistance for the flowing fluid.

The permeability in the Darcy flow regime has been determined for replicated aluminium sponges, sintered nickel and copper sponges of different porosities and pore diameter [41, 57, 132-135]. Shown in Figure 2-8 is the typical linear relationship of pressure gradient with frontal fluid velocity at the Darcy flow regime. This method is widely used to determine the permeability at the Darcy regime by using Equation 2.1. At these low flow rates, the linear relationship between pressure drop and flow velocity was observed, while pressure drop decreased with increase of both pore diameter and porosity.

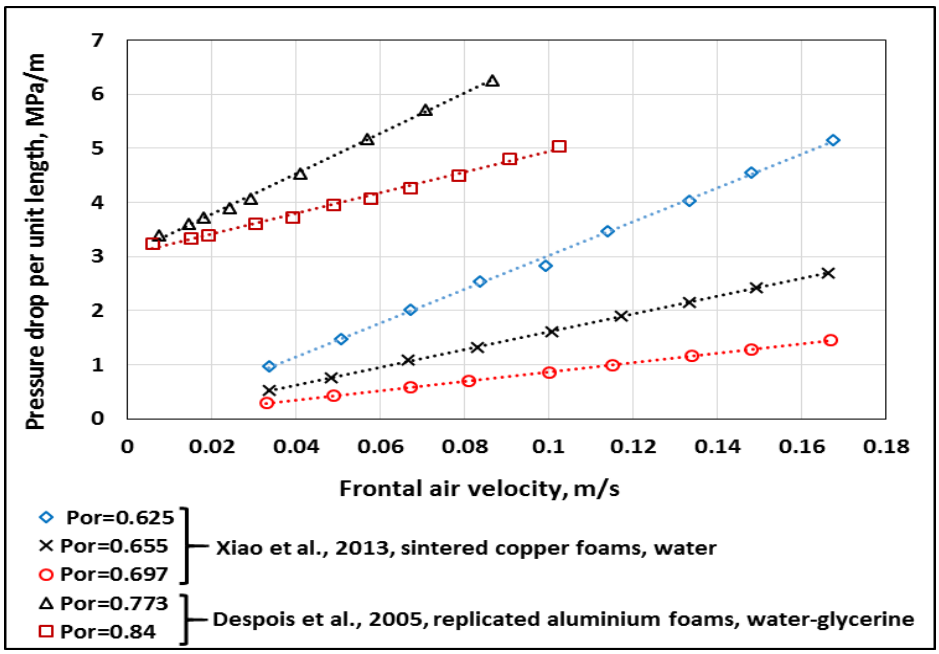

Figure 2-8 The typical linear relationship at Darcy flow regime

For the granular packed beds of particles, the permeability is commonly found by using the following equation [66, 77, 89, 136]

$$K = \frac{\varepsilon^3 {d_p}^2}{150(1-\varepsilon)^2} \qquad 2.7$$

The effect of different base materials (which can impact on the surface roughness) on pressure drop has been obsevered when metal foams with the same

porosity and PPI are examined [97, 137]. Inconel samples induced higher pressure due to their surface roughness compared with copper and NiFeAlCr foams. The copper foam provides higher pressure drop than FeCrAly [137]. Samples have also been compressed in order to reduce the porosity to enhance the specific area [96, 138]. Increasing the compression ratio increases the pressure drop and form and inertia coefficients, yet reduces the permeability [78, 96, 139].

In order to describe the hydraulic energy loss in nondimensional form, the permeability based friction factor is widely used to describe the hydraulic resistance in porous media [19, 39, 77, 90-92, 97, 115, 140]. A number of expressions have been demonstrated in terms of the permeability based friction factor as function of the Reynolds number. These expressions have been tested [39, 41] and no expression was found to be suitable for the tested samples. The likely source of inconsistencies is the material microstructure differences in terms of ligament shape and thickness [39, 41, 141]. Shown in Figure 2-9 is the friction factor against Reynolds number for different classes of metal foams. It is clear that the friction factor increases with decrease of porosity and equals $1/Re_k$ during the Darcy flow regime. It is also worth noting that the friction factor tends to inertia coefficient when the fluid velocity reaches infinity [39, 64] and at the turbulent flow regime [104].

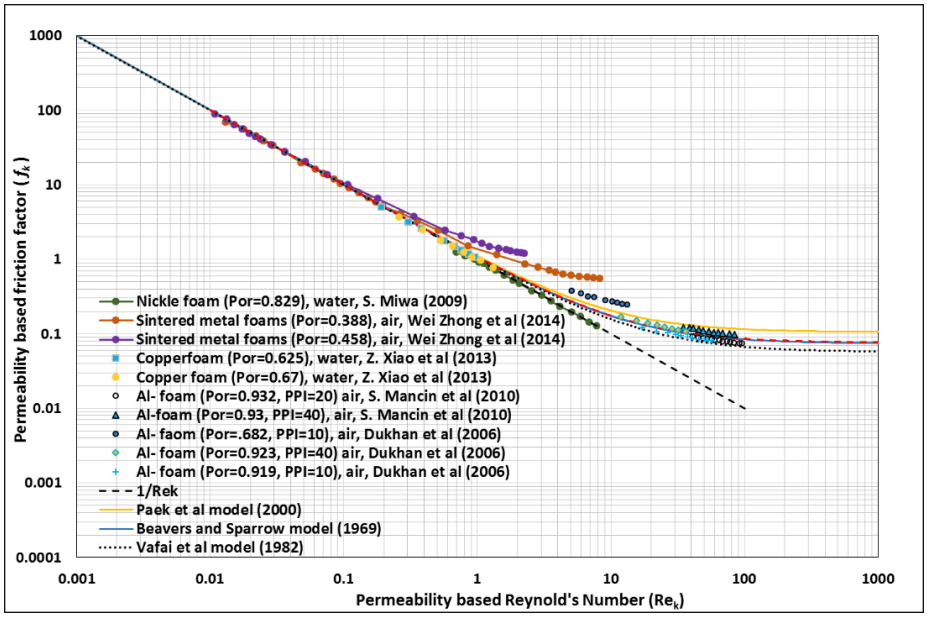

Figure 2-9 Permeability based friction factor against Reynolds number

The characteristics length used to determine friction factor is also an issue. Three different characteristics lengths have been reported in literature; pore diameter [76, 120, 142], the equivalent spherical diameter [103, 126] and the permeability [39, 90, 92, 97, 104, 127]. The most widely accepted in literature to describe the friction factor is permeability.

In order to compare the performance of different types of metal foams, it is necessary that the material properties are defined in a consistent way. Furthermore, the equations for characterising the flow should be consistently defined. This is not presently the case resulting in considerable variation in reported data.

The information about the flow regime borders in metal foams is still scarce and there has been disagreement about the points of transition from regimes. The morphological parameters in terms of porosity and pore size (or PPI) have been found to have a measurable effect on the transition bounds of the flow regimes [78, 90, 91, 104, 107]. In contrast, the roughness of the cell surface in terms of different base materials has also affected the transition boundaries [97].

Identification of flow regimes in porous materials is vital in order to quantify accurate hydraulic parameters. The most examined porous materials thus far have been those with high porosity. In contrast, the reported low porosity metal sponges have been examined only at low flow rates (Darcy regime) to find the permeability [41, 57, 132-135]. At relatively low porosities the information about hydraulic parameters in terms of inertia and drag coefficients is spare. As a result the effect of pore size and porosity has not been quantified. The contradiction in results for the same class and geometrical parameters of materials could be a result of the exhibition in different flow regimes as stated by Dukhan et al. [104]. Mancin et al. [39] also pointed out that the different approaches in terms of the friction factor failed to validate the experimental results as shown in Figure 2-9. Therefore, there is no approach which can be generalized to quantify the friction factor. The manufacturing defects' effect on the pressure drop is also uncommon in open literature. The variety of the porous materials parameters in terms of the

manufacturing technique used has been also mentioned as a cause of the discrepancies between results.

Permeability is a key parameter of the porous matrix and has been found to have different values in different flow regimes [66, 78, 97, 104]. The disagreement in the values of the hydraulic parameters, including permeability, inertia and form drag coefficients has been noticed for porous materials with the same porosity and microstructure [104]. This has been explained by the effect of the thickness along and perpendicular to the flow direction [128, 134, 143], exhibited in the values of those parameters at different flow regimes [67, 78, 104]. In contrast, a fairly conclusive body of evidence shows that increasing the porosity and pore size increases the permeability and decreases both drag and inertia coefficients [17, 19, 39, 68, 103, 109, 112, 117-126] . A number of approaches to predict the permeability in cellular material as a function of microstructure parameters (pore size and porosity) have been reported in literature [18, 116, 132, 144]. Inconsistency in the predicted permeability results with various aporoaches were reported [18, 132].

There have been a number of attempts to model the fluid flow through the metal foams analytically based upon the morphological network [17, 18, 39, 75, 116, 117, 145, 146]. Two methods of geometric modelling have been widely quoted in literature, based on different representative unit cells (RUC) [18, 75, 116, 117, 146, 147] and a simple analogy of the Forchheimer and Ergun's equations with equivalent specific area [17, 111, 117]. Although different RUC's of the foam geometry have been proposed depending on the porosity range, equivalent results have been exhibited for high porosity ($\varepsilon > 0.9$) with different models [17, 111, 146]. It has also been reported that high deviations have been observed at low porosities due to a change of strut shape and configuration with various porosities [18, 111, 146].

Analytical models based on the representative unit cell shapes have shown that no general model can be used due to the complexity in morphology of the microstructure [17, 39, 117]. Lu et al. [148] derived an analytical solution for pressure gradients in foams and used an analogous flow through a bank of cylinders. In

contrast, there have been a number of geometrical models for high porosity metal sponges based on a representative unit cell (distributed rectangular unit cell [116, 145], cubic cell [18, 74, 117], tetrakaidecahedron [75] and based on microstructure parameters measurements [39]).

Du Plessis et al. [145] and Du Plessis et al. [116] derived a model to predict the pressure gradient in Newtonian fluid flowing through the porous matrix based on the microstructure parameters. In these models, the concepts of the volume averaging approach were applied to the Navier-Stokes equation with uniformly distributed velocity and the representative unit cell shaped as a rectangular geometrical distribution in Cartesian coordinates [116, 145]. The configuration of the ligaments in the cell is comprised of two inclined across the flow direction and one aligned parallel to flow direction. In the above mentioned models, the permeability was normalised by the pore diameter and expressed in terms of porosity and tortuosity of the cellular matrix [116] as in Equation 2.8.

$$\frac{K}{d_p^2} = \frac{\varepsilon^2}{36X(x-1)} \qquad 2.8$$

Here the tortuosity (X) is defined as the ratio of the overall length of winding way available in the unit cell for the flow to the basic stream wise length scale in the cellular matrix and expressed as function of porosity [116, 149].

$$\frac{1}{X} = \frac{3}{4\varepsilon} + \frac{\sqrt{9-8\varepsilon}}{2\varepsilon}\, Cos\left\{\frac{4\pi}{3} + \frac{1}{3} Cos^{-1}\left[\frac{8\varepsilon^2 - 36\varepsilon + 27}{(9-8\varepsilon)^{3/2}}\right]\right\} \qquad 2.9$$

This model showed a good agreement with their experimental data for high porosity metal foams (0.973-0.978) and high pore density (PPI=45-100).

The other model was derived by the Bhattacharya et al. [18] by adapting the model of Du Plessis et al. [116] with the same final expression as in Equation 2.8 but estimated different unit cell structure. As they stated [18], the model used by Du Plessis et al. [116] was found to overestimate their samples permeability experiments results by the factor 1.4 to 1.7. They modified the expression of the

tortuosity and included the shape factor (G) that accounts the cross-section variation with porosity [18], and there has been a good agreement with their experimental results. The modified expression of the tortuosity as function of porosity and shape function is shown in Equation 2.10 [18].

$$\frac{1}{X} = \frac{\pi}{4\varepsilon}\left\{1 - \left[1.18\sqrt{\frac{(1-\varepsilon)}{3\pi}}\,\frac{1}{G}\right]^2\right\} \qquad 2.10$$

$$G = 1 - e^{-(1-\varepsilon)/0.04} \qquad 2.11$$

The shape factor and tortuosity expressions were modified to match the experimental results for the copper and aluminium foams [110]. The calibration coefficient 0.04 in shape factor expression was changed to 0.0283 for aluminium and 0.0336 for copper. The coefficient of 1.18 for the tortuosity expression was also changed to 1.08 and 1.25 for aluminium and copper foams respectively.

An approach which is based on the microstructure of the pores as bottlenecks which are formed by the ligaments of the solid phase material was derived by Despois and Mortensen [132]. In this model, along the fluid way the total resistance for flowing fluid is only that be faced within these bottlenecks. As they stated, a number of open cell porous materials almost contain spherical shape pores. The two types of open cell metal foams which can be categorized by this class of material are replicated metal foams and polymeric and moulded ceramics foams. In these open cellular materials, the bottlenecks are the windows that connect the adjacent pores together and represented as uniform circular bores. The final form of this model was expressed in terms of porosity (ε), initial packing porosity of the particles ($\varepsilon_0 = 0.64$) and the initial radius of the particles (r) as

$$K = \frac{\varepsilon\, r}{\pi}\left[\frac{\varepsilon - \varepsilon_0}{3(1-\varepsilon_0)}\right]^{3/2} \qquad 2.12$$

This model predicts that when the void fraction of the solid phase reaches 36 % the windows shrink and can be locked off.

Moreira et al. [144] proposed a correlation for the ceramic foams in terms of pore diameter and porosity. They started by using Ergun's Equation and a number of combinations were tested. They replaced the numerical values in Ergun's Equation by the fitting coefficients of the experimental data. The best fit was found when using the porosity and the pore diameter as the microstructure parameters. The final expression for this correlation is shown in Equation 2.13.

$$K = \frac{\varepsilon^3 d_p^{0.264}}{1.36x10^8(1-\varepsilon)^2} \qquad 2.13$$

The form drag force during the flowing fluid over the ligaments formed the porous network is quantified by the inertia factor. This factor is strongly dependant on porosity, strut thickness and shape, pore diameter and the shape of both the pore and fibre [18, 19, 52, 110-113]. The vital impact on strut shape and thickness has been noticed as a result of porosity change, different manufacturing techniques and different base material [111, 112, 114]. The fibre cross section shape is strongly depending on the porosity, which varies with the change of porosity [18, 32, 52]. Furthermore, the pore density (PPI) is also an apparent morphological parameter that has an impact on the hydraulic resistance. Increasing the PPI or decreasing the pore diameter increases the number of the fibres, and thus the flow resistance [18, 110]. The total flow resistance across the porous media is the contribution of both viscous and inertia forces [112]. Generally, the conducted measurements in this topic confirmed that the pressure drop in porous matrix follows the Forchheimer equation and permeability and inertia coefficient depend on the foam structure characterisations [17, 111].

The differences in manufacturing methods and the base materials also resulted in different strut morphologies, and thus the correlations based on analogy technique are also limited to describe the pressure drop [17, 111, 146]. From the review of the models, it has been noticed that the strut expressions presented the different dependences on porosity but same dependence on pore diameter [17, 111]. The source of discrepancies in results of the models is most likely due to the

characteristic length in friction factor and Reynolds number, which is also a subject of ambiguity [17]. Inconsistencies in results not only have been noticed in geometric modelling, but also in experimental results, where, at the same porosity different inertia coefficient values have been reported.

The models based on the RUC and analogy of Forchheimer and Ergun equations were developed and correlated with empirical factors to validate the experimental results. These models presented in terms of porosity, normalised permeability with pore diameter, tortuosity and strut diameter [18, 75, 116, 117, 145, 146]. A wide review of the pressure drop correlations was presented [17, 150] and were the only models which by Du Plessis et al. [116], Fourie et al. [75], Bhattacharya et al. [18] and Lacroix et al. [117] do not involve fitting coefficients from experimental data. These models can be adopted to predict permeability and inertia coefficient with deviation ± 30 % [17]. However, it has been stated that no model can be adopted to predict these hydraulic parameters at low porosities [111, 146].

The inertia factor was expressed as a function of porosity (ε), normalised permeability ($\frac{\sqrt{K}}{d_p}$) and tortuosity (χ) by Du Plessis et al. [116] and without tortuosity by Zhao et al. [151] respectively and is shown in Equations 2.14 and 2.15

$$f = \frac{2.05\chi(\chi-1)}{\varepsilon^3(3-\chi)}\frac{\sqrt{K}}{d_p} \qquad 2.14$$

$$f = C[(1-\varepsilon)^n]\frac{\sqrt{K}}{d_p} \qquad 2.15$$

The effect on which the sample behaves as a porous medium was examined when metal foams were presented in different thicknesses [124, 152]. The permeability and form coefficient were found to have fluctuate at medium thickness, becoming fairly constant at a certain value with increase of thickness. However, studies have not found any sensitive effect on pressure gradient as a result of the foam thickness [57, 153].

The available models have been reviewed and assessed against the experimental data [17, 39, 150]. Edouard et al. [17] have concluded that the models

provided by Lacroix et al. [117] and by Du Plessis et al. [116] were more appropriate to evaluate the pressure gradient in metal foams. It has been also pointed out by Mancin et al. [39] that the best estimations are those of Du Plessis et al. [116], Bhattacharya et al. [18] and Lacroix et al. [117] whereas that of Fourie et al. [75] gave results that under predicted the level for all experimental points.

Although previous analytical approaches have been based on a simple representative unit cell, recent researches have focused on 3D computed tomography scan imaging to obtain the real sponge structure [32, 52, 114, 154, 155]. This is an effective technique for quantification of the effect of real structural parameters such as strut size, shape, and cell shape on the thermal and hydraulic characterisations. The strut shape and size in metal foams was found to vary with porosity [18, 20, 32], where variations occur from a circle shape at a porosity of 0.85 to an inner concave triangle when the porosity reaches 0.97. The type of material and manufacturing process also play a measurable role on the microstructure parameters and may cause inconsistencies with analytical models [111, 112]. The results of numerical modelling based on CT-Scan of real structure metallic materials is well validated by the experimental results available in open literature[32, 52, 114, 154, 155].

2.2 Effective thermal conductivity of metal foams

Accuracy of data regarding heat transfer and the thermo-physical properties of metal foams is a prerequisite for the design and modelling of heat transfer applications incorporating metal foams [32, 71, 156, 157]. The conductive heat exchange phenomena in porous structures is complex and takes place in two phases of the material [20, 32, 70, 158]. These are the network of the ligaments of solid materials that has high thermal conductivity, and the fluid itself, which has low thermal conductivity. Although the basic principle of heat transfer in metal foams is conduction through both phases, the effect of convection and radiation cannot be necessarily neglected in all cases [36, 159]. The effective thermal conductivity of porous metal materials depends on the morphological parameters of the solid phase

such as its porosity and pore size. A further problem with these materials is that the repeatability of the morphology is not constant, even when the same manufacturing conditions are employed, resulting in an inherent scatter in the material properties unless very large samples are tested [19, 71, 160].

Maxwell [161] was the first to investigate the ETC in saturated fluid porous media [63, 162]. Although there are now a number of models to determine ETC in porous media focused on packed beds of spheres and cylinders [63, 162], they are not applicable to metal foams as a result of the considerable differences of morphological structure [63, 163].

The topic of ETC determination has received great attention, both theoretically and experimentally, with existing literature focusing on both lower and upper bounds of ETC [163]. A number of analytical and empirical correlations have been reported. These are based on one, two and three dimensional unit cells or arrangements of infinite cylinders, and based on the distinguished lower and upper bounds of ETC under the consideration of solid and fluid phase's thermal resistance arrangement (series or parallel) for one dimensional heat transfer [18, 70, 73, 156, 163-168]. The available models and empirical correlations have been reviewed and classified in three groups based on the applied methodological method. These are; asymptotic solutions, empirical correlations and representative unit cell models [168]. The asymptotic solutions correspond to the lower and upper bounds arrangement of ETC; the lower limit of the arrangement is in series and the upper limit of the arrangement is in parallel [70, 163, 168].

The effect of different manufacturing technique and the type of base material in terms of ligament shape and size on ETC has been reported, as well as the distribution of the pores and each phase [20, 71, 156, 160, 168-170]. A review of the theoretical and empirical approaches for the prediction of ETC in porous media reveals that each approach defines a specific morphology which is limited in terms of its application with other types of material [34, 71, 160, 167-169, 171]. Good results have been reported when approaches have been calibrated by the experimental

fitting coefficients [168, 169, 171]. Figure 2-10 depicts the discrepancy of selected models with reported experimental results. At the relative low porosities, the ETC is underestimated while at high porosities are overestimated. One of the most likely causes for these inconsistencies is the differences between the assumed unit cell shape in analytical models and the actual shape. Manufacturing defects are also a possible source of the inconsistencies, closed cells and inclusions (common in low porosities) increase the ETC whilst missing cells or ligaments (common in high porosities) decrease the ETC [34, 172].

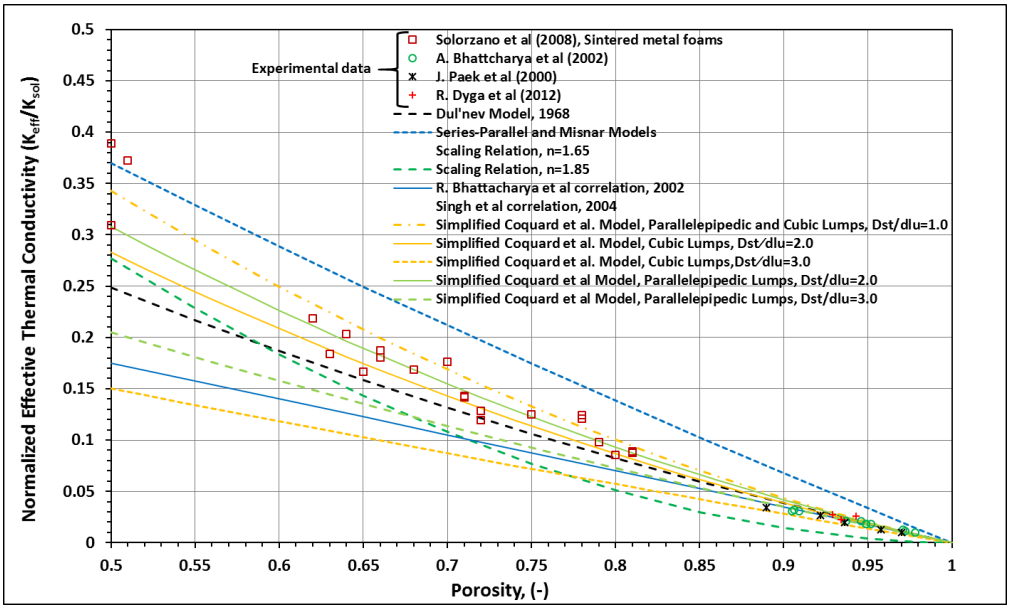

Figure 2-10 The models and experimental results of ETC against porosity

In other cases, researchers have relied heavily on experimental work in order to measure ETC and validate the models' results. Both steady state and transient techniques have been widely accepted to measure the ETC of metal foams [18, 19, 34, 36, 70, 158, 171, 173-175]. In the transient method, the temperature gradient through the sample is measured instantaneously with time. The most common transient method used is the Transient Plane Source (TPS) [176, 177]. TPS has been widely used to measure the ETC of porous materials [34, 71, 174, 175]. On the other hand, the steady state method has been also used. Its principle is to measure the temperature difference normal to the tested surface at thermal equilibrium. There

are a number of steady state methods which have been used to measure the ETC in porous materials [18, 19, 36, 70, 158, 159, 171, 178, 179].

The porosity of the metal foams varies with the volume of the solid phase and it was found to have a significant effect on the effective thermal conductivity, decreasing as the porosity increases [18, 19, 34, 70, 159, 180, 181]. The effect of morphological parameters (porosity and pore size) on the process of heat transfer in metal foams is hard to generalize. This is because the contact points between the solid ligaments differ with the manufacturing process and porosity. It should be noted that the sintered metal foams provide a higher effective thermal conductivity than non-sintered materials due to better solid-solid contact area [182].

The measurement results show that the porosity of porous materials has a highly sensitive effect on ETC, increasing as porosity decreases [18, 19, 34, 70, 159, 171, 180, 181]. Figure 2-11 illustrates the effect of porosity on ETC, it is clear that the ETC of closed celled porous materials is higher than those of open celled due to microstructure differences [171].

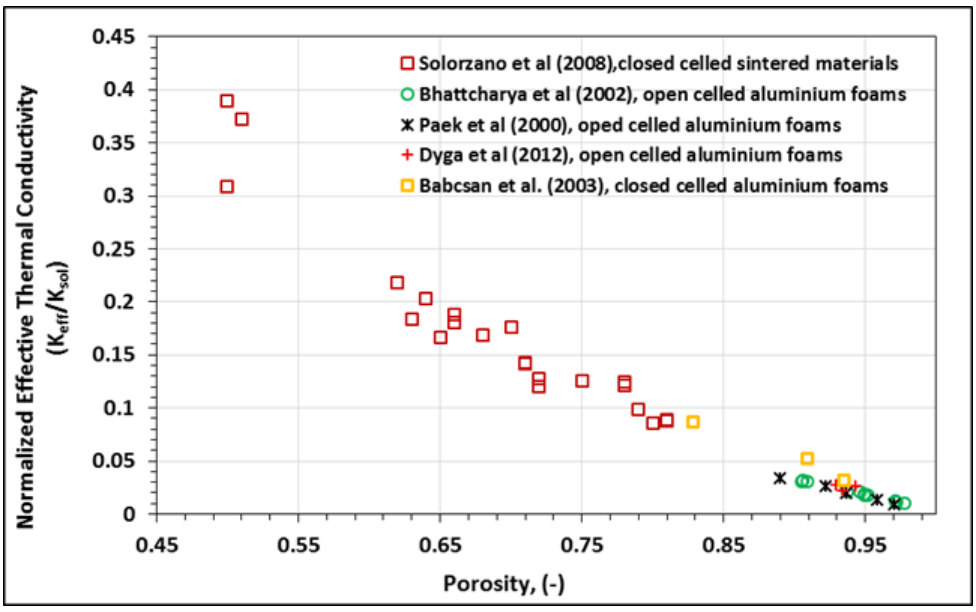

Figure 2-11 ETC against porosity for different class of materials

The pore size effect on ETC has also been studied and no significant influence has been reported at moderate temperatures [18, 19, 70, 158, 171, 183], provided

the pore size is below a certain value shown to be 4 mm diameter in closed cell polymer foams, which is sufficient to suppress convection [50, 184, 185]. In contrast, the effect of pore size has been reported at high temperatures when the thermal radiation contribution cannot be neglected, where radiation contribution increases with pore size and temperature [159, 167, 169, 183]. No measurable effect on ETC has been reported by radiation at temperatures less than 300°C [36, 183]. The contribution of radiation to the effective thermal conductivity at 800°C has been found to be three times more than that at room temperature [159].

Moreover, the contribution of natural convection in ETC measurements cannot be neglected in all cases [169, 171], indeed, the natural convection contribution was found to increase with fluid thermal conductivity [158] as compared to vacuum measurements [159, 183]. It was also found to increase with porosity as a result of an increased pathway for to air to move is provided [171].

As the shape and size of fibres and interconnection junctions vary with solid phase material type, porosity and manufacturing technique, no generalized model can be used [20, 50, 167, 171, 185]. The methodological strategies take the way of analysing the real internal structure of the foam obtained by 3D Scan computed tomography [71, 114, 168, 175]. This technique becomes acceptable to support the improvement of more accurate generic correlations and models [36, 71, 167]. The numerical simulation based upon 3D Scan computed tomography to estimate the ETC of porous foams shows an excellent agreement with experimental results at high porosities [32, 36, 114, 175]. This method can provide a viable alternative in comparison to the experimental effort. However, the ETC due to pure conduction transport still needed as input for simple models based on this technique [36].

Following this comprehensive review of the existing literature, it can be concluded that most of the reported results in the topic of ETC are focused on high porosity metal sponges. The only reported measurement results for low porosities were for closed celled metal sponges [34]. Although there are a significant number

of analytical and empirical models to predict the ETC published in open literature, no general approach can be used to predict the ETC at relatively low porosities. Some of these are examined and calibrated by fitting coefficients based on the experimental measurements to validate the results [18, 70, 165, 167]. Therefore, measurements of ETC at low porosities of metal sponges are indispensable due to the insufficiency of information in this range of porosity.

2.3 Convective heat transfer in porous media

Convective heat transfer in porous materials is still a formal and complex subject due to the intricate microstructure and the heterogeneity of pores and ligaments [52, 55, 186]. The enhancement of heat transfer in porous media can be achieved by two major mechanisms [47, 48]. Firstly, ligaments orientated normally to the flow direction provide tortuous pathways to enhance the flow mixing and promoting vortices [63, 159, 187]. Secondly, boundary layer disruption increases the fluid turbulence [47-49, 52]. They also play a measurable role in extended heat transfer surfaces due to high thermal conductivity [36, 47, 48, 55, 188].

The demand to improve the heat transfer enhancement at surfaces has sharply increased in recent years [12, 13, 127, 188]. The development of cellular materials has become a competitive and alternative solution as a potential choice for many applications due to their characteristic features [13, 55, 127, 148]. Accordingly, theoretical and experimental studies of convective heat transfer performance in cellular materials has received considerable interest over the past decade and has achieved substantial growth and attention in the thermal research area [69, 72, 127, 148, 189].

In thermal regenerators and heat exchangers, the convective heat transfer in the prism can be described in terms of number of transfer units (NTU_m) [8, 21, 22, 24, 28, 190-197], convective and volumetric heat transfer coefficients (h, h_v) [11, 28, 48, 54, 59, 64, 69, 121, 122, 130, 186, 198-203] and Nusselt number (Nu_{vdp}) [5, 23, 47, 48, 52, 54, 69, 72, 122, 127, 188, 189, 198, 199, 204-213]. Two types of convective

heat transfer coefficients have been used to characterise the heat transfer in porous media: the wall or global heat transfer coefficient (h) and the interstitial or volumetric heat transfer coefficient (h_v) [122]. The wall heat transfer coefficient determines the universal extent of heat transfer enhancement from the attached porous media to wall surfaces. Utilization of this coefficient is useful for designing cooling electronic applications [30, 69, 122, 212, 214-217]. The volumetric coefficient gives the heat exchange between the solid phase matrix and the flowing fluid stream and can be applied to compact heat exchangers and energy storage devices [5, 16, 48, 122, 202, 203, 218].

The number of transfer units is the indicative parameter that accounts for the size of heat exchangers and thermal regenerators and the amount of thermal energy that can be transferred. It is also a dimensionless parameter that determine the effectiveness of these thermal applications [8, 219]. The NTU_m can be expressed in terms of convective and volumetric heat transfer coefficients as shown in Equations 2.16 and 2.17.

$$\mathrm{NTUm} = \frac{h\, A_h}{\dot{m}_f C_f} \qquad 2.16$$

$$\mathrm{NTUm} = \frac{h_v V_s}{\dot{m}_f C_f} \qquad 2.17$$

where A_h is the heat transfer area, V_s volume of the prism, $\dot{m}_f$ the fluid mass flow rate and C_f the fluid specific heat.

The convective heat transport phenomena in porous media has been predominantly investigated using three methodological techniques; experimentally, analytically based on unit cell geometry and numerically based on 3D CT-scan tomography [52, 72]. Steady state and transient experimental techniques have been widely used to measure convective heat transfer performance [47, 48, 198]. A significant number of experiments have been performed to study the thermal features of open celled metal foams [53, 213].

The measurement of structural parameters of porous materials such as, specific area, windows size and pore diameter is difficult [11, 186]. The structure of the metal foams is complex and results in difficulties and insufficient accuracy in temperature gradient measurement at pore scales [11, 52]. This can also result in an unreliable heat transfer area and will affect the global or wall convective heat transfer coefficient. Consequently, a number of researchers have adopted the volumetric heat transfer coefficient as the governing volume averaged energy equations can be solved analytical and numerically [11, 52].

The forced convective heat transfer is analysed by both microscopic and macroscopic approaches. The former involves the numerical simulation of the flow in a representative two phase system. The macroscopic approach is the integration of the transport governing equations over the entire control volume and categorized into one equation or two equations models [11, 70, 72, 202].

The Local Thermal Equilibrium (LTE) model has been used to describe the temperature gradient in a two-phase medium by assuming the solid and fluid phases are in thermal equilibrium and hence can be described by one energy equation [11, 54, 69, 115, 203, 210]. In this case, the dominant heat transfer mode is thermal dispersion [203]. Thermal dispersion occurs due to fluid movement in a complex solid skeletal structure and is a hydrodynamic phenomenon predominant at high flow rates [69, 122]. Calmidi et al. [69] stated the thermal dispersion can be neglected when the fluid to solid phase thermal conductivity ratio is very small (<<1) for example if air is the working fluid. This model is not appropriate for some situations, such as thermal energy storage devices, unsteady heat transfer and when the heat transfer is combined with heat generation or radiation [48, 220, 221]. The validity of this approach is also restricted to low Reynolds numbers [55, 148, 187, 222] and when there is no difference between the solid and fluid temperatures [54].

The Local Thermal Non-Equilibrium (LTNE) model accounts for the convective heat transfer between two phases with two separate energy equations [11, 54, 69, 115, 203, 210]. The volumetric heat transfer coefficient governs heat transfer [11, 52, 54, 202, 203]. Models of this type are more general and are a more realistic

representation of heat transfer in porous media [148, 223, 224]. They can be applied to transient processes where the fluid and solid temperatures difference is larger than those at steady state due to the shorter time period [203].

An understanding the influence of morphological parameters in terms of porosity, pore size (or PPI) and fibre (ligament) diameter on thermal characteristics is essential for designing different applications. The convective heat transfer coefficient (h), volumetric heat transfer coefficient (h_v), volumetric Nusselt number (Nu_{vdp}) and number of transfer units (NTUm) were measured in different base material types of metallic foams and traditional porous media [5, 8, 21, 47, 48, 51, 52, 57-59, 64, 69, 121, 122, 187, 188, 195, 197, 199, 225]. Two heat transfer coefficients h and h_v have been found to increase with a decrease of porosity and increase of frontal fluid velocity and Reynolds number [5, 8, 21, 47, 48, 51, 52, 57-59, 64, 69, 121, 122, 187, 188, 195, 197, 199, 225]. The effect of porosity on convective heat transfer coefficient can be seen in Figure 2-12. Increasing the frontal flow rate subsequently increases the interstitial flow velocity and decreasing the porosity, while also increases both the interstitial velocity and specific area. Increasing both of these factors; specific area and interstitial velocity, increases the value of h. The decrease of h below a certain value of porosity is most likely due to the decrease in specific area.

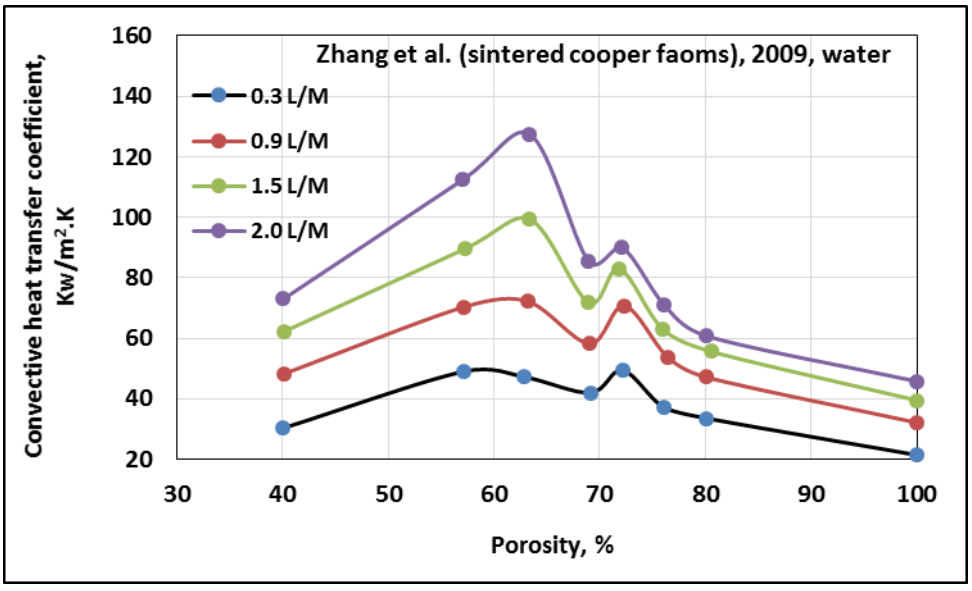

Figure 2-12 The effect of porosity on convective heat transfer coefficient

Contradictory findings regarding the influence of pore density (PPI) on the thermal characterisations in metal foams has been reported in published results [127]. In some situations, when decreasing the pore density, the convective heat transfer coefficient has been found to increase [51, 59, 64, 121, 225]. In contrast, the increase of convective and volumetric heat transfer coefficients has been reported with an increase of pore density (decrease of pore size) in different types of metallic foams [11, 28, 48, 54, 130, 186, 197-201]. The thermal performance parameters were also found to increase with the decrease of particle diameter and pitch size in packed beds of spheres and mesh wire screens [5, 6, 16, 23, 24, 197, 226-229]. The decrease of porosity and pore size was reported both with higher interstitial (or pore) velocity and heat transfer area, which led to enhancement in thermal performance in terms of convective and volumetric heat transfer coefficients [40, 48, 122, 199, 200, 230, 231]. Figure 2-13 shows the effect of different combinations of microstructure parameters for different types of solid phase base materials on h_v.

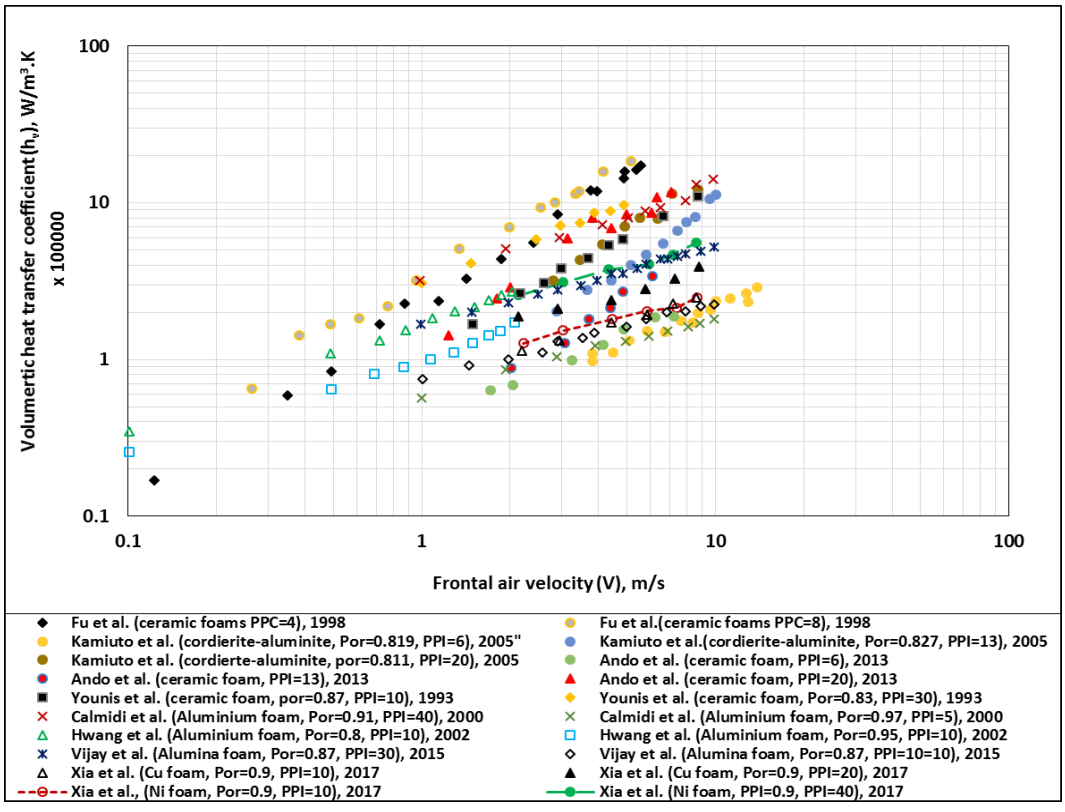

Figure 2-13 The effect of microstructure on volumetric heat transfer coefficient

The convective heat transfer performance in porous media is also presented in non-dimensional parameters in the forms of Nusselt number (Nu_{vdp}) and the number of transfer units (NTUm). The characteristic length term used to quantify the Nusselt number is also of specific interest as it is used as particle diameter or pore diameter in granular packed beds and metal foams [9, 11, 16, 47, 48, 122, 199, 200, 224, 226, 232, 233]. Alternatively, the equivalent strut or fibre diameter, equivalent spherical diameter, sample thickness along or perpendicular to the flow, hydraulic diameter and square root of permeability were also used to determine the Nusselt number [5, 23, 43, 52, 54, 69, 72, 127, 189, 198, 205-212].

With an increase in Reynolds number, the Nusselt number increases for all types of porous media [5, 16, 47, 48, 54, 69, 122, 127, 199, 210, 212, 226, 234]. Although there is no significant effect of pore density on Nu_{vdp} reported, the proportional increase of Nusselt number with pore density has been observed [127, 234] as shown in Figure 2-14. Moreover, the substantial heat transfer augmentation in terms of Nusselt number has been also observed with low permeability mediums and lower porosities [72, 210, 212], whereas in such cases the higher permeable foams were found to provide higher Nu_{vdp} [69].

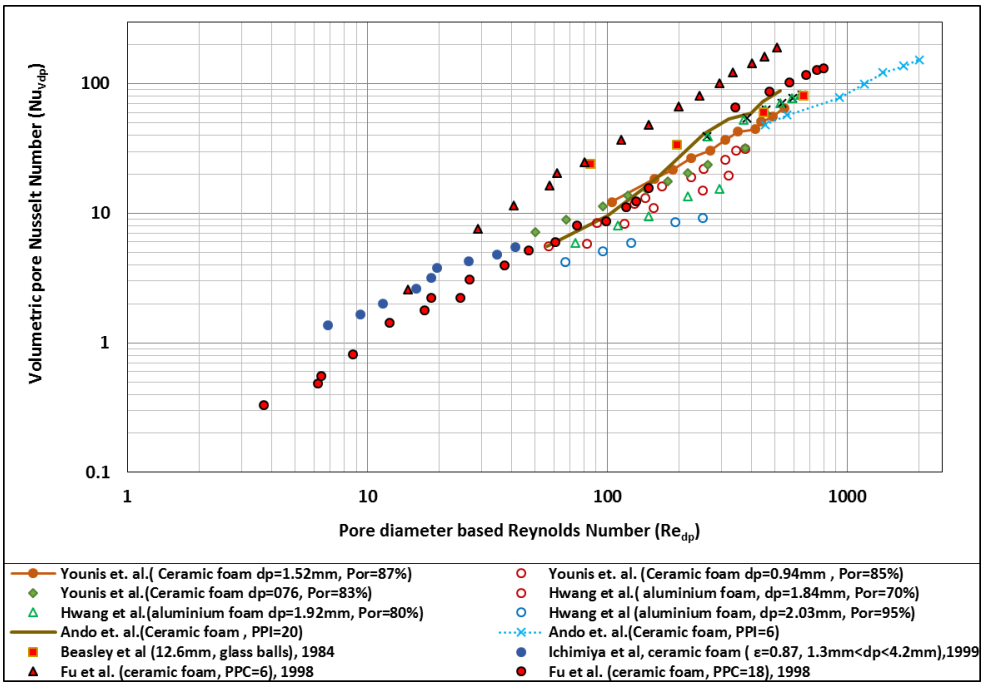

Figure 2-14 Nusselt number against Reynolds number for different of metal foams

The porosity and pore size impact on Nu_{vdp} was also observed [47, 48, 122, 130, 199, 207, 224], as was the material type, which was predominantly determined by the change in thermal conductivity [199]. The sample thickness has been also been found to effect the Nu_{vdp}, as when the thickness increased, the Nu_{vdp} also increased [12, 208, 217].

The decrease in porosity and pore size and the increase in thickness result in an increase of the solid-fluid surface interface area and an increase in pore velocity. These combined effects are the most likely the cause for the thermal performance to increase in terms of Nu_{vdp}.

There is a demand for improvements in convective heat transfer in micro-electronic cooling systems due to the sudden increase in heat generation in integrated circuits, which is expected to increase in the future [14, 148, 235]. To meet this challenge, the design of more efficient cooling sinks for these applications is essential by using metal foams in order to augment heat transfer [14, 43, 148, 217]. Previous investigations have shown that aluminium metallic foams cooling sinks are more efficient compared with commercial ones [30, 69, 212, 214-217]. Another possible solution is the utilisation of cellular materials in boiling heat transfer applications to improve the thermal performance by absorbing more dissipated heat [14, 207, 236]. In the subject of extended heat transfer surfaces, metal foams have been investigated and found to be more efficient compared with different commercial kinds of heat exchangers and empty channels [12, 31, 131, 237, 238].

In thermal energy devices and chemical reactor applications, the most commonly used forms of porous structures are packed bed of spheres and mesh wire screens [8, 15, 21-24, 28, 190, 193, 196, 232, 239-241]. Alternatively, metal foams have the potential to provide a more competitive class of materials in these applications and provide better thermal performance due to their structural features [8, 15, 28, 197]. The packing arrangement of the particles and the material type were also found to have a measurable impact on pressure drop and thermal performance

of thermal regenerators [16, 242]. Although, in most of the single blow models, the holder effect has been excluded, as it has been found to decrease the effectiveness of thermal regeneration by 18% [196].

The most commonly used non-dimensional parameter in thermal storage devices and heat exchangers to assess the thermal performance is the NTUm. The NTUm value decreased with an increase of Reynolds number, pore size and porosity [8, 21, 22, 24, 28, 190, 193-197]. This is attributed to an increase the of solid-fluid interface area attributed to the decrease in porosity and pore size. This also increases the interstitial velocity which is the most likely cause for enhancement of heat transfer in terms of turbulence and dispersion. With increasing flow rate or Reynolds number, the total energy content in the flowing fluid increases and a certain amount of this energy can be transferred based on the interface surface area. This explains why the increase in flow rate causes a decrease of the NTUm.

The theoretical analysis of heat exchange between the flowing fluid and the fibres surfaces at pore scales based on a well-known representative unit cell has been carried out [53]. Using analytical approaches, the internal structure of the foam was simplified as cylinders and rods in a periodic array [243] and a cubic periodic arrangement [223]. The cylindrical ligaments with cubic nodes of tetradecahedron shape was demonstrated first by Lord Kelvin [244] is commonly used [11, 35, 164, 202].

The alternative approach used to define the geometrical structure of the foams uses a 3D Computed Tomography Scan (3D CT-scan) which defines the real internal structure of the foam [32, 52, 53, 72, 155]. The good agreement for predicting the convective heat transfer coefficient based on real structure simulation has been reported compared to those based on a representative cell shape [53]. These approaches need a supportive experimental bank of data over a different range of porosities to provide for validation.

As evident from this review, there is an inconsistency in the literature as there is no generalized characteristic length used to describe the non-dimensional parameters such as Reynolds and Nusselt numbers. The variety of sample thickness might influence the thermal results [122, 203]. It is also the case that the comparison is made sometimes between completely two different microstructures as a result of different manufacturing techniques [203]. The results from different experimental techniques (steady state and transient) is also a possible source of contradiction in results as mentioned by Fuller et al. [47].

In the topic of convective heat transport phenomena most of the published literature has focused on high porosity materials. Generally, the convective heat transfer coefficient has been found to increase with a decrease of porosity. The only work to achieve the optimum porosity was conducted by Zhang et al. [58], in sintered copper sponges by single phase flow of water. The numerical and analytical approaches based on the representative unit cell in some cases contradicted the experimental results due to ligament geometry [53] and the inclination of cell and strut tapering [52, 245]. The simulation based on CT-Scan generation of the real internal structure has been shown to be more efficient than numerical modelling based on a representative unit cell compared with measurement results [52, 53]. This technique still needs reliable experimental results for validation at relative low porosity with different working fluids.

This project aims to study the convective heat transfer through relative low porosity metal foams with different pore diameters. The current metal foams can be assumed to be a different class of cellular porous materials according to the relevant manufacturing technique. This study also aims to explore the potential to use these materials as thermal regenerators in terms of NTUm and h_v and extended heat transfer surfaces in terms of Nu_{vdp} and h. The transient method (single blow technique) was adopted to measure the thermal characteristics.

Chapter 3

3. Experimental methods and processing techniques

3.1 Steady state pressure drop measurements

Transport phenomena in porous materials has been a topic of interest in a number of research studies. The porous matrix structure is complex and is composed of random fibres and struts that form tortuous passages [32, 64, 187]. The fluid undergoes continuous changes in direction and throttling through the cell windows resulting in high pressure drops [77, 104]. As the result of the complexity of the matrix, the exact solutions of the transport equations are difficult to obtain. There have been various attempts to model the transport phenomena in porous materials [17, 18, 111, 117, 146, 147]. However, no model can be generalised and a wide range of predicted pressure drops have been reported as a result of differences in strut shape [18, 111, 146]. Therefore, the experimental study of the pressure drop remains an effective method of understanding flow in porous media [39, 104].

3.1.1 Pressure drop analysis and hydrodynamics parameters determination

Understanding the pressure drop induced by the metal sponges during fluid flow applications is importance for the design and measurement of hydraulic parameters [39]. These parameters are permeability, inertia coefficient and drag coefficient. The porous materials are characterized by permeability (K), friction factor (f) and form coefficient (C_E). These above parameters are defined by (Darcy and Forchheimer–extended Darcy) equations [18, 19, 39, 78, 80, 117, 121, 246].

$$\frac{\Delta P}{L} = \frac{\mu}{K} V \qquad 3.1$$

$$\frac{\Delta P}{\Delta X} = \frac{\mu.V}{K} + \frac{\rho.f.V^2}{\sqrt{K}} = \frac{\mu.V}{K} + C_E.\rho.V^2 \qquad 3.2$$

The most commonly used methodology that has been adopted to determine these parameters is the use of a curve fitting technique of the pressure drop and flow measurement data [39, 67, 90]. The pressure gradient in the Darcy and Forchheimer equations is reduced by the frontal fluid velocity in order to identify the flow regime.

$$\frac{\Delta P}{\Delta X}\frac{1}{V} = a \qquad 3.3$$

$$\frac{\Delta P}{\Delta X}\frac{1}{V} = a + bV \qquad 3.4$$

The inertia coefficient accounts for the contribution of the inertial forces into the hydraulic resistance and strongly depends on the internal cell curvature [82] and roughness of the pore surface [97, 247]. The Forchheimer or extended Darcy equation (Equation 3.2) is widely adopted to describe the pressure gradient in metal foams at higher flow rates [18, 39], where *a* and *b* are determined and used to calculate the porous media properties [18, 19, 39, 66-68, 78, 91, 93, 96, 107, 117, 139, 143, 248].

In order to find the constants *a* and *b* in Equation 3.4, the least squares method was applied to the pressure and velocity measurement data. There have been two methods to estimate *a* and *b*; using regression analysis of Equation 2.5 or Equation 3.4 [18]. Antohe et al. [96] found that the final results of permeability and inertia coefficient estimated by the parabolic fit had a higher error compared with a linear fit. However, Bhattacharya et al. [18] examined the two methods and found the difference in the values of *K* and *f* can be neglected. The linear fit is more widely accepted and is more convenient to use [18, 19, 39, 66-68, 78, 91, 93, 96, 107, 117, 139, 143]

$$k = \frac{\mu}{a} \quad , \quad f = \frac{b\sqrt{K}}{\rho} \quad , \quad C_E = \frac{b}{\rho} \qquad 3.5$$

The fitting coefficients *a* and *b* of pressure and flow experimental data are used to find the porous materials characteristics [39, 67, 90]. The permeability was determined in the Darcy regime (Equation 3.3) and the inertia and form coefficients at Forchheimer regime (Equation 3.4).

3.1.2 Friction factor

The friction factor predicts the energy dissipation due to friction loss at any flow rate and can be used to estimate the required pumping power for an application. It has been used to describe the pressure loss across several types of

permeable medium [142] and has been presented in a number of recent studies [39, 84, 87, 91-93, 104, 106].

The square root of permeability is generally accepted as the characteristic length for the Reynolds number and friction factor [19, 39, 41, 78, 90, 92-97, 127]. In this case the friction factor (f_k) is expressed as

$$f_k = \frac{\left({}^{dp}/_{dx}\right)\sqrt{K}}{\rho V^2} \qquad 3.6$$

In Darcy's regime this simplifies to (Equations 2.1 and 3.6)

$$f_k = \frac{1}{Re_k} \qquad 3.7$$

Within the Forchheimer regime the friction factor can be found using the Reynolds number and a constant (F) [19, 92, 115, 127, 249]

$$f_k = \frac{1}{Re_k} + F \qquad 3.8$$

Dybbs and Edwards [106] calculated the friction factor for packed beds of spheres and they found f_k behaved according to the following relation

$$f_k = \frac{C_1}{Re_K} + C_2 \qquad 3.9$$

Where the constants C_1 and C_2 depend on the structure of the porous media and are adjustable, these are the same as used in the Ergun correlation. Equation 3.9 has been recommended for application to porous media as opposed to Equation 3.8 [104].

3.1.3 Pressure drop experimental setup

Shown in Figure 3-1 is a schematic of the experimental setup for the measurement of pressure drop at low flow rates. It consisted of an open circuit wind tunnel of cylindrical cross section, made using 2 inch ABS plastic pipe and fittings. The measured internal diameter was 52.9 mm. In order to ensure the fluid flow was fully developed before entering the test section, the pipe length was 138 diameters in length. This length should be greater than the entrance length which was determined using $L_e/D = 0.06\ Re$ [250]. The test section was approximately 60 mm long and built

made using ABS plastic pipe with same diameter of the main pipe as shown in Figure 3-1(b).

The air was provided by the laboratory's compressed air supply which was passed through a tank to damp any fluctuations. A needle valve was also used to precisely control the flow rate. Flow rates and pressure drop measurements across the samples were taken with the flow at steady state conditions. To check for leakage, the test stand was closed from both sides and pressurised to 3.0 bar for 24 hours.

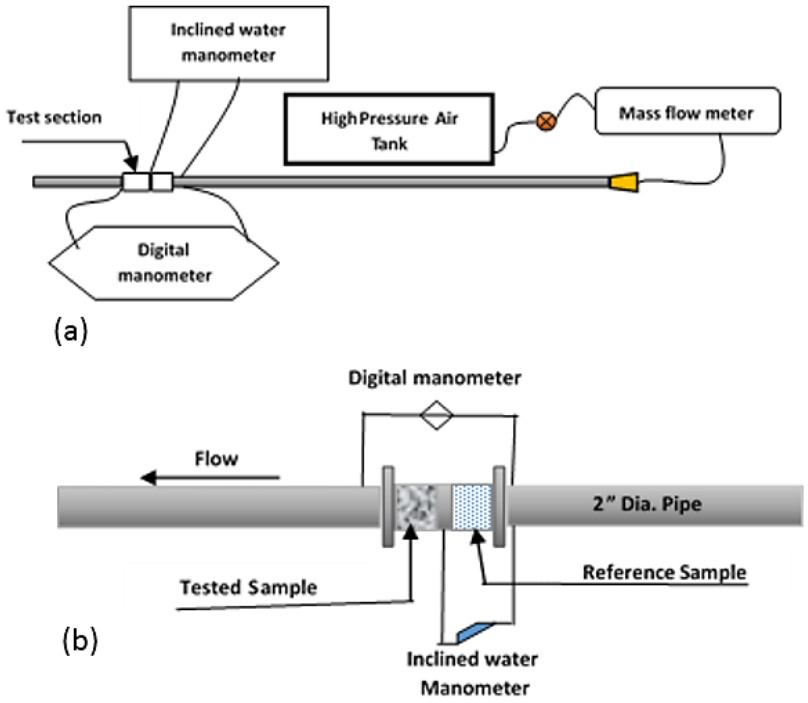

Figure 3-1 (a) Layout of the experimental apparatus for the low flow hydraulic measurements; (b) Schematic of test section with tested and reference samples

At low flow rates (creeping flow), the pressure drop across the metal foams was small. To improve the accuracy of the pressure measurements a reference sample was used to increase the pressure drop in conjunction with the test sample as recommended by Dukhan et al. [104]. The reference sample was an extended thickness aluminium foam with small porosity and pore size. Three pressure taps were provided before and after the samples and were connected to pressure measuring instruments as shown in Figure 3-2. The pressure drop was measured by inclined liquid and digital manometers.

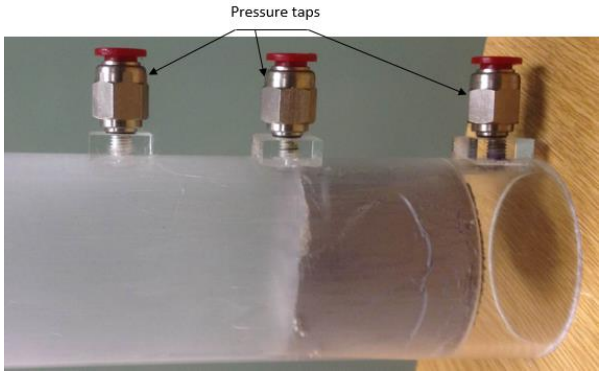

Figure 3-2 Test section with pressure taps

The pressure drop across the sample was found by using the difference of two measurements. The pressure loss across the both samples was measured using a digital manometer (Furness Controls Limited FC016 with accuracy of ± 1% of reading). The pressure drop across the reference sample was measured by an inclined liquid manometer. To prevent air bypassing between the sample and holder wall, layers of PTFE tape were used as a seal. The flow rate was measured by a Roxspur air mass flowmeter (FFLM0035) with the range of 0.5 LPM to 50 LPM with accuracy of (0.8% of reading + 0.2% FS). Flow rates above this range were measured with an Omega air mass flow meter (FMA-LP1600A) with the range of 2.5 LPM to 500 LPM with accuracy of (0.8% of reading + 0.2% FS).

In order to measure the air properties, a K-type thermocouple was inserted before the test section to measure the temperature. The atmospheric pressure and temperature were also measured.

The high flow rate experimental test rig was designed and built to study both hydraulic and thermal air flow through porous matrices, such as metal foams, packed bed of ball bearings and mesh wire screens [28]. A schematic of the test rig used for high flow rates pressure measurements is shown in Figure 3-3.

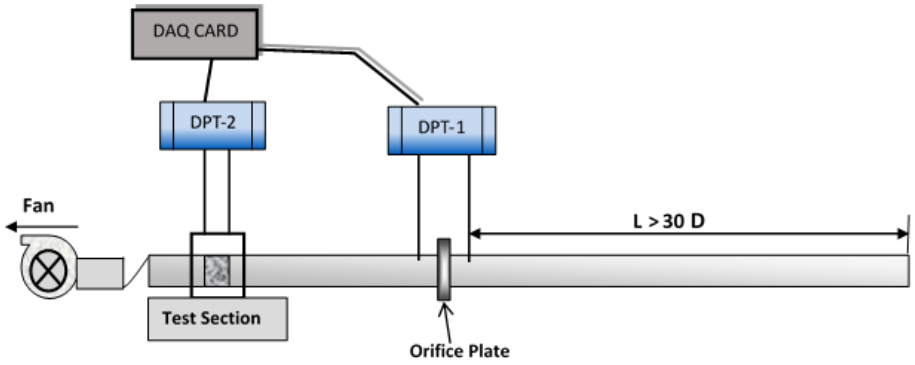

Figure 3-3 Layout of the experimental apparatus used for high flow rate pressure measurements

To conduct both pressure drop and thermal experiments, the test rig included two test sections. Section A was used for conducting pressure drop tests and consisted of ABS flanges used to hold the sample. Two pressure taps were provided before and after the sample and were connected to an Omega differential pressure transducer DPT-2 (DPGM409DIFF-350HDWU, 0.08% combined linearity). To prevent air bypassing between the sample and wall, layers of PTFE tape were used as a seal. The air flow rate was measured using an orifice plate connected to a differential pressure transducer, DTP-1 (Furness Controls –Model 332- 4W). This orifice plate was designed according to ISO Standards [251, 252]. The positions of the pressure taps were located according to the standards in BS EN ISO 5167-1 [252]. The orifice plate and differential pressure transmitter were calibrated against a flow meter (Cussons Technology P7250) [28]. The discharge coefficient of the orifice plate was found to equal 0.632 with maximum deviation of 0.5% [28]. The flow was passed through a pipe of 30 D length to ensure it was fully developed turbulent flow prior to the orifice plate. This length was determined using $L_e/D = 4.4\ Re^{1/6}$ [250]. The air flow was drawn into the rig by two centrifugal fans. An 8 amp variable transformer was used to control the input current to the fans and control the air flow rate.

To determine the mass flow rate, the atmospheric air density was required; it was found by measurements of ambient temperature (mercury thermometer) for pressure measurements and by a thermocouple inserted before the orifice plate. The pressure loss through the samples was measured at 15 different flow rates, over the range of velocities from approximately ≈1.3 m/s to 7 m/s (170 LPM to 920 LPM).

The pressure losses across the samples were measured at a range of flow rates from 0.5 LPM to 500 LPM at steady state conditions. The measurements were repeated three times at each flow rate. Sixty-eight aluminium foams, three mesh wire screens and two packed beds of steel balls were tested.

3.2 Porous materials effective thermal conductivity measurements

There are two techniques widely used to measure the ETC in porous materials; steady state and transient. The transient method was first demonstrated by Gustafsson et al. [253] in 1979 for ETC measurements of insulating materials. There are a number of different transient techniques available to measure the ETC of metal sponges. For example; the Flash technique [167] and Transient Plane Source technique (TPS) [34, 174, 176, 177]. The most common type of transient measurement is the Transient Plane Source technique (TPS) [34, 71, 174, 176, 177] , where a single element acts as both temperature sensor and heat source. It has been widely used to measure the ETC of porous materials [34, 71, 174]. The TPS element is positioned between two samples with similar characteristics and measures the instantaneous temperature gradient with time [34, 176, 177]. The main advantages of this approach are that the tests are quick and easy, and it is possible to measure a wide range of thermal conductivities [34, 36]. The analysis can be complex and quantification of uncertainty is difficult [36]. Special care of the thermal contact resistance in terms of surface roughness and contact pressure is required [34].

In contrast, there are a number of steady state methods which are widely used to measure the thermal conductivity [36]. The basic principle of a steady state method is to measure the temperature gradient along a sample length under thermal equilibrium conditions. One-dimensional conductive heat transfer can be applied perpendicularly to the tested sample surface. The most common steady state methods are the comparative-longitudinal and reference techniques [158, 178], guarded hot-plate method [159] and panel test technique[18, 36, 70]. At steady state, the rate of heat transfer is obtained by measuring the temperature difference across a known reference material [158, 178] or using the dissipated heat from a hot

water bath or dissipated from an electric heater[18, 19]. The main advantages of this method are the simplicity of the evaluation technique, good precision and accuracy and the opportunity to conduct unidirectional measurements [36]. While the main disadvantages are the long times required to achieve steady state conditions, complicated instrumental procedures and the potential difficulties due to thermal contact, which can be especially challenging for a porous matrix [36]. In the current study, the comparative-longitudinal steady state technique [158] was adopted to measure the ETC for the sixty nine replicated aluminium sponges. It was chosen as it is simple to evaluate and quantify the ETC and offers good accuracy.

3.2.1 ETC Experimental Apparatus

Figure 3-4 shows a schematic of the test apparatus used to measure the effective thermal conductivity. The apparatus was constructed around two cylindrical aluminium blocks located above and below the sample. The other key parts are a cooling source (bath of water), an electric heater and insulation.

Heat flux up to 100 W was supplied by the electric heater. The temperature at the upper surface of the upper aluminium block was kept constant by adjusting the heating controller. The electric heater coil (OMEGALUX FGR-30/240) was wrapped around an aluminium block with a diameter of 60mm which acted as a source of distributed heat flux. This was in contact with the upper aluminium block that sandwiched the sample. Insulation (rock wool) covered the electric coil (Figure 3-5) and both the heater and upper heat flux meter were connected as shown in Figure 3-5. To reduce the heat loss from the top of the heater, a ceramic insulation board and rock wool insulation were used.

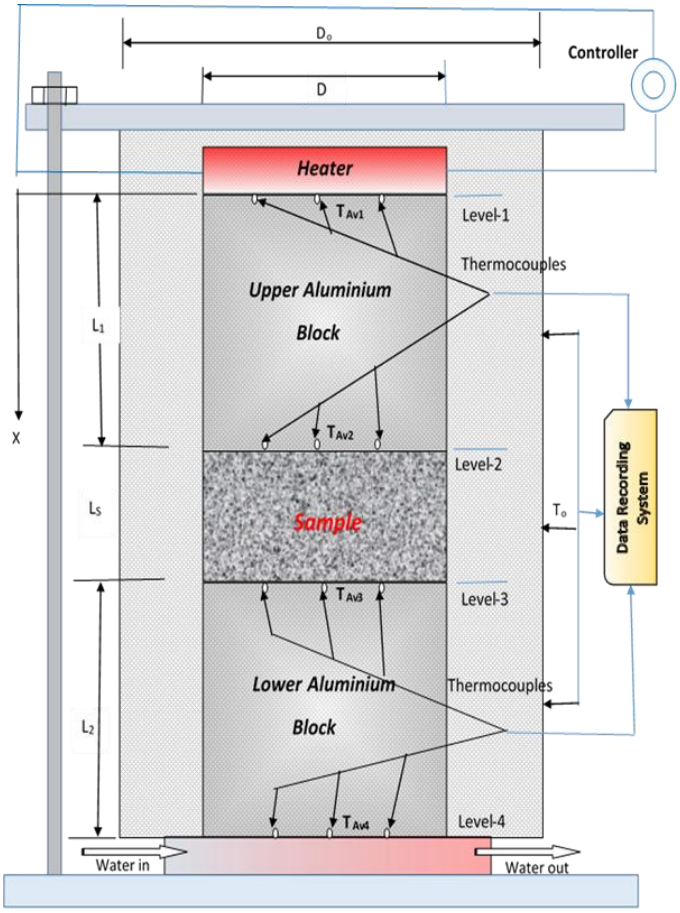

Figure 3-4 Schematic diagram of a comparative steady state technique used for effective thermal conductivity measurements

The temperature at the upper surface of the upper aluminium block was measured using three thermocouples. The controller (WEST-6100) was connected to 240V AC and reduced the output voltage to the heater based on the adjusted temperature.

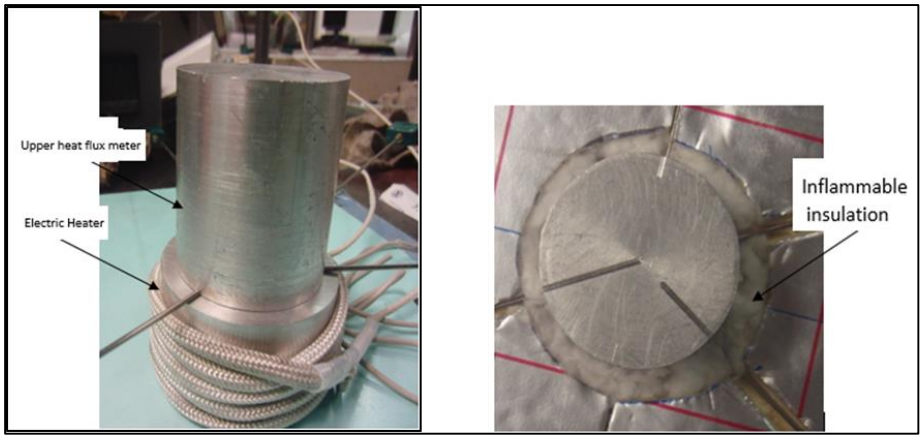

Figure 3-5 Electric heater and upper heat flux meter connection

To remove heat from the rig, a bath of cold flowing water was placed at the bottom of the rig in direct contact with the lower aluminium block. The cooling water was circulated through a chiller and had an adjustable temperature. Polyisocyanurate rigid foam insulation (thermal conductivity of 0.022 W/m.K*)* surrounded the rig.

The thickness of both aluminium blocks was 50 mm and their diameter was equal to the average diameter of the tested samples (50.1 mm). Each sample was positioned between the heated and cooled aluminium blocks, whose surfaces were polished to improve thermal contact. Thermal grease was also used to minimise contact resistance. The temperatures were recorded at all contact surfaces by twelve K-type thermocouples (diameter 1.5mm). To determine radial distribution of temperature along the contact faces, three groves were drilled at three different radial locations to retain the thermocouples as shown in Figure 3-6. They were distributed as follows; one at the centre (R=0.0 mm), the second at R=7.5 mm and the third at R=19.5 mm, where R is the radius of the block.

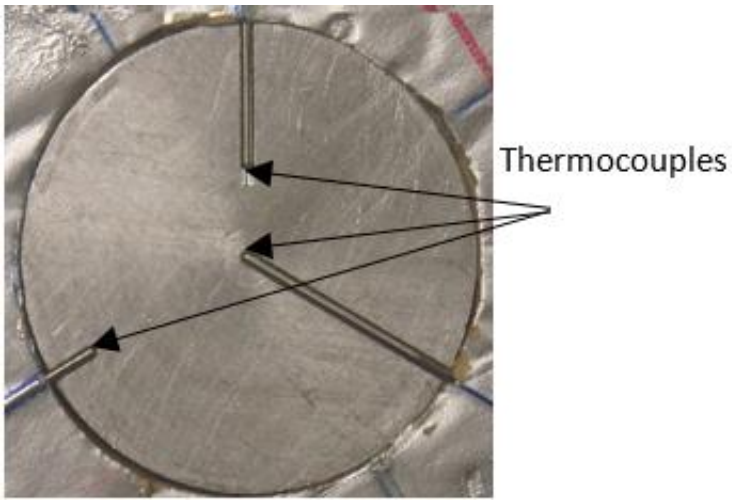

Figure 3-6 Thermocouples places on contact faces

The rig was supported by two aluminium plates located at the top and bottom, bolted together to achieve good contact between all surfaces as shown in Figure 3-7. The assembly could accommodate the slightly different thicknesses of the samples.

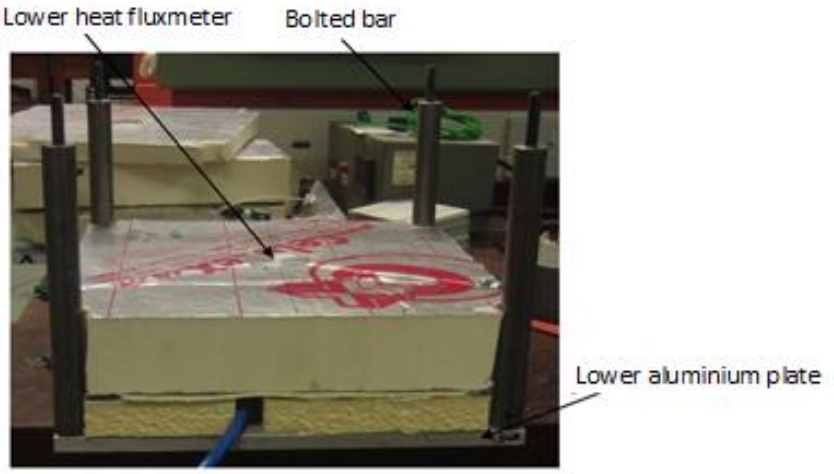

Figure 3-7 The bolted bars and lower support plate

Two USB TC-08 Thermocouple Data Loggers were used to record the temperatures at one second intervals. Three temperatures at different radial placements were recorded at each contact surface. During these experiments, the heater was set to provide a temperature of 50°C and the chiller was adjusted to provide circulating water at 5°C. This ensured all samples were measured at similar temperatures. The temperature at the outer surface of the insulation (T_o) was recorded at three vertical axial locations on the rig, as shown in Figure 3-4, to find the heat loss to the environment.

The thermocouples were calibrated against a mercury thermometer using the water boiling point and ice melting points, which were taken as reference points. It was found the maximum deviation did not exceed ±0.2°C. The test arrangement was calibrated by measuring the thermal conductivities of solid aluminium, brass and steel. The results were ≤ 5% deviation of published values [254]. More details of the calibration technique can be found in Appendix-2. Two values of ETC were found by rotating the contact faces of each sample and their average value was calculated and reported.

The direction of the heat flow (upwards or downwards) was found to have an impact on the contribution of natural convection in thermal conductivity [158]. In this work, four large pore size samples with different porosities were tested in order to understand the possible contribution of natural convection. The purpose was to

measure the effect of porosity on natural convection phenomena due to air movements inside the foam cells. This was achieved by changing the source location of heat from above the sample to below it, and maintaining the average source temperature of 50°C at both locations. This configuration should encourage air movement due to buoyancy forces. In this case, the measured heat transfer comprises conduction through both the solid and fluid phases and natural convection surface to upper on is the summation of conduction through the solid phase and the convection by the air movement.

3.2.2 Effective thermal conductivity determination

In this work, the effective thermal conductivity was found by a steady state comparative technique. During the experimental measurements, the rig was allowed to reach thermal equilibrium conditions, this took around 20 minutes. Shown in Figure 3-8 is the temperature history of an experiment. For the calculations, the average temperatures over 25 minutes in the steady state period were used. In this work, the majority of the samples were tested in the up to down configuration to minimise natural convection.

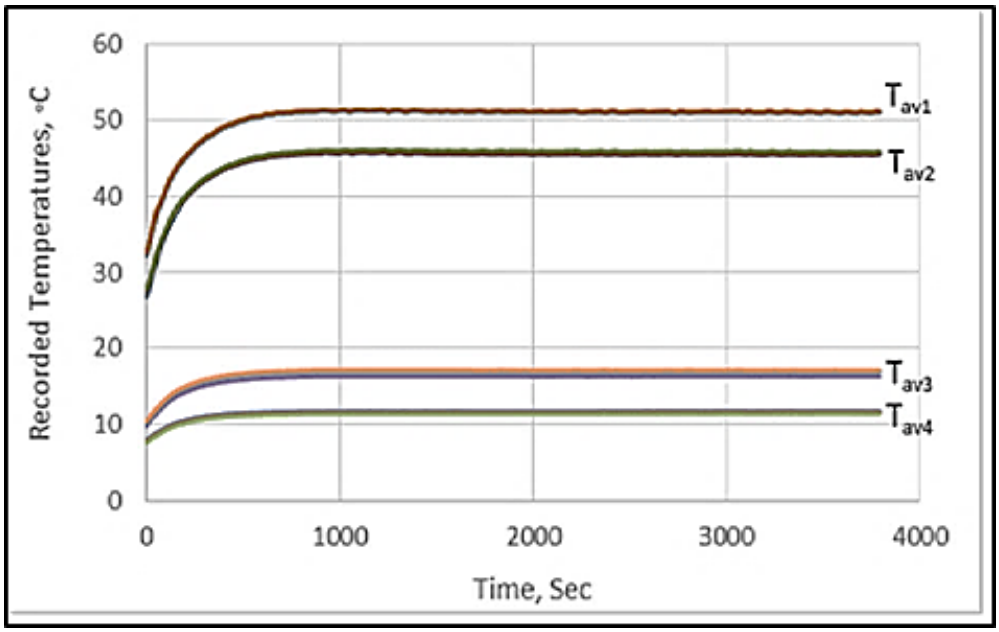

Figure 3-8 Experimental recorded temperature

The heat loss to the surroundings was calculated based on the outer diameter of the insulation (D_o =300mm) and the diameter of the block (D_i =50.1mm). The maximum recorded temperature at the outer insulation surface was 22.7˚C and the maximum temperature at the surface of the block was at level 1 and equaled 50.8˚C. In this case, the heat loss was 0.3 Watts. In the same case, the upper fluxmeter calculated heat was 44.1 Watts and the lower fluxmeter heat was 43.4 Watts.

The radial temperature distribution was also examined and the deviation of the temperatures along the radial distance at the each level was found with less than 1˚C, as shown in Figure 3-9.

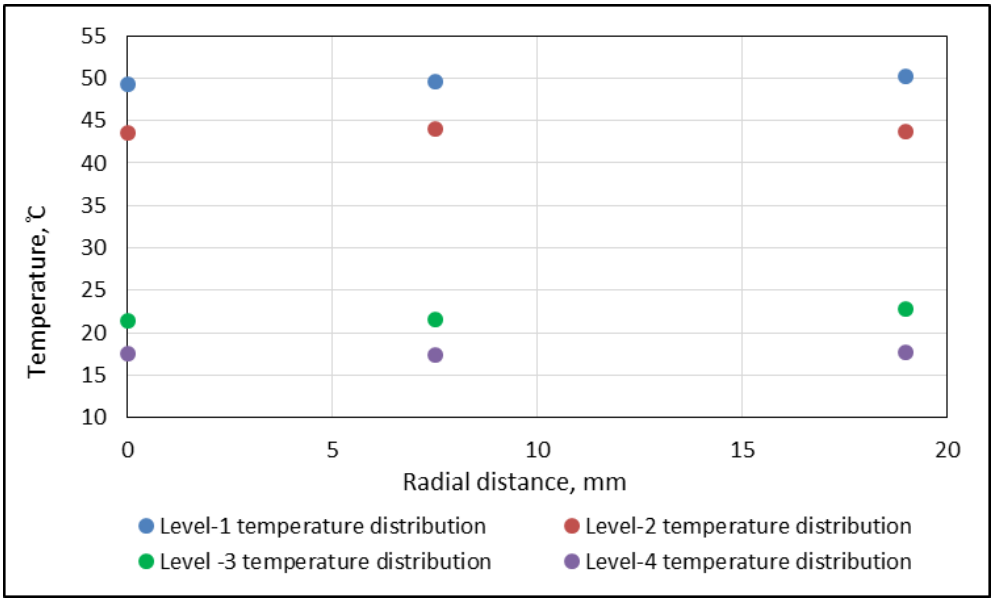

Figure 3-9 Radial temperature distribution

The one-dimensional steady state heat transfer method has been widely used to measure the effective thermal conductivity of metal foams. The contribution from radiation and convection heat transfer is generally neglected [18, 19, 70, 158, 164]. The contribution of radiant heat transfer between the contact faces and between the adjacent solid phase layers inside the samples has been found less than 1% and 0.5% respectively for other experiments on porous metals [181, 255]. Consequently, as there is no radial heat exchange due to high thermal diffusivity of the aluminium and

neglecting the radiant and convective heat transfer, Fourier's Law can be applied along the aluminium blocks as shown in Figure 3-10.

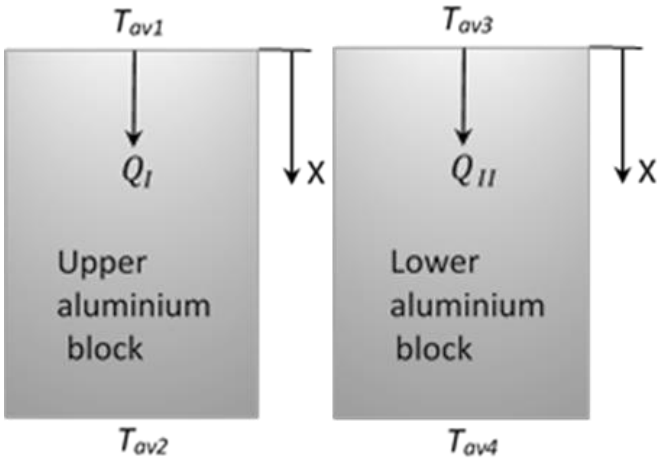

Figure 3-10 Heat transfer across the aluminium blocks

The one dimensional heat transfer method was applied in the upper and lower aluminium blocks and the porous metal sample at the thermal equilibrium (steady state) conditions. The average of the heat transfer rates in the upper and lower aluminium blocks was used to obtain the ETC of the porous material sample.

Assuming no radial conduction, radiation or convection heat transfer, the heat flux is a function of the sample thickness only. The heat balance equations through the upper and lower blocks are:

$$Q_I = -A.K_{sol}\frac{\partial T}{\partial X} = A.K_{sol}\frac{(T_{Av1}-T_{Av2})}{L_1} \qquad 3.10$$

$$Q_{II} = -A.K_{sol}\frac{\partial T}{\partial X} = A.K_{sol}\frac{(T_{Av3}-T_{Av4})}{L_2} \qquad 3.11$$

The heat loss (Q_{loss}) to surroundings through the insulation material was calculated by applying the thermal energy exchange equation; the inner side temperature of the insulation (T_i) was expressed by the average of outer temperatures at all levels, the heat loss was found to be small compared with heat flux through the both fluxmeters. Consequently, the heat loss can be described as

$$Q_{Loss} = \frac{2\pi L_s K_{in}(T_i - T_o)}{\ln(D_o/D)} \quad 3.12$$

Where:

A= sample and aluminium block cross sectional area, m^2

K_{sol}= aluminium block material thermal conductivity, W/m.K

K_{in}= insulation material thermal conductivity, W/m.K

L_1, L_2 and L_s are the lengths of the upper block, lower block and sample thickness respectively.

The amount of heat flow across the sample (Q_s) was calculated as the average of heat transfer through the both aluminium blocks modified by extracting the amount of heat loss to the environments

$$Q_s = \frac{Q_I + Q_{II}}{2} - Q_{Loss} \quad 3.13$$

Figure 3-11 is a schematic to show the heat transfer across the sample at steady state conditions.

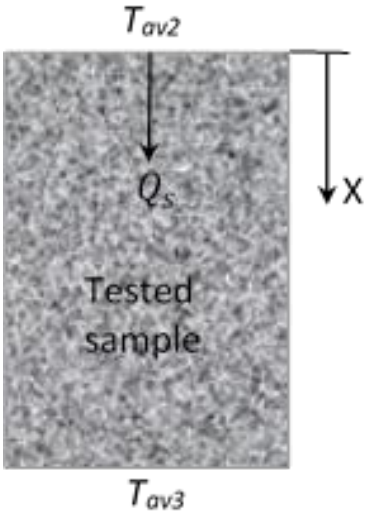

Figure 3-11 Heat transfer across the tested sample

Therefore, the effective thermal conductivity of the examined foams can be found by the thermal energy balance equation as

$$K_{eff} = Q_s . L_s / A(T_{Av2} - T_{Av3}) \quad 3.14$$

3.3 Convective heat transfer in porous media

3.3.1 Introduction

Heat transfer in porous media is a complex phenomenon due to its complicated microstructure. The estimation of the interstitial heat transfer coefficient in metal foams is a challenge due to non-repeatability of its morphology. The steady state and transient methods are commonly used to estimate the thermal performance of heat exchangers and enhanced heat transfer surfaces such as in packed beds, mesh wire screens and metal foams [256, 257]. The empirical correlations and approaches adopted in literature are limited to certain porosities and are defined for specific structures. Therefore, the experimental methodology is still the most effective method to study the thermal characteristics of metal sponges. Convective heat transfer has mainly been studied in high porosity metal foams. Literature on convective heat transfer in low porosity metal sponges is sparse. It has been noted however, that convective heat transfer increased with a decrease in porosity [57, 58, 64]. The maximum convective heat transfer has been found to occur at a porosity of 62% (the fluid was water) [58].

The purpose of this work was to study heat transfer in low porosity aluminium sponges with different pore diameters. The working fluid was air. It was also aimed at studying these cellular materials as alternative matrix for thermal regenerators in comparison to packed beds of spherical balls and mesh wire screens. Both convective heat transfer coefficients and NTUm were calculated.

3.3.2 Convective heat transfer characteristics measurements

The determination of heat transfer parameters such as the convective heat transfer coefficient and NTUm in metal foams is a challenge as a result of its complex structure [18, 20]. There are significant difficulties in measuring temperatures and velocities inside the pores of the matrix. Consequently, the average value of the convective heat transfer coefficient is usually measured to assess the thermal performance of a porous matrix [11, 194, 218].

There are two main techniques to measure the convective heat transfer coefficient; the steady state and transient techniques. In open literature, both techniques have been used to measure the thermal parameters of heat exchangers and enhanced heat transfer surfaces in configurations such as granular packed beds, mesh wire screens, and metal foams [23, 47, 122, 193, 194, 199, 200, 256-258]. In this study, the transient method (single blow technique) was used and the working fluid was air.

3.3.2.1 Steady State Technique

For this technique, a continuous heat flux is supplied to the substrate surface using hot flowing fluid or an electrical power supply (Q_c) [47, 256]. The convective heat transfer coefficient is determined by applying the Newton's law of cooling at the steady state (thermal equilibrium) conditions. The difference between the average fluid and average substrate surface temperatures is used for determination of the convective heat transfer coefficient [47, 69, 202, 204, 256, 259]. There is a transverse temperature gradient through the cellular matrix with the result that the temperature on the outer surface is higher than that in the centre of the medium. For this reason, the heat transfer coefficient measured by this method will be underestimated [47].

By measuring fluid mass flow rate ($\dot{m}_f$), outlet and inlet fluid temperatures (T_{f0}, T_{fi}) and average wall temperature (T_w), the convective heat transfer coefficient can be calculated [43, 59]

$$h = \frac{Q_c}{A_{Hm}(T_w - T_{fb})} = \frac{\dot{m}_f Cp_f (T_{f0} - T_{fi})}{A_{Hm}(T_w - T_{fb})} \qquad 3.15$$

This method is relatively expensive and time consuming compared with the transient method [209, 260]. However, the convective heat transfer coefficient is easily calculated and the heat transfer model is not required as is the case for the transient method [209]. Some inconsistency in the results due to the Biot number effect has been reported and there may also be issues due to neglecting thermal dispersion [202, 203].

3.3.2.2 Transient Technique

The use of the transient technique to measure the average convective heat transfer coefficient has been common for many years. Here, a fluid is blown through the porous matrix to remove or add heat and the outlet fluid temperature is recorded and matched with a predicted one. This technique is widely employed to measure the average heat transfer characteristics for heat exchangers and complex heat transfer surfaces such as packed beds of porous media [5, 16, 21-24, 48, 191, 194, 196, 226, 260-263]. The transient method is simpler, quicker and cheaper than the steady state technique [24, 191, 209]. It has a variety of names such as "starting stage operation" by Anzelius in 1926, "single blow" by Nusselt in 1927 and "transient test technique" by Schumann in 1929 [260].

There are two transient methods, the single blow and the periodic technique which differ with the variation of inlet fluid temperature with time [256, 264]. In the single blow method, the matrix is subjected to a step change in temperature whilst a sinusoidal variation is used in the periodic technique [23, 191, 256, 264]. The periodic method was initially used for a limited range of NTUm between 0.4 and 4.8 but has subsequently been developed for a wide range of NTUm from 0.2 to 50 [264]. The periodic method requires a more complex test apparatus.

In the single blow technique a step change in temperature is desired but this can be difficult to achieve as inlet fluid temperature variations have an impact on the measured NTUm value. A step change was used in the first model proposed by Schmann et al. [265]. It was also used by Pucci et al. [260] and Howard et al. [266]. An exponential function has also been adopted by Liang et al. [256] and Halkarni et al. [5]. Sim et al. [209] used cubic spline polynomial to describe the inlet fluid temperature.

The transient technique consists of three main items: an experimental apparatus, a mathematical model which predicts recorded fluid temperature (and in which the heat transfer coefficient is varied) and an evaluation scheme which compares the measured and predicted outlet fluid temperatures [256, 262]. The

most common schemes of the evaluation are direct curve matching, maximum gradient and initial rise [24, 262, 267].

3.3.3 Single Blow Technique Models and Assumptions

One of the important elements affecting the single blow method is the mathematical model. The accuracy of evaluation in the single blow method depends on the assumptions used in the model [5, 209, 262]. These assumptions can be a source of the error if the model cannot validate and describe completely the actual experiment [209, 262]. The thermal energy capacity ($\dot{m}_f C_f$) plays an important role in the heat transfer process and as a result, the single blow model can be classified in two main categories; infinite and finite thermal capacity models [268]. Infinite thermal capacity may occur when the energy change of the passing fluid is latent (phase change) at constant temperature, or the fluid is liquid with high heat capacity leading to a small temperature difference [268]. The thermal conductivity and thermal resistance of the solid may also be important, therefore, the infinite approach is further categorised in two types as shown in Table 3-1.

Table 3-1 Classification of infinite fluid capacity models

Infinite fluid heat capacity [268]	
Infinite thermal conductivity (Neglected temperature gradient of solid phase material)	Infinite thermal conductivity (Included temperature gradient of solid phase material)
Assumptions -Infinite thermal fluid capacity. -The thermal resistance by the convective film at solid-fluid interface is the major to the heat transfer. -Uniform solid phase temperature.	Assumptions - Infinite thermal fluid capacity. - Thermal resistance by the convective film in the same order of that by the storage material. - Temperature gradient of solid material is significant.

The finite heat capacity model is used when the fluid is a gas, as the thermal capacity of the gas is small compared with that of the solid [260, 268]. This model is again sub-classified into two approaches based on the thermal resistance in the solid-fluid interface, which are detailed in Table 3-2.

Table 3-2 Classification of finite fluid heat capacity models

Finite Fluid Thermal Capacity [268]	
Neglected thermal resistance model	Simplified model (Schmann-Hausen model)
Assumptions - Finite thermal fluid capacity - Finite thermal conductivity of the bed Material - Convective heat transfer coefficient is very large - The thermal resistance by the convective film at solid-fluid interface is neglected - The solid and fluid temperature difference equal zero - Uniform initial temperature	Assumptions - Finite thermal fluid capacity - Infinite thermal conductivity of the bed material in the transverse direction - Zero thermal conductivity of the bed material in flow direction - Housing wall is adiabatic. - Uniform initial bed temperature. - Uniform convective heat transfer coefficient. - The function of inlet temperature is step Change.

3.3.4 Single blow technique model development

The single blow method was first proposed by Schumann [265] in 1929. He solved the governing energy equations analytically assuming a step change in the inlet fluid temperature. He presented analytical derived breakthrough temperature curves against the non-dimensional time for different NTU_m values. There was a single outlet fluid temperature curve for each value of NTU_m. In 1932, Furnas [269] built an experimental rig based on the assumptions of Schumann's model. He was able to measure the average convective heat transfer coefficient by directly matching the experimental outlet fluid temperature history with Schumann's curve. In 1957, Creswick [270] first considered that axial conduction through the solid material may have a measurable impact on the predicted heat transfer parameters and solved the governing equations using the numerical technique. This work was extended by Howard [266], who used the finite difference method to solve the differential equations and found that the axial thermal conduction could not be ignored. Loehrke [262] found that ignoring longitudinal conduction within the solid can result in the underestimation of the NTUm value by a factor of 2 and the error increased with the increasing NTU_m. It is now generally accepted that longitudinal thermal conduction cannot be ignored for $NTU_m \geq 3$ [271] and it is of significance when NTUm > 2 [260].

It is generally assumed that the sample is perfectly insulated from its holder. In this case, the thermal exchange between the fluid and the holder are neglected. Chen et al. [190] included heat losses through the wall and found the NTU_m value was underestimated by greater than 10 % if this was ignored. The effect of the Joule-Thomson coefficient may also be of significance, which can occur at high gas flow rates. Chen et al. [193] studied the effect of the Joule-Thomson coefficient for packed beds of 200 mesh wire screen layers and showed that the temperature decreased by 3% when the pressure drop was 0.2 MPa.

3.3.5 Governing equations of single blow technique model

3.3.5.1 Energy balance equations

The thermal exchange between the fluid and the solid is complicated. The temperature distribution of the fluid is difficult to predict due to the complexity of the solid structure [115, 187, 210]. Therefore, most investigations have relied on experimental work to characterise the thermal parameters of the porous medium. The solid and the fluid are initially assumed to be at uniform temperature then the air flow temperature is changed. Shown in Figure 3-12 is an element of the porous matrix within which the heat fluxes occur. These are obtained by applying the local volume average technique and LTNE [199, 203, 218] on the element. The assumptions employed to simplify the mathematical model are:

- Finite fluid thermal capacity.
- The one-dimensional longitudinal conductive heat transfer is considered.
- The solid, wall and fluid temperatures vary along the flow direction.
- The thermal diffusivity of the solid is high, there is no heat exchange perpendicular to the flow direction.
- The properties of the fluid are temperature independent.
- Incompressible and steady fluid flow.
- The porous medium is homogeneous (uniform porosity) and isotropic.
- Uniform inlet air velocity and temperature.

- Non-adiabatic holder walls.
- The Joule-Thomson effect is neglected due to low pressure drop across the samples.

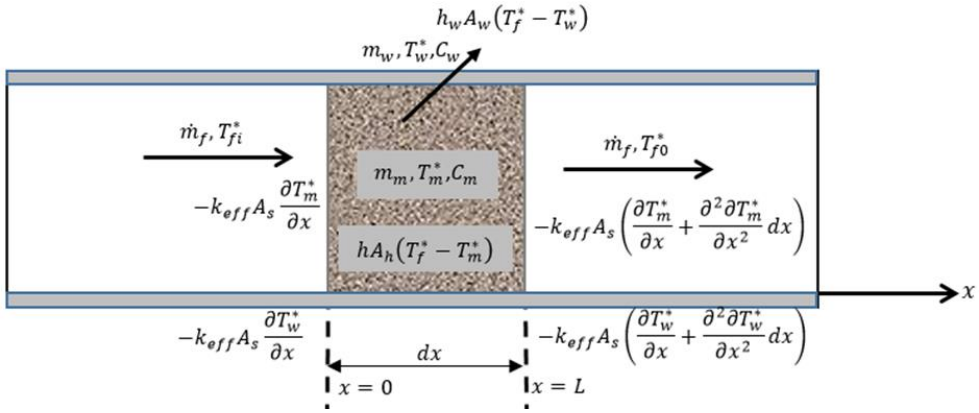

Figure 3-12 Control element of the complex

The air flows at high temperatures through the matrix, hence heat is transferred to the matrix and the wall simultaneously at all positions along the flow direction as shown in Figure 3-13. Starting with the first law of thermodynamics, the energy content of the entering fluid equals the energy transferred to the wall and matrix materials and the energy in the leaving air.

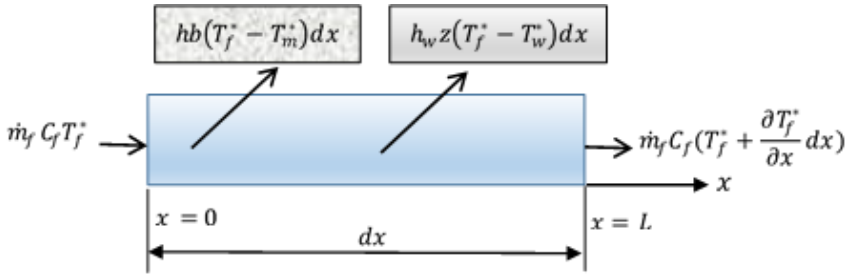

Figure 3-13 Energy balance in control volume element of flowing air

[Content energy in entering air] = [energy transfers to porous matrix] + [energy transfers to holder wall] + [the content energy in the leaving air]

$$\dot{m}_f C_f T_f^*|_x = hb(T_f^* - T_m^*)dx + h_w z(T_f^* - T_w^*)dx + \dot{m}_f C_f T_f^*|_{x+dx} \qquad 3.16$$

The heat transfer area of the control volume to the matrix material is bdx and to the housing wall is zdx.

As, $T_f^*|_{x+dx} = T_f^*|_x + \frac{\partial T_f^*}{\partial x}dx$. This can be substituted into equation 3.12 and after rearrangement

$$hb\left(T_f^* - T_m^*\right)dx + h_w z\left(T_f^* - T_w^*\right)dx + \dot{m}_f C_f \frac{\partial T_f^*}{\partial x}dx = 0 \qquad 3.17$$

When the hot air passes through the matrix, the majority of the heat is transferred to the porous material rather than the wall due to high heat transfer area. Applying the first law to an element of the solid matrix, as shown in Figure 3-14, in addition to the energy transferred by convection from the air, there is also energy entering by conduction. These equal the thermal conduction from the element and the accumulative energy stored in the matrix ($C_m S_m dx$).

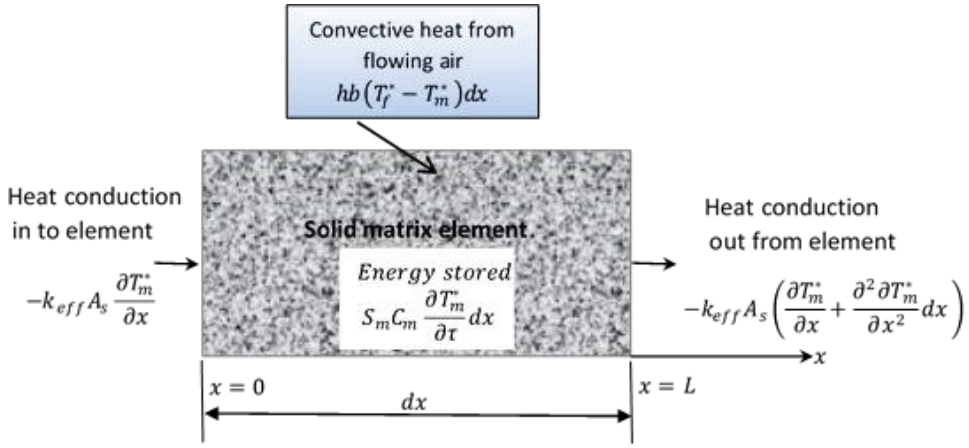

Figure 3-14 Energy balance in control volume element of solid matrix

[Entering conductive heat transfers to porous element] + [convective heat transfers to porous matrix] = [energy stored in porous material] + [conductive heat leaving from the porous element]

$$-K_{eff}A_s\frac{\partial T_m^*}{\partial x} + hb\left(T_f^* - T_m^*\right)dx = S_m C_m \frac{\partial T_m^*}{\partial \tau}dx - k_{eff}A_s\left(\frac{\partial T_m^*}{\partial x} + \frac{\partial^2 T_m^*}{\partial x^2}dx\right) \qquad 3.18$$

Noting that the conduction equation can be simplified by

$$-k_{eff}A_s\left(\frac{\partial T_m^*}{\partial x}+\frac{\partial^2 T_m^*}{\partial x^2}dx\right)=-k_{eff}A_s\frac{\partial T_m^*}{\partial x}-k_{eff}A_s\frac{\partial^2 T_m^*}{\partial x^2}dx,$$

then the Equation 3.18 becomes

$$S_m C_m\frac{\partial T_m^*}{\partial \tau}dx+h_w z\left(T_f^*-T_m^*\right)dx-k_{eff}A_s\frac{\partial^2 T_m^*}{\partial x^2}dx=0 \qquad 3.19$$

As the warm air flows through the porous matrix, a portion of its energy will be transferred to the holder. The energy balance in the control volume of the holder is shown in Figure 3-15. The energy transferred from the air plus the conduction energy entering to the wall element are equal to the stored energy in the wall material plus that lost to conduction in the flow direction.

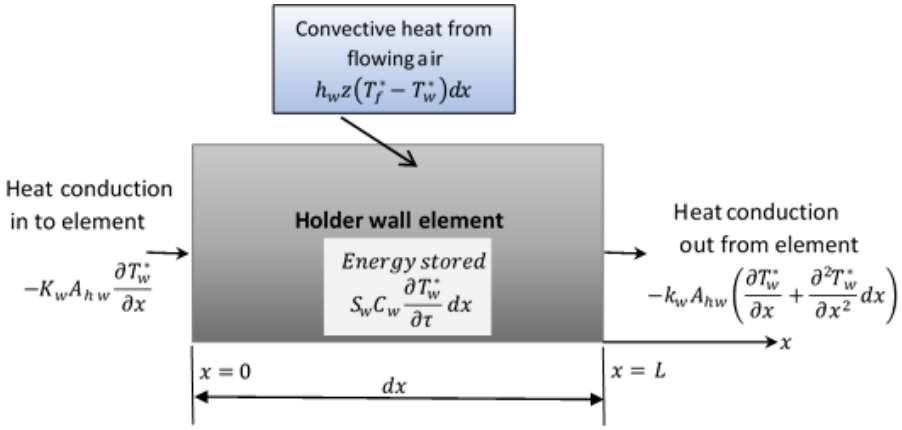

Figure 3-15 Energy balance in control volume element of holder wall

[Entering conductive heat transfers to wall element] + [convective heat transfers to wall element] = [energy stored in wall material] + [conductive heat leaving from the wall element]

$$-K_w A_{hw}\frac{\partial T_w^*}{\partial x}+h_w z\left(T_f^*-T_w^*\right)dx = S_w C_w\frac{\partial T_w^*}{\partial \tau}dx-k_w A_{hw}\left(\frac{\partial T_w^*}{\partial x}+\frac{\partial^2 T_w^*}{\partial x^2}dx\right) \qquad 3.20$$

The conduction balance in the conduction heat transfer second term on the left hand side can be simplified as

$$-k_w A_{hw}\left(\frac{\partial T_w^*}{\partial x}+\frac{\partial^2 T_w^*}{\partial x^2}dx\right)=-k_w A_{hw}\frac{\partial T_w^*}{\partial x}-k_w A_{hw}\frac{\partial^2 T_w^*}{\partial x^2}dx$$

$$S_w C_w\frac{\partial T_w^*}{\partial \tau}dx-h_w z\left(T_w^*-T_f^*\right)dx-k_w A_{hw}\frac{\partial^2 T_w^*}{\partial x^2}dx=0 \qquad 3.21$$

Equations 6.17, 6.19 and 6.21 can be simplified by dividing all terms by dx and are then converted to a non-dimensional form by using the following terms [8, 190, 191, 193, 194]

$$T_f=\frac{T_f^*-T_0}{T_{fmax}-T_0}\quad,\ T_m=\frac{T_m^*-T_0}{T_{fmax}-T_0}\quad,\ T_w=\frac{T_w^*-T_0}{T_{fmax}-T_0},\quad X=\frac{x}{L},$$
$$t=\frac{\tau}{t^*},$$

$$R_{tc}=\frac{M_m C_m}{M_w C_w},\qquad \lambda_m=\frac{K_{eff}A_m}{\dot{m}_f C_f L},\quad \lambda_w=\frac{K_w A_w}{\dot{m}_f C_f L},\quad NTU_m=\frac{hA_h}{\dot{m}_f C_f},$$
$$NTU_w=\frac{h_w A_{hw}}{\dot{m}_f C_f} \qquad 3.22$$

After simplification, the porous matrix heat transfer area is ($A_h=bL$) and for the holder wall is ($A_w=zL$).

The non-dimensional groups in Equation 3.22 and the fluid total heat capacity ($\dot{m}_f.C_f$) are put in the Equations 3.17, 3.19 and 3.21 and the equations are rearranged into their final form

For fluid:

$$\frac{\partial T_f}{\partial X}+NTU_m\left(T_f-T_m\right)+NTU_w\left(T_f-T_w\right)=0 \qquad 3.23$$

For matrix:

$$\frac{\partial T_m}{\partial t}-\lambda_m\frac{\partial^2 T_m}{\partial X^2}+NTU_m\left(T_m-T_f\right)=0 \qquad 3.24$$

For side wall:

$$\frac{\partial T_w}{\partial t}-R_{tc}\,\lambda_w\frac{\partial^2 T_w}{\partial X^2}+R_{tc}\,NTU_w\left(T_w-T_f\right)=0 \qquad 3.25$$

In the above single blow model, the side holder is non-adiabatic. Consequently, there are three unknown temperatures; the fluid temperature, core matrix temperature and holder wall temperature. The above equations have been used by a number of researchers to determine the NTU_m and convective heat transfer coefficient in different classes of porous media, e.g., Chen et al. [22], Hwang et al. [122], Geb et al. [23], Barari et al. [8] and later on Ranganayakulu et al.[191], Vijay et al. [203], Halkarni et al. [5] and Xia et al. [48]. These equations are resolved numerically with the appropriate initial and boundary conditions.

Initial conditions

At $t = 0,\ T_f(X) = T_m(X) = T_w(X) = T_0$

Boundary conditions

$$T_f(0,t) = 1 - e^{\left(-t/\beta\right)}$$

For $t \geq 0$

At $X = 0,\ \frac{\partial T_m}{\partial X} = \frac{\partial T_w}{\partial X} = 0$

At $X = 1,\ \frac{\partial T_m}{\partial X} = \frac{\partial T_w}{\partial X} = 0$

The constant, β, was found using the curve fitting method for each experiment. From the NTU_m, the wall and volumetric heat transfer coefficients can be determined.

3.3.5.2 Numerical solution

Numerical methods are utilized to find an approximate solution. This can be performed by the discretization of independent variables and replacement of the partial derivatives by approximations [272, 273]. Equations 3.24 and 3.25 are second order parabolic partial differential equations (PDE) and Equation 3.19 is a first order differential equation, and need to be solved by different numerical techniques. In this work the fully explicit finite difference scheme was employed and all the partial

derivatives were centrally differenced [23, 122]. A FORTRAN code was written to solve these equations. Equation 3.23 was discretized in space and solved by using a forward explicit difference approximation. Equations 3.24 and 3.25 were discretized in space and solved by a centred symmetric difference approximation, and in the time domain they were solved by a forward explicit difference approximation. As shown in Figure 3-16, the spatial discretization divides the porous prism sample matrix and holder wall into equally located nodes. The solution of the equations is achieved at increment integral values of non-dimensional time. The numerical solution yields the fluid, solid phase and holder wall temperatures as a function of time and location.

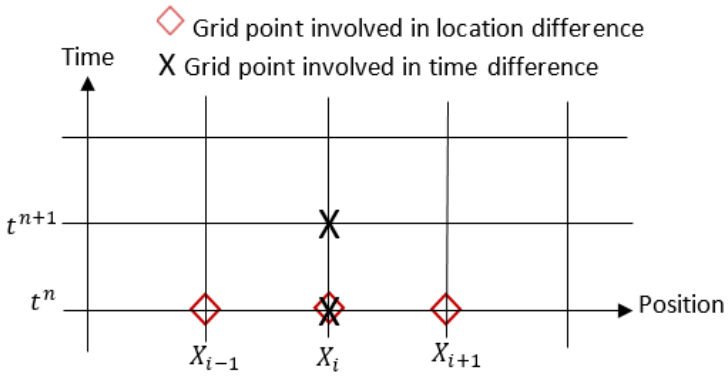

Figure 3-16 Computational discretization for the explicit form

The forward finite difference describes the approximation of the first order PDE in the spatial discretization and the time as

$$\frac{\partial T}{\partial X} = \frac{T_{i+1}^n - T_i^n}{\Delta X} \qquad 3.26$$

$$\frac{\partial T}{\partial t} = \frac{T_i^{n+1} - T_i^n}{\Delta t} \qquad 3.27$$

The centred symmetric finite difference approximation used to approximate the second derivatives as

$$\frac{\partial^2 T}{\partial X^2} = \frac{T_{i+1}^n - 2T_i^n + T_{i-1}^n}{(\Delta X)^2} \qquad 3.28$$

The above finite difference expressions were substituted into the partial differential equations (3.19, 3.20 and 3.21) to find the final finite differences forms.

$$\frac{T_{fi+1}^{n} - T_{fi}^{n}}{\Delta X} + NTU_m \left(T_{fi}^{n} - T_{mi}^{n}\right) + NTU_w \left(T_{fi}^{n} - T_{wi}^{n}\right) = 0 \qquad 3.29$$

$$\frac{T_{mi}^{n+1} - T_{mi}^{n}}{\Delta t} - \lambda_m \left(\frac{T_{mi+1}^{n} - 2T_{mi}^{n} + T_{mi-1}^{n}}{(\Delta X)^2}\right) + NTU_m \left(T_{mi}^{n} - T_{fi}^{n}\right) = 0 \qquad 3.30$$

$$\frac{T_{wi}^{n+1} - T_{wi}^{n}}{\Delta t} - R_{tc}\lambda_w \left(\frac{T_{wi+1}^{n} - 2T_{wi}^{n} + T_{wi-1}^{n}}{(\Delta X)^2}\right) + R_{tc} NTU_w \left(T_{wi}^{n} - T_{fi}^{n}\right) = 0 \qquad 3.31$$

The convergence and stability of any numerical technique is important to ensure the method is applicable and that a reliable solution is achieved. The method is convergent when the finite difference results approach the analytical solution as Δt and ΔX approach zero. It is considered stable when the errors during any stage of the computation progress are attenuated [272, 273]. To assess the stability and convergence of the explicit method, the diffusion factor ($\lambda = k\frac{\Delta t}{(\Delta X)^2}$) was used, in this case $k = \lambda_m$ for Equation 3.30, and $k = R_{tc}\lambda_w$ for Equation 3.31. It has been shown that the explicit method was stable and convergent when $\lambda \leq 0.5$ but that errors might oscillate [273]. It was also found by setting $\lambda \leq 0.25$, the solution oscillation could be prevented and if $\lambda \leq 0.16$, the truncation error is reduced [273].

The impact of the time increment Δt and the number of nodes on the position i of the sample on the stability and accuracy of the explicit scheme was checked [122]. This was done by systematically increasing the number of nodes until no difference in fluid temperature was found. From this study it was found that 100 ($\Delta X = 0.01$) nodes was sufficient. The time step was also examined, and no substantial difference between 0.05 and 0.01 was found [122]. At both the spatial and temporal resolutions used, the solutions were found to be grid independent.

The thermal conductivites of the samples were different and the thermal conductivity of the holder material was small compared with the porous material. In order to prevent oscillation and to reduce the truncation error, the diffusion factor,

(λ), was kept under the condition of $\lambda \leq 0.16$. This factor was calculated for each sample and flow rate to check it was less 0.16 by changing the time increment (Δt) to ensure stability and convergence.

3.3.6 Evaluation methods

The evaluation scheme was used to compare the experimental and modelled results. There are a number of evaluation methods; direct curve matching, maximum slope, the differential fluid enthalpy and the initial rise [24, 262, 274]. Furnas [269], first used the direct curve matching method when he found the average heat transfer coefficient by matching the experimental fluid temperature with Schumann's analytical curves. The entire predicted outlet fluid temperature profile was compared with the measured temperatures for a given $\mathrm{NTU_m}$. The value of $\mathrm{NTU_m}$ was adjusted and the calculation repeated until the mean residuals (difference between experiment and model) reached the acceptable value. This method has been widely utilized to assess heat exchangers, thermal regenerators and to measure the convective heat transfer coefficient, and works for all ranges of $\mathrm{NTU_m}$ [5, 16, 23, 48, 122, 186, 199, 203, 232, 263, 275].

The maximum slope method was first used by Locke [276] in 1950 in order to decrease the amount of data reduction in the direct matching technique. He excluded axial conduction and gave a unique value of the maximum slope of outlet fluid temperature for a given $\mathrm{NTU_m}$. Howard [266], in 1964, extended this method with the inclusion of longitudinal conduction and employed an explicit finite difference method to solve the equations. He recommended that the maximum slope method should not be used when $\mathrm{NTU_m}$<3.5. Kohlmayr [277] indicted that at low $\mathrm{NTU_m}$ values ($\mathrm{NTU_m}$<2) there is no inflection point of the outlet fluid temperature history, making it difficult to identify the maximum gradient. He developed an indirect curve matching method by finding the centroid of area under the fluid temperature curve to cover the range 0.5 < $\mathrm{NTU_m}$< 3.5. Despite these issues, the maximum gradient evaluation method has been used by number of researchers [8, 21, 22, 28, 190, 191, 193, 260, 278]. For low $\mathrm{NTU_m}$ samples, the

"initial rise" method developed by Mondt and Siegla [267], where a unique relationship between $\mathrm{NTU_m}$ and the step fraction rise in the measured fluid temperature at zero time, is assumed.

The differential fluid enthalpy technique has also been developed. Here, the inlet and outlet temperatures difference at specific times, and the inlet forcing function time constant must be measured [24]. The differential fluid enthalpy is obtained by measuring the inlet and outlet fluid temperatures and the total heat capacity of the fluid. It is essential to identify the time constants of the thermocouples used to record the inlet and outlet fluid temperatures; the heat exchange parameter between the wall and the fluid (NTU_w); and finally the exponential signal of the inlet fluid temperature time constant [24, 279].

Kohlmayer [280] recommend using two or more evaluation methods and accept only results in agreement. Heggs et al. [24] assessed the four common methods (least squares, maximum slope, differential fluid enthalpy and the shape factor) using a simple mathematical model. He found that the accuracy of the maximum slope and the shape factor were lower than the other two methods. He also mentioned that the results obtained by direct matching technique and differential fluid enthalpy were more consistent. The most commonly used methods in literature to measure the thermal performance are direct matching technique and maximum gradient.

In this work, these two methods (direct matching and maximum gradient techniques) were employed to measure the number of transfer units of each sample. The first step after smoothing the experimental data was to employ the direct matching technique for both experimental and predicted outlet fluid temperatures. Firstly, an estimated NTU_m and NTU_w were used to solve Equations 3.23, 3.24 and 3.25 and the measured inlet fluid temperature was used as boundary condition for the solution. The NTU_m was iterated until the satisfied accuracy between the predicted and experimental outlet fluid temperatures was achieved. Secondly, the NTU_m was confirmed by using the gradient method in order to obtain a reliable result.

3.3.7 Experimental apparatuses and data reduction

3.3.7.1 Experimental Setup

Shown in Figure 3-17 is the layout of the test apparatus used to obtain thermal measurements. The fans used to blow the air and the office plate to measure flow rate are the same used for pressure measurements (section 3.1.3). The thermal test section (Test section B) was made from 2" PVC pipe and four PVC flanges to hold the sample as shown in Figure 3-18. Shown in Figure 3-19 is the schematic of the thermal test section. The thermocouples were positioned at the entrance and exit of the test section.

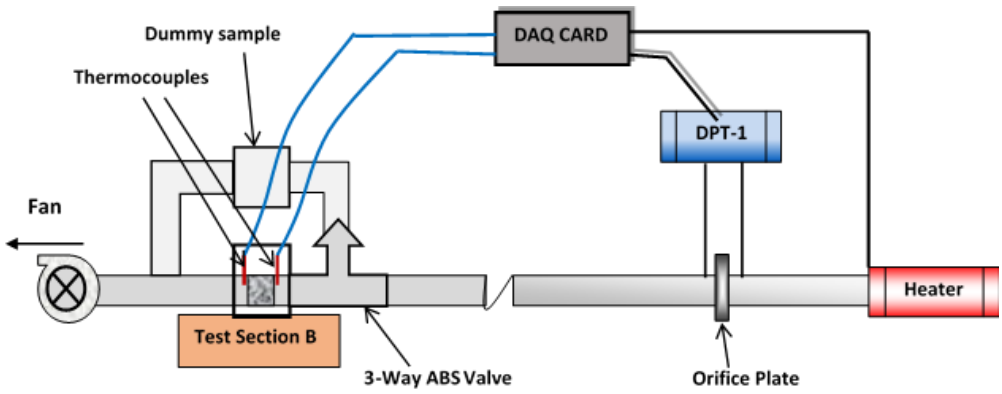

Figure 3-17 Layout of the experimental apparatus used for thermal measurements

A three-way solenoid valve was used to achieve a step change of inlet temperature. This valve was operated by pneumatic rotary actuator (Norgren M/60284/90). The heated air flow was initially directed through dummy samples (used to provide a pressure drop) and then through the test section, during which the changeover took less than 0.15 seconds. The temperatures of the air before and after the tested samples were measured by unsheathed K-type thermocouples of 0.25 mm diameter arranged in the centre of the pipe of *52.9 mm* (2 inch) inside diameter. Thermocouple transmitters (Farnell 300 TX with ± 0.2 % accuracy of thermocouple range) were used to amplify and linearize the signals. The outputs from transducers and thermocouples were collected by a data acquisition system. The connections and fittings were tested for leakage using soap foams and sealing and pressurising the rig up to 3.0 bar for 24 hour for both test stands.

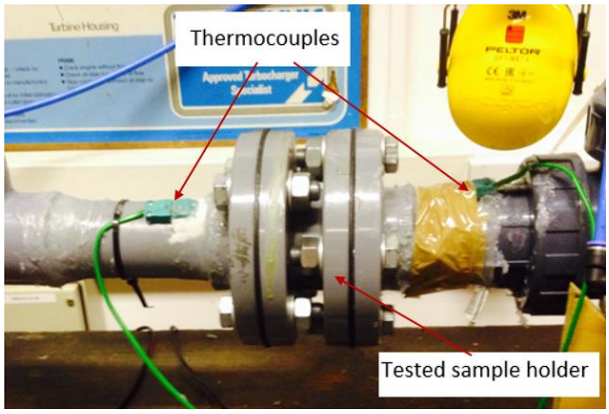

Figure 3-18 Thermal test section

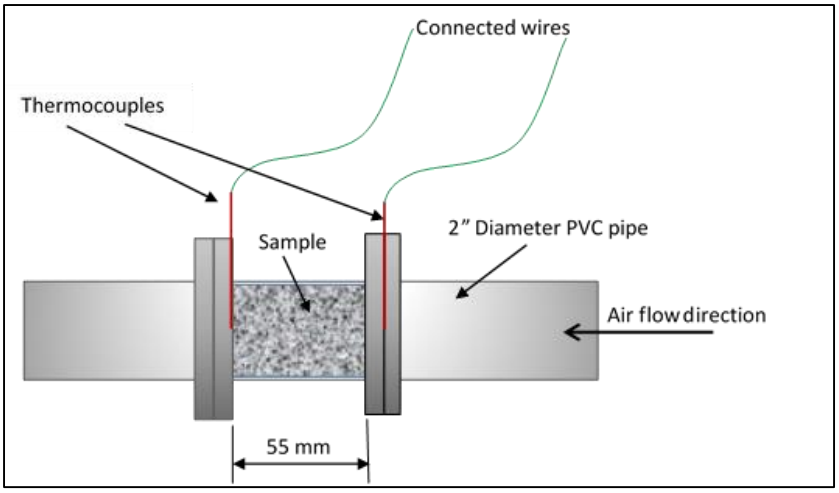

Figure 3-19 Schematic of thermal test section

Thermal tests were performed at six different flow rates. The incoming air was heated to 55°C by an AC heater (AHF-14240 Omega) placed in the entrance of the rig. To adjust the temperature of the incoming air, a solid state zero crossing relay (SSR) was used to switch the input power on and off at 7 Hz. The temperature after the heater was controlled by a 0.5 mm K-type thermocouple to provide feedback to a PID Lab-View code [28].

An orifice plate was used to measure the air mass flow rate at room temperature conditions. Details can be found in Section 3.1.3. The flow rates at elevated temperatures were then calculated. One of the key parameters to determine the mass flow rate according to ISO Standards [251, 281] is the fluid density at the inlet of the orifice plate. There was a pressure drop due to the heater,

which was measured and accounted for in the flow rate calculations in terms of air density. This loss was found to increase with the flow rate as shown in Figure 3-20.

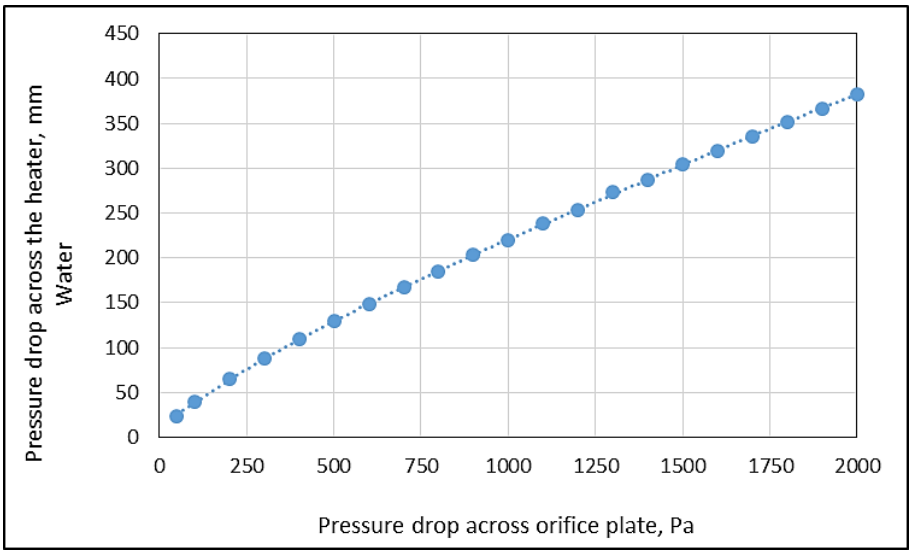

Figure 3-20 Pressure drop across the heater

3.3.7.2 Experimental data reduction

The three measured parameters in the thermal experiment are the pressure drop across the orifice plate and the outlet and inlet air temperatures as function of time. The average value of the pressure drop across the orifice plate was used to determine the air mass flow rate. Shown in Figure 3-21 are typical measured inlet and outlet fluid temperatures.

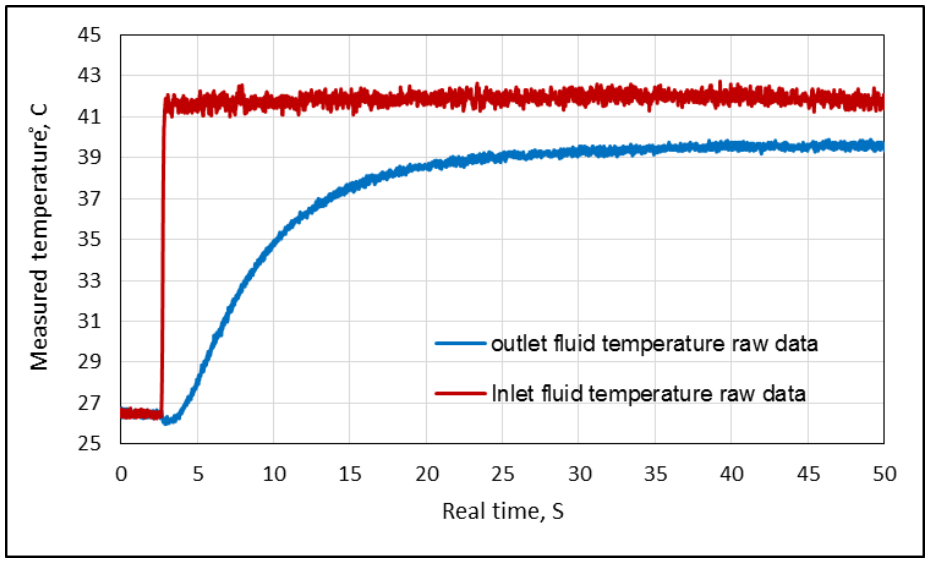

Figure 3-21 Measured inlet and outlet temperature versus time

From Figure 3-21, it can be seen that both temperatures were the same prior to opening the valve and subjecting the sample to a step change at ~3 s. The average value of these temperatures was taken as the initial temperature at time zero (T_0). When the valve was opened, hot air passed through the test section and there was a sharp increase in the inlet fluid temperature, achieving a maximum value at 0.22 seconds after opening. The outlet fluid temperature also increased but took a longer time to reach a constant, certain value. After 35 seconds, the experiment reached steady state. There was a fixed difference between the temperatures due to heat loss through the holder wall.

Measured data before the opening of the valve were not taken in account in the analysis. Both measured temperatures and the time were non-dimensionalised before being matched with the modelling results [8, 24, 28, 190, 191, 193, 194]. The system time (t^*) was used to non-dimensionlise the measured time (τ), using Equation 3.32. The fluid temperature was non-dimensionalised by the initial and maximum fluid temperatures (T_0, T_{fmax}), as in Equation 3.33. The average value of the steady state inlet fluid temperature was taken as maximum fluid temperature.

$$t = \frac{\tau}{t^*}\ , \qquad t^* = \left({}^{m_m . C_m}\Big/_{\dot{m}_f . C_f}\right) \tag{3.32}$$

$$T_f = \frac{T_f^* - T_0}{T_{fmax} - T_0} \tag{3.33}$$

3.3.8 Smoothing and fitting data

The next step was to smooth the experimental data as the temperature measurements contained noise and some outlier data. The source of the noise might be from the rotors, fans, the electric and electronic devices, vibrations and turbulent flow. There are a number of common smoothing techniques used to remove noise and filter the experimental data [282, 283]. In this work, the Savitzky-Golay filtering method was used [283]. There are some outliers which can be observed due to their deviation from the overall trend of the graphed data as shown in Figure 3-22. To improve the accuracy of smoothed data, the outlier data was removed. The filter

coefficients were derived by an unweighted linear least-squares fit by a given polynomial degree. Increasing the polynomial degree achieved a higher level of smoothing but did not affect the data features [283]. The polynomial degree was increased until two consecutive degrees gave the same results. In most of the examined samples, after the ninth degree the difference was very small. Shown in Figure 3-22 is sample of the smoothing data for one of the samples tested.

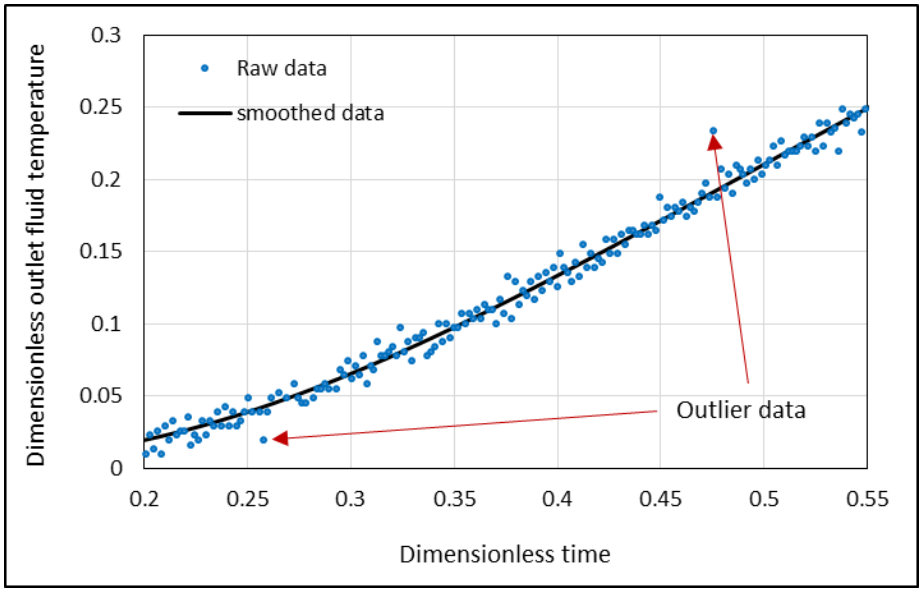

Figure 3-22 Outlet fluid temperature versus time Smoothed data

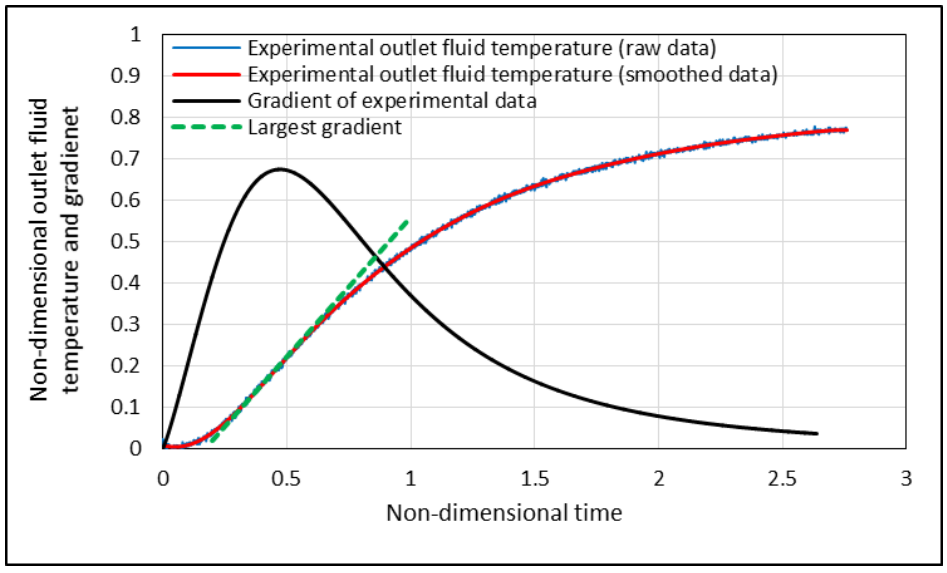

Figure 3-23 Experimental outlet fluid temperature and gradient

The gradient of the experimental data was found from the derivative of the polynomial function. Shown in Figure 3-23 is a representative outlet fluid temperature and its gradient. The maximum gradient occurred at the inflection in the curve, as shown in the figure.

The inlet fluid temperature forcing function ($T_{fi} = f(t)$) is a description of its change with time and is defined as $T_{fi}(t) = 1$ for the single blow method and $T_{fi}(t) = \sin(\omega\, t)$ for the periodic method. Liang et al. [256] first used an exponential function to describe the forcing inlet fluid temperature. Both the step change and the exponential function are used in the literature to define the inlet fluid temperature in the single blow model [5, 16, 191, 195, 284].

In this work, an exponential function was used to define the inlet fluid temperature, and curve fitting was utilised to find the necessary coefficients. A typical sample of the measured inlet fluid temperature is shown Figure 3-24. The rapid rise in the inlet fluid temperature obtained in these tests meant that the implementation of the exponential function had no measurable effect compared to using a step change. The coefficient, β, was found to have an average value of 0.013.

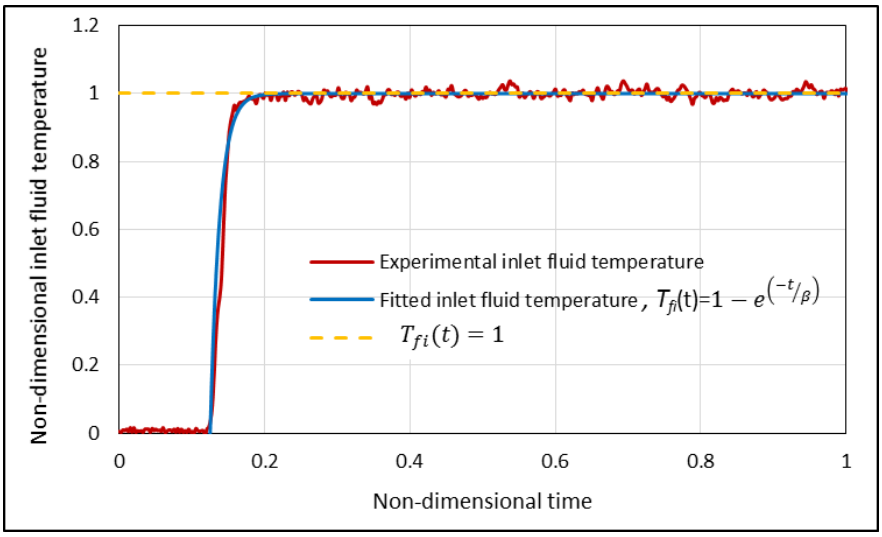

Figure 3-24 Inlet fluid temperature as function of time

3.3.9 Fluid temperature prediction and matching technique

Prediction of the exit fluid temperature is essential for accurate curve matching as it accounts for thermal losses to the pipe and holder. The effective

thermal conductivity of the porous material was measured and the thermal conductivity of holder and wall (ABS plastic) was provided by the manufacturer. These were utilised in Equation 3.22 to give λ_m and λ_w. The heat capacity ratio of the tested sample to holder (R_{tc}) should also be known.

Some previous studies have excluded heat lost to the side wall because the core matrix area is much larger than the holder wall [191]. However, in these tests it was found that ignoring thermal exchange with the holder resulted in a measurable error in determining the convective heat transfer coefficient [190, 191]. In order to predict the fluid temperature, the values of $\mathrm{NTU_m}$, $\mathrm{NTU_w}$ were assumed at the start of the analysis [190], and effect of the side wall on the exit fluid temperature response was assessed by introducing R_{NTU}, where

$$R_{NTU} = \frac{NTU_w}{NTU_m} \qquad 3.34$$

It was initially assumed that its value equals the ratio of areas of the wall to matrix heat transfer area [190, 191]. Before starting the matching technique, it is important to understand the impact of each parameter on the response of exit fluid temperature. Shown in Figure 3-25 is the effect of $\mathrm{NTU_m}$ on the predicted temperature response for constant values of $\mathrm{R_{tc}}$, $\mathrm{NTU_w}$ and $\mathrm{\lambda_m}$.

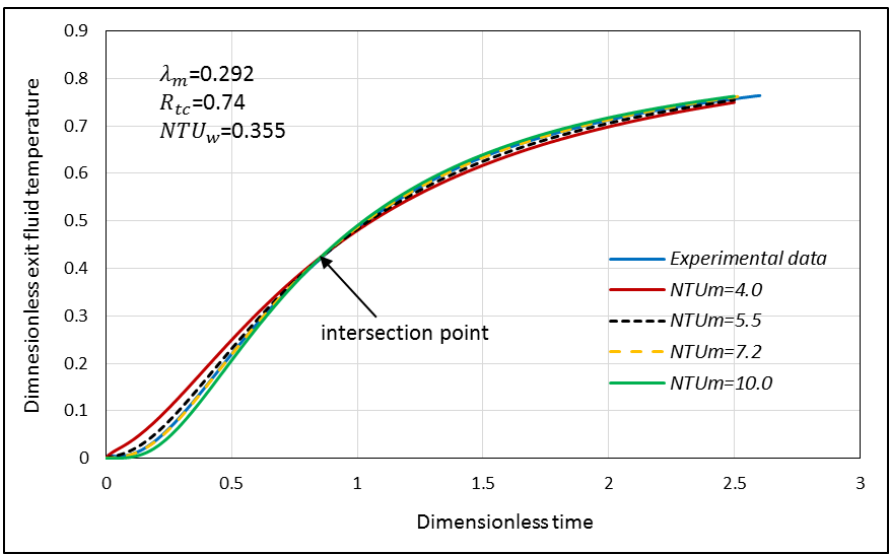

Figure 3-25 The effect of NTU_m on the exit fluid temperature response

As $\mathrm{NTU_m}$ increases, the fluid temperature is initially reduced. There then follows an intersection point and then it increases. This is brought about by a relative increase in the amount of energy being absorbed by a porous matrix due to an increase in the heat transfer area of the matrix or its total heat capacity or a decrease of the fluid mass flow rate. The impact of changing $\mathrm{NTU_m}$ is largest before the intersection point.

A portion of the incoming heat is transferred to the side wall and this continues until thermal equilibrium is achieved. This can be assessed by changing $\mathrm{NTU_w}$ as shown in Figure 3-26. Heat transfer to the side wall has a measurable impact on the exit fluid temperature and as a result, the maximum slope is reduced. Initial heat transfer to the matrix is therefore due to its high heat transfer area and total heat capacity compared with the side wall. As $\mathrm{NTU_w}$ increased, the maximum slope decreased. Therefore, the side wall could not be assumed to be adiabatic and the effect of $\mathrm{NTU_w}$ should be considered when the maximum slope technique is used.

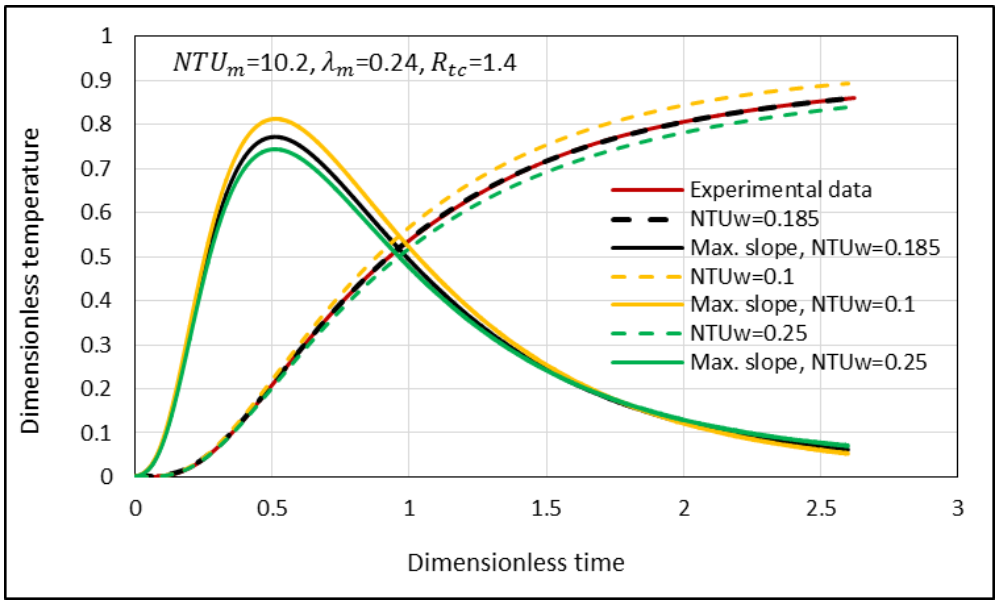

Figure 3-26 The effect of NTU_w on the maximum slope and exit fluid temperature response

The impact of the thermal capacity ratio ($\mathrm{R_{tc}}$) is illustrated in Figure 3-27 (for constant $\mathrm{NTU_m}, \mathrm{NTU_w}$ and λ_m). For t<1.0, there is no measurable effect on the

breakthrough curve of the exit fluid temperature or the maximum gradient. Therefore, most of the heat content in the incoming air is transferred to the porous matrix rather than to the wall due to its high area. It can also be noted that the effect of R_{tc} is similar to $\mathrm{NTU_w}$, as it has most impact in the later stages of the temperature rise. For the case at $\mathrm{NTU_w} = 0.185$, remarkable differences in the outlet fluid temperature breakthrough curve only occur for t>1.0 with different values of $\mathrm{R_{tc}}$. An explanation for this is that the matrix material reached the thermal equilibrium state and no more energy could be stored in the core. Increasing $\mathrm{R_{tc}}$ decreases the thermal capacity of the holder, which means that less energy can be stored in the holder and therefore, the outlet fluid temperature increases as shown in Figure 3-27.

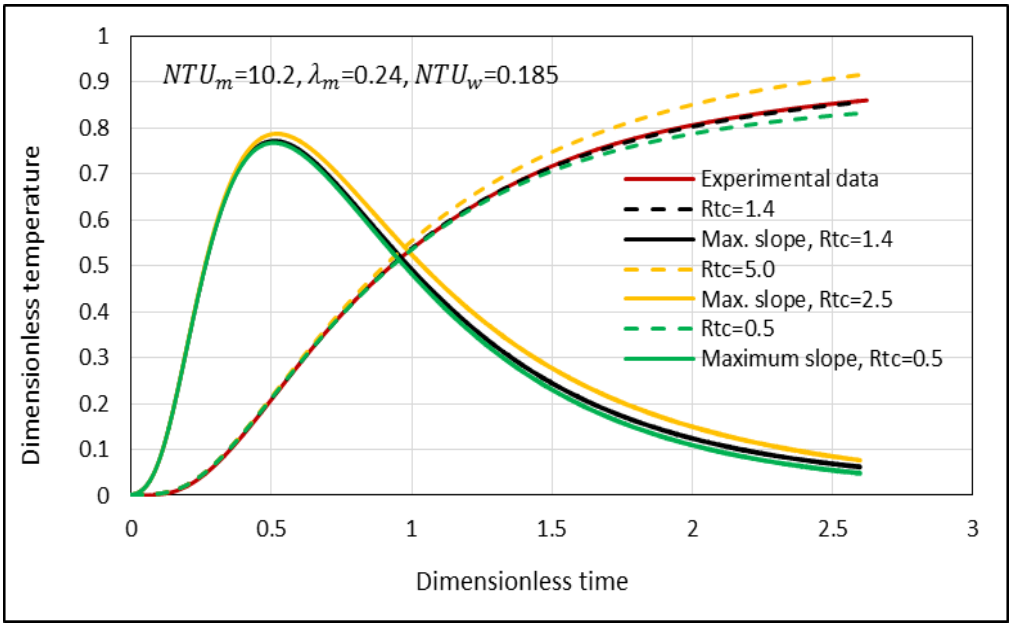

Figure 3-27 The effect of R_{tc} on the maximum slope and exit fluid temperature response

From the above, it can be seen that the impact of $\mathrm{NTU_m}$ is greatest at the initial stages of the heating process whereas, the impact of both $\mathrm{R_{tc}}$ and $\mathrm{NTU_w}$ is greatest during the later stages. It is also worth noting that at the last stage, the thermal exchange phenomena has multiple relationships in terms of both $\mathrm{R_{tc}}$ and $\mathrm{NTU_w}$.

Increasing $\mathrm{R_{tc}}$ might decrease the heat transfer area of the holder and thus the $\mathrm{NTU_w}$. Therefore, identifying the impact of both these parameters on the outlet

fluid temperature and the thermal exchange individually is difficult. In the last portion, the outlet fluid temperature history is more sensitive to the change of $\mathrm{NTU_w}$ than that of $\mathrm{R_{tc}}$. Where the effect of $\mathrm{NTU_w}$ change started at t≈0.5, whereas that of $\mathrm{R_{tc}}$ started at t≈1.0. This is because increasing the $\mathrm{NTU_w}$ increases the heat transfer to the holder and thus to the environment at constant wall heat capacity. At constant $\mathrm{NTU_w}$, increasing the $\mathrm{R_{tc}}$ decreases the thermal capacity of the wall and thus the energy stored by the holder material.

As there is an effect of these parameters on the breakthrough curve of the outlet fluid temperature, so excluding the holder might have an impact on the heat transfer results. In order to obtain reliable results, the physical parameters used to determine the R_{tc} value should be measured carefully. As recommended by Heggs et al. [24], relying on more than one technique to determine the thermal parameters is importance to achieve reliable results.

3.3.10 Matching method

A trial and error approach was used to match the predicted and experimental exit fluid temperatures. Values of $\mathrm{NTU_m}$ and $\mathrm{NTU_w}$ were assumed and the exit fluid temperature was determined by solving the Equations from 6.9 to 6.11. Then, the values of both NTU_m's were modified until the difference between experimental and predicted exit fluid temperatures was acceptable (in this case $<10^{-3}$). Both the direct matching and maximum slope techniques were used. The role of the maximum slope method was mainly to confirm the values of $\mathrm{NTU_m}$ and $\mathrm{NTU_w}$ obtained by the direct matching method. An example of the iterative steps is given below, the results are shown in Figure 3-28.

1. Start with Equation 6.23. For the case at $\mathrm{R_{tc}} = 1.4$ (sample V.S-1) the area ratio was found ≈ 0.0162, then the $\mathrm{R_{NTU}}$ equals the same value.
2. A first guess of $\mathrm{NTU_m}$ was 8.0, then from the Equation 6.23 $\mathrm{NTU_w}$=0.13.
3. $\mathrm{NTU_m}$ was modified until the predicted temperature matched the experimental one at $\mathrm{NTU_m} = 10.2$.

4. $\mathrm{NTU_w}$ was modified until satisfactory matching was reached at $\mathrm{NTU_w} = 0.185$.
5. The values of $\mathrm{NTU_m}$ and $\mathrm{NTU_w}$ were changed and iterations continued until an acceptable value of least squares (R) was achieved [5, 24] between the predicted and experimental exit fluid temperatures ($T_{fpred.i}$,$T_{fexp.i}$).

$$R = \sqrt{\sum_{i=1}^{i=n} \left[\left(T_{fpred.i} - T_{fexp.i} \right)^2 \right]} \qquad 6.24$$

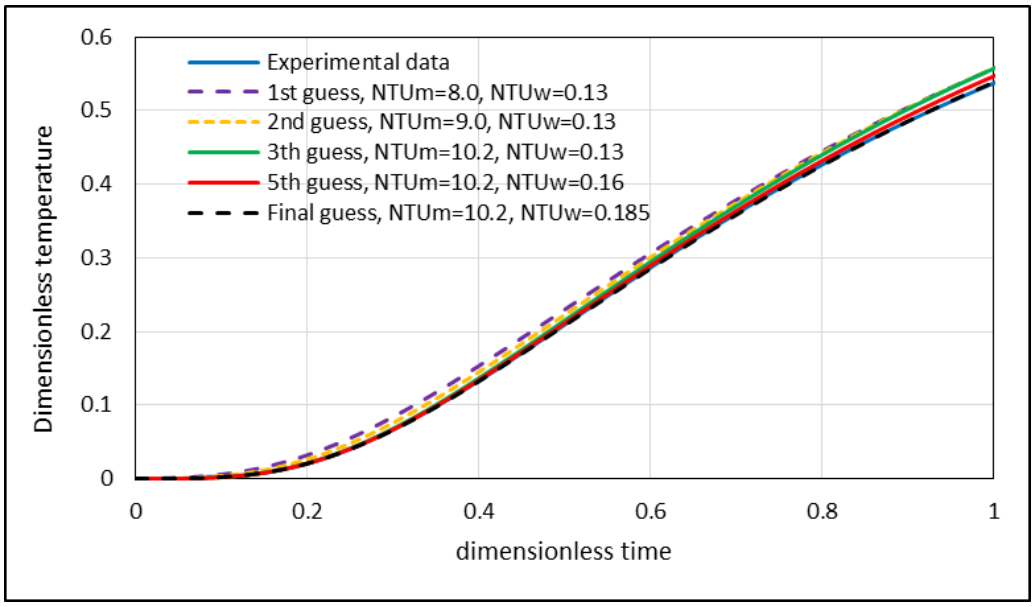

Figure 3-28 The trials of the matching technique

The final step was to confirm that the curves had the same maximum slope. Shown in Figure 3-29 is the final match between the predicted and experimental exit fluid temperatures. The value of $\mathrm{NTU_m}$ predicted by maximum slope was 10.25.

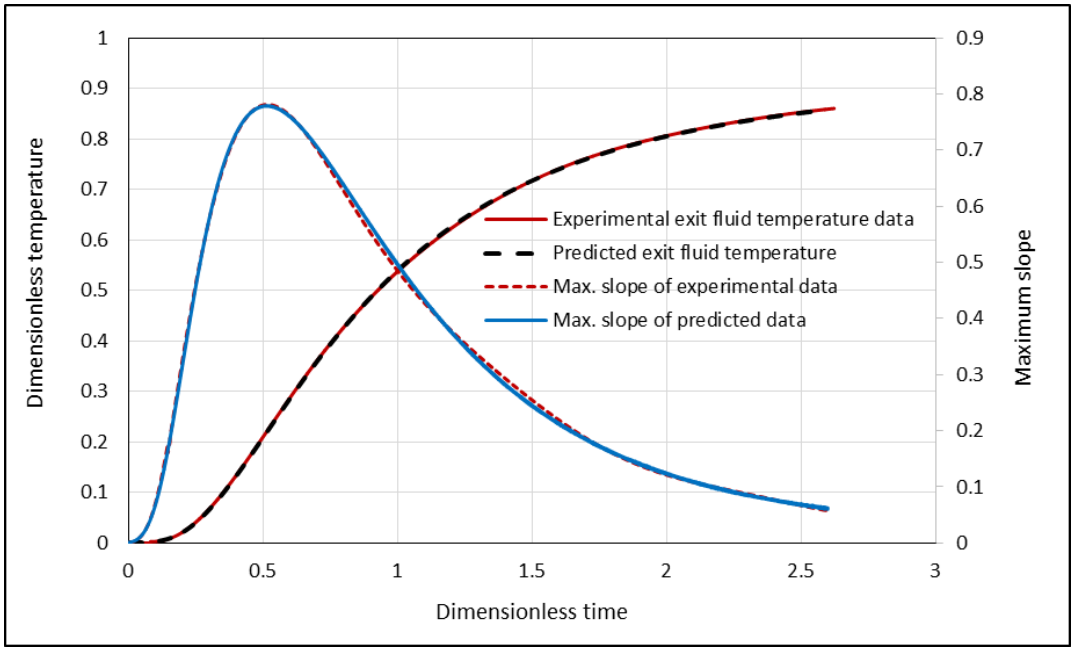

Figure 3-29 Final fit of exit fluid temperature by maximum slope method

Chapter 4

4. Porous material production

4.1 Introduction

Porous materials are cellular bodies made up of a solid skeleton surrounded by pores or voids. They have received great interest for a number of applications due to their thermo-physical and mechanical properties such as: permeability, high stiffness and low specific mass [38, 285]. For heat transfer applications they offer a high specific surface area and high thermal conductivity. Porous materials are available in many materials, including aluminium, nickel, copper, ceramics, polymers and other metal alloys [17, 39-41]. They can be produced with different porosities and pore size depending on the application. There are a number of methods used for their manufacture, including the replication method, vapour deposition and electrochemical deposition. The manufacturing methods are classified according to the state of the material and the properties of the final product [38, 285]. A full review of manufacturing methods can be found in reference [38].

The replication method (Casting) was used in this work to produce repeatable aluminium foam structures with porosities over 60% [286]. The basic principle of this method was to infiltrate melted aluminium through spaces between packing salt (sodium chloride) particles (preform) [132, 287]. The salt was then washed away with water to make void spaces in the cellular sponges. The preform material (NaCl) must have three properties [27, 28, 288]: (i) its melting point must be higher than that of molten metal sued for casting; (ii) be chemically stable within the casting metal; (iii) be easy to remove after the cast metal has solidified. The main attraction of the replication method is that it allows the production of different pore shapes [133].

In this work, the aim was to produce aluminium metal sponges with four different average pore diameters using the spherical and irregular pre-form salt

shapes. The different pore diameters were classified into four groups depending on the average grain diameter as; 'Very Small' (d_p=0.71-1.0mm), 'Small' (d_p=1.0-1.18mm), 'Medium' (d_p=1.4-1.7mm) and 'Large' (d_p=2.0-2.36mm). The spherical pre-form salts are regenerated with Hydraulic water softening granules of sodium chloride (NaCl), (http://www.aquadition.co.uk/shop/granular-water-softener-salt). Shown in Figure 4-1 are examples of the spherical and crushed pre-form salt used.

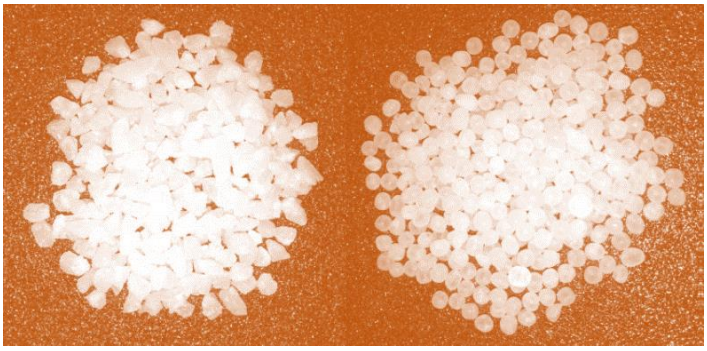

Figure 4-1 Spherical and crushed salt

The pre-form salt was prepared from raw salt by sifting using graded sieves. Both crushed and spherical salt particles were manufactured for each grade except for the Very Small where only spherical particles were used. The raw salt was hydro-soft water softening particles. Shown in Figure 4-2 is the arrangement of the sieves grades used to prepare the salt grains.

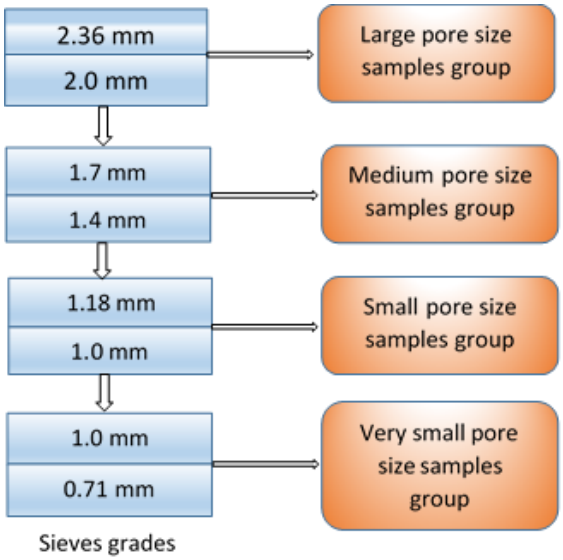

Figure 4-2 The sieves grades used for each pore size group

For the irregular shaped grains, the raw salt was first crushed. It was then passed (by shaking) through the first sieve with a grade 2.36 mm. The salt which remained was further crushed. The salt which passed through was then sieved using the 2.0 mm sieve. If it was retained in this sieve it was collected to use for manufacturing the large pore diameter foams. This process was repeated as the salt became smaller.

4.2 Replication manufacturing process

The manufacturing method is described in full detail in previous studies [27, 28, 197, 289], although a brief description is given here. The salt was poured into the mould and shaken to improve the particle packing. The amount of salt varied between 100g and 300g depending on the height of the sample. To allow the air inside the mould to move from the preform, 100g of fine salt (approximately one fourth of preform grain size) was poured first [27, 197].

Shown in Figure 4-3 is the mould as it was setup before processing. The aluminium block, which was melted, sat above the preform and fine salt. The inside and outside diameters of the mould were 51mm and 60mm respectively. The mould was made of stainless steel and was 150 mm high.

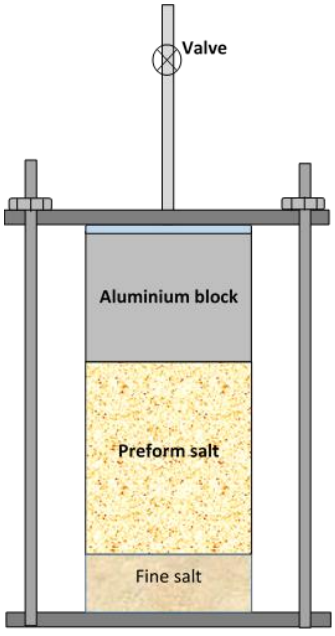

Figure 4-3 The schematic of the mould used for the replication method

After the preform and the aluminium were arranged in the mould it was bolted together and connected to a vacuum pump and argon supply. A schematic of the manufacturing configuration is shown in Figure 4-4. Initially, valves 1 and 2 were closed and the valves 3 and 4 were opened and then the vacuum pump turned on until a vacuum pressure of 720 torr was achieved. Then, the vacuum pump was switched off and left 5 minutes to test the vacuum inside the mould.

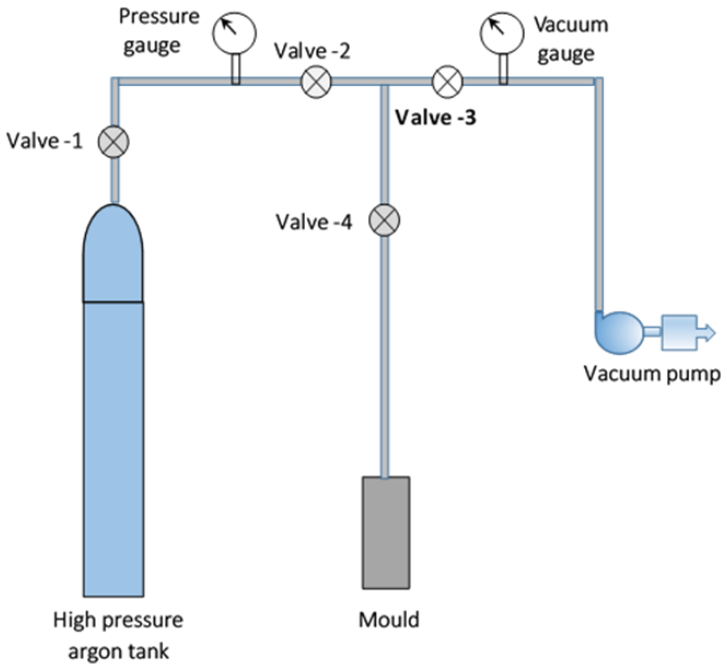

Figure 4-4 The arrangement of the replication method connections

To melt the aluminium, the mould was placed in a furnace for 50 to 60 minutes at a temperature of 740°C. The NaCl salt can crack at high temperatures as a result of its reaction with oxygen [28] where it turns to ashes, which will have an effect on the structure of the metal sponge. This issue was resolved by heating up the salt under vacuum and infiltration using argon [27, 28, 132]. Once the aluminium was thought to be melted, valves 3 and 4 were closed and the argon infiltrated through the sample. The infiltration pressure was controlled by valve 1 after valves 2 and 4 were opened to start the process. After 1 minute, the mould was taken out from the furnace and left to cool, causing the melted aluminium to solidify. The infiltrated aluminium sponge still in the mould is shown in Figure 4-5.

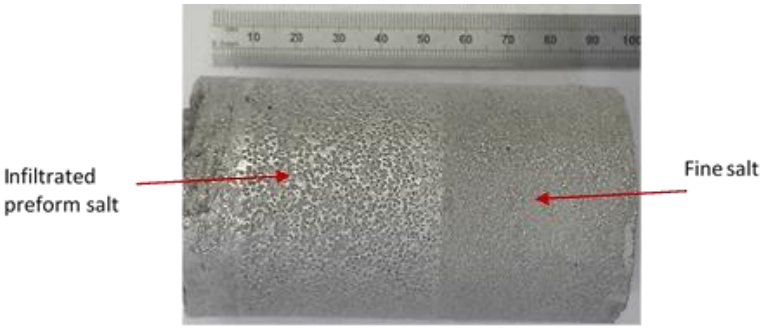

Figure 4-5 Infiltrated sample after solidification

Microstructure parameters, such as the pore diameter and porosity can be controlled during the manufacturing process. The porosity can be controlled by the infiltration pressure [27, 287]. The size of the preform and its packaging quality (for example by vibration the mould) have also be shown to change porosity [286, 290, 291].

4.3 Produced metal sponges samples

The techniques were used to produce sixty-nine aluminium sponges from pure aluminium (99.9%) with different porosities and pore sizes. Shown in Figure 4-6 are the photos of the four different pore size samples.

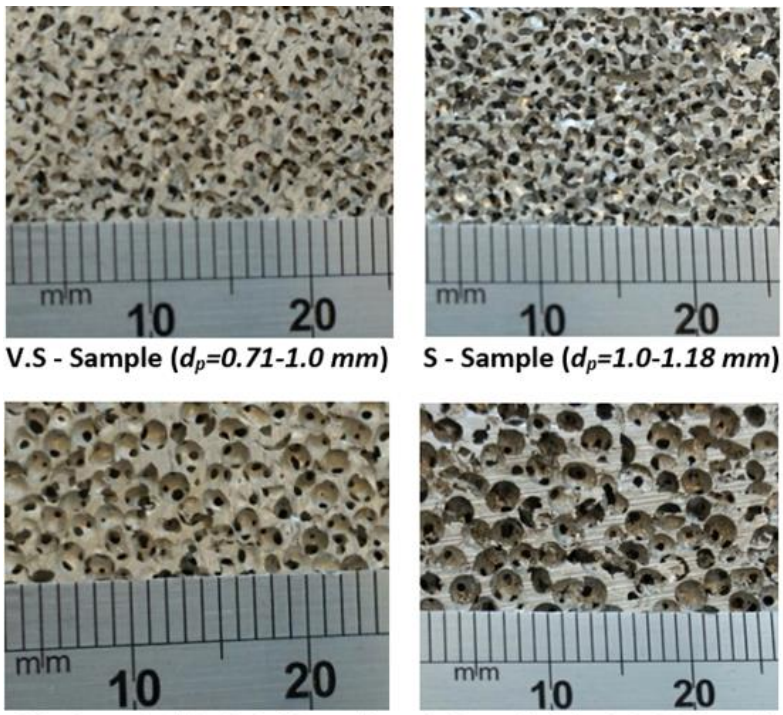

Figure 4-6 Photos of appearance surfaces

Geometrical parameters of the sample examined in this work are tabulated in Table 4-1, Table 4-2, Table 4-3 and Table 4-4.

Table 4-1 Geometrical parameters of Very Small pore size samples (PPI=20-25, dp=0.71-1.0 mm)

Sample Name	Weight, gr	Thickness, (mm)	Volume, (mm^3)	Porosity, %
V.S-1	39.24	25.78	50781	0.7225
V.S-2	36.94	21.71	42764	0.6962
V.S-3	38.82	21.22	41799	0.666
V.S-4	46.77	25.00	49245	0.659
V.S-5	48.50	27.26	53696	0.6822
V.S-6	50.58	27.07	53322	0.6595
V.S-7	48.11	26.12	51451	0.6643
V.S-8	37.06	23.70	46684	0.715
V.S-9	58.04	31.60	62245	0.665
V.S-10	47.34	24.19	47649	0.643
V.S-11	47.68	27.16	53499	0.680
V.S-12	44.00	25.00	49245	0.679

Table 4-2 Geometrical parameters of Small pore size samples (PPI=15-20, dp=1.0-1.18 mm)

Sample Name	Weight, gr	Thickness, (mm)	Volume, (mm^3)	Porosity, %
S-1	48.10	23.70	46684	0.6301
S-2	48.78	23.65	46585	0.6272
S-3	51.70	24.70	48654	0.6184
S-4	51.30	25.10	49442	0.6272
S-5	42.22	25.13	49501	0.6960
S-6	41.71	25.33	49895	0.6992
S-7	38.02	25.64	50505	0.7302
S-8	45.43	24.95	49146	0.6683
S-9	45.84	25.07	49382	0.6680
S-10	41.71	25.17	49579	0.6990
S-11	35.80	23.64	46566	0.7246
S-12	40.11	25.23	49698	0.7107
S-13	45.14	25.40	50033	0.6770
S-14	38.23	25.15	49540	0.7227

Table 4-3 Geometrical parameters of Medium pore size samples (PPI=10-15, dp=1.4-1.7 mm)

Sample Name	Weight, gr	Thickness, (mm)	Volume, (mm^3)	Porosity, %
M-1	52.33	24.50	50245	0.6103
M-2	50.22	24.12	49466	0.6205
M-3	49.13	24.35	49937	0.6323
M-4	47.13	24.03	49281	0.6425
M-5	49.63	24.50	50245	0.6308

M-6	52.55	23.95	49117	0.6000
M-7	49.9	23.80	48700	0.6369
M-8	52.0	26.50	54200	0.6415
M-9	48.7	24.50	50100	0.6168
M-10	44.03	26.10	51411	0.6922
M-11	42.53	24.96	49166	0.6902
M-12	44.51	25.10	49442	0.6766
M-13	34.10	26.70	52593	0.7628
M-14	30.96	25.75	50722	0.7796
M-15	33.89	25.19	49619	0.7527
M-16	46.81	23.05	45404	0.6317
M-17	34.98	26.05	51313	0.7578
M-18	41.19	23.85	46979	0.6853
M-19	43.24	24.65	48555	0.6816
M-20	39.91	25.70	50623	0.7170
M-21	42.49	25.15	49540	0.6919
M-22	39.91	24.75	48752	0.7091
M-23	38.33	25.65	50525	0.7306
M-24	44.09	25.82	50860	0.6896
M-25	41.29	25.22	49678	0.7018
M-26	41.51	24.70	48654	0.6937

Table 4-4 Geometrical parameters of Large pore size samples (PPI=5-10, dp=2.0-2.36 mm)

Sample Name	Weight, gr	Thickness, (mm)	Volume, (mm^3)	Porosity, %
L-1	54.03	25.63	52563	0.6158
L-2	54.80	24.62	50491	0.5943
L-3	49.18	24.70	50655	0.6371
L-4	41.14	24.00	49220	0.6116
L-5	49.68	24.05	49322	0.6235
L-6	48.82	23.46	48112	0.6207
L-7	47.40	25.50	52296	0.6612
L-8	48.80	25.30	51886	0.6492
L-9	51.40	26.70	54757	0.6491
L-10	41.66	24.97	49185	0.6974
L-11	38.79	23.92	47117	0.7075
L-12	38.95	25.55	50328	0.7224
L-13	44.08	25.81	50840	0.6929
L-14	43.89	25.78	50781	0.6907
L-15	38.19	24.98	49205	0.7222
L-16	37.79	25.45	50131	0.7311

4.4 Other porous materials

Two other types of more traditional porous materials were used in this study for comparison; packed beds of spherical stainless steel balls and mesh wire screens.

Packed beds of spherical stainless steel balls were prepared by pouring the balls into a holder which was then shook to improve the distribution of the packaging. Two different steel balls samples were used in this study; 1.5 mm and 2.0 mm diameter balls. The mesh wire screens were produced using a Norton 6DB fly press to cut circles of diameter 51mm from sheets of mesh as described in [197]. The three packed beds of mesh wire samples with different pitches were used in the pressure drop study. In the thermal study, only type of pitch was used but the number of layers was varied. The structural parameters of the packed beds of spheres and mesh wire screens samples are tabulted in Table 4-5.

Table 4-5 Geometrical parameters of traditional porous matrix (Packed beds of balls and mesh wire screens)

Sample	porosity (ε)	P_t, mm	Particle diameter, mm	Wire diameter (d_w), mm	Material
Mesh-1	0.746	1.0	-	0.36	Stainless steel
Mesh-2	0.878	1.4	-	0.24	Aluminium alloy
Mesh-3	0.784	2.0	-	0.56	Stainless steel
Ball-1	0.362	-	1.5	-	Stainless steel
Ball-2	0.393	-	2.0	-	Stainless steel

The porosity (ε) of the replicated metal sponges were defined as the void volume to the total volume of the sample(V_t) [39, 117, 173]. It can be determined by measuring the sample mass (m_s) and knowing the densities of the air and solid material [173].

$$\varepsilon = \frac{\rho_{sol} - m_s/V_t}{\rho_{sol} - \rho_{air}} \qquad 4.1$$

The porosity of the packed beds of spheres was obtained by the total volume of the holder and the volume of all spheres. For the packed beds of mesh wire screens the porosity was been obtained by the expression given by Chang [228, 292].

$$\varepsilon = 1 - \frac{\pi\, n\, d_w^2}{2\, p_t\, D}\left(1 + \frac{d_w^2}{p_t^2}\right)^{1/2} \qquad 4.2$$

The heat transfer area for the packed beds of spheres can be obtained using the number of balls and the surface area of one ball. For the packed beds of mesh wire screens, it can be obtained by the using the expression [228].

$$A_h = 4\,A_c L(1-\varepsilon)/d_w \qquad 4.3$$

Where the n, d_w, p_t, D, A_c , L are the number of screens layers, diameter of the wire, screens transverse pitch, diameter of the sample, cross sectional area of the sample and thickness of the sample respectively. The microstructure parameters used to chractersise the porous sponges were porosity, pore diameter, strut thickness and node diameter. For the spherical ball packed beds, the main parameters were the porosity and particle diameter. The chracterisation parameters for the mesh wire screen packed beds are porosity, transverse pitch, and wire diameter.

Chapter 5

5. Pressure drop results and discussion

5.1 Pressure drop measurements results

The pressure drop measurements are typically presented in terms of pressure drop per unit length against the frontal air velocity. Shown in Figure 5-1 is a sample of the measurement data demonstrating the agreement between the 3 repeated tests.

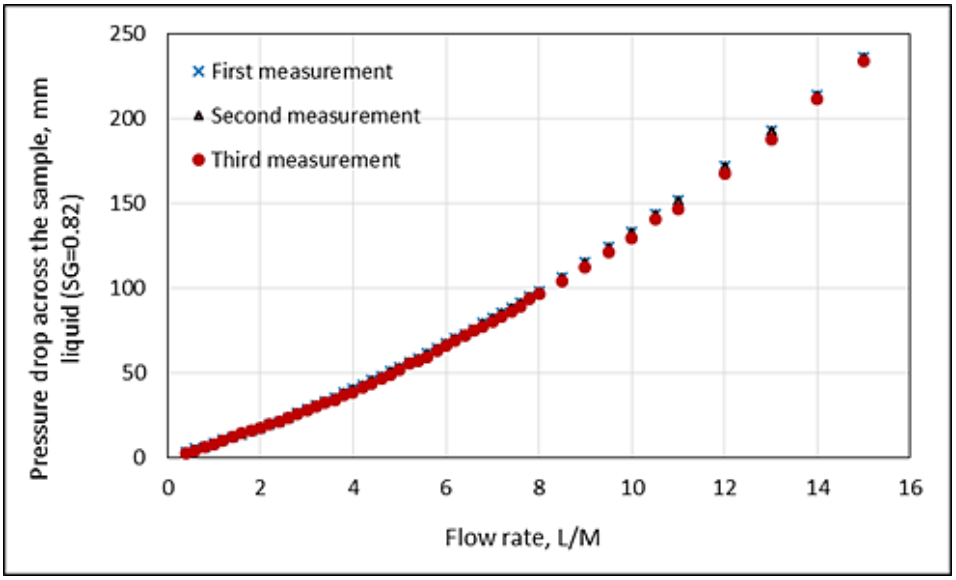

Figure 5-1 Typical values of pressure measurements

The main aim of the low flow rate experiments was to find the permeability in Darcy's regime which can be identified when the pressure gradient increases linearly with flow velocity. Shown in Figure 5-2 to Figure 5-6 are the pressure drops per unit length versus frontal air velocity of four groups of aluminium foam samples.

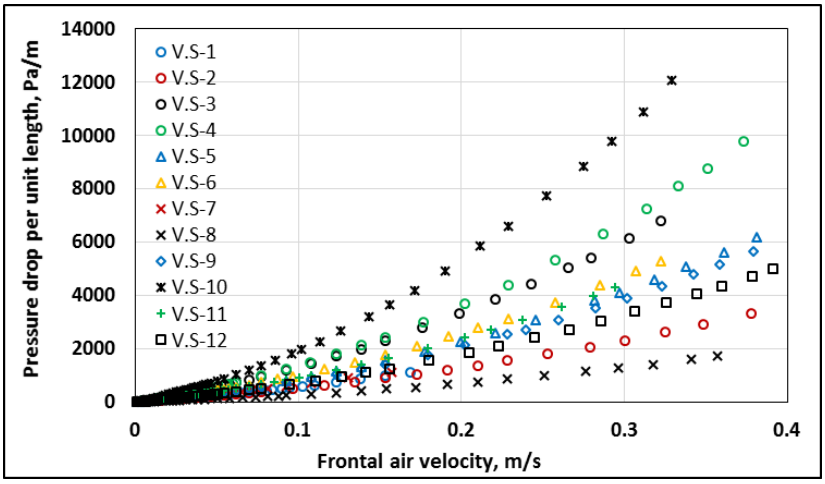

Figure 5-2 Measured pressure drop per unit length versus frontal air velocity (Very Small pore size samples)

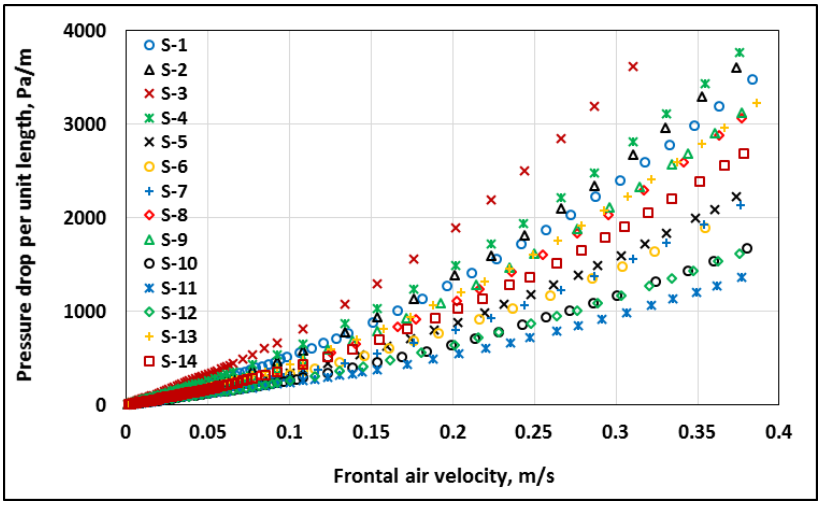

Figure 5-3 Measured pressure drop per unit length versus frontal air velocity (Small pore size sample)

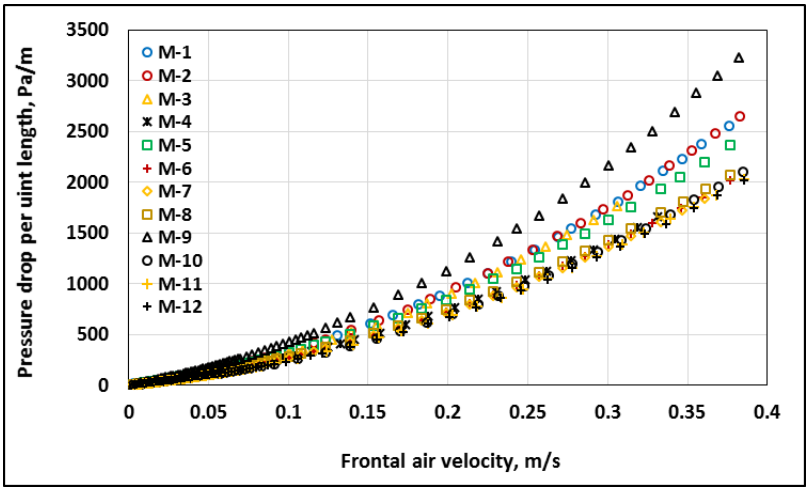

Figure 5-4 Measured pressure drop per unit length versus frontal air velocity (Medium pore size sample)

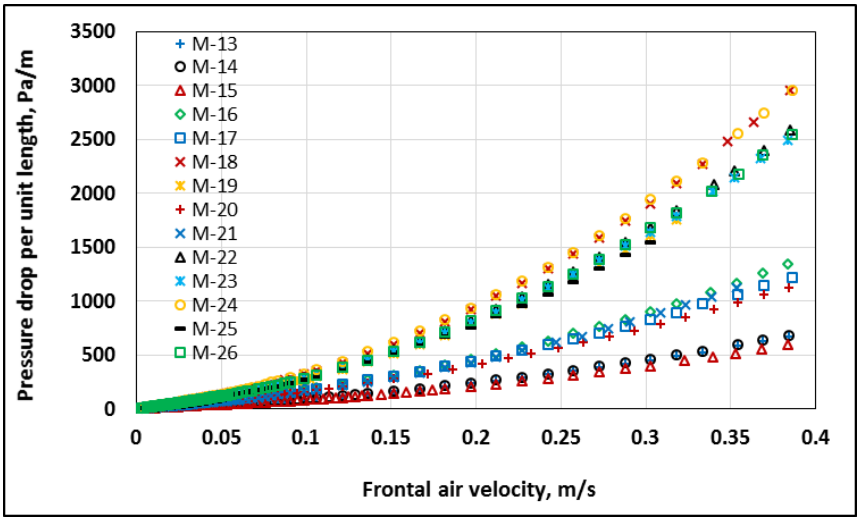

Figure 5-5 Measured pressure drop per unit length versus frontal air velocity (Medium pore size samples)

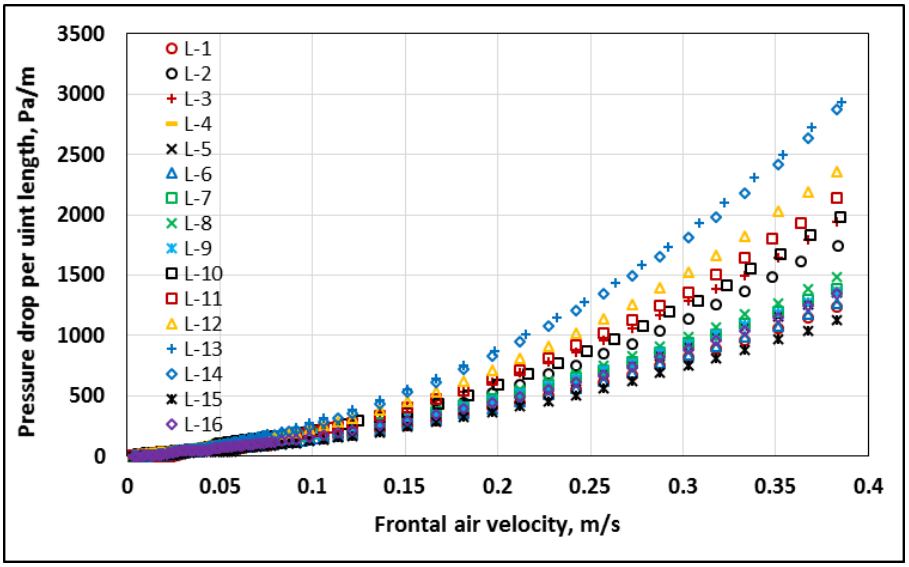

Figure 5-6 Measured pressure drop per unit length versus frontal air velocity (Large pore size samples)

The impact of particle diameter on packed beds of spheres and pitch size in mesh wire screens was also studied and the experimental pressure results are shown in Figure 5-7 and Figure 5-8. Also shown in Figure 5-8 is predicted pressure drop calculated using the Ergun Equation which agreed well with the experimental results.

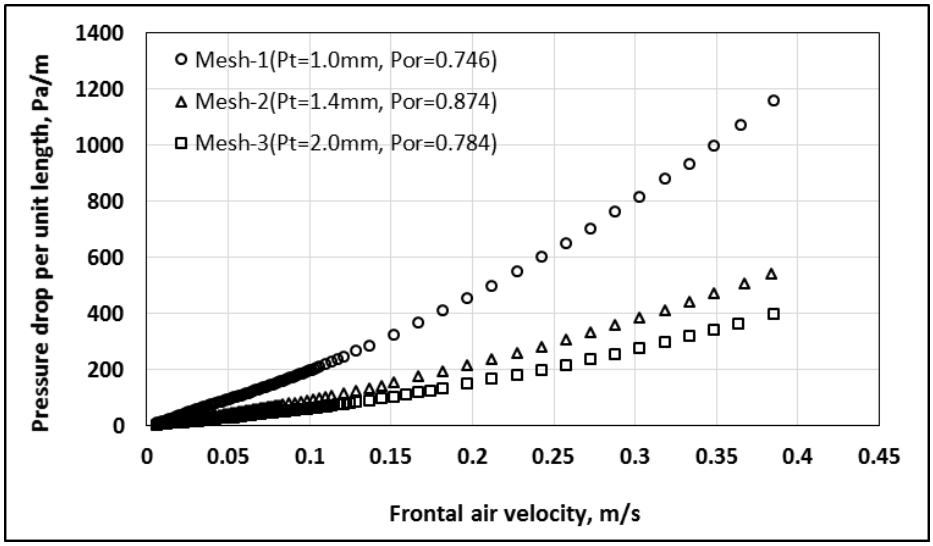

Figure 5-7 Measured pressure drop per unit length versus frontal air velocity (Mesh wire screens)

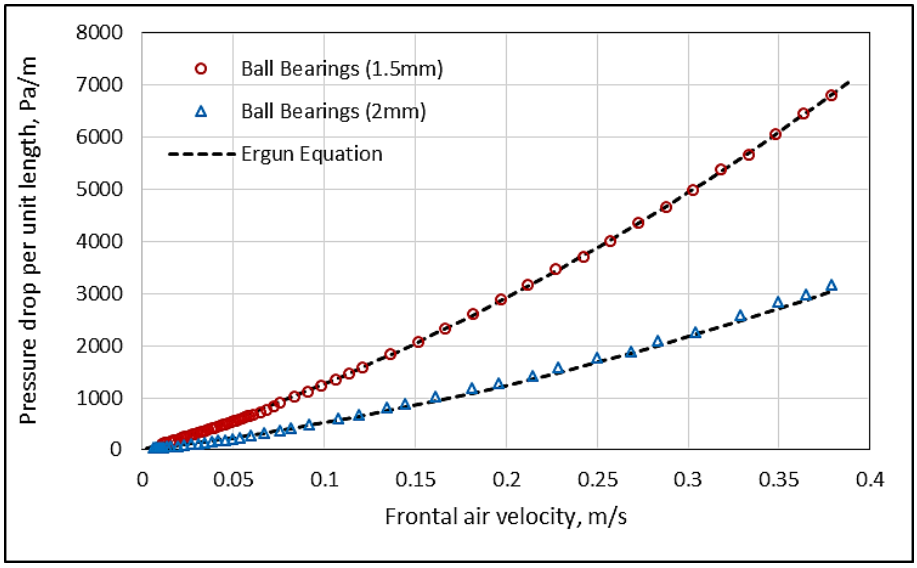

Figure 5-8 Measured pressure drop per unit length versus frontal air velocity (Ball Bearings)

In order to identify the end of Forchheimer flow regime and the transition to turbulent flow regime, the flow rate was increased. The experiments were conducted over a range of velocities from 1.3 to 8.0 m/sec. Shown in Figure 5-9 to Figure 5-13 are the pressure drops per unit length versus the frontal air velocity for four different pore sizes.

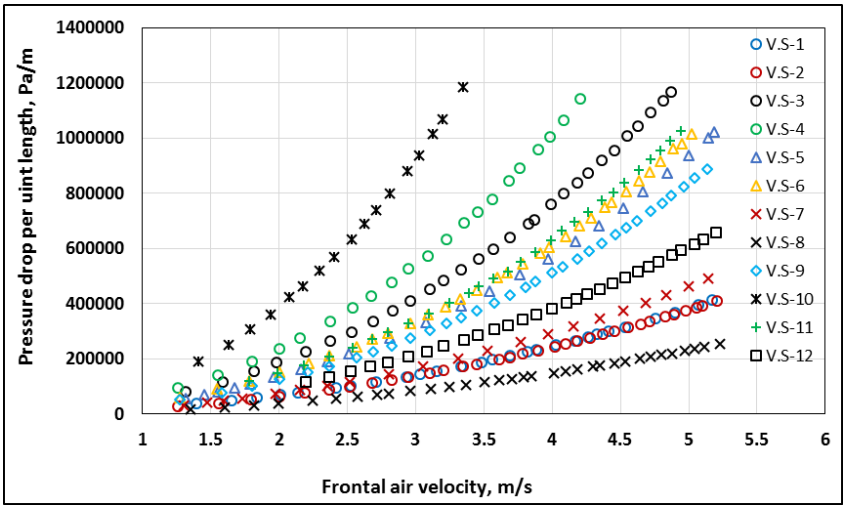

Figure 5-9 Measured pressure drop per unit length versus frontal air velocity (Very Small pore size samples)

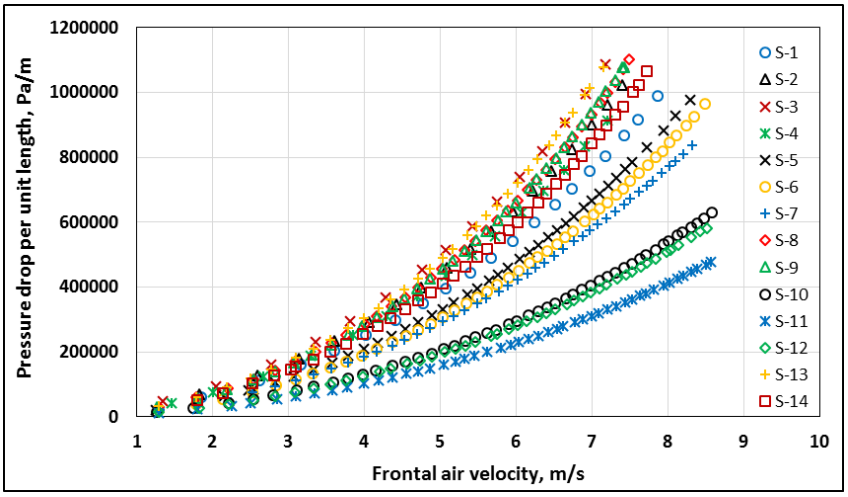

Figure 5-10 Measured pressure drop per unit length against frontal air velocity (Small pore size samples)

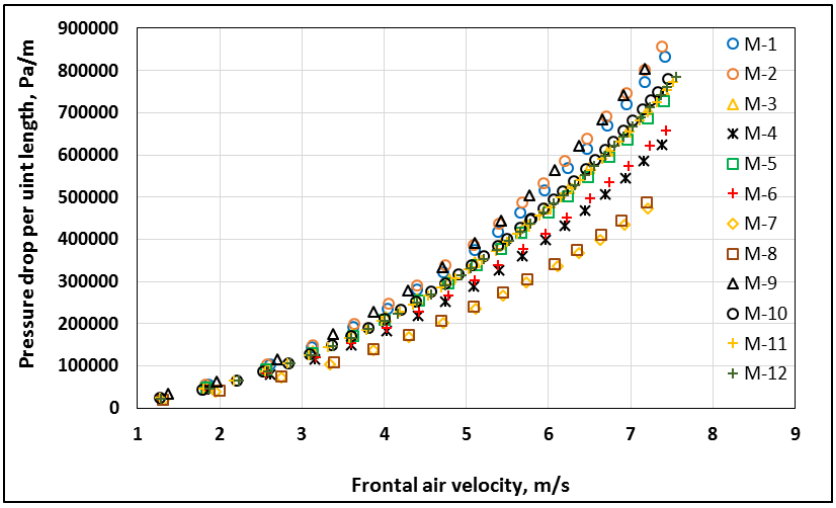

Figure 5-11 Measured pressure drop per unit length against frontal air velocity (Medium pore size samples)

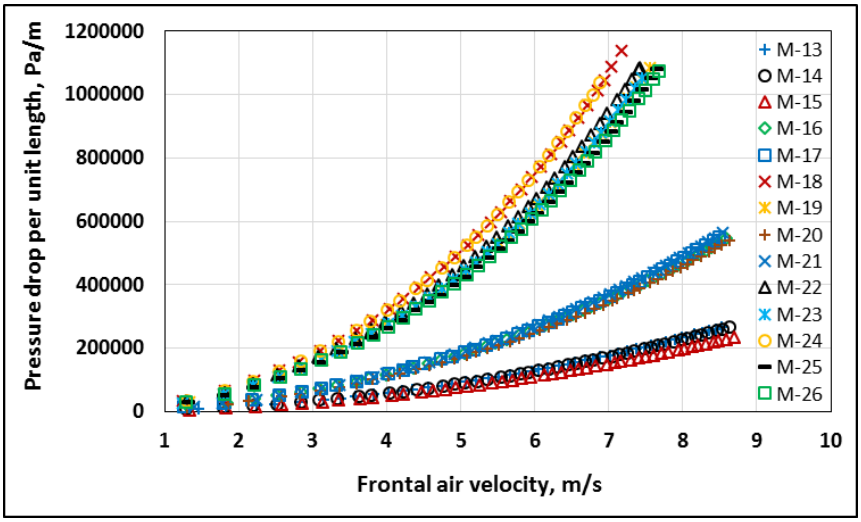

Figure 5-12 Measured pressure drop per unit length against frontal air velocity (medium pore size samples)

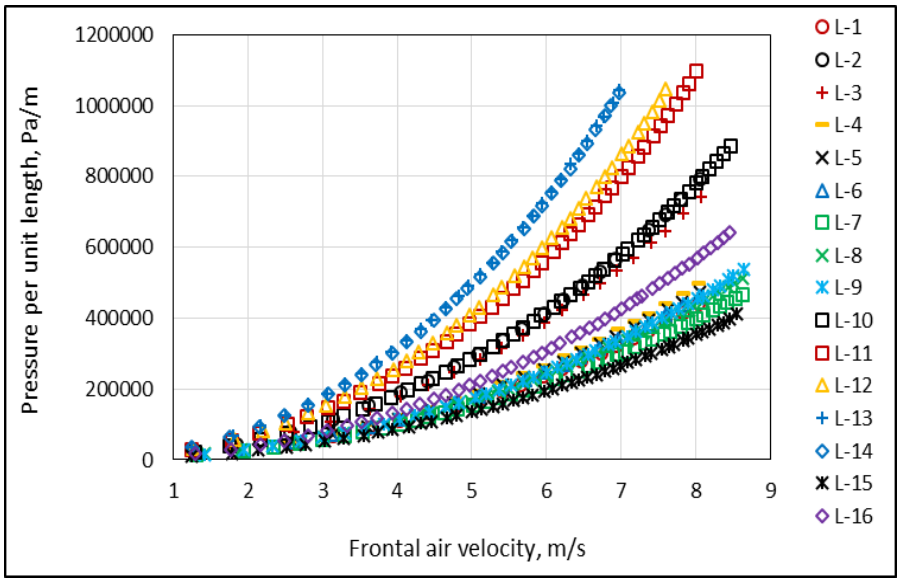

Figure 5-13 Measured pressure drop per unit length against frontal air velocity (Large pore size samples)

5.2 Flow regimes in porous media

The identification of flow regimes and pressure characterizations in different classes of porous media has been a topic of interest in a number of engineering applications. The experimental outcomes relating to flowing fluids in porous media has shown the existence of four regimes of flow [86, 87, 90, 91, 93, 104, 106]: pre-Darcy, Darcy, Forcheimer and turbulent. The reduced pressure drop has been presented against frontal air velocity [87, 91, 93] and against Reynolds number [86]

to identify the flow regimes. The change in gradients as the flow is increased indicates the transition between regimes. The aim of this study was to identify the bounds of the flow regimes for samples at lower porosities than the data available in the literature and to obtain permeability for each sample in the Darcy regime.

5.2.1 Pre Darcy's and Darcy's flow regimes

The boundaries of Darcy regime are likely to be influenced by pore size and porosity. Here, experiments were performed for metal foams with different porosities and pore sizes in order to identify their impact on the boundaries of the Darcy regime and to measure the permeability in the Darcy regime.

To determine the permeability of the porous media, Darcy's law (Eq. 2.1) was used. The Darcy regime can be identified when the normalized pressure gradient plotted against the frontal air velocity is horizontal (slope=0) [78, 87, 91, 93, 94, 97]. It can also recognized by the linear relationship between the pressure gradient and the flow velocity [41, 57, 132, 134, 240]. Examples of normalized pressure drop and pressure gradient against frontal air velocity are shown in Figure 5-14 and Figure 5-15.

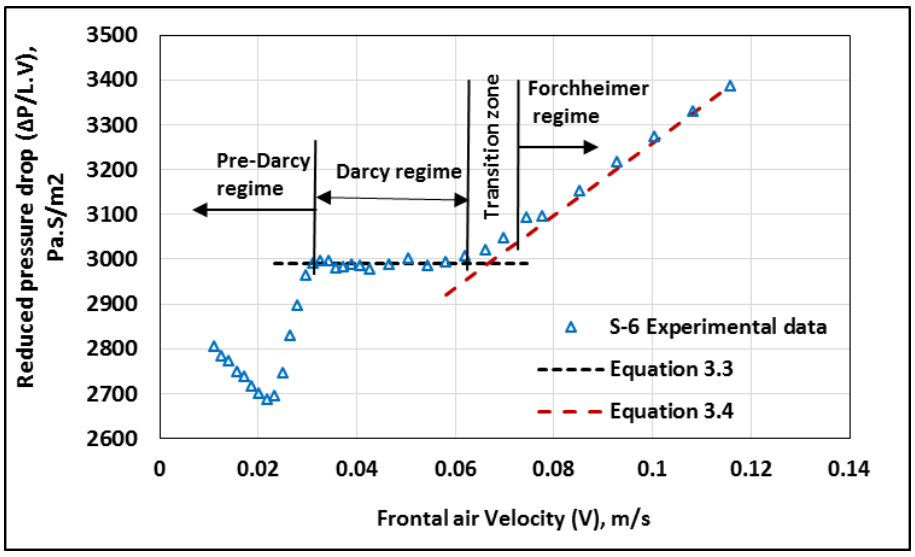

Figure 5-14 Reduced pressure drop against frontal air velocity

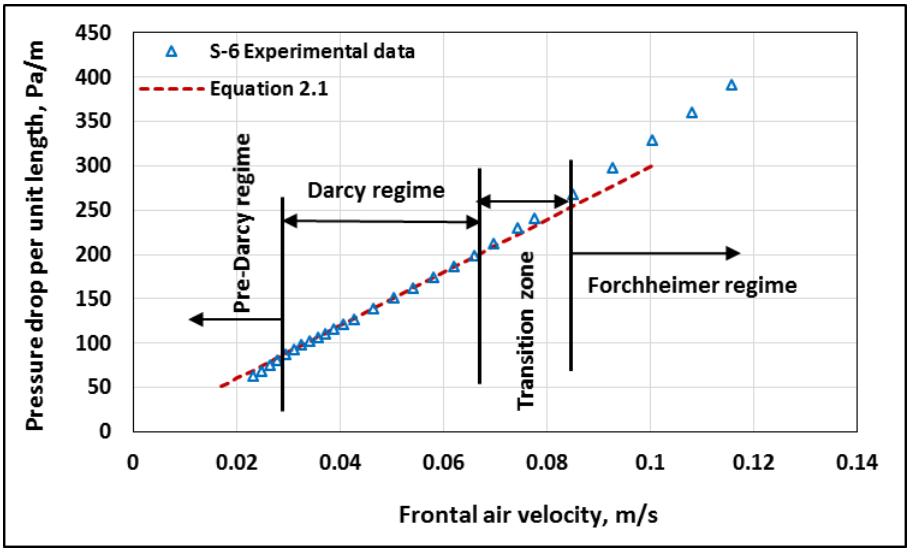

Figure 5-15 Pressure drop per unit length versus frontal air velocity for a Small sample S-6

For the samples tested, the permeability was found by using curve fitting for the linear pressure gradient and velocity data as shown in Figure 5-16.

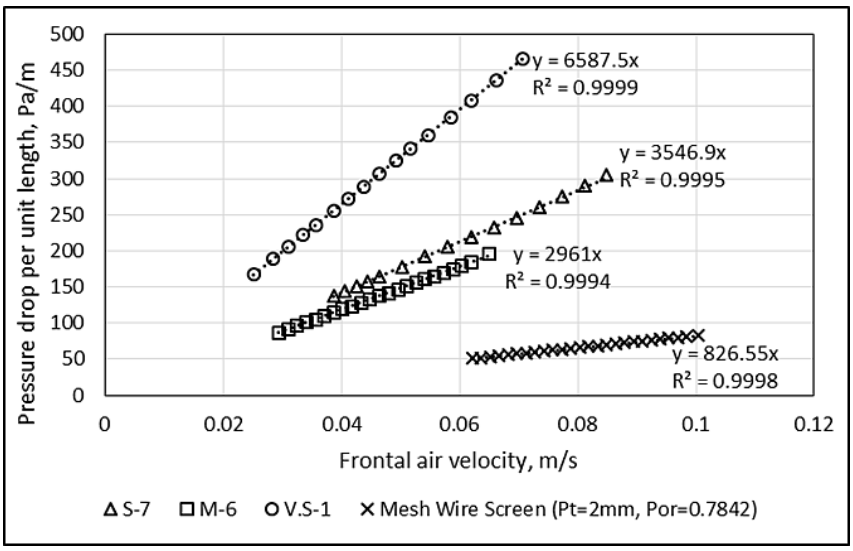

Figure 5-16 Curve fitting of pressure drop against air velocity data in the Darcy regime.

Shown in Figure 5-16 are linear least square fits to the experimental data in the Darcy regime. For the packed beds of spheres, the permeability was determined and compared with those obtained by Equation 2.7. The difference in the permeability between the measured and calculated values was less than 1.6% and 1.8% for 1.5 mm 2 mm packed beds respectively. The measured permeability and

boundaries within the Darcy regime of the samples tested for this work and those available in open literature are presented in Table 5-1 to Table 5-7.

Table 5-1 Geometrical and Darcy's regime limitations of Very Small pore size samples (dp=0.71-1.0 mm &PPI=20-25)

Sample	*ε*	*K X10^{-9} m^2*	*Darcy's Regime limitations*	*Sample*	*ε*	*K X10^{-9} m^2*	*Darcy's Regime limitations*
V.S-1	*0.7225*	*3.40*	*0.087< Re_k <0.29*	*V.S-7*	*0.6643*	*3.20*	*0.10< Re_k <0.18*
V.S-2	*0.6962*	*3.86*	*0.041< Re_k <0.15*	*V.S-8*	*0.715*	*5.31*	*0.20< Re_k <0.46*
V.S-3	*0.666*	*1.64*	*0.032< Re_k <0.085*	*V.S-9*	*0.665*	*2.81*	*0.047< Re_k <0.11*
V.S-4	*0.659*	*1.67*	*0.041< Re_k <0.10*	*V.S-10*	*0.643*	*1.24*	*0.042< Re_k <0.081*
V.S-5	*0.6822*	*2.62*	*0.045< Re_k <0.095*	*V.S-11*	*0.680*	*2.32*	*0.086< Re_k <0.18*
V.S-6	*0.6595*	*2.19*	*0.033< Re_k <0.086*	*V.S-12*	*0.679*	*3.09*	*0.090< Re_k <0.15*

Table 5-2 Geometrical Darcy's regime limitations of Small pore size samples (dp=1.0-1.18 mm & PPI=15-20)

Sample	*ε*	*K X10^{-9} m^2*	Darcy's Regime limitations	Sample	*ε*	*K X10^{-9} m^2*	Darcy's Regime limitations
S-1	0.6301	3.93	0.16< Re_k <0.23	S-8	0.6683	4.94	0.16< Re_k <0.30
S-2	0.6272	4.55	0.067< Re_k <0.13	S-9	0.6680	4.74	0.14< Re_k <0.23
S-3	0.6184	2.80	0.095< Re_k <0.20	S-10	0.6990	7.55	0.19< Re_k <0.36
S-4	0.6272	3.58	0.071< Re_k <0.14	S-11	0.7246	7.72	0.33< Re_k <0.81
S-5	0.6960	5.93	0.176< Re_k <0.31	S-12	0.7107	7.63	0.20< Re_k <0.37
S-6	0.6992	6.17	0.164< Re_k <0.31	S-13	0.6770	5.05	0.12< Re_k <0.19
S-7	0.7302	6.35	0.19< Re_k <0.38	S-14	0.7227	5.54	0.13< Re_k <0.21

Table 5-3 Geometrical and Darcy's regime limitations of Medium pore size samples (dp=1.4-1.7 mm & PPI=10-15)

Sample	*ε*	*K X10^{-9} m^2*	Darcy's Regime limitations	Sample	*ε*	*K X10^{-9} m^2*	Darcy's Regime limitations
M-1	0.6103	6.90	0.11< Re_k <0.20	M -14	0.7796	19.03	0.31< Re_k <0.58
M -2	0.6205	6.42	0.11< Re_k <0.21	M -15	0.7527	21.13	0.53< Re_k <0.90
M -3	0.6323	7.07	0.16< Re_k <0.26	M -16	0.6317	10.53	0.34< Re_k <0.50
M -4	0.6425	7.40	0.154< Re_k <0.265	M -17	0.7578	11.16	0.25< Re_k <0.44
M -5	0.6308	6.74	0.18< Re_k <0.28	M -18	0.6853	6.96	0.16< Re_k <0.28
M -6	0.6000	7.60	0.17< Re_k <0.31	M -19	0.6816	7.40	0.19< Re_k <0.32
M -7	0.6369	7.72	0.22< Re_k <0.33	M -20	0.717	12.10	0.27< Re_k <0.56
M -8	0.6415	7.95	0.16< Re_k <0.25	M -21	0.6919	13.01	0.26< Re_k <0.40
M -9	0.6168	5.52	0.10< Re_k <0.16	M -22	0.7091	8.63	0.12< Re_k <0.22
M -10	0.6922	9.11	0.14< Re_k <0.26	M -23	0.7306	8.01	0.14< Re_k <0.24
M -11	0.6902	9.70	0.14< Re_k <0.25	M -24	0.6896	6.93	0.14< Re_k <0.26
M -12	0.6766	8.60	0.18< Re_k <0.32	M -25	0.7018	8.01	0.20< Re_k <0.34
M -13	0.7628	20.71	0.28< Re_k <0.55	M -26	0.6937	7.76	0.13< Re_k <0.23

Table 5-4 Geometrical and Darcy's regime limitations of Large pore size samples (dp=2.0-2.36 mm & PPI=5-10)

Sample	*ε*	*K X10^{-9} m^2*	Darcy's Regime limitations	Sample	*ε*	*K X10^{-9} m^2*	Darcy's Regime limitations
L-1	0.6158	17.21	0.29< Re_k <0.42	L -9	0.6491	12.03	0.34< Re_k <0.43

L -2	0.5943	11.55	0.27< Re_k <0.39	L -10	0.6974	10.48	0.29< Re_k <0.42
L -3	0.6371	11.30	0.25< Re_k <0.36	L -11	0.7075	11.74	0.24< Re_k <0.36
L -4	0.6116	11.98	0.071< Re_k <0.14	L -12	0.7224	9.78	0.25< Re_k <0.36
L -5	0.6235	11.40	0.36< Re_k <0.52	L -13	0.6929	9.79	0.14< Re_k <0.24
L -6	0.6207	14.73	0.41< Re_k <0.56	L -14	0.6907	10.79	0.16< Re_k <0.28
L -7	0.6612	11.02	0.36< Re_k <0.53	L -15	0.7222	15.90	0.45< Re_k <0.58
L -8	0.6492	15.17	0.35< Re_k <0.48	L -16	0.7311	12.82	0.34< Re_k <0.44

Table 5-5 Geometrical and Darcy's regime limitations of metal sponges reported in literature

Reference	Metallic foam type	ε	PPI	Pore size, mm	Darcy's Regime limitations
Boomsma et. al [78]	Aluminium	0.921	10	6.9	Re_k <26 .5
Boomsma et. al [78]	Aluminium	0.920	20	3.6	Re_k <22.3
Boomsma et. al [78]	Aluminium	0.928	40	2.3	Re_k <14.2
Dukhan et al. [91]	Aluminium	0.89	10	NA	12.5< Re_k <29.2
Dukhan et al. [91]	Aluminium	0.9	20	NA	12.5< Re_k <29.2
Dukhan et. al [104]	Aluminium	0.87	20	NA	1.2< Re_k <1.9
Bagci et al. [90]	Aluminium	0.885	10	NA	1.3< Re_k <3.9
Bagci et al. [90]	Aluminium	0.885	40	NA	1.3< Re_k <2.1
Bagci et al. [90]	Aluminium	0.876	20	NA	1.2< Re_k <1.9
Kouidri et al. [97]	Copper	0.93	20	1.2	4.5< Re_k <7
Kouidri et al. [97]	NiFeCr	>0.91	20	1.2	4< Re_k <5.4
Kouidri et al. [97]	Inconel	>0.92	20	1.2	3< Re_k <3.88

Table 5-6 Geometrical and Darcy's regime limitations of mesh wire screen packed beds and Darcy's bounds

Sample	ε	P_t, *mm*	$K\ X10^{-9}, m^2$	Darcy's Regime Limitations
Mesh-1	0.746	1.0	9.69	0.17< Re_k <0.45
Mesh-2	0.878	1.4	21.1	0.29< Re_k <0.56
Mesh-3	0.784	2.0	29.62	0.72< Rek <1.10

Table 5-7 Geometrical and hydraulic parameters of packed beds of balls samples and Darcy's bounds

Sample	ε	*Particle diameter , mm*	$K\ X10^{-9}, m^2$ *Experimental*	$K\ X10^{-9}, m^2$ *Equation (4.7)*	Darcy's Regime limitations
Ball-1 (current study)	0.362	1.5	1.72	1.75	0.034< Re_k <0.085
Ball-2 (current study)	0.393	2.0	4.31	4.39	0.060< Re_k <0.12
Kecocioglu et. al [95]	0.40	3.0mm	NA	NA	0.062< Re_k <0.12
Kecocioglu et. al [95]	0.40	6.0mm	NA	NA	0.062< Re_k <0.12
R. Fand et al [87]	0.357-0.359	2.098 - 4.029	NA	NA	Re_k <0.26 (±0.01)
Bagci et al [93]	0.3501	1.0	0.69	NA	0.29< Re_k <0.77
Bagci et al [93]	0.3558	3.0	6.423	NA	0.02< Re_k <0.59
Kundu et al. [82]	0.4174	2.5	18.79	NA	0.003≤ Re_k ≤0.2
Kundu et al. [82]	0.3696	3.5	28.19	NA	0.004≤ Re_k ≤0.3
Kundu et al. [82]	0.3478	5	49.90	NA	0.006≤ Re_k ≤0.15
Kundu et al. [82]	0.3913	3.25 (Mixed)	22.53	NA	0.004≤ Re_k ≤0.2

Both geometrical parameters (pore size and porosity) are found to have an effect on the bounds of the Darcy flow regime. As an example, Figure 5-17 depicts the effect of porosity on the departure border from Darcy flow for two Very Small pore size samples V.S-1 and V.S-6 (same nominal pore size) with porosities 0.723 and 0.66 respectively. The flow departed from the Darcy regime in samples with lower porosity ($Re_k \approx 0.092$) than those with higher porosity ($Re_k = 0.29$). The lower porosity sample has a higher blockage area resulting in higher velocities within the matrix. In contrast, the higher porosity sample has more free area and the flow can easily penetrate the foam structure. This phenomena was visualised by Hwang et al. [122] by using the wire-smoke technique.

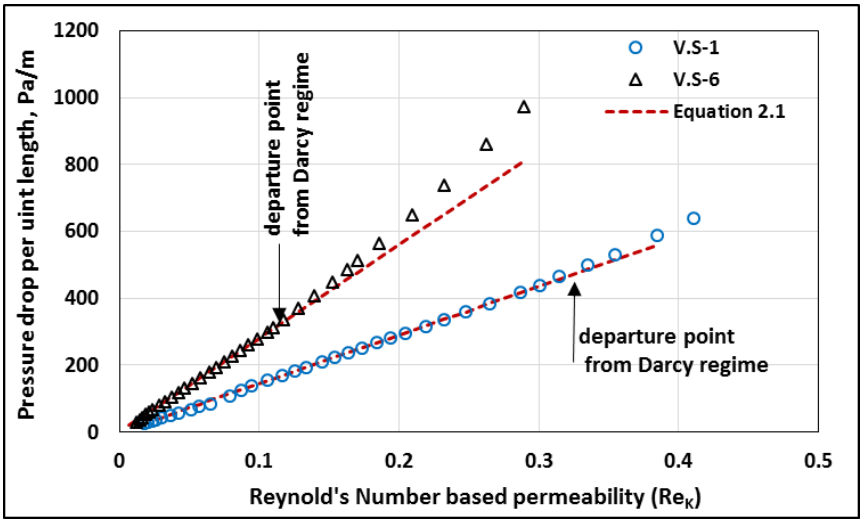

Figure 5-17 Measured pressure drop per unit length against permeability based Reynold's Number (metal foams)

The free flow area can be observed by image processing photographs of the samples. Shown in Figure 5-18 are the threshold images for both samples. The sample V.S-6 (porosity = 0.66) provides 17% free flow area to total cross sectional area and the sample V.S-1 (porosity = 0.723) provides 27%.

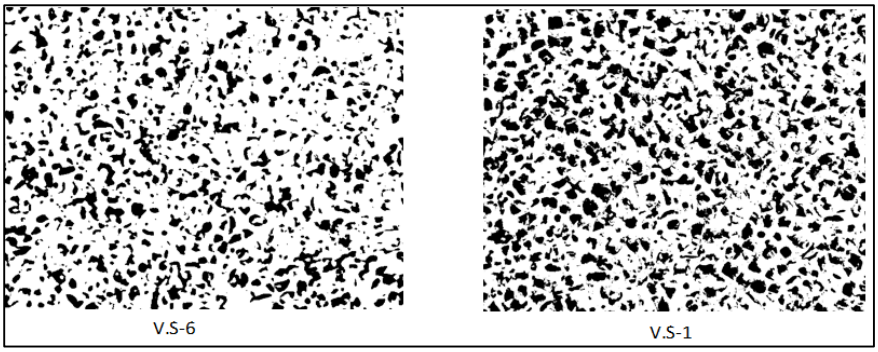

Figure 5-18 Threshold images of V.S-1 and V.S-6

Figure 5-19 shows the effect of the pore size on the departure from the Darcy regime for two samples with the same porosity (*0.63*). The flow starts departing from the Darcy regime for the small pore size sample before the medium sample. This is due to the greater inertial forces in the smaller pore size samples resulting in higher pressure losses. At the same frontal air velocity, the interstitial pore velocity is higher in lower pore size and porosity samples than those that have higher porosities and a high pore size. This higher pore velocity results in higher drag and inertial forces.

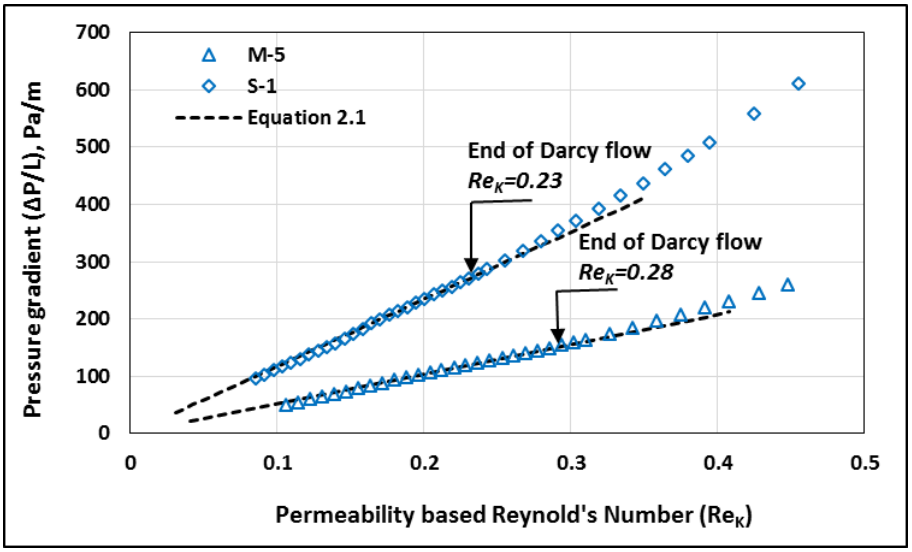

Figure 5-19 Measured pressure drop per unit length against permeability based Reynold's Number (metal foams)

Shown in Figure 5-20 and Figure 5-21 are the pressure drops per unit length versus the frontal air velocity across the different microstructure of mesh wire screens and packed beds of balls. Both the particle diameter in granular packed beds and transverse pitch in mesh screens influence the bounds of the

flow regime. As with the porous media, the flow departs from the Darcy regime where the pores are smaller, resulting in higher velocities within the media.

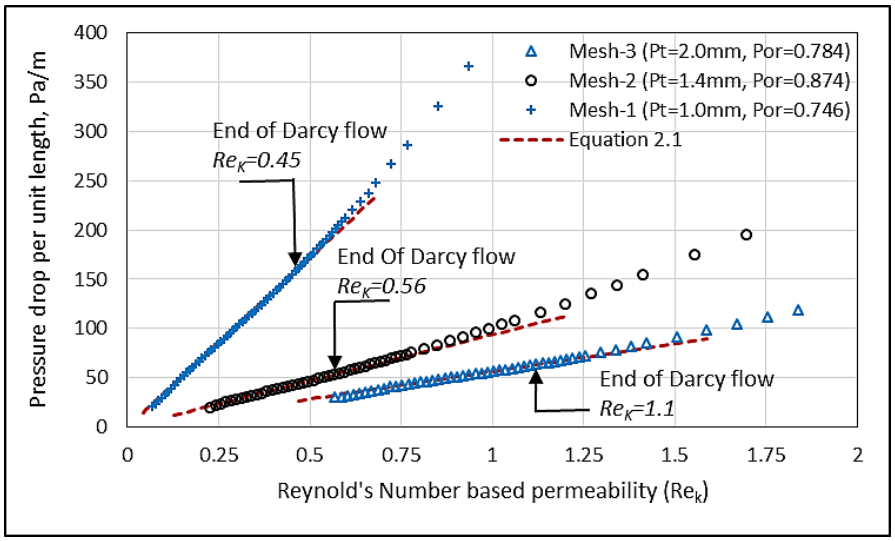

Figure 5-20 Measured pressure drop per unit length versus Reynold's number based permeability (Mesh wire screens packed beds)

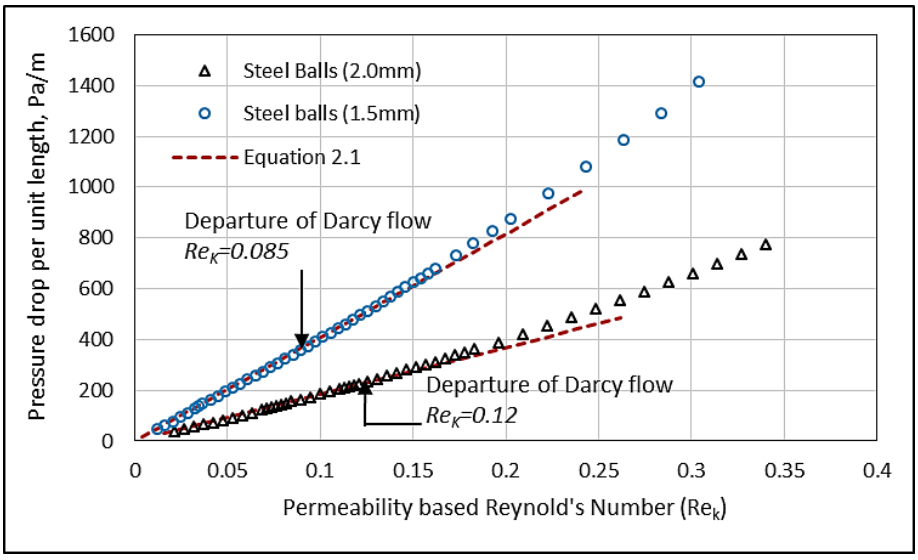

Figure 5-21 Measured pressure drop per unit length versus Reynold's number based permeability (balls packed beds)

5.2.2 Forchheimer flow regime

As the flow rate increases, there is a further transition to another laminar regime where inertial forces govern the flow [76]. The pressure gradient relationship with frontal fluid velocity becomes non-linear and the inertia forces become pronounced. The pressure gradient has a quadric non-linear relationship with the

fluid velocity and can be described by the Forchheimer equation (Equation 2.5) [93, 107]. However, the flow in this regime remains laminar and steady [87, 94]. This regime of flow can be identified by the linear relationship of the reduced pressure gradient and superficial fluid velocity by the constant gradient as shown Figure 5-22 and Figure 5-23 for the lower and higher bounds.

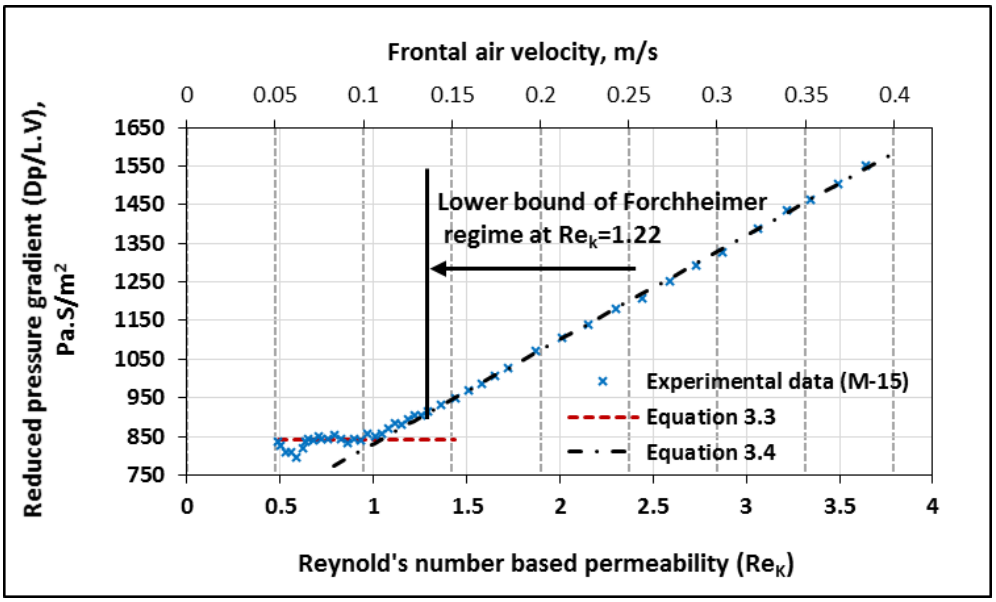

Figure 5-22 Reduced pressure drop against frontal air velocity and permeability based Reynold's Number (the lower bound of Forchheimer Flow)

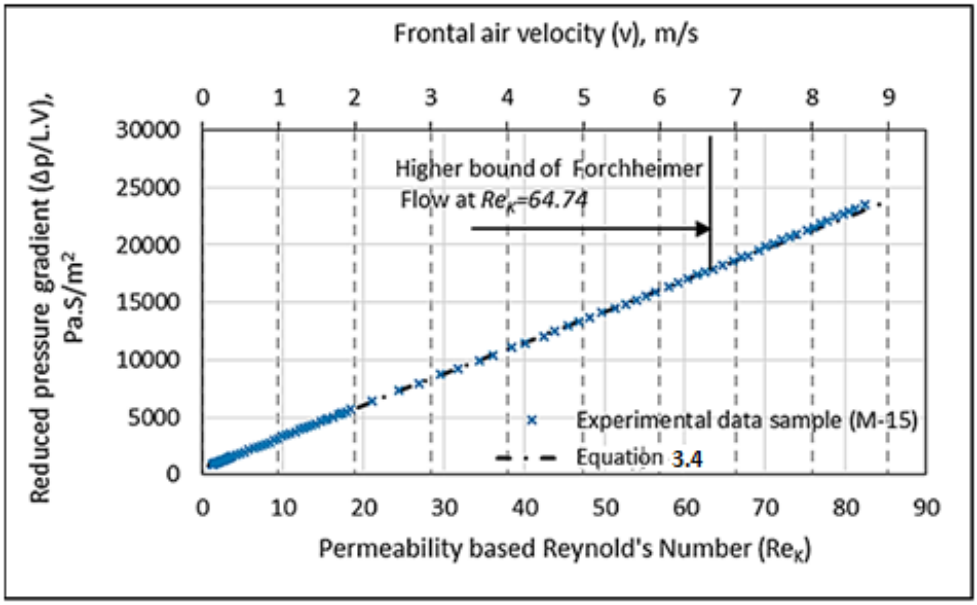

Figure 5-23 Reduced pressure drop against frontal air velocity and permeability based Reynold's number (the upper bound of Forchheimer flow)

Similarly, as for Darcy regime, there has been disagreement as to at which Reynolds number the flow enters and departs the Forchheimer regime [86, 87, 91, 93, 106]. The five studies which provided the borders of the transition zones of the Forchheimer regime in metal foams (Dukhan et al. [91, 104], Boomsma et al. [78], Bağcı et al. [90] and Kouidri et al. [97]) have no agreement. This is likely to be due to the fact that the microstructure parameters (such are the pore size and porosity) have a measurable impact on the transition [78, 91]. In packed beds of spheres, the borders of the flow regimes are different depending on whether the characteristic length of the Reynolds number was the square root of permeability or particle diameter [86, 87, 93]. The contradiction of the transition point of flow regimes in packed beds of spheres was also reported depending on the balls diameter and porosity [77, 82, 86, 87, 93, 99]. In the current work, the lower and upper bounds of the Forchheimer regime was affected by the microstructure parameters in terms of porosity and pore size in all classes of porous media.

5.2.3 Turbulent flow regime

The fourth flow regime in porous media is the turbulent regime, which is associated with the formation of flow vortices in the porous matrix [87, 106]. Various methods have been used to examine the nature of the flow in this regime. These include flow visualization in packed beds of spheres and cylindrical rods [106] and the electrochemical technique [293, 294]. The transition from laminar to turbulent flow in porous media has been demonstrated to be gradual as opposed to the clearly defined transition observed in pipe flow [294]. There is a little available information about this regime in metal foams. Only four studies (Kouidri et al. [97], Bağcı et al.[90], Dukhan et al. [104] and Lage et al. [107]) have reported the lower bound of this regime. The smoke wire technique was used to study the effect of porosity on the flow patterns inside the pores [122]. At a porosity of 0.7, a large number of eddies were observed at the rear face compared with a porosity of 0.95, where the flow was still laminar and at the same incoming fluid velocity [122].

The transition regime was again identified by an increase in slope of reduced pressure gradient with flow velocity [86, 87, 91, 93, 107]. From Figures 5-24 and 5-25, a measurable impact on the transition zone with porosity and pore size can be observed. For a Small sample (S-3, porosity 61.84%), the flow departed the Forchheimer regime at $Re_k=12.45$ and entered the turbulent regime at $Re_k=14.21$. This increased to Reynolds numbers of 25.1 and 26.12 for a higher porosity sample (S-7, porosity 73.02%). The same scenario was noticed for all groups of pore size samples. The change in pore size also impacted on the transition zone as seen in Figure 5-25. For a Small sample (porosity of 69.62%), the flow departed the laminar regime at $Re_k=20.21$ and entered the turbulent regime at $Re_k=22.0$, whereas, for a Large sample of the same porosity it increased to 32.43 and 42.04. This is the result of the porosity or pore size decreasing the flowing fluid area and hence increasing the interstitial velocity.

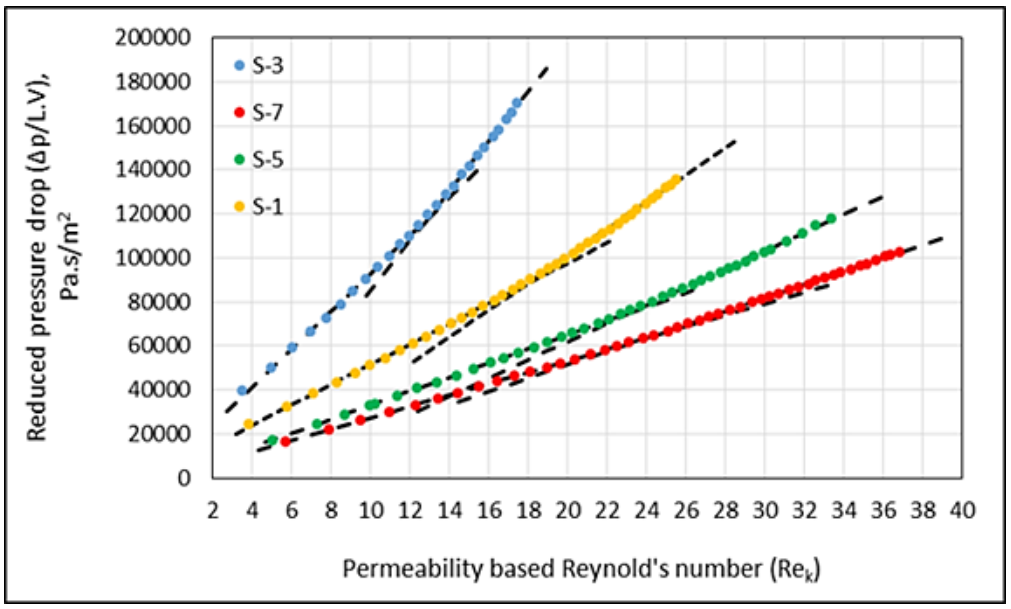

Figure 5-24 The effect of porosity on the upper borders of Forchheimer regime and lower borders of turbulent regime

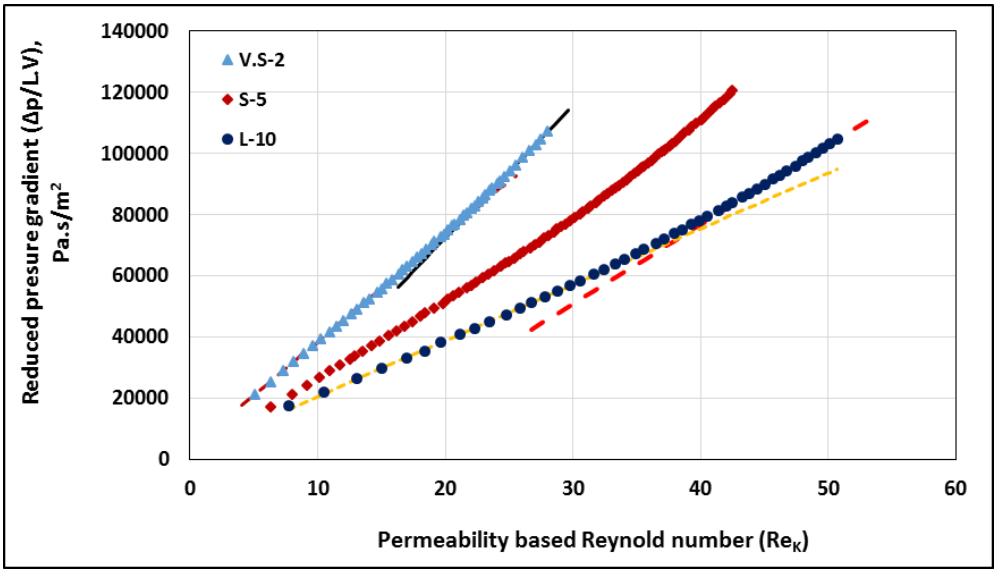

Figure 5-25 The effect of pore size on borders of Forchheimer and turbulent regimes

The above scenario can also be seen in traditional porous media, such as packed beds of spheres when the ball diameter changed as shown in Figure 5-26. The borders of the Forchheimer and turbulent regimes in all the tested samples and available in literature are reported from Table 4-8 to Table 4-13.

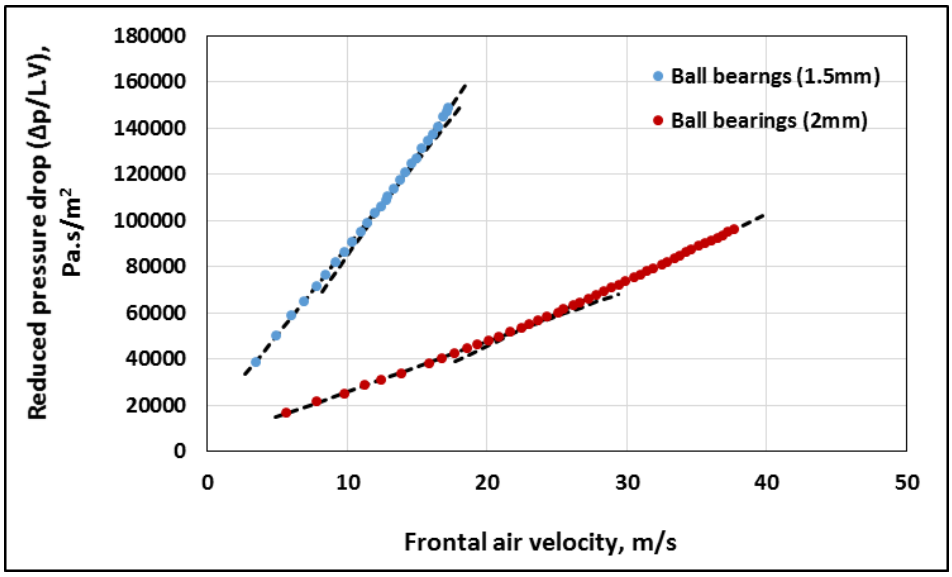

Figure 5-26 The particle diameter effect on borders of Forchheimer and turbulent regimes

5.3 Permeability models and measurements results

The permeability of the porous matrix is the key parameter in a number of engineering applications and was the formal subject in the previous investigations

[132]. In recent years there have been a number of studies examining the impact of foam properties on the pressure drop. Clearly, the pressure drop will depend on the size porous media. Therefore, to remove this influence, just the permeability is quoted. At low fluid flow rates, Darcy's law (Equation 2.1) is a widely accepted method to measure the permeability for different classes of porous media [76, 86, 87, 91, 93, 132, 133].

The experimentally measured permeabilities are presented from Table 5-1 to Table 5-4 and presented in Figure 5-27 and Figure 5-28. Permeability increases with both porosity and pore size. The irregular pore shape samples provide higher permeability than those with spherical pores. These findings agree with studies performed using dimensional analysis, where the permeability was non-dimensionalised by the average pore diameter [18, 49, 132, 144].

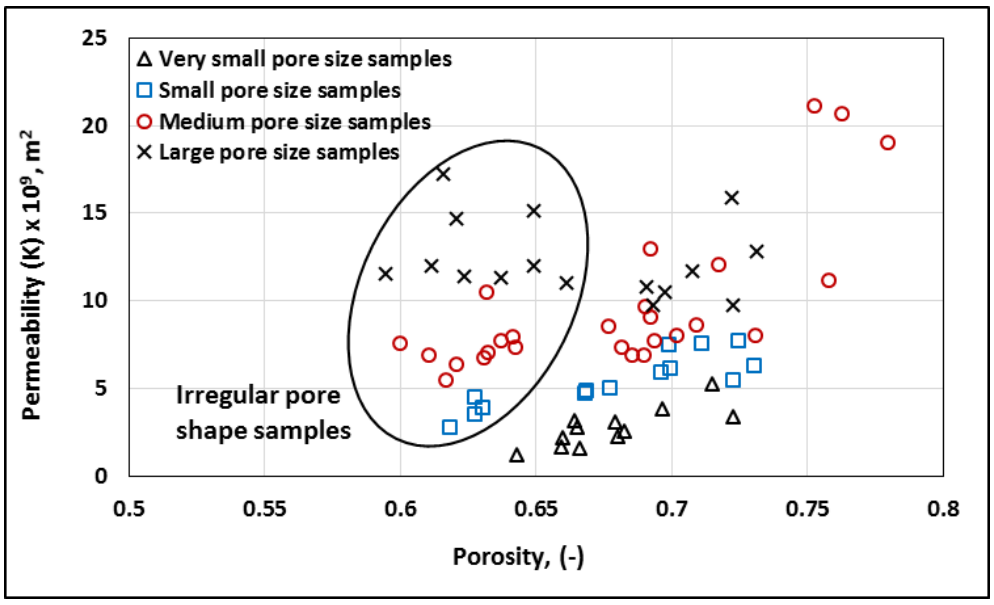

Figure 5-27 Permeability versus porosity

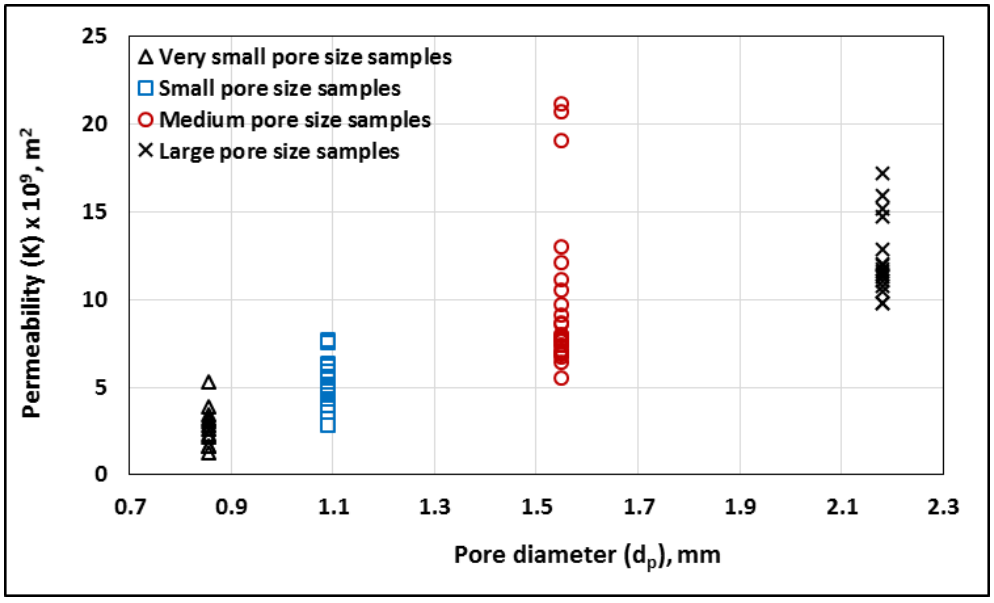

Figure 5-28 Permeability versus pore size

The normalised permeability is often non-dimensionalised by the square of the average pore diameter. Here, the particle size of the infiltration salt was used [132, 133, 144, 248, 291]. Shown in Figure 5-29 is the normalised permeability against the solid phase fraction of the metal foams for samples from this study and those in the literature. The value of $\frac{K}{d_p^2}$ increased with porosity.

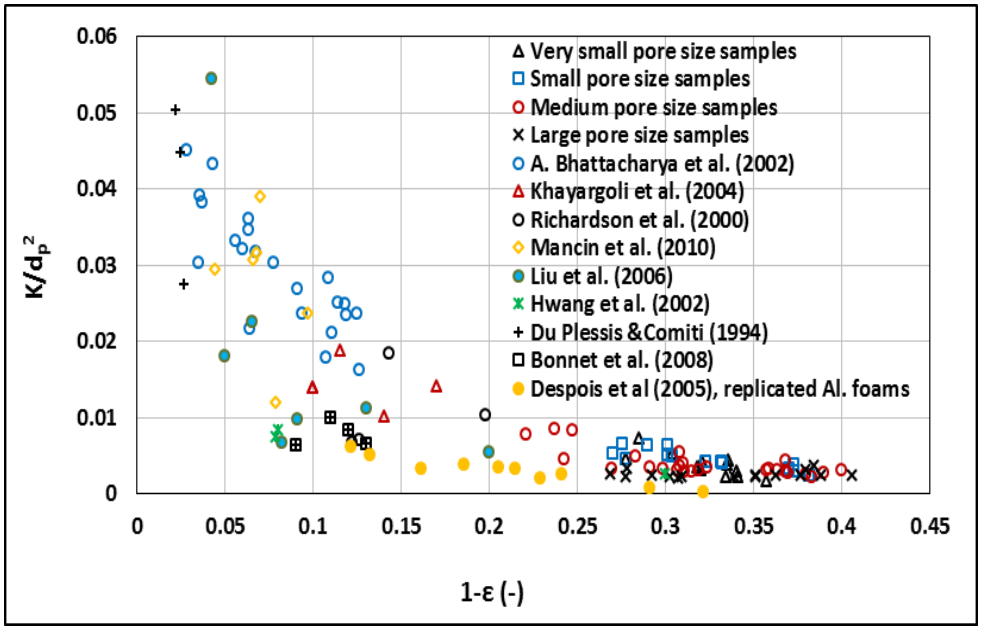

Figure 5-29 Normalized permeability versus a solid phase fraction

In Figure 5-30, two predicted permeability models were plotted with the

experimental results. The Fourie and Du Plessis [75] model over predicts the entire range of the porosities. The Despois et al. [132] model under predicts most experimental data, but fits well with their own. There is a noticeable decrease in the permeability predicted by this model when the porosity reaches 0.64. This is because the model assumes that the windows will close at that porosity and so is not applicable for the current samples whose porosity was less than 64%.

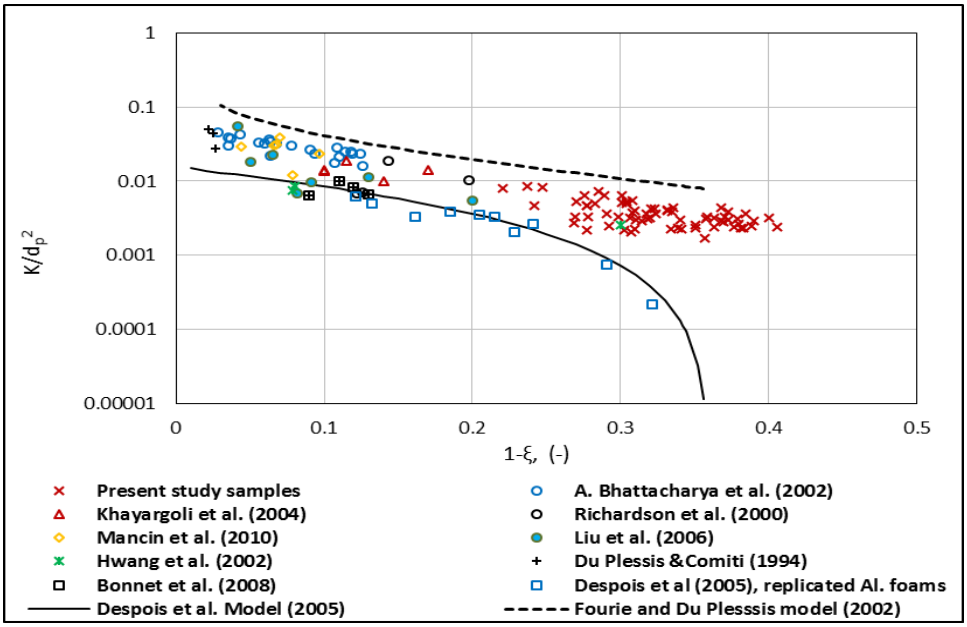

Figure 5-30 Permeability models as a function of solid phase fraction

The empirical correlation prepared by Moreira et al. [144] from the fitting of ceramic sample results is compared with the experimental measurement as shown in Figure 5-31. The predicted data found by this correlation is mismatched with most of experimental results. This might be due to differences in the microstructure between the samples that Moreira et al. [144] used and those of others.

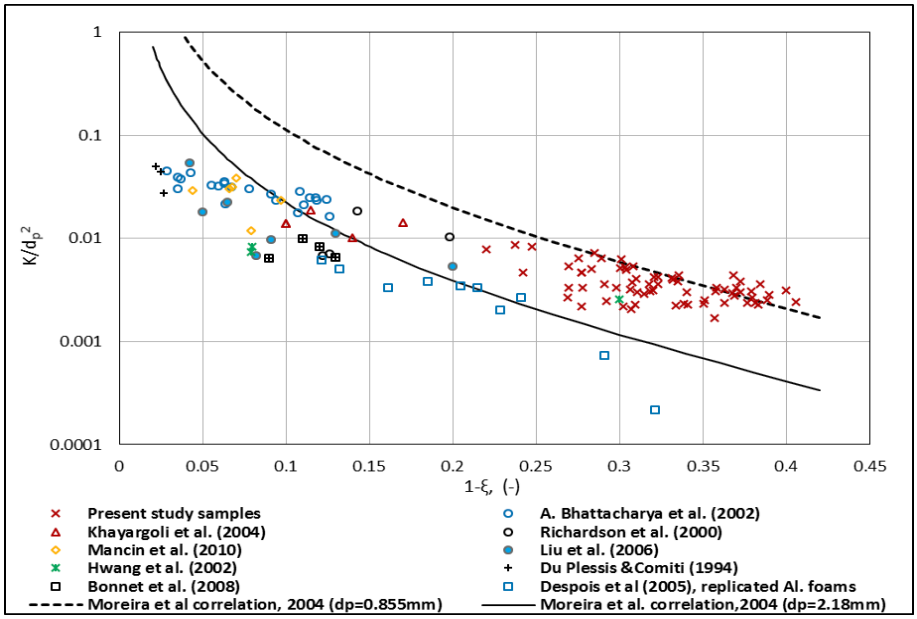

Figure 5-31 Permeability empirical correlation with different pore size as a function of solid phase fraction

From these results, it can be seen that the permeability increased with both porosity and pore size. As permeabilty increases there is more space within the material resulting in less friction area inside the pores [18, 19, 78, 144]. As none of the existing models or correlations can predict permeability for the entire range of porous media data available, an empirical expression was developed

$$\frac{K}{d_p^2} = A(B + e^{C(1-\varepsilon)}) \qquad 5.1$$

The constants *A* and *B* were found by curve fitting both the available data in the literature [18, 39, 103, 116, 118, 122, 124, 126, 132, 142] and present experimental tests. The constants are *A=0.0514, B=0.028* and *C=10.7*. Shown in Figure 5-32 is a comparison of the fit with the experimental data. Generally, Eq. 5.1 represents the experimental database well. This approach should be treated with some reservation, as different types of porous media are being tested and there may be differences in the method of measurement of the permeability [104]. There are two exceptions that do not fit particular well with the other data; Despois et al. [132] and Bonnet et al. [142], which both sit below the correlation. The results of Despois et al. [132] are replicated in aluminium foams with a very small pore size (75 µm and 400 µm), and the pore windows may not be fully open. The samples used by Bonnet

et al. [142] were produced from nickel chromium, which may have an impact on the cell shape in reducing the permeability.

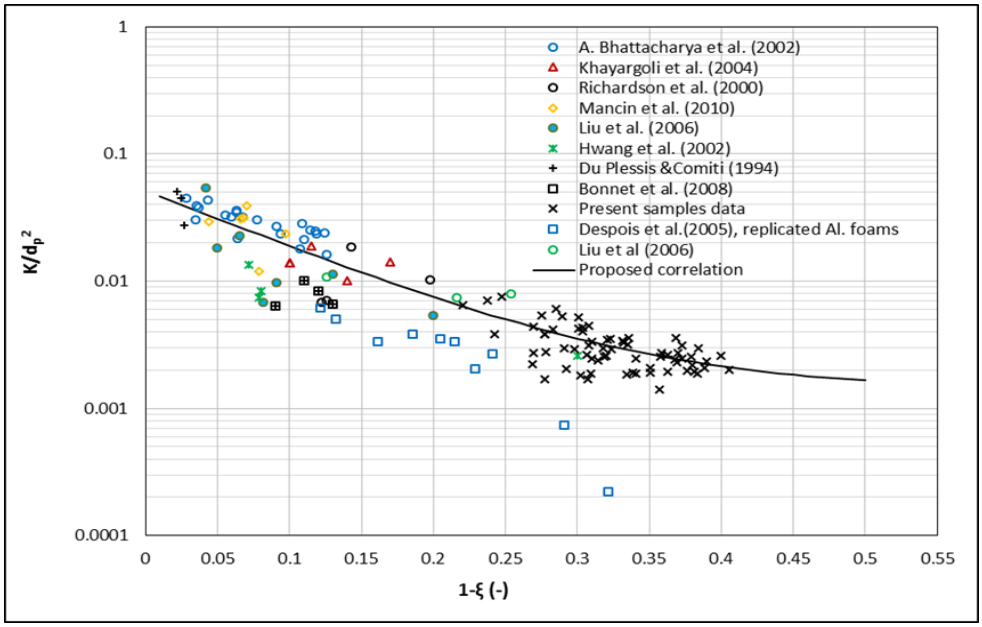

Figure 5-32 Normalised Permeability as function of solid phase fraction

5.4 Inertia and Form Drag coefficients results

In the present study, the borders of the Forchheimer regime were identified for all the samples. Both linear and quadric least squares fits were applied to the data. The difference between them was small (<2%), as shown from Figure 5-33 to Figure 5-35.

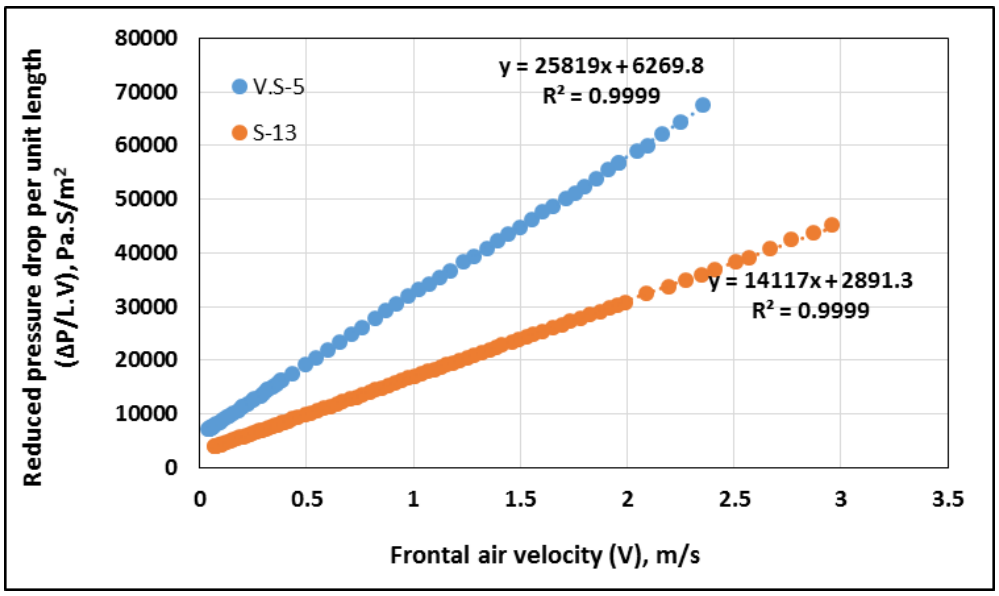

Figure 5-33 Reduced pressure drop per unit length versus frontal air velocity

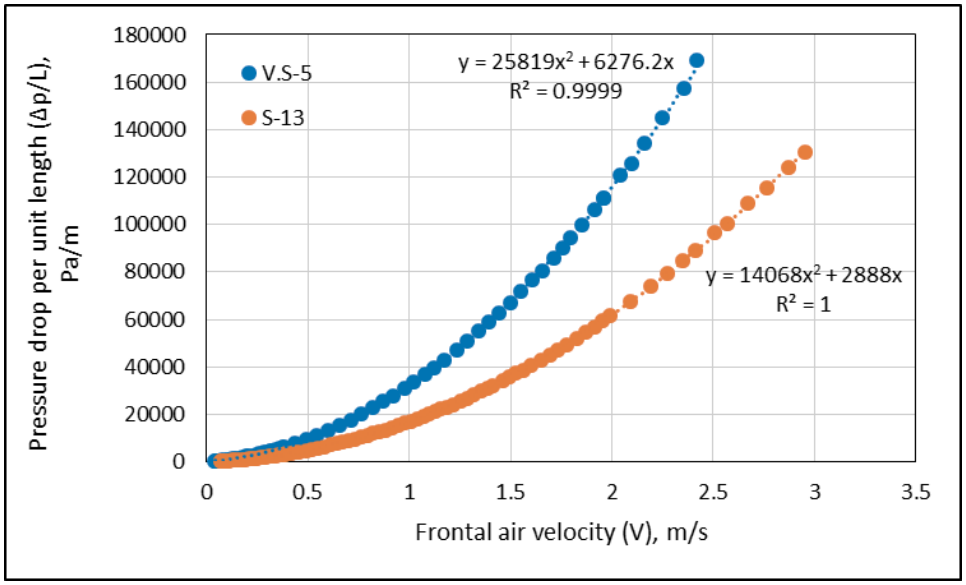

Figure 5-34 Pressure drop per unit length versus frontal air velocity

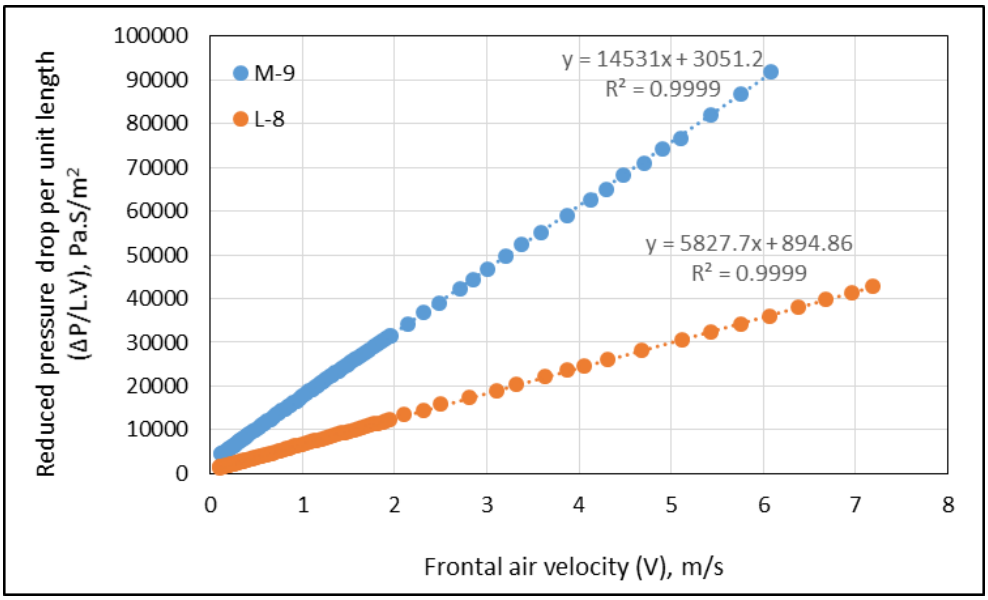

Figure 5-35 Reduced pressure drop per unit length versus frontal air velocity

The permeability, inertia and drag coefficients were determined in the Forchheimer regime and tabulated in Tables 5-8 to Table 5-11.

Shown in Figures 5-36 to 5-39 are the effects of the porosity and pore diameter on the inertia factor and form drag coefficient. Both inertia and drag coefficients decreased with increasing porosity and pore diameter. However, the results split into two groups: samples which were produced using crushed salt

(irregular shape) had lower inertia and drag coefficients than those produced with spherical salt.

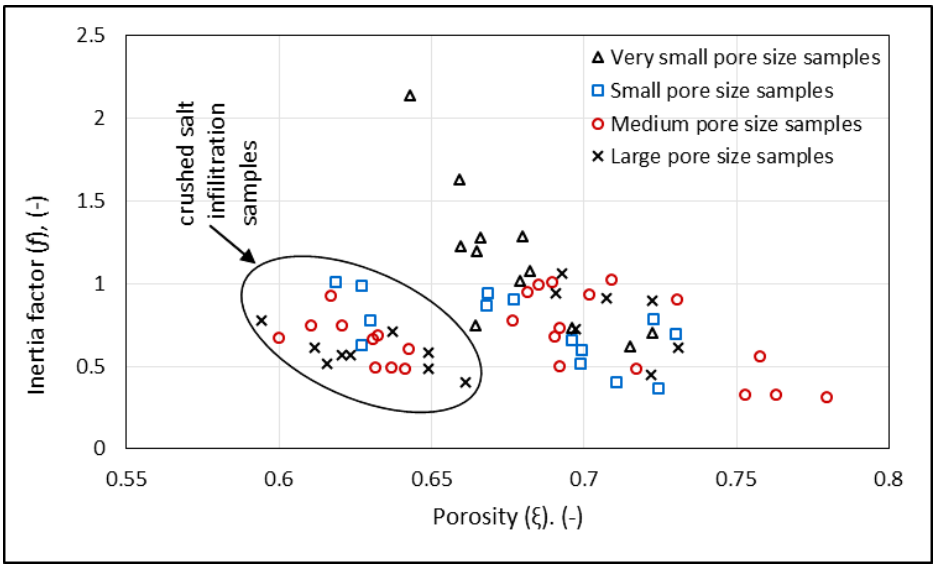

Figure 5-36 Inertia factor versus porosity

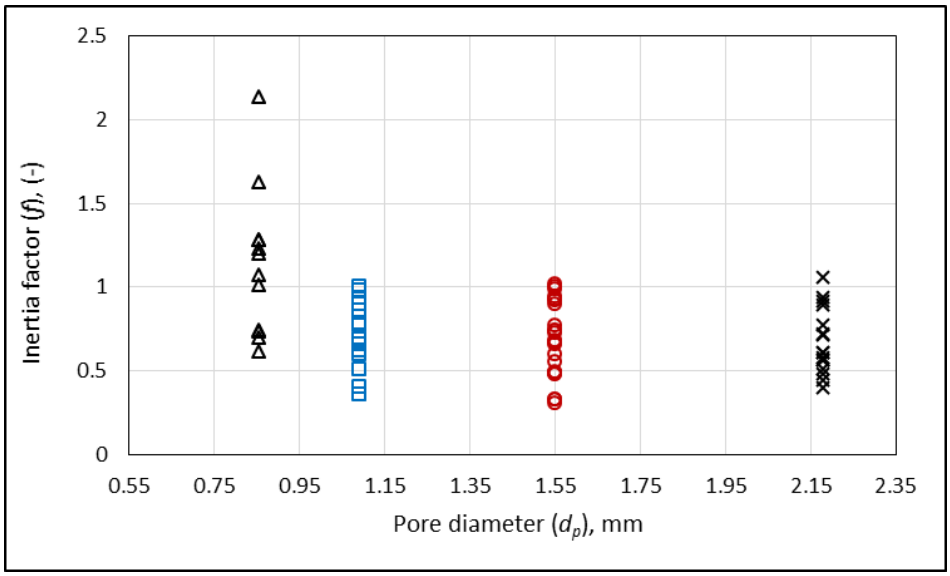

Figure 5-37 Inertia factor versus pore diameter

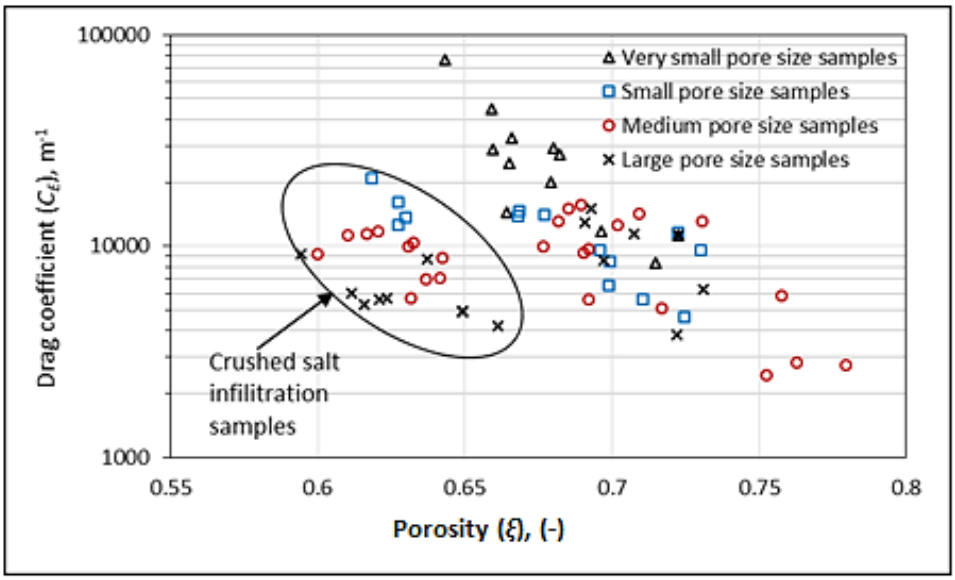

Figure 5-38 Form drag coefficient versus porosity diameter

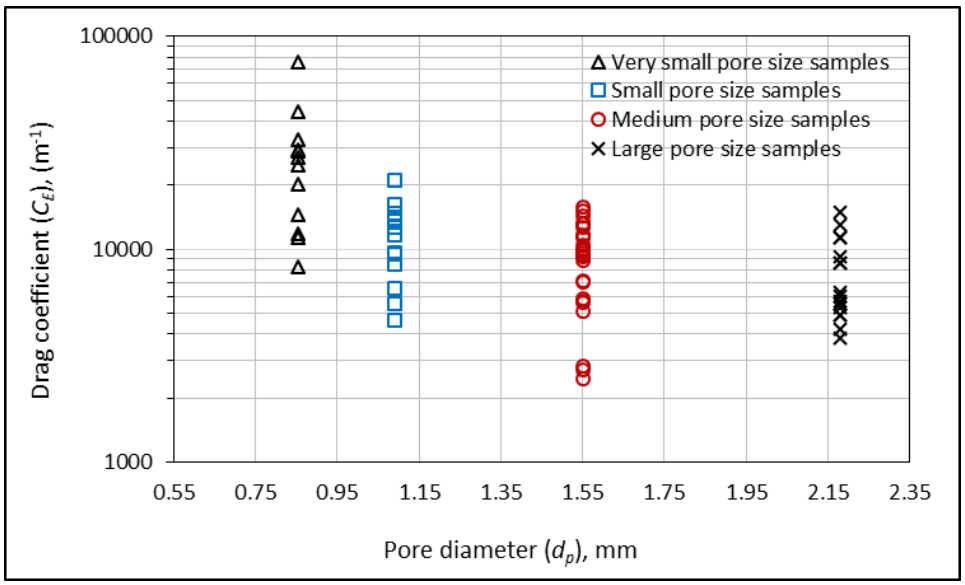

Figure 5-39 Form drag coefficient pore diameter

There have been a anumber of attmepts to predict the inertia factor and the form drag coefficient [18, 75, 116]. Bhattacharya et al. [18] applied the model of Du Plessis et al. [116] to their samples and found it did not work. They concluded that the inertia coefficient is more senstive to changes in porosity than the pore size and strongly affected by the cross-section of the ligament shape. The shape and the thickness of the fibre formed the porous network, which also vary with different manufacturing method used and variation in base materials [17, 111, 146].

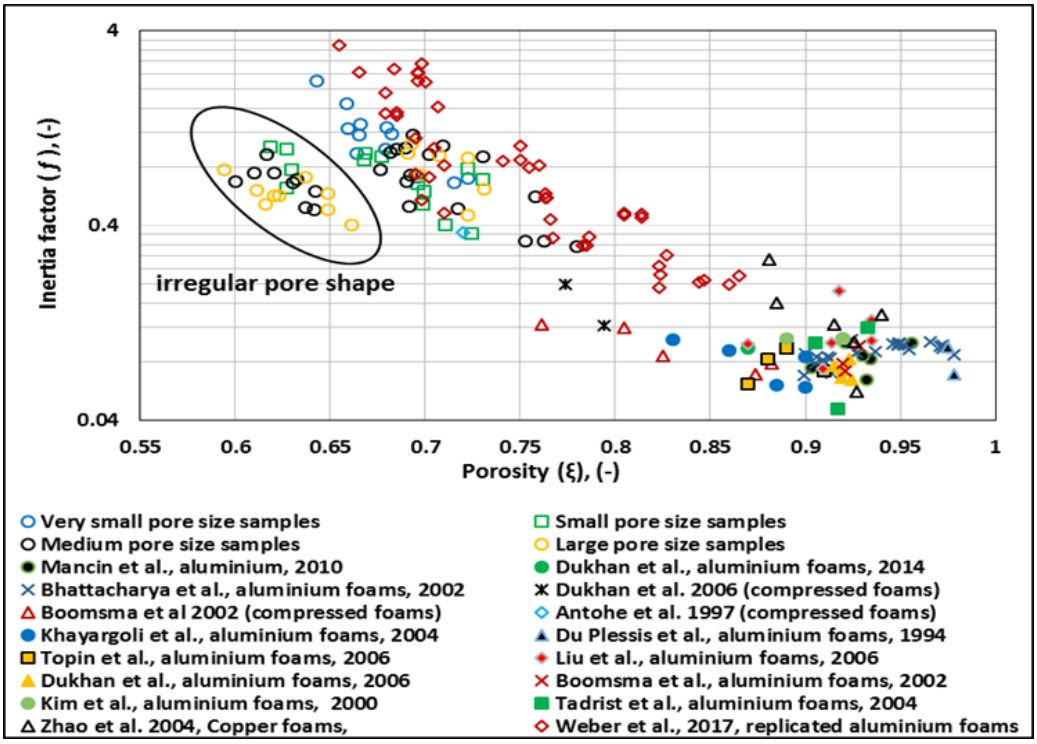

Figure 5-40 Inertia coefficient as a function of porosity

Shown in Figure 5-40 are the measured inertia coefficient (f) against porosity for the current samples and those available in literature. It is clear from these results the f decreases with an increase of porosity and is more sensitive to porosity than pore size.

The scattering in results is most likely due to the differences in pore size and pore density (PPI). Increasing the PPI (decreasing the pore diameter) increases the number of fibres forming the structure, and thus the flow resistance [18, 110]. In addition, the different thicknesses of struts in the direction and perpendicular to flow, and the inertia coefficient encountered in different flow regimes are also a possible cause of inconsistency [104, 134, 143].

Photographs of the two types of sample are shown in Figure 5-41. These differences are due to the variation in flow area, which is higher in the crushed salt samples as windows between the cells are more open. Similar results have been demonstrated by others [19, 109, 120].

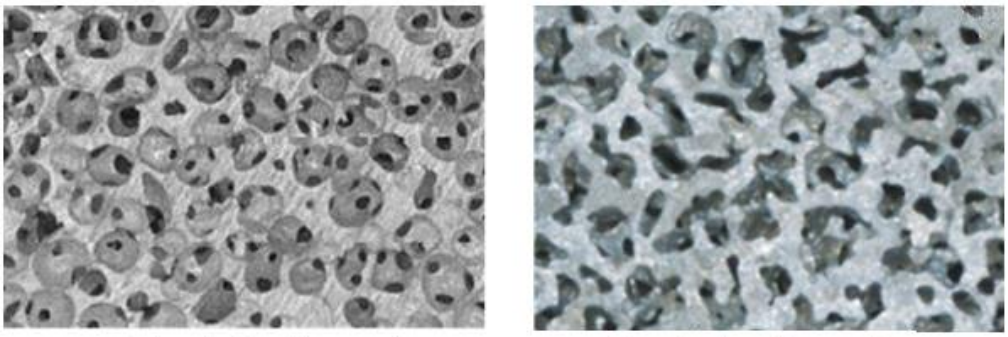

Figure 5-41 Photos of different infiltration salt samples

A wide range of pressure drop correlations were presented [17, 150] and the only the models used by Du Plessis et al. [116], Fourie et al. [75], Bhattacharya et al. [18] and Lacroix et al. [117], do not involve fitting coefficients from experimental data. These models can be adopted to predict permeability and the inertia coefficient with a deviation ± 30 % [17]. However, it has been stated that no model can be applied to predict these hydraulic parameters at low porosities [111, 146]. Therefore, three models have been adopted that apply to current results; the Du Plessis et al. model [116], the Zhao et al. correlations [151] and the Bhattacharya et al. model [18], which has been excluded because it is applicable only for high porosities.

In order to generalise the relationship and to improve scattering in the data, the inertia factor experimental data has been normalised by the value $(\frac{\sqrt{K}}{d_p})$ as shown in Figure 5-42. It is also worth noting the current results are in the same order with those reported in literature. From the comparison of Figure 5-40 and Figure 5-42, the scattering is still the same and is likely a result of the differences in microstructure in terms of fibre shape and thickness, the differences in pore density (PPI) and variation of base material. The defects and differences in manufacturing technique are also a possible cause of this scattering.

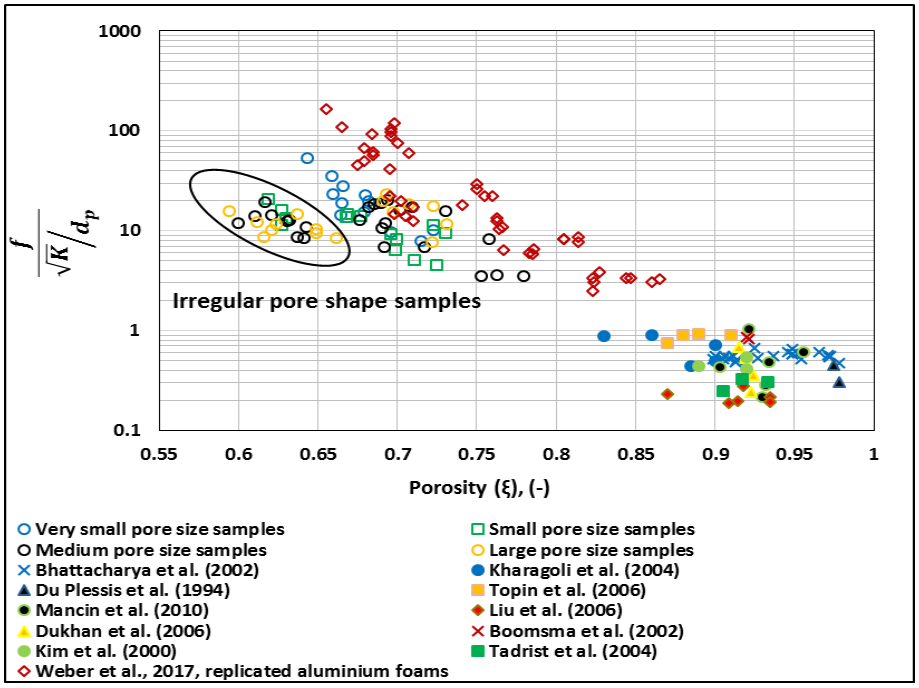

Figure 5-42 Normalised inertia factor versus porosity

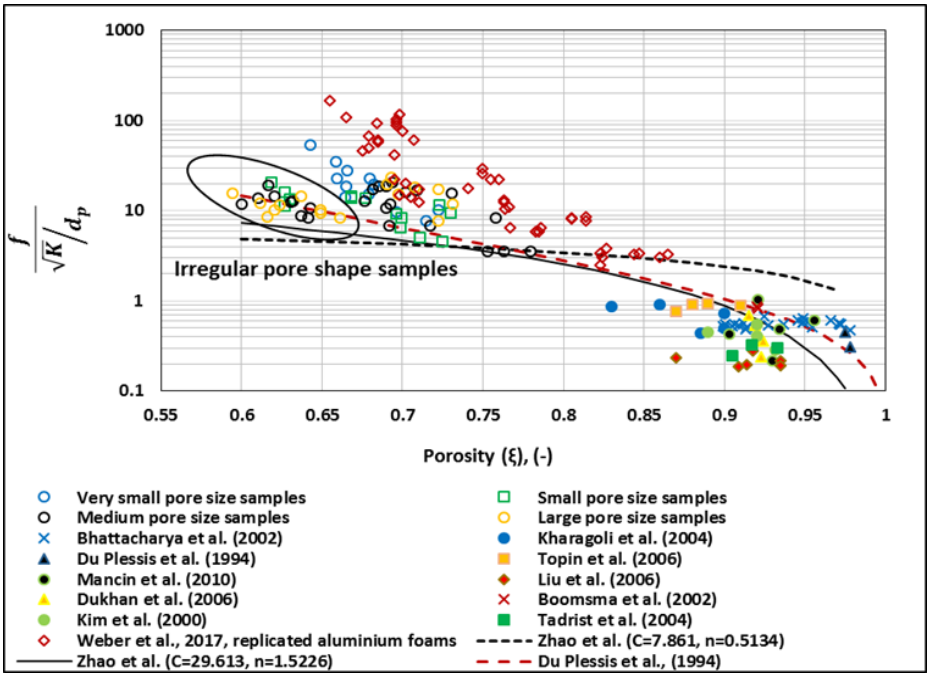

Figure 5-43 Normalised inertia factor versus porosity

As clear from Figure 5-43, the above expressions defined their own respective sample and no one can be generalised. The inertia coefficient is under predicted at low porosity. Extending at low porosities, the Du Plessis [116] model only agrees with crushed salt samples. Therefore, the pore and ligament shapes have a measurable impact on the hydraulic parameters. The analytical model's approaches are based on

identical typical shapes of pores without any manufacturing imperfections and misalignment taken into account. Shown in Figure 5-44 are inertia factor against porosity for the replicated aluminium foams with spherical pore shape.

For the current replicated aluminium samples and those used by Weber et al. [248] and Zhao et al. [151], techniques and expressions have been adopted to obtain a relationship of inertia factor with porosity. The expression proposed here is a function of pore diameter, permeability and porosity;

$$f = C[(\varepsilon)^n]\frac{\sqrt{K}}{d_p} \qquad 5.2$$

The current sample's results and those of Weber have been used to find the empirical fitting coefficients. The factor found are; n = -4.4 and the coefficient C is 0.192 for spherical shape sample and 0.05 for irregular shape samples. Equation 5.2 is used to determine the value of $(\frac{\sqrt{K}}{d_p})$. The validity of these expressions is shown in Figure 5-44.

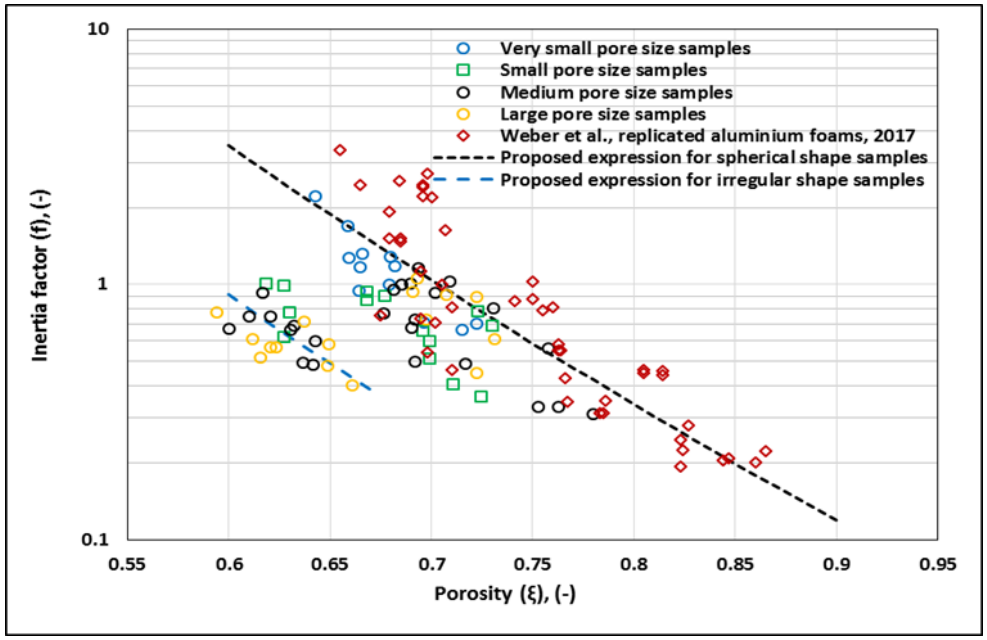

Figure 5-44 Inertia coefficient expression for replicated aluminium foams

The results of the measured hydraulic parameters and the transition points of Forchheimer and turbulent flow regimes for current samples and those reported in literature are tabulated in Tables 5-8 to 5-13.

Table 5-8 Geometrical and hydraulic parameters of very small pore size samples (d_p=0.71-1.0 mm & PPI=20-25)

Sample	ε	Permeability (K) x10^{-9}, m^2	Frochhiemer Regime	Turbulent Regime	Inertia Coefficient (*f*)	Drag Coefficient C_E, m^{-1}
V.S-1	0.7225	4.21	0.38< Re_k <16.18	Re_k>20.41	0.72	11367
V.S-2	0.6962	4.58	0.31< Re_k <20.21	Re_k>22.0	0.735	11804
V.S-3	0.666	1.93	0.18< Re_k <10.35	Re_k>11.06	1.280	32596
V.S-4	0.659	2.00	0.21< Re_k <8.25	Re_k>10.91	1.630	44524
V.S-5	0.6822	2.94	0.20< Re_k <8.25	Re_k>10.95	1.23	27153
V.S-6	0.6595	2.48	0.18< Re_k <9.85	Re_k>11.97	1.228	28853
V.S-7	0.6643	4.21	0.29< Re_k <16.96	Re_k>21.0	0.743	14479
V.S-8	0.715	9.49	0.57< Re_k <32.5	Re_k>35.0	0.622	8317
V.S-9	0.665	3.27	0.18< Re_k <11.17	Re_k>13.44	1.20	24924
V.S-10	0.643	1.54	0.16< Re_k <6.07	Re_k>7.38	2.46	76272
V.S-11	0.680	2.93	0.26< Re_k <12.61	Re_k>14.64	1.283	29347
V.S-12	0.679	3.62	0.22< Re_k <19.11	Re_k>21.28	1.016	20168

Table 5-9 Geometrical and hydraulic parameters of small pore size samples (d_p=1.0-1.18 mm & PPI=15-20)

Sample	ε	Permeability (K) x10^{-9}, m^2	Frochhiemer Regime	Turbulent Regime	Inertia Coefficient (*f*)	Drag Coefficient C_E, m^{-1}
S-1	0.6301	4.88	0.32< Re_k <18.11	Re_k>23.53	0.774	13625
S-2	0.6272	5.13	0.30< Re_k <19.3	Re_k>26.0	0.986	16213
S-3	0.6184	3.28	0.31< Re_k <12.45	Re_k>14.21	0.960	21033
S-4	0.6272	4.21	0.30< Re_k <19.87	Re_k>25.93	0.625	12624
S-5	0.6960	8.84	0.46< Re_k <23.16	Re_k>24.32	0.660	9538
S-6	0.6992	7.53	0.47< Re_k <26.42	Re_k>35.2	0.600	8442

S-7	0.7302	8.90	0.55< Re_k <25.1	Re_k>26.12	0.691	9568
S-8	0.6683	6.89	0.42< Re_k <24.0	Re_k>33.81	0.939	14715
S-9	0.6680	6.10	0.40< Re_k <19.0	Re_k>28.0	0.868	13906
S-10	0.6990	9.27	0.474< Re_k <29.57	Re_k>36.2	0.513	6518
S-11	0.7246	11.0	1.05< Re_k <33.92	Re_k>40.45	0.385	4646
S-12	0.7107	9.45	0.562< Re_k <32.20	Re_k>39.1	0.406	5576
S-13	0.6770	6.29	0.295< Re_k <25.0	Re_k>30.0	0.905	14038
S-14	0.7227	6.90	0.295< Re_k <25.4	Re_k>31.0	0.787	11616

Table 5-10 Geometrical and hydraulic parameters of medium pore size samples (d_p=1.4-1.7 mm & PPI=10-15)

Sample	ε	Permeability (K) x10^{-9}, m^2	Frochhiemer Regime	Turbulent Regime	Inertia Coefficient (*f)*	Drag Coefficient C_E, m^{-1}
M-1	0.6103	8.65	0.31< Re_k <27.4	Re_k>34.7	0.747	11376
M -2	0.6205	8.56	0.32< Re_k <27.95	Re_k>34.7	0.749	11728
M -3	0.6323	9.54	0.36< Re_k <29.43	Re_k>35.27	0.689	10410
M -4	0.6425	10.0	0.38< Re_k <30.0	Re_k>35.83	0.601	8820
M -5	0.6308	8.65	0.375< Re_k <28.74	Re_k>35.8	0.664	10051
M -6	0.6000	10.13	0.42< Re_k <30.34	Re_k>36.6	0.672	9169
M -7	0.6369	10.08	0.46< Re_k <32.5	Re_k>37.6	0.495	6970
M -8	0.6415	9.72	0.35< Re_k <29.3	Re_k>36.5	0.483	7079
M -9	0.6168	6.05	0.29< Re_k <24.8	Re_k>33.0	0.965	11510
M -10	0.6922	13.82	0.44< Re_k <32.43	Re_k>42.04	0.731	9667
M -11	0.6902	12.67	0.43< Re_k <33.91	Re_k>47.6	0.676	9358
M -12	0.6766	13.27	0.52< Re_k <34.3	Re_k>48.6	0.773	9934
M -13	0.7628	32.37	0.99< Re_k <56.7	Re_k>61.3	0.343	2813
M -14	0.7796	28.11	1.01< Re_k <57.9	Re_k>64.1	0.312	2725

M -15	0.7527	32.03	1.22< Re_k <64.74	Re_k>74.0	0.331	2445
M -16	0.6317	16.16	0.99< Re_k <33.30	Re_k>39.82	0.495	5707
M -17	0.7578	14.39	0.67< Re_k <35.0	Re_k>50.21	0.562	5847
M -18	0.6853	11.60	0.45< Re_k <24.6	Re_k>35.2	0.994	15108
M -19	0.6816	13.18	0.50< Re_k <26.2	Re_k>37.5	0.951	13231
M -20	0.717	16.52	0.69< Re_k <44.3	Re_k>56.3	0.488	5094
M -21	0.6919	17.77	0.65< Re_k <36.5	Re_k>51.6	0.500	5612
M -22	0.7091	11.19	0.33< Re_k <28.0	Re_k>38.8	1.024	14359
M -23	0.7306	11.47	0.35< Re_k <28.5	Re_k>39.0	0.905	13230
M -24	0.6896	9.85	0.40< Re_k <21.4	Re_k>32.4	1.006	15794
M -25	0.7018	12.32	0.43< Re_k <24.4	Re_k>38.8	0.930	12633

Table 5-11 Geometrical and hydraulic parameters of the large pore size samples (d_p=2.0-2.36 mm & PPI=5-10)

Sample	ε	Permeability (K) x10^{-9}, m^2	Frochhiemer Regime	Turbulent Regime	Inertia Coefficient (*f*)	Drag Coefficient C_E, m^{-1}
L-1	0.6158	25.84	0.51< Re_k <47.9	Re_k>54.7	0.516	5299
L -2	0.5943	18.65	0.47< Re_k <41.4	Re_k>48.1	0.777	9232
L -3	0.6371	29.95	0.42< Re_k <37.0	Re_k>46.1	0.713	8667
L -4	0.6116	18.51	0.30< Re_k <19.87	Re_k>25.93	0.611	6041
L -5	0.6235	18.11	0.65< Re_k <43.1	Re_k>49.8	0.567	5715
L -6	0.6207	25.51	0.68< Re_k <44.9	Re_k>58.0	0.568	5573
L -7	0.6612	16.66	0.66< Re_k <43.6	Re_k>49.3	0.404	4208
L -8	0.6492	20.63	0.63< Re_k <43.5	Re_k>55.7	0.605	4910
L -9	0.6491	16.84	0.53< Re_k <37.6	Re_k>45.0	0.482	4918
L -10	0.6974	15.91	0.56< Re_k <31.6	Re_k>42.0	0.726	8562

L -11	0.7075	22.72	0.47< Re_k <33.5	Re_k>48.0	0.914	11412
L -12	0.7224	19.42	0.45< Re_k <32.2	Re_k>39.1	0.894	11276
L -13	0.6929	15.79	0.32< Re_k <26.4	Re_k>35.4	1.06	15014
L -14	0.6907	20.79	0.37< Re_k <27.4	Re_k>36.8	0.939	13064
L -15	0.7222	27.21	0.67< Re_k <45.1	Re_k>56.6	0.450	3803
L -16	0.7311	19.58	0.57< Re_k <38.6	Re_k>49.6	0.612	6293

Table 5-12 Geometrical and hydraulic parameters of packed beds of balls samples and flow regimes bounds

Reference	Metallic foam type	ε	PPI	Pore size, mm	Forchheimer Regime	Turbulent Regime
Boomsma et. al [78]	Aluminium	0.921	10	6.9	Re_k >26.5	NA
Boomsma et. al [78]	Aluminium	0.920	20	3.6	Re_k >22.3	NA
Boomsma et. al [78]	Aluminium	0.928	40	2.3	Re_k >14.2	NA
Dukhan et al. [91]	Aluminium	0.89	10	NA	Re_k >96.1	NA
Dukhan et al. [91]	Aluminium	0.9	20	NA	Re_k >29.2	NA
Dukhan et. al [104]	Aluminium	0.87	20	NA	6.4< Re_k <37.5	Re_k>50.0
Bagci et al. [90]	Aluminium	0.885	10	NA	6.2< Re_k <45.2	Re_k>46.2
Bagci et al. [90]	Aluminium	0.885	40	NA	3.9< Re_k <39.1	Re_k>47.1
Bagci et al. [90]	Aluminium	0.876	20	NA	6.4< Re_k <37.5	Re_k>50.0
Kouidri et al. [97]	Copper	0.93	20	1.2	Re_k >21	NA
Kouidri et al. [97]	NiFeCr	>0.91	20	1.2	8.15< Re_k <16.5	Re_k>19
Kouidri et al. [97]	Inconel	>0.92	20	1.2	4< Re_k <12.3	Re_k>14.5

Table 5-13 Geometrical and hydraulic parameters of packed beds of balls samples and flow regimes bounds

Sample	ε	*Particle diameter, mm*	*K X10^{-9} ,m^2 Experimental*	*K X10^{-9} ,m^2 Equation (4.7)*	Darcy's Regime limitations	Forchheimer Regime	Turbulent Regime
Ball-1 (current study)	0.362	1.5	1.72	1.75	0.034< Re_k <0.085	0.11< Re_k <9.8	Re_k>11.48
Ball-2 (current study)	0.393	2.0	4.31	4.39	0.060< Re_k <0.12	0.21< Re_k <19.28	Re_k>22.44
Kecocioglu et al. [95]	0.40	3.0mm	NA	NA	0.062< Re_k <0.12	0.34< Re_k <2.3	Re_k>3.4

Kecocioglu et al. [95]	0.40	6.0mm	NA	NA	0.062< Re_k <0.12	0.34< Re_k <2.3	Re_k>3.4
R. Fand et al. [87]	0.357-0.359	2.098 - 4.029	NA	NA	Re_k <0.26 (±0.01)	0.57< Re_k <9	Re_k>13.5
Bagci et al. [93]	0.3501	1.0	0.69	NA	0.29< Re_k <0.77	1.28< Re_k <9	NA
Bagci et al. [93]	0.3558	3.0	6.423	NA	0.02< Re_k <0.59	1.81< Re_k <6.21	Re_k>7.16
Kundu et al. [82]	0.4174	2.5	18.79	NA	0.003≤ Re_k ≤0.2	Re_k>0.3	NA
Kundu et al. [82]	0.3696	3.5	28.19	NA	0.004≤ Re_k ≤0.3	Re_k>0.4	NA
Kundu et al. [82]	0.3478	5	49.90	NA	0.006≤ Re_k ≤0.15	Re_k>0.25	NA
Kundu et al. [82]	0.3913	3.25 (Mixed)	22.53	NA	0.004≤ Re_k ≤0.2	Re_k>0.3	NA

5.5 Friction factor

The friction factor is presented as a function of Reynold's number. Shown in Figure 5-45 is the friction factor for one sample showing the borders of the flow regimes. The friction factor was found to follow the $1/Re_k$ line over the entire range of Darcy's regime. Dukhan et al. [104] stated that the friction factor and pressure drop increased with the decrease of porosity and pore size.

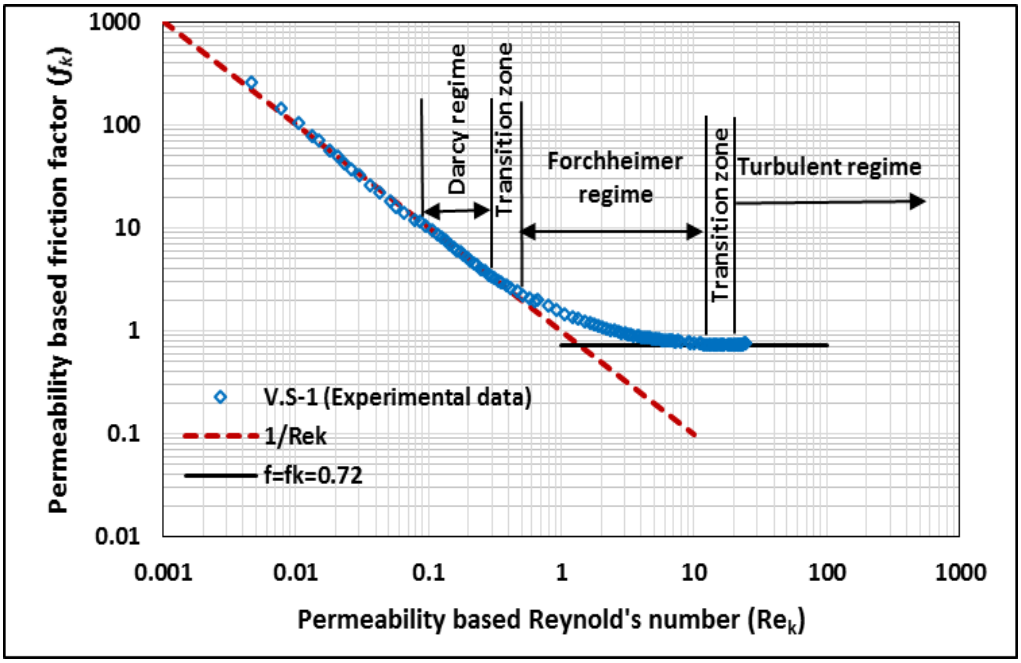

Figure 5-45 Friction Factor versus Reynold's Number

At high Reynold's numbers (or in the turbulent regime flow), the friction factor tends to the inertia coefficient as stated by Dukhan et al. [104] and Mancin et al. [39]. This can be seen in Figure 5-46, where at the highest Reynolds numbers, corresponding to the turbulent Regime, the friction factor tends to the inertia coefficient. The same scenario can be noticed for all the results in this study as shown in Figure 5-46. The black horizontal continuous lines are the inertia coefficients for each sample.

The same scenario can be noticed for all samples, and may be because the inertia coefficient is itself a function of the fluid velocity [295]. For the present samples, the inertia coefficient was estimated over the entire Forchheimer regime. According to Equation 3.8 the friction factor in the Forchheimer regime was estimated from the permeability and inertia coefficient. The later was found from pressure data over the full Forchheimer regime.

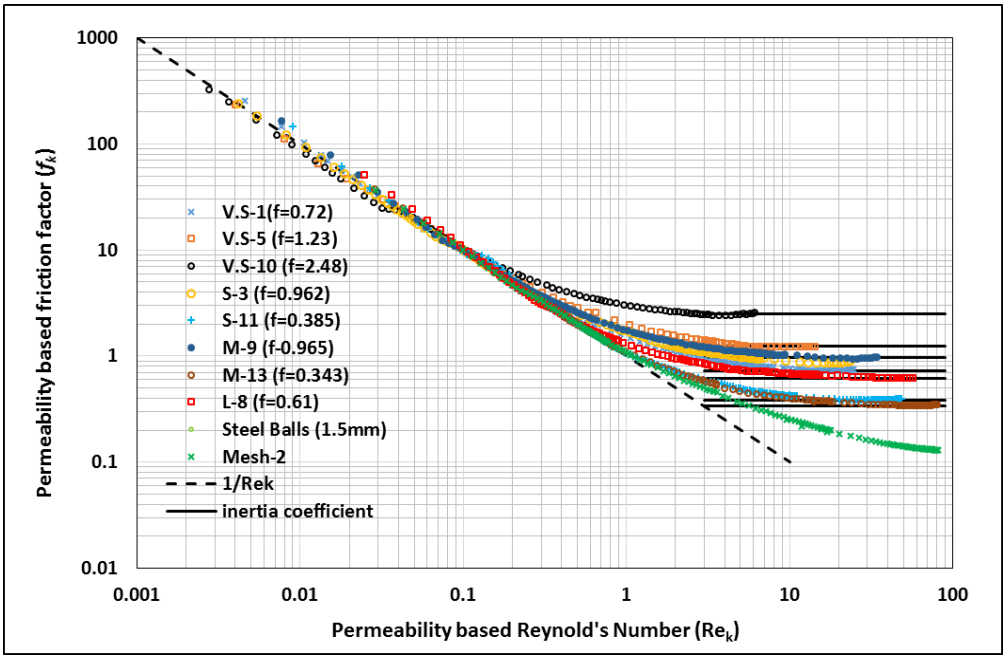

Figure 5-46 Friction Factor versus Reynold's Number

Figure 5-47 shows a comparison of Equation 3.8 with selected experimental results. It can be seen that there is a consistent overestimate of the friction factor predicted by Equation 3.8 in the Forchheimer regime. For example, for the sample V.S-10, the overestimated friction factor can be observed when $Re_k<1$ and for M-9 at $Re_k<2$.

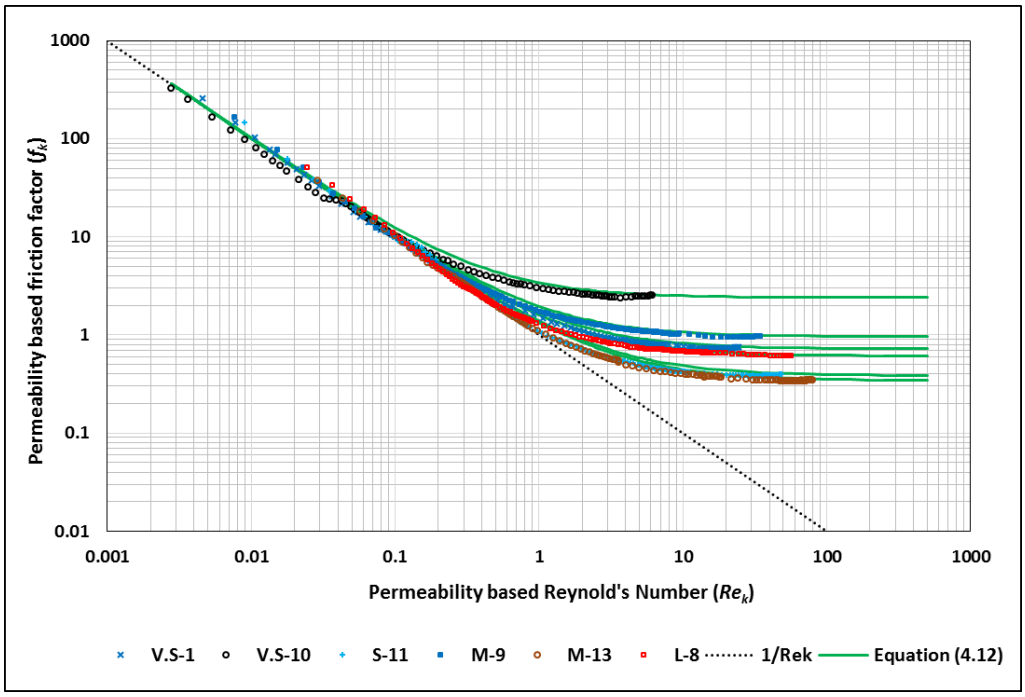

Figure 5-47 Experimental and predicted friction factor against Reynold number

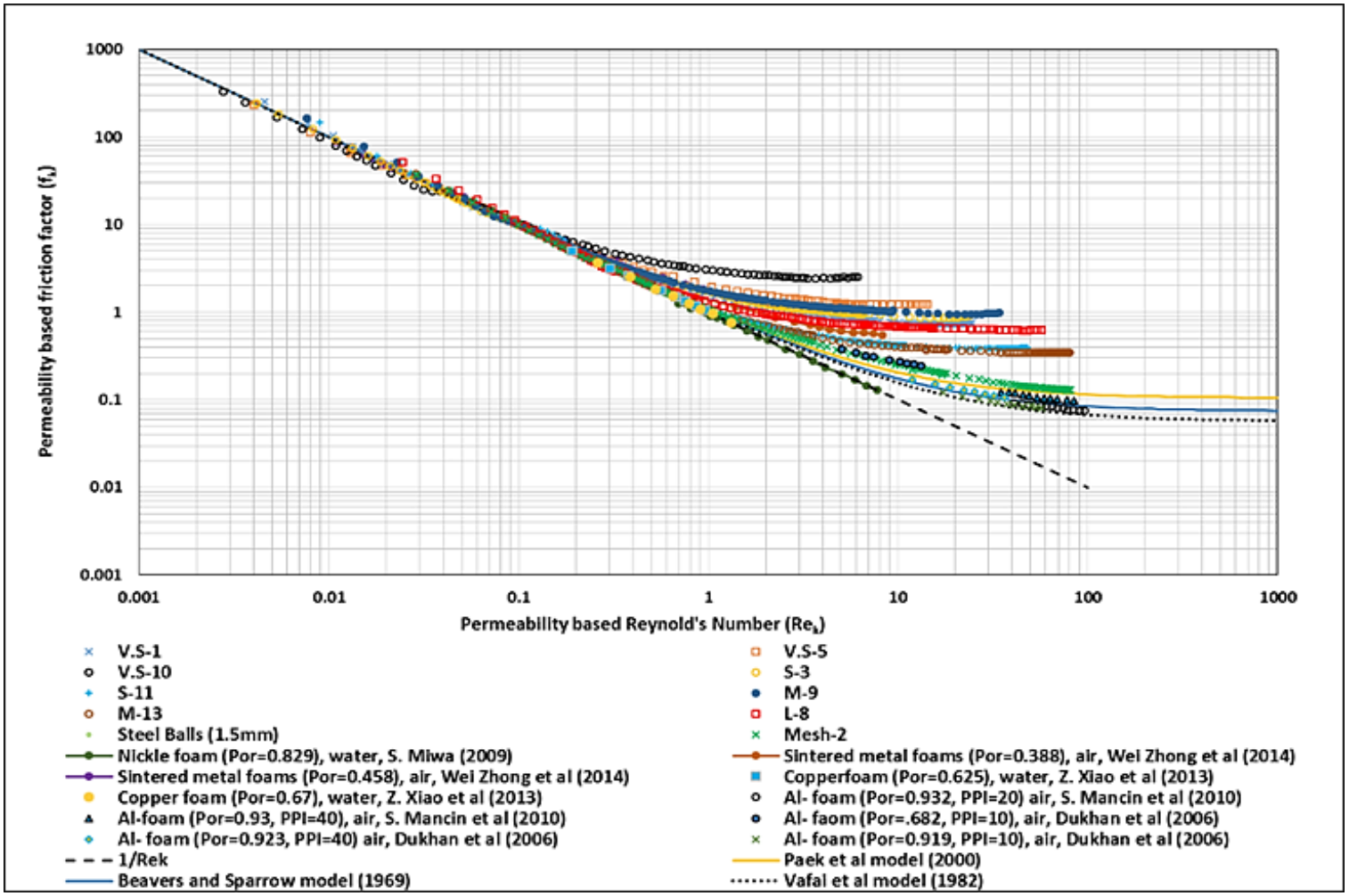

Figure 5-48 Friction Factor versus Reynolds Number

The constant *F* in Equation 3.8 has been found to have different values; examples are 0.074 for Beavers et al. [92], 0.057 for Vafai et al. [115], 0.105 for Paek et al. [19] and 0.076 for Hamaguchi et al. [249]. In each case, these figures for *F* were recommended as universal. Mancin et al. [39] assessed these values for aluminium foams and found that none of the above values agreed with the experimental results. It has been shown that the constant *F* tended to the inertia coefficient when the velocity was high [39, 104] or in the turbulent regime [104]. As shown in Figure 5-48, a single value of *F* would not be suitable for the present tested samples or other samples in literature.

The contribution of the inertia forces increases with flow rate and is proportional to the square of fluid velocity [99]. At relatively high velocities, the first term in Equation 2.5 is small compared with inertia term and can be neglected. The inertia coefficient (Ergun coefficient) depends on the microstructure parameters strongly; namely pore diameter, porosity and strut thickness [18, 19, 52, 110-113].

The contribution of inertia has been investigated inside the pores by the electrochemical probes measurement technique in terms of onset velocity fluctuation [294, 296-298]. In this technique, the rate of velocity gradient fluctuation is evaluated by the probes positioned in different places. The stability of the fluctuation rate with Reynolds number corresponds to the turbulent flow regime [294, 296, 298]. It has been found that the contribution on the inertia at the end of the laminar regime was about 68 % in packed beds of spheres [294, 297, 299], where as in synthetic foams was more than 80 % [297].

Shown in Figures 5-49 and 5-50 are the lower and upper bounds of the Forchheimer flow regime for a selected sample (M-9). From Figure 5-51, it can be seen that the inertia coefficient increased until certain a Reynolds number and then settled at constant value.

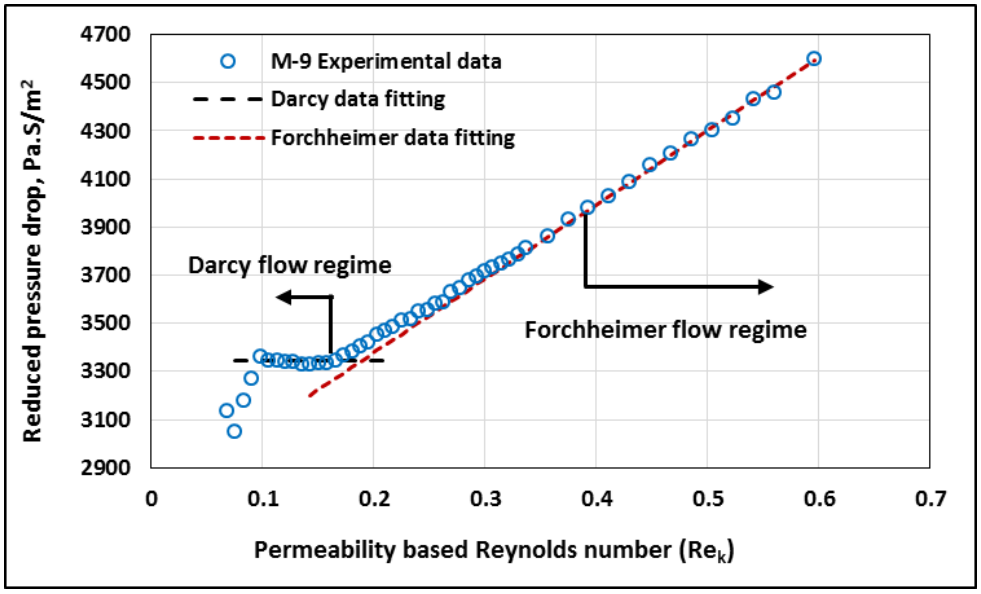

Figure 5-49 Reduced pressure drop against permeability based Reynolds number

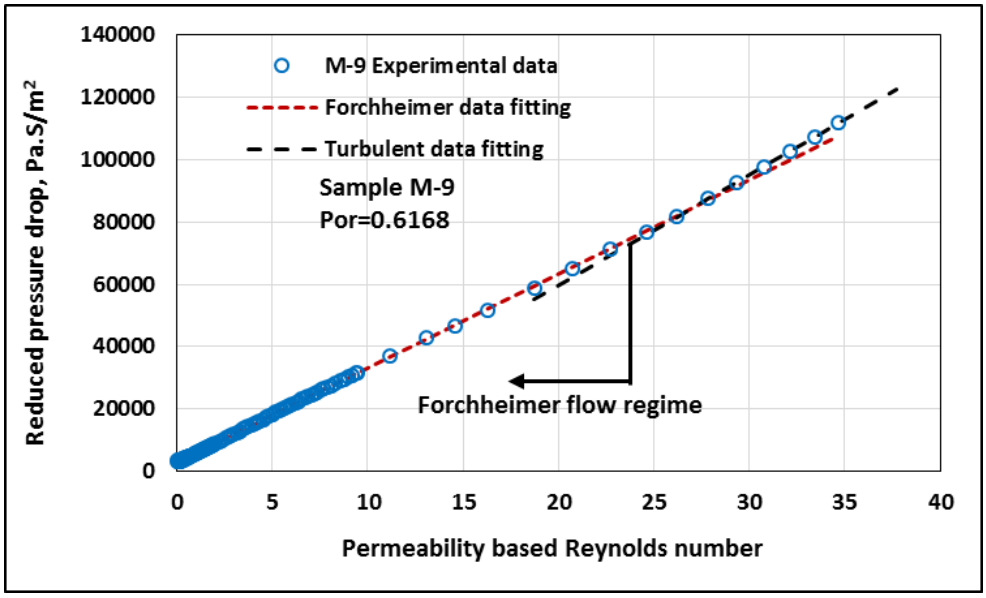

Figure 5-50 Reduced pressure drop versus permeability based Reynolds number

In order to identify the impact of flow characteristics on the inertia coefficient, the inertia coefficient was determined for each measured single flow velocity and pressure drop. Therefore, for the current samples, the inertia coefficient was found to increase with fluid velocity over the Forchheimer regime until it became constant.

Figure 5-51 shows the impact of Reynolds number and morphology on the inertia coefficient. The small pore size and low porosity samples have higher inertia coefficients at the same Reynolds Number. The inertia coefficient initially increased with Reynolds Number and then becomes constant.

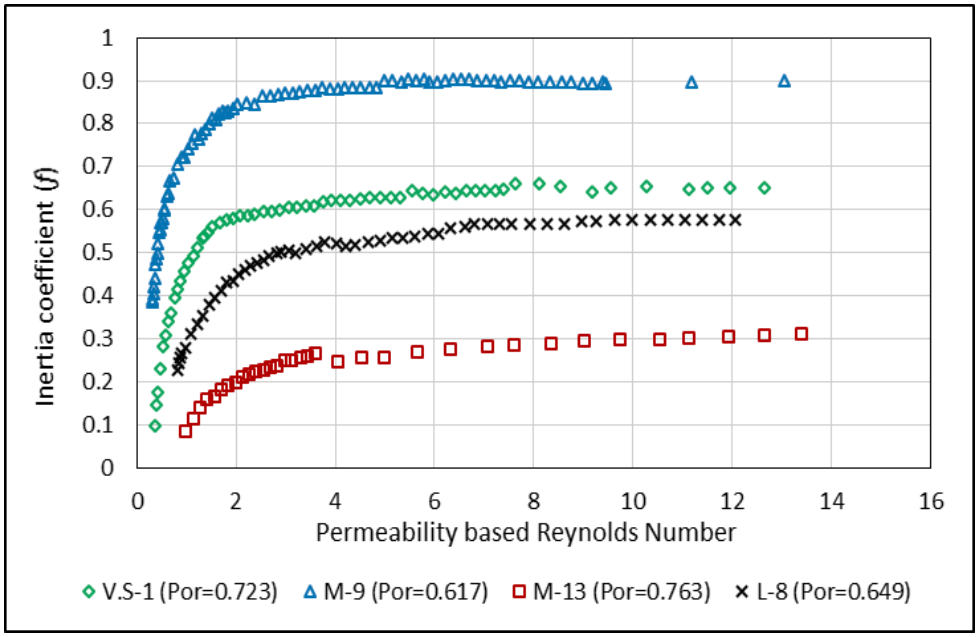

Figure 5-51 Inertia coefficient as function of Reynold number

As mentioned earlier there have been a number of attempts to identify the inertia contribution at pore scales. The portions of the viscous and inertia contributions were determined based on the general correlation of the friction factor as function of particle or pore diameter and Reynolds number [294, 298-300]. For the selected sample (M-9), the proportion of the viscosity and inertia were determined from the experimental data by using the Forchheimer Equation. The same technique used in literature was also adopted by using the Equation 3.9 [294, 298-300]. From Equation 3.9, the theoretical proportions of viscous (Vc) and inertia (Ic) contributions can be estimated as

$$Ic = \frac{0.79}{0.79+fRe_K} \qquad 5.3$$

$$Vc = \frac{f\,Re_K}{0.79+fRe_K} \qquad 5.4$$

Shown in Figure 5-52 is the contribution portions of the viscosity and inertia on the pressure drop over the flow regimes.

The viscous contribution decreased whereas that of the inertia increased with Reynolds number and at the end of Darcy regime are 92% and 10% respectively. It is also clear that the contribution of the inertia is about 94% at the end of Forchheimer

flow regime, which is confirmed with the results of Comiti et al. [299], Seguin et al. [294] and Hirech et al. [298].

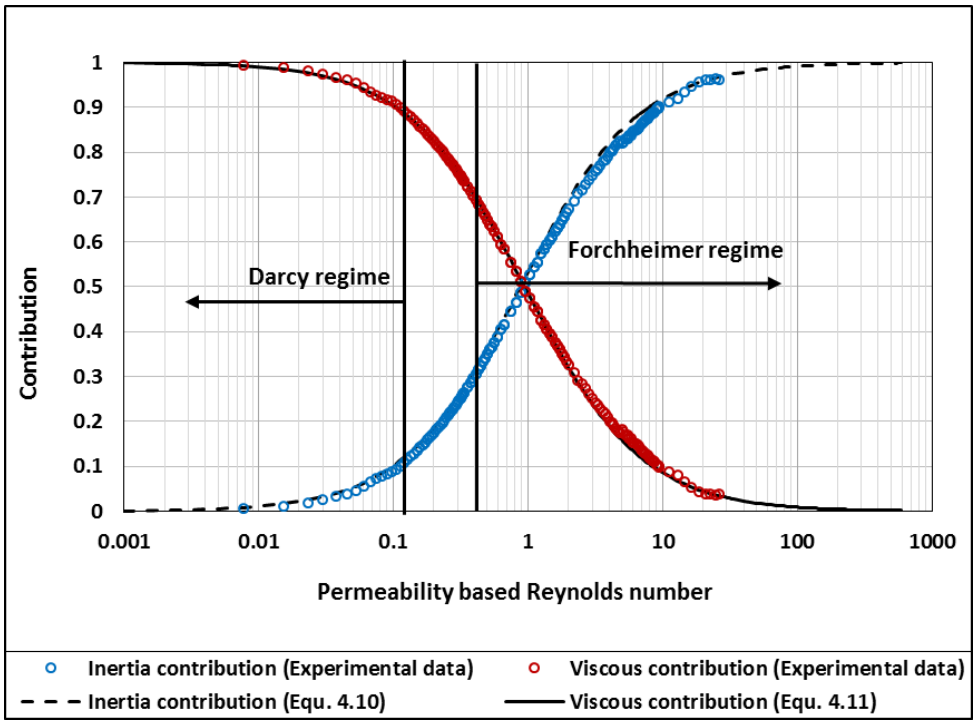

Figure 5-52 Viscous and inertial contributions

As Equation 3.8 was found not to work with these results particularly well, Equation 3.9 [106] was applied to these results instead. This required the determination of two constants. Good agreement with the experimental data was obtained when the constant C_1 was found to equal 0.79 and constant C_2 was expressed as the inertia coefficient for each sample. Shown in Figure 5-53 is the validity of the Equation 3.9 with experimental results of the friction factor.

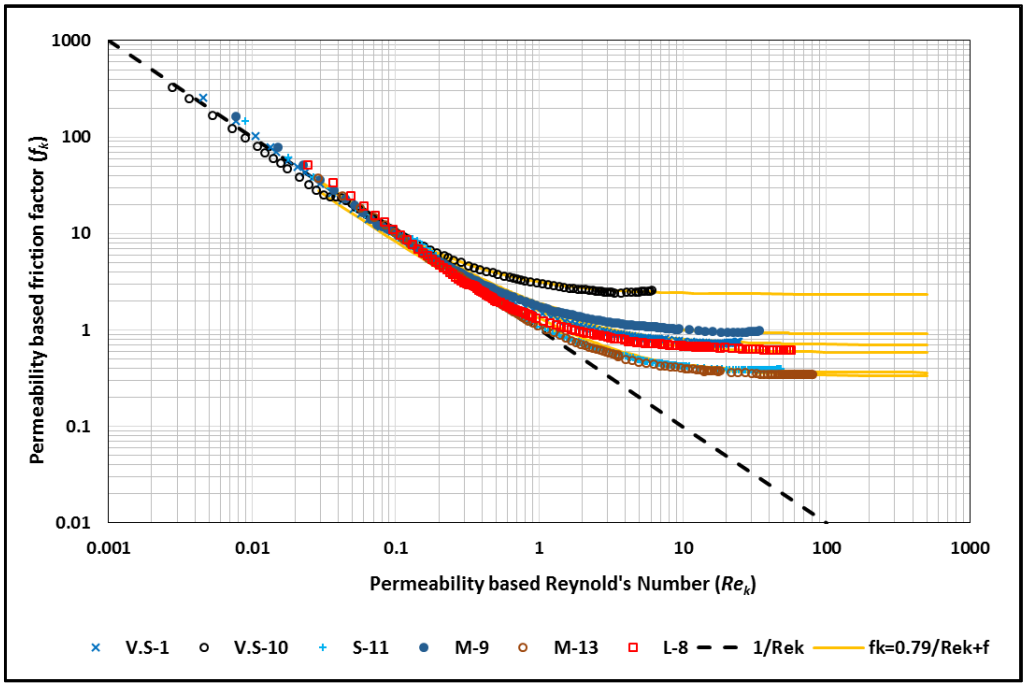

Figure 5-53 Modified friction factor model and experimental

5.6 Uncertainty analysis

5.6.1 Velocity uncertainty

In this work, the air flow rate is measured by three instruments depending on the range of the velocity measurements. The uncertainties in the flow rates of the mass flow meters were calculated based on the equipment uncertainties provided by the manufacturer. The fractional uncertainty of the flow rate measured by the orifice plate was determined according to (EN ISO 5167-2-2003 and EN ISO 5167-1:1997) [251, 281] by this formula

$$\frac{\delta \dot{m}}{\dot{m}} = \sqrt{\left(\frac{\delta C}{C}\right)^2 + \left(\frac{\delta \varepsilon_1}{\varepsilon_1}\right)^2 + \left(\frac{2\beta^4}{1-\beta^4}\right)^2 \left(\frac{\delta D}{D}\right)^2 + \left(\frac{2}{1-\beta^4}\right)^2 \left(\frac{\delta d}{d}\right)^2 + \frac{1}{4}\left(\frac{\delta \Delta P}{\Delta P}\right)^2 + \frac{1}{4}\left(\frac{\delta \rho_1}{\rho_1}\right)^2} \qquad 5.5$$

The diameter ratio β, was 0.46, therefore the uncertainty of the discharge coefficient (C) in the orifice plate was be taken as 0.5% when $\beta \leq 0.6$ [281]. The expansibility factor (ε_1) was estimated as

$$\varepsilon_1 = 1 - (0.41 + 0.35\,\beta^4)\frac{\Delta P}{K\,P_1} \qquad 5.6$$

According to the ISO Standards, the error in the expansion factor was estimated by this formula

$$\delta\varepsilon_1 = 4\frac{\Delta P}{P_1} \qquad 5.7$$

The maximum uncertainty of the expansion factor was ≤ 5%, and was found at the maximum flow rate. The maximum value for $\frac{\delta D}{D}$ may be taken as 0.4% and 0.07% for $\frac{\delta d}{d}$ according to EN ISO 5167-1:1997 [281]. The error of the measured pressure drop across the orifice plate was considered to be 5.0 %. The individual errors were used to calculate the total uncertainty of the mass flow rate and it was found to equal 4.5%. The summary of uncertainties of flow rates depending on the instruments are tabulated in Table 5-14.

Table 5-14 Flow rates uncertainties

Instrument type	Flow rate range	Uncertainty
Roxspur Air Mass Flowmeter (FFLM0035)	0.5 - 50 LPM 0.003 - 0.38 m/s	5.8%
Omega Air Mass Flowmeter (FMA-1612A-V2)	50 – 500 LPM 0.38 – 3.8 m/s	2.8%
Orifice Plate	3.34 – 20 g/s 1.26 – 7.5 m/s	4.5%

5.6.2 Pressure drop Uncertainties

The error in the pressure measurements was found using the uncertainties in the instruments and by the repeatability for the inclined liquid manometer. The maximum error in pressure measurements was found to be 4% for the inclined manometer.

5.6.3 Permeability uncertainty

Before starting to find the error in the permeability, the parameters which were used in calculation should be known with their uncertainties. The maximum deviation in sample thickness was found to be 0.4%. Equation 2.1 was used to determine the permeability, so the permeability can be written as a function of the measured and calculated parameters as

$$K = f(\Delta P, L, \mu, V) \quad 5.8$$

The total error of the permeability measurements can be found by the contributions from the uncertainties of all relevant parameters which are summarized by Equation 5.8 by the uncertainty propagation analysis [18, 39, 157, 181, 301]

$$\frac{\delta K}{K} = \sqrt{\left(\frac{\delta \Delta P}{\Delta P}\right)^2 + \left(\frac{\delta L}{L}\right)^2 + \left(\frac{\delta \mu}{\mu}\right)^2 + \left(\frac{\delta V}{V}\right)^2} \quad 5.9$$

The calculated permeability error is the maximum possible error relating to maximum uncertainties of relevant parameters.

5.6.4 Reynolds Number Uncertainty

Equation 2.4 describes all of the relevant parameters in the uncertainty of Re_k. Consequently, the Re_k can be expressed as a function of those parameters as

$$Re_k = f(\rho, K, \mu, V) \quad 5.10$$

The uncertainty propagation analysis can be applied to obtain the error in Reynolds Number.

$$\frac{\delta Re_k}{Re_k} = \sqrt{\left(\frac{\delta \rho}{\rho}\right)^2 + \left(\frac{\delta K}{K}\right)^2 + \left(\frac{\delta \mu}{\mu}\right)^2 + \left(\frac{\delta V}{V}\right)^2} \quad 5.11$$

5.6.5 Friction factor uncertainty

Using the Equation 3.6 the related parameters are summarized as

$$f_k = f(\rho, K, \Delta P, L, V) \quad 5.12$$

The uncertainty of the friction factor was found using

$$\frac{\delta f_k}{f_k} = \sqrt{\left(\frac{\delta \rho}{\rho}\right)^2 + \left(\frac{\delta K}{K}\right)^2 + \left(\frac{\delta \Delta P}{\Delta P}\right)^2 + \left(\frac{\delta L}{L}\right)^2 + \left(\frac{\delta V}{V}\right)^2} \quad 5.13$$

The summary of all parameter uncertainties are reported in Table 5-15. These listed errors are the maximum expected uncertainty for each parameter.

Table 5-15 Summary of uncertainties of parameters

Parameter	Unit	Uncertainty
Thickness	m	0.4 %
Pressure	Pa	4.0 %
Dynamics Viscosity	$N.S/m^2$	0.1 %
Velocity	m/s	5.8 %
Density	Kg/m^3	0.1 %
Permeability	m^2	6.4 %
Reynolds Number	-	8.0 %
Friction factor	-	8.1%

It is worth noting that the error in Reynolds Number varied with flow rate and the value reported in the Table 5-14 is a maximum at low flow rates.

Chapter 6

6. ETC experimental results and discussion

6.1 Experimental results

The measured values of ETC were presented against the macroscopic porosity. In Table 6-1 Geometrical parameters and experimental results of replicated aluminium foams effective thermal conductivity were reported. Shown in Figure 6-1 are the measured effective thermal conductivities of the tested samples plotted against porosity. There was some scatter in the results which is inherent from the nature of porous metals, the manufacturing process and the size of samples that could be manufactured.

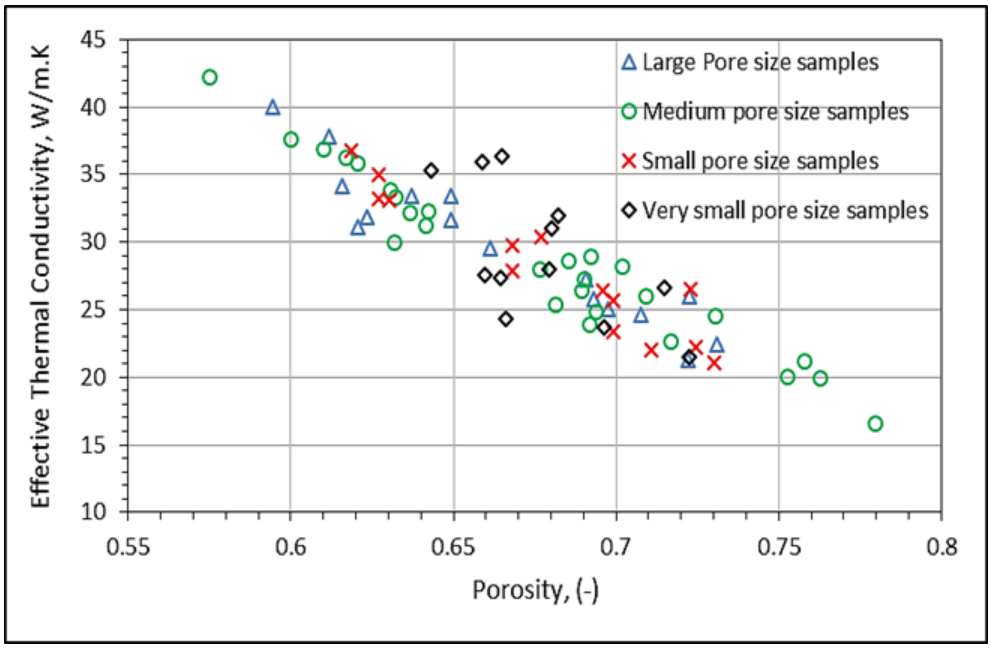

Figure 6-1 The ETC versus porosity (K_{sol}=205 W/m.K, temperature is 33◦C)

In order to compare the measured values of ETC with those available in the literature, the ETC is presented (Figure 6-2) and normalized with the thermal conductivity of solid phase material from which the porous structure is made. The results of other researchers are also presented.

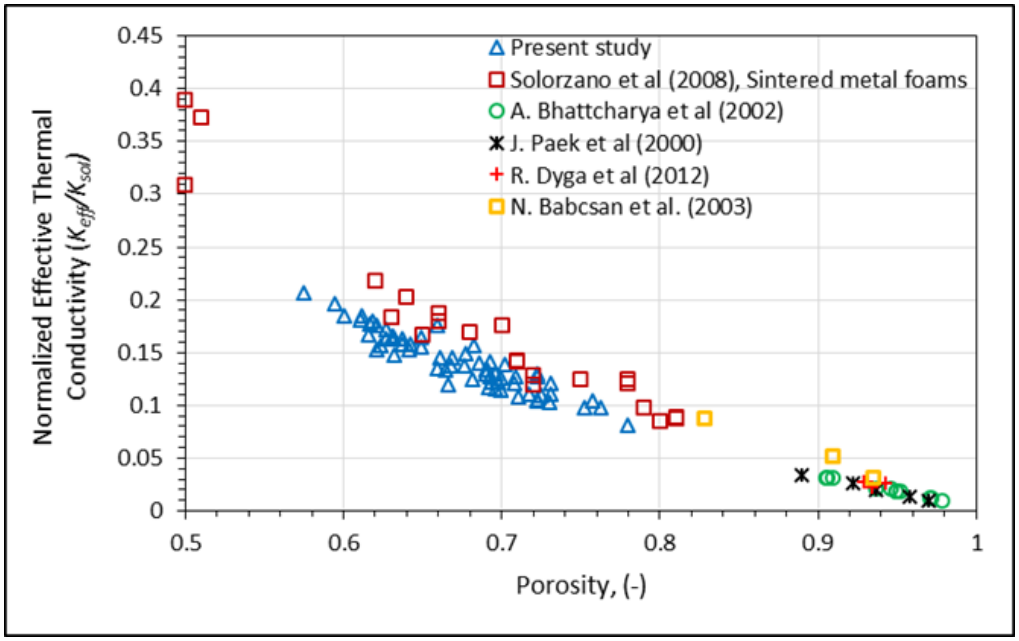

Figure 6-2 Normalised effective thermal conductivity versus porosity

It can be seen that for the samples tested here and those of others, the ETC decreased as the porosity increased. The foams manufactured by Solórzano et al. [34] by the powder metallurgical method resulted in closed cells with a similar range of porosities to those manufactured in this work. They used the Transient Plane Source (TPS) technique to determine the ETC. The closed cell metal foams examined by Babcsan et al. [179] are also plotted. Three representative measurements of high porosity metal foams manufactured using investment casting have been included. The samples tested in Paek et al. [19] and Bhattacharya et al. [18] are Duocel foams, produced by the ERG Materials and Aerospace Corp. Dyga and Witczak [158] do not mention the origin of their samples but are reported as ranging from 20 to 40 PPI. All used a similar method to determine the ETC as the one used here.

Table 6-1 Geometrical parameters and experimental results of replicated aluminium foams effective thermal conductivity

Sample [A]	ε	K_{eff} W/m.K	Sample [B]	ε	K_{eff} W/m.K	Sample [C]	ε	K_{eff} W/m.K	Sample [C]	ε	K_{eff} W/m.K	Sample [D]	ε	K_{eff} W/m.K
V.S-1	0.7225	21.45	S-1	0.6301	33.15	M-1	0.6103	36.92	M-17	0.7578	21.22	L-1	0.6158	34.17
V.S-2	0.6962	23.67	S-2	0.6272	33.20	M-2	0.6205	35.80	M-18	0.6853	28.58	L-2	0.5943	40.00
V.S-3	0.666	24.34	S-3	0.6184	36.76	M-3	0.6323	33.29	M-19	0.6816	25.42	L-3	0.6371	33.39
V.S-4	0.659	35.98	S-4	0.6272	35.00	M-4	0.6425	32.31	M-20	0.7170	22.67	L-4	0.6116	37.80
V.S-5	0.6822	31.96	S-5	0.6960	26.37	M-5	0.6308	33.79	M-21	0.6919	23.90	L-5	0.6235	31.85
V.S-6	0.6595	27.61	S-6	0.6992	25.71	M-6	0.6000	37.62	M-22	0.7091	26.01	L-6	0.6207	31.10
V.S-7	0.6643	27.34	S-7	0.7302	21.11	M-7	0.6369	32.19	M-23	0.7306	24.55	L-7	0.6612	29.54
V.S-8	0.715	26.63	S-8	0.6683	29.73	M-8	0.6415	31.22	M-24	0.6896	26.38	L-8	0.6492	31.60
V.S-9	0.665	36.32	S-9	0.6680	27.93	M-9	0.6168	36.23	M-25	0.7018	28.20	L-9	0.6491	33.44
V.S-10	0.643	35.3	S-10	0.6990	23.39	M-10	0.6922	28.93	M-26	0.6937	24.84	L-10	0.6974	25.01
V.S-11	0.680	31.0	S-11	0.7246	22.26	M-11	0.6902	27.30	M-27	0.5750	42.21	L-11	0.7075	24.65
V.S-12	0.679	28.0	S-12	0.7107	22.04	M-12	0.6766	28.00				L-12	0.7224	26.04
			S-13	0.6770	30.38	M-13	0.7628	19.90				L-13	0.6929	25.83
			S-14	0.7227	26.50	M-14	0.7796	16.60				L-14	0.6907	27.24
						M-15	0.7527	20.00				L-15	0.7222	21.27
						M-16	0.6317	30.00				L-16	0.7311	22.44

A- Very small pore size samples (d_p=0.71-1.0 mm & *PPI*=20-25)

B- Small pore size samples (d_p=1.0 -1.18 mm & *PPI*=15-20)

C- Medium pore size samples (d_p=1.4 -1.7 mm & *PPI*=10-15)

D- Large pore size samples (d_p=2.0 - 2.36 mm & *PPI*=5-10)

It can be seen that the ETC decreased as the porosity increased in both closed and open cell sponges. The measurements encompass samples with pore sizes ranging from 0.7mm to 2.4mm. No measurable impact of pore size could be determined. In these tests, the fluid phase (air) had a lower thermal conductivity compared with solid phase and the ratio of K_s/K_f is more than 10^3. As a result of this, Argento et al. [302] have suggested that the main mechanism of heat exchange is by conduction through the struts and ligaments which form the porous network. The reduction in the volume fraction of the fluid phase (decrease in porosity) leads to the increase of the fraction of solid phase ligaments, hence the thickness of the skeletal fibres increases. As a result, the ETC is dependent on the change in the solid phase volume fraction. For the same reason as stated by Dias et al. [182], the sintered material foams provide a higher ETC at the same range of porosity in comparison with the non-sintered ones.

The dependence of sample properties on convection was explored by testing four large pore size samples (d_p=2.0-2.4mm) with different porosities in both upward and downward configurations. Shown in Figure 6-3 is the effect of porosity on the contribution of convective heat transfer to ETC, including data from a high porosity aluminium foam [158], whose pore size is roughly equivalent to the pore size tested here.

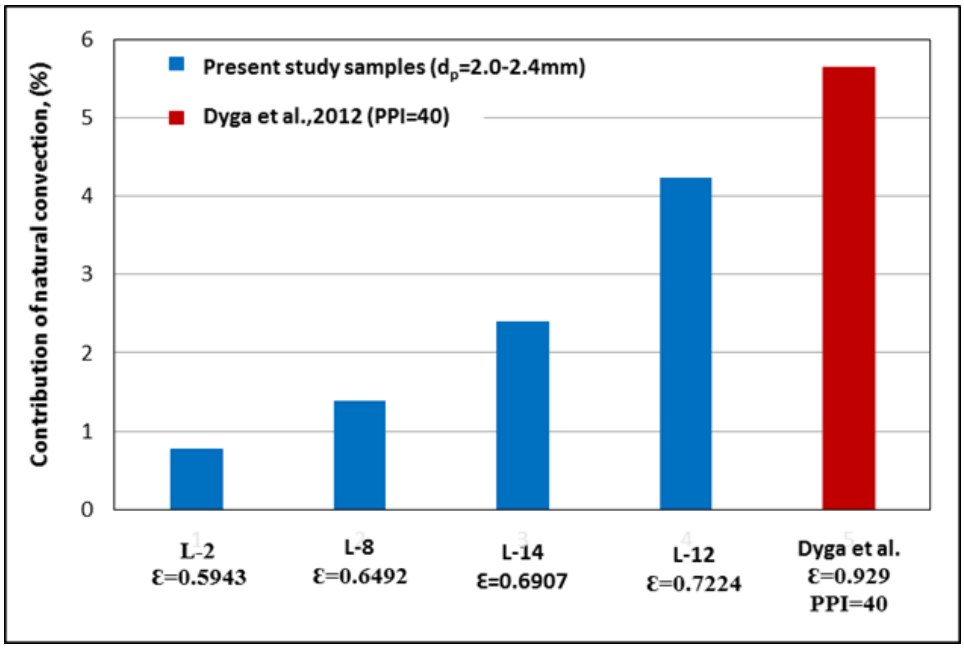

Figure 6-3 The effect of porosity on the natural convection contribution on ETC (33°C)

The contribution of natural convection is calculated as the percentage increase in ETC when measured with heat flow vertically upwards, over the value when it flows in the opposite direction (suppressing the convection contribution), and is found to increase with porosity as a result of increased fluid space. However, the overall contribution from natural convection remains low. Subsequent measurements were performed with the direction of heat downwards to minimize the influence of convective heat transfer.

While in this analysis, natural convection was assumed to be negligible, previous researchers have demonstrated that it can contribute to heat transfer in this type of test [158]. To test for its impact, the rig was rotated such that the heat source was below the sample. This configuration has been shown to encourage air movement within the pores due to buoyancy forces [158]. Natural convection depends on temperature, and so measurements were performed for at a range of heater temperatures; the results for which are shown in Figure 6-4 for large pore size samples. The effective thermal conductivity increased with temperature, as might be expected as both the thermal conductivity of air and aluminium increase with temperature. However, once these factors were taken into account, it was found that the relative contribution of convection also increased by ~1% for an 18°C rise in the air temperature.

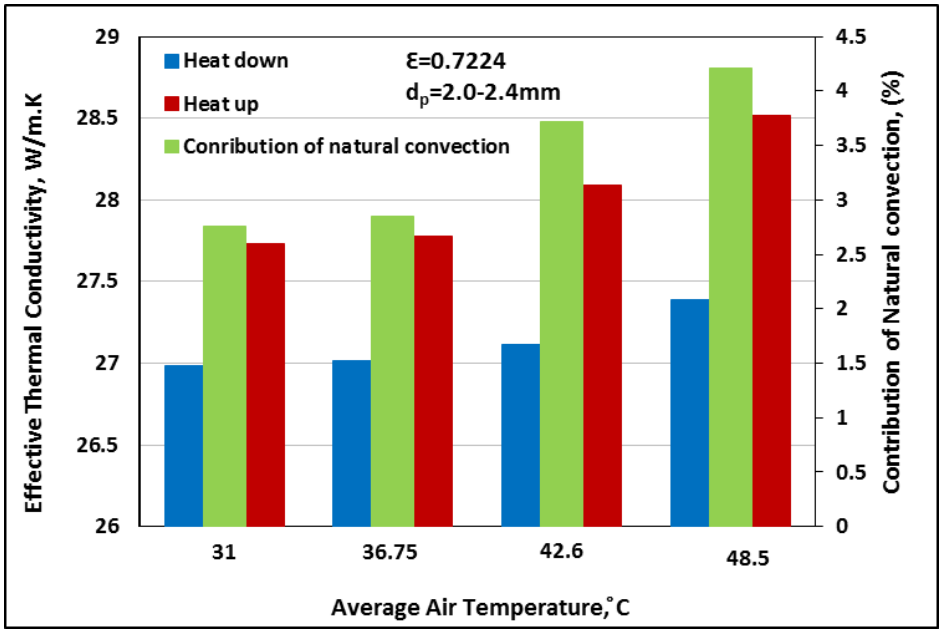

Figure 6-4 The impact of temperature on the contribution of natural convection to ETC

6.2 Models and correlations validity and assessment

Since their development, there have been a number of studies on high porosity metal foams and sponges (ε > 90%). The ETC's found have been shown to be strongly influenced by the morphology of the unit cell [19, 169]. Empirical and structural based models have been developed. However, theoretical models of ETC often still rely on experimentally determined constants to account for manufacturing variability and the difficulties in representing the complex three-dimensional structures [160, 169]. Models have often been based on a number of structures such as a two-dimensional array of hexagonal cells [18] and 3D tetrakaidecahedron cells [167, 303].

The materials studied here have lower porosities and a more random structure than some other types of porous material, so their ETC would not necessarily be expected to agree with equations derived for alternative types of metal foams or sponges. However, it is desirable to have an expression that can predict ETC for porous metals over the range of porosities from 0.5 to values approaching 1.0. A number of models and correlations have been selected and compared to available measurements of ETC, which are shown in Table 6-2.

Table 6-2 Effective thermal conductivity models and empirical correlations

Name	Expression	
Models:		
Series – Parallel [34]	$K_{eff} = K_{sol}\left(1-\varepsilon^{2/3}\right) + \frac{K_s\ \varepsilon^{2/3}}{K_f+(K_s-K_f)\ \varepsilon^{1/3}}$	6.1
Misnar Model [34]	$K_{eff} = K_{sol}\left(1+\frac{1-K_s/K_f}{1-\varepsilon^{1/3}\ (1-K_s/K_f)}\right)$	6.2
Dul'nev Model [73]	$K_{eff} = K_{sol}t^2 + K_f(1-t)^2 + \frac{2t(1-t)K_{sol}K_f}{K_{sol}(1-t)+tK_f}$ Where $t = \frac{1}{2} + \cos\left(\frac{1}{3}cos^{-1}(2\varepsilon-1) + \frac{4\pi}{3}\right)$	6.3
Scaling Relation [34, 285]	$K_{eff} = K_{sol}(1-\varepsilon)^n$ Where $n \in [1.65, 1.85)$	6.4
Progelhof [304]	$K_{eff} = K_f\left(1 + K_{sol}/K_f\ \varepsilon^n\right)$	6.5
Empirical Correlations for high porosity foams:		
Bhattacharya et al. [18]	$K_{eff} = A(\varepsilon K_f + (1-\varepsilon)K_{sol}) + \frac{1+A}{\frac{\varepsilon}{K_f}+\frac{1-\varepsilon}{K_{sol}}}$	6.6

	where A= 0.35	
Singh et al. [165]	$k_{eff} = K_I^{(1-F)} K_{II}^F \quad 0 \le F \le 1$ $K_I = \frac{K_{sol}K_f}{(1-\varepsilon)K_f + \varepsilon K_{sol}}$ $K_{II} = \varepsilon K_f + (1-\varepsilon)K_{sol}$ $F = 0.9683\ (0.3031 + 0.0623\ln(\varepsilon\ \frac{K_{sol}}{K_f}))$	6.7
Coquard et al. model [167]	$K_{eff} = K_{sol}(\ \alpha\ (1-\varepsilon) + \chi(1-\varepsilon)^2)$ $\alpha = f\left({}^{D_{st}}/_{d_{lu}}\right),\ \chi = f\left({}^{D_{st}}/_{d_{lu}}\right)$	6.8
Maxwell Model [34, 163]	$K_{eff} = \frac{2\,K_{sol}+K_f-2(K_{sol}-K_f)\varepsilon}{K_{sol}+K_f+(K_{sol}-K_f)\varepsilon}$	6.9

There are some of models which can be simplified according to the assumption $K_f << K_{sol}$ [34] and when the $K_{sol} / K_f > 10^3$, the main mechanism of heat transfer is conduction along the solid – solid contact area [182]. Five models were used; one based on the assumption that conduction through the solid material can be either in series or parallel. A Misnar model, which proposed that for porous materials consisting of solid ligaments with random air, inclusion is used. A simple scaling expression was proposed for the metal foams and the exponent *n* as a fitting coefficient [285]. An empirical model used the scaling expression fitted to experimental results of polymeric foams by Progelhof [304]. The model proposed by Dul'nev et al. [73] was also used, and in this model the fibrous structure was a random arrangement of infinitely cylinders, as shown in Figure 6-5. Although, it was also stated the replacement of the cylinders with the same cross sectional square bars will not effect the ETC.

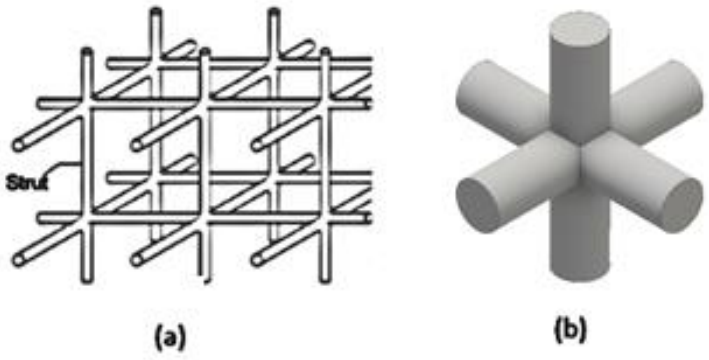

Figure 6-5 (a) Infinite cylinders arrangement, reproducing from [32] with permission of Elsevier; (b) unit cell intersection

An analytical model based on the numerical and 3D tomographic structure parameters in terms of ratio between the thickness of the struts and the nodes (referred to as lumps in the originating work, and preserved in the notation here, D_{st}/d_{lu}) and the node shape is also used [167]. Two empirical expressions for high porosity (> 90%) foams are also compared to our experimental measurements. This is beyond their range of applicability and the object of including them was to observe if they might extend to lower porosity materials.

The final expressions of the simplified models [34] are tabulated in Table 6-3. A simple scaling relation and simplified Progelhof model take the same expression. The series –parallel and Misnar models give the same equation. All of them give the function of porosity and solid phase thermal conductivity.

Table 6-3 Simplified models

Name	Expression	
Simplified models:		
Simplified Series – Parallel and Misnar Models [34]	$K_{eff} = K_{sol}(1-\varepsilon^{2/3})$	6.10
Dul'nev Model [73]	$K_{eff} = K_{sol}t^2 + K_f(1-t)^2 + \frac{2t(1-t)K_{sol}K_f}{K_{sol}(1-t)+tK_f}$ Where $t = \frac{1}{2} + \cos\left(\frac{1}{3}cos^{-1}(2\varepsilon - 1) + \frac{4\pi}{3}\right)$	6.11
Scaling Relation [34, 285] 6.12	$K_{eff} = K_{sol}(1-\varepsilon)^n$ Where $n \in [1.65, 1.85)$	
Simplified Coquard et al. model [167]	$K_{eff} = \alpha(1-\varepsilon) + \chi(1-\varepsilon)^2$ $\alpha = f\left({D_{st}}/{d_{lu}}\right),\ \chi = f\left({D_{st}}/{d_{lu}}\right)$	6.13
Empirical Correlations for high porosity foams:		
Bhattacharya et al. [18]	$K_{eff} = A(\varepsilon K_f + (1-\varepsilon)K_{sol}) + \frac{1+A}{\frac{\varepsilon}{K_f}+\frac{1-\varepsilon}{K_{sol}}}$ where A= 0.35	6.14
Singh et al. [165]	$k_{eff} = K_I^{(1-F)}K_{II}^F \quad 0 \le F \le 1$ $K_I = \frac{K_{sol}K_f}{(1-\varepsilon)K_f+\varepsilon K_{sol}}$ $K_{II} = \varepsilon K_f + (1-\varepsilon)K_{sol}$ $F = 0.9683\ (0.3031 + 0.0623\ln(\varepsilon\ \frac{K_{sol}}{K_f}))$	6.15
Maxwell Model [34, 163]	$K_{eff} = K_{sol}\frac{2(1-\varepsilon)}{(2+\varepsilon)}$	6.16

The simplified expressions have been examined by a comparison of predicted ETC with the original models. The deviation in predicted ETC by the simplified series - parallel model at porosity 0.5 ≈ 1.0% and increased gradually after a porosity of 0.8 reached 26.6% when the porosity increased to 0.98. This can be explained, as in this case the mechanism of heat transfer is through conduction along the solid –fluid-solid instead along finite contact area. The possible reason for that is the decrease of the solid phase volume.

The experimental results from this study and those of other researches are presented in Figure 6-6 with expressions given in

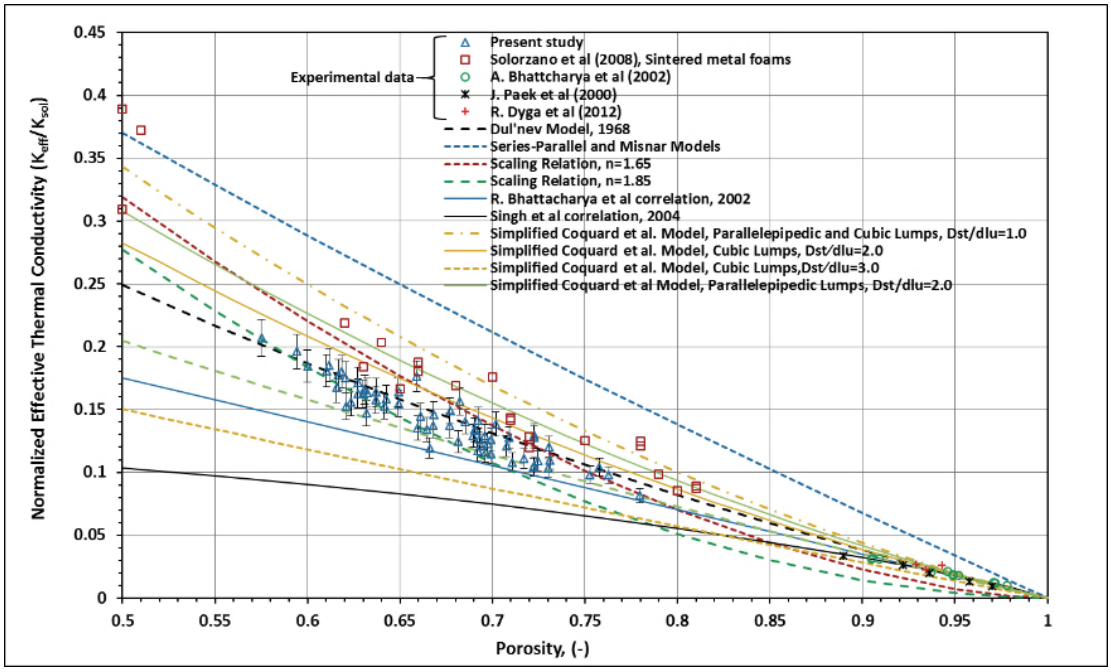

Figure 6-6 Empirical correlations and simplified models assessment

From Figure 6-6, it can be seen that there is considerable variation in the predicted ETC, with mismatches between empirical correlations and the experimental results across the full range of porosity. The experimental data might be considered to be in better agreement than the proposed fits; the scatter observed here between the samples tested being less than that of the predictions. This, in part, reflects the lack of experimental data that has been available for porous materials and the necessity for further measurements. The series-parallel or Minsar models over predicted the ETC at all porosities by 65%, at a porosity of 70% and 86% at a

porosity of 95%. The two models derived for high porosity materials, Bhattacharya et al.[18], and Singh et al.[165], tend to under predict the ETC at lower porosities by 24% and 50% at a porosity of 60% respectively, which indicates some material or structural difference at this range from the higher porosity form. Scaling relationships gave reasonable agreement for some of the measurements but tended not to work for materials where the porosity was greater than 90%, which under predicted ETC by 77% at a true porosity of 95%. The Dul'nev model predicted ETC well across the whole range of porosities, although the values of the effective thermal conductivity for the high porosity foams are so low that the relative error will be significant. The successful predictions of this model are likely to relate to the fact that the fibrous structure in the model is assumed to be an infinite random arrangement of cylinders. The replacement of the cylinders with square bars of the same cross sectional area will not affect the ETC [73], and so this random arrangement is a good representation of the strut structure of the tested foams.

Further to this, the shapes of the nodes and struts have a measurable effect on the predicted ETC. The cross sectional shape of metal fibres (strut) changes with porosity, from a circle at a porosity of 85% to a concave triangle when the porosity reaches 97% [18, 20, 32] as show in Figure 6-7 . It depends strongly on the porosity and the type of material and manufacturing process also have an important impact on the topological structure of the foams [146]. Therefore, incorrectly considered shapes and cross sections of struts which comprise different forms is a possible reason of the discrepancies in the predicted ETC by models for the very high porosity foams [20].

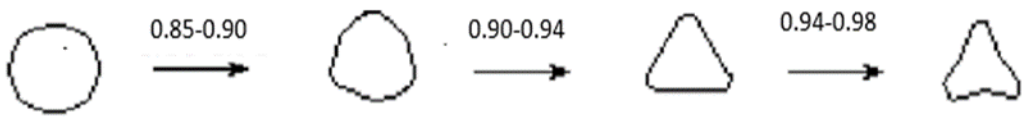

Figure 6-7 Strut cross sections at different porosities. Reproducing from [18] with permission of Elsevier

To include the effect of the thickness ratio of the nodes and struts, the predicted ETC from the Coquard et al. model [167] was compared with experimental results with cubic and parallelepipedic node shapes. For both shapes at high D_{st}/d_{lu},

the ETC was under predicted at low porosity by 15% and 36% for parallelepipedic and cubic nodes respectively, and tends to good estimation at very high porosities with high and low ratio. The overestimated values were found at lower porosities with very low D_{st}/d_{lu}. When the ratio is 2.0, the shape of the nodes tends to a measurable difference of around 8% at a porosity of 65%. In this model, the thickness ratio between the nodes and struts needs to be obtained accurately in order to be able to predict a reliable ETC value.

The analytical and numerical approaches describe the typical shape of unit cells as homogenous, without any misalignment or other defects, which in reality will be present [34, 172]. Such features will be the origin of the differences between the predictions and the experimental results.

As can be seen from Figure 6-6, no empirical correlation or model can be generalized to predict the ETC over the whole range of porosity. Thereby, the objective of this work was to modify one of the available models to cover the whole experimental range. The scaling relation was proposed for open cells metal foams to find the thermal properties, such as thermal conductivity and specific heat [285]. In the scaling relation (Equ. 6.4), the exponent *n* varied from 1.65 to 1.85 [34, 285]. Therefore, *n* was modified so the exponent fit all experimental results. From Figure 6-6, the impact of differences in material properties on the ETC can be observed. This is particularly noticeably between the metal foams with porosities from 0.6 to 0.8 and the foams with porosities greater than 0.9. In order to find the values of exponent *n* as a function of porosity, current experimental results and those reported in open literature were used in the scaling relation. Thus, the value of exponent *n* was allowed to vary with the porosity of the metal foams.

This can be expressed as:

$$K_{eff} = K_{sol}(1-\varepsilon)^{n=f(\varepsilon)} \qquad 6.17$$

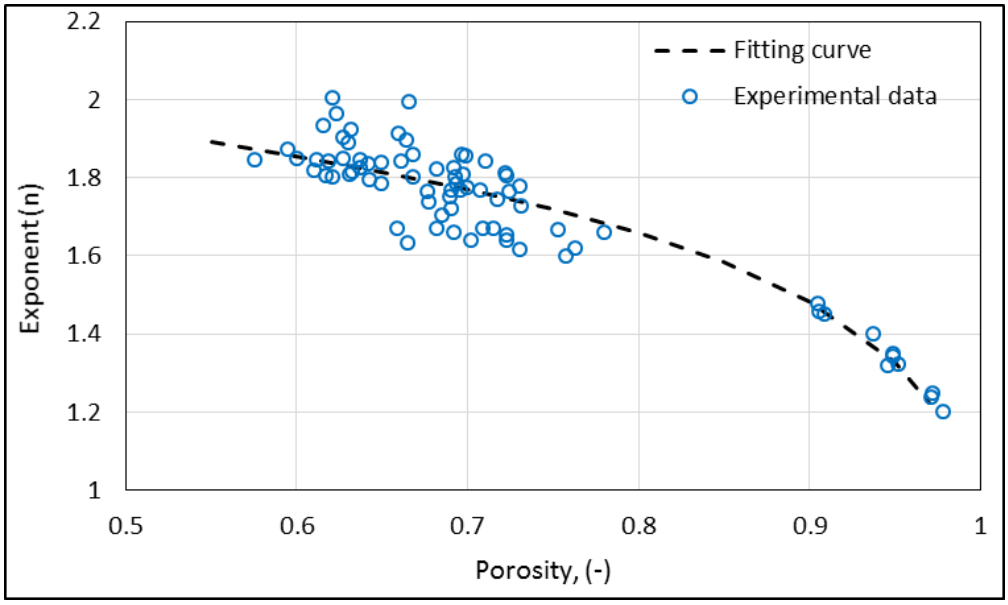

Figure 6-8 Exponent n as function of porosity

From Figure 6-8, the value of n was observed to gently decrease with increasing porosity, but then rapidly tail off beyond a porosity of 0.8. In order to fit this data, a power law was investigated, also shown in Figure 6-8, as a dashed line. The best fit was found to be

$$n = 2.15(1-\varepsilon)^{0.16} \qquad 6.18$$

Resulting in the final form of the empirical scaling law for porous metals for with pore fractions ranging from 0.5 to 0.98 to be

$$K_{eff} = K_{sol}(1-\varepsilon)^{2.15(1-\varepsilon)^{0.16}} \qquad 6.19$$

Figure 6-9 shows the predicted ETC using Equation 6.19 in comparison with the experimental results. The error bars show the respective percentage error. The alternative expression of ETC (Equ. 6.19) is in a good agreement with experimental results of open cell metal foams. It also under predicts by 20% for closed celled sintered porous materials due to the different in microstructure. The comparison is reported in Figure 6-9. The Maxwell model was obtained for a material consisting of solid spheres randomly dispersed in the second phase and is not valid for the metal foams due to the differences in microstructure [34, 163]. There is a mismatch between Maxwell model and experimental data and the model overestimated the ETC over all the range of porosity.

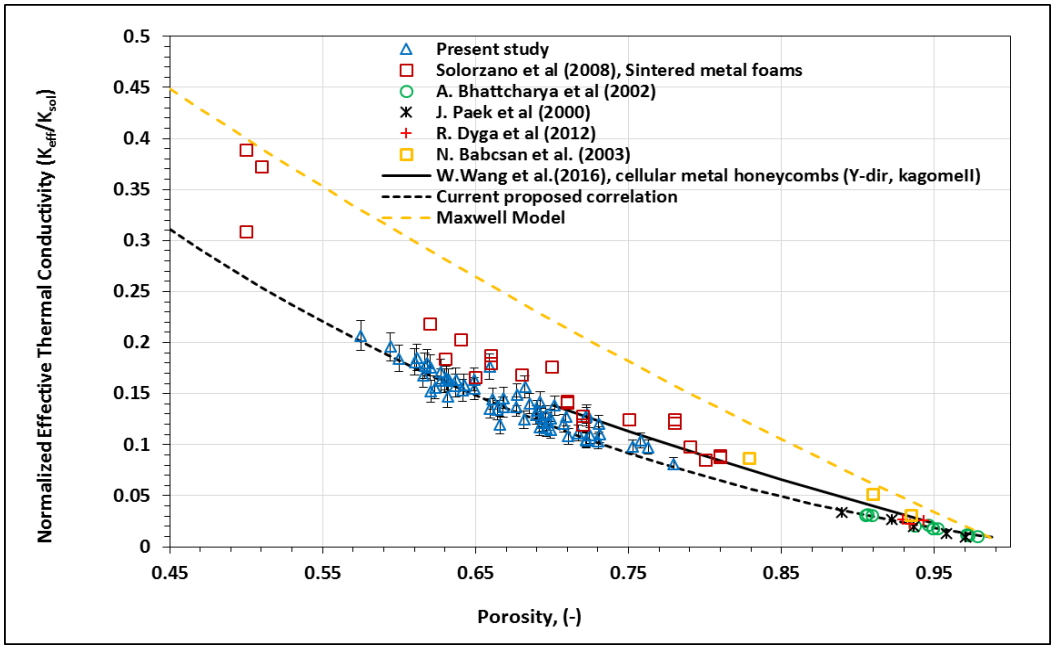

Figure 6-9 Predicted effective thermal conductivity by modified scaling relationship versus porosity

Shown in Figure 6-10 is selected experimental data with the proposed empirically derived scaling law given in Equation 6.19. The agreement with all three forms of porous material is considered to be good. There is some deviation with the 'low' porosity sintered metal foams (which are closed cell) [34] which had a slightly higher ETC than the open celled materials most likley due to the structural difference.

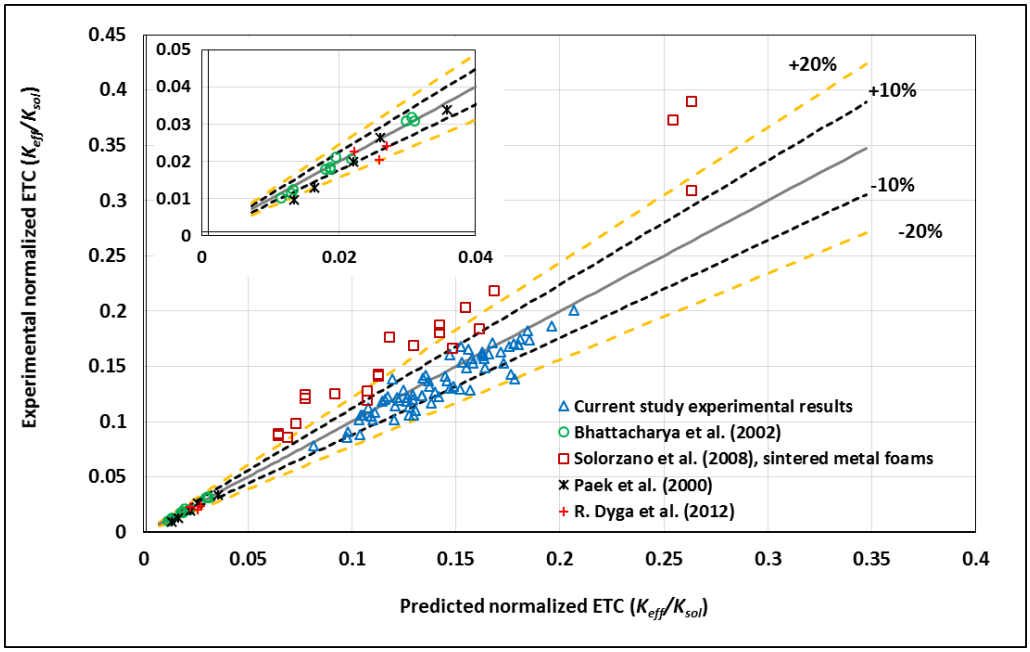

Figure 6-10 Predicted versus experimental ETC

Also shown in Figure 6-9 is the prediction by an analytical expression for cellular metal honeycombs [305]. Here, the thickness and height of the solid material decreases in proportion as the porosity increases, as the cells become smaller and the walls thinner. The reduction in effective thermal conductivity with porosity is more linear in this situation. It should be noted that these results are only applicable for unidirectional heat transfer and that there is a different correlation for heat transfer in alternative planes. In contrast, the high porosity metal foams (ε>0.9) are characterised by thickened intersections with thinner walls resulting in relatively lower values of ETC than might be expected if the material was distributed evenly in the matrix.

The empirical expression derived here clearly has its limitations. However, it provides better agreement with the full range of experimental data than the existing analytical expressions. While methods that make links between the structure and its behaviour clearly have great potential to yield understanding of the mechanisms and could lead to accurate predictions, accessing all of the required parameters experimentally can be challenging. Structural differences inherent in different manufacturing techniques (e.g. the thin strut thicknesses seen in the high porosity investment cast foams), and changes in structure over large ranges of porosity, mean that a general correlation for ETC will be difficult to achieve.

6.3 Uncertainty analysis

The possible uncertainties in measured parameters result in an accumulative error in the ETC. As the porosity has a strong influence on the ETC, this will also be determined. The error in porosity, can be expressed as a function of geometrical dimensions and the mass of the sample.

$$\varepsilon = f(L_s, A_s, m_s) \qquad 6.20$$

Where the important parameters are cross sectional area (A_s), length (L_s) and mass (m_s) of the sample. The uncertainty of the porosity can be estimated as [18, 159, 181, 301] as:

$$\frac{\delta\varepsilon}{\varepsilon}=\sqrt{\left(\frac{\delta A}{A}\right)^2+\left(\frac{\delta L_s}{L_s}\right)^2+\left(\frac{\delta m_s}{m_s}\right)^2} \tag{6.21}$$

The key parameters in error in ETC are uncertainty in upper and lower heat fluxes (Q_I, Q_{II}), the geometrical dimensions of the samples and temperature differences (ΔT) as

$$Q_s = f(L_s, A, Q_I, Q_{II}, \Delta T) \tag{6.22}$$

Therefore, the uncertainty can be found as

$$\frac{\delta Q_s}{Q_s}=\sqrt{\left(\frac{\delta A}{A}\right)^2+\left(\frac{\delta L_s}{L_s}\right)^2+\left(\frac{\delta Q_I}{Q_I}\right)^2+\left(\frac{\delta Q_{II}}{Q_{II}}\right)^2+\left(\frac{\delta \Delta T}{\Delta T}\right)^2} \tag{6.23}$$

Considering the relation which used to calculate the effective thermal conductivity the related parameters can be expressed as follows

$$K_{eff} = f(L_s, A, Q_s, \Delta T) \tag{6.24}$$

Then the uncertainty of the effective thermal conductivity can be as

$$\frac{\delta K_{eff}}{K_{eff}}=\sqrt{\left(\frac{\delta A}{A}\right)^2+\left(\frac{\delta L_s}{L_s}\right)^2+\left(\frac{\delta Q_s}{Q_s}\right)^2+\left(\frac{\delta \Delta T}{\Delta T}\right)^2} \tag{6.25}$$

The uncertainties of parameters which were used in the valuation of effective thermal conductivity are tabulated in Table 6-4. From the above calculation the uncertainty of the porosity was found <1.8% and the uncertainty of the effective thermal conductivity <6.1%. The test rig was examined by the three known material, aluminium, brass and steel. The deviation compared with published values [254] was found <1.5%, < 2% and 5% respectively.

Table 6-4 Uncertainties of parameters

Parameter	Uncertainty
Sample length (L_s)	0.4%
Sample Area (A)	0.8%
Sample Weight (m_s)	0.25%
Porosity (ε)	1.8%
Temperature Difference (ΔT)	0.25°C

Chapter 7

7. Convective heat transfer experimental results and discussion

The thermal performance of different classes of porous material is generally presented by plotting the thermal parameters against pore Reynolds number. The pore velocity can be obtained by using the sample porosity (ε) [23, 47, 122]. However in section 3.1 the permeability based Reynolds number was used due to uncertainty in the definition of the pore size. Both will be presented here.

$$Re_{dp} = \frac{\rho_f V_f d_p}{\mu_f \varepsilon} \quad 7.1$$

$$Re_K = \frac{\rho_f V_f \sqrt{K}}{\mu_f \varepsilon} \quad 7.2$$

The heat transfer area of the metal foams was obtained by assuming the pores were spherical with an average pore diameter of the preform salt. For the steel balls samples the surface area of one ball was calculated and multiplied by the number of balls. The heat transfer area for the mesh wire screens was a function of porosity, sample thickness (L), frontal area (A_f) and wire diameter (d_w) and can be obtained as [229].

$$A_h = \frac{4\, A_f L(1-\varepsilon)}{d_w} \quad 7.3$$

The volumetric heat transfer coefficient is typically expressed in dimensionless form as the pore Nusselt number [47, 122, 198, 199].

$$Nu_{Vdp} = \frac{h_V d_p^2}{K_f} \quad 7.4$$

The thermal conductivity of the air (K_f) was taken at average of inlet and exit fluid temperatures.

7.1 Number of transfer units

The thermal experimental results are first presented in terms of NTU_m against permeability based Reynolds number. The number of transfer units is the indicative parameter to assess thermal performance of heat exchangers and thermal regenerators. It is a measure of the amount of energy transferred from the fluid to

the matrix or vice versa. Three different classes of porous material were examined, including four different pore size metal foams, mesh wire screens and steel balls packed beds. Shown in Figures 7-1 to 7-5 are the number of transfer units results against permeability based Reynolds number for all different classes of porous media.

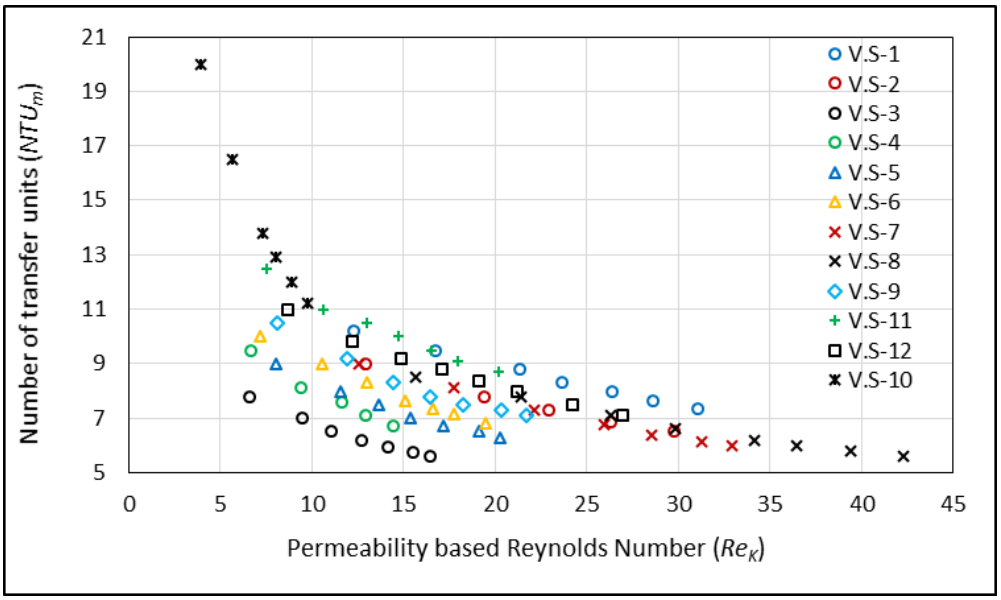

Figure 7-1 Very Small samples NTUm against Reynolds number based Permeability

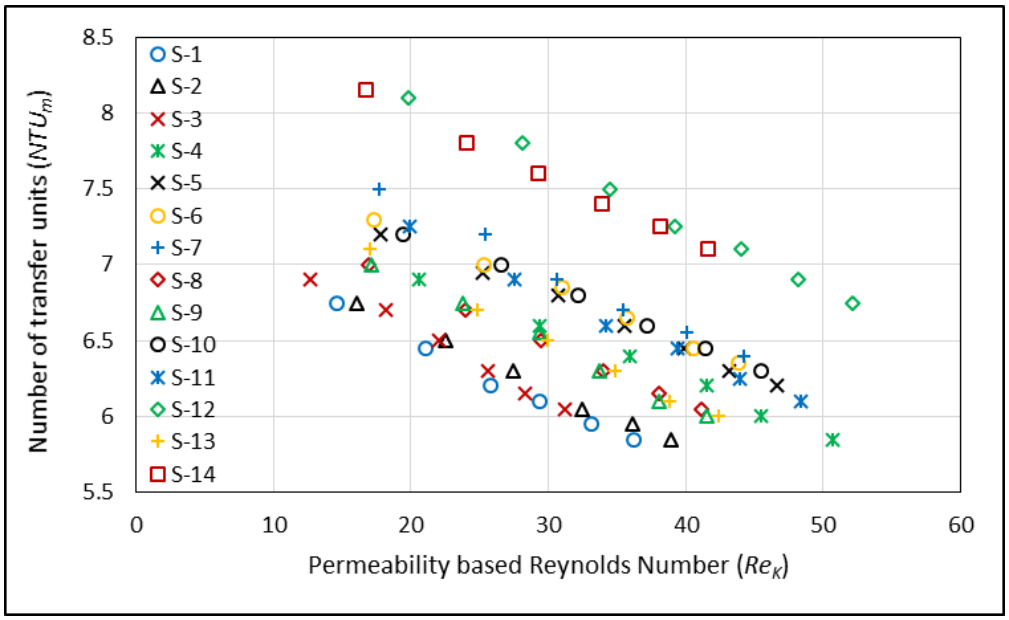

Figure 7-2 Small samples NTUm against Reynolds number based Permeability

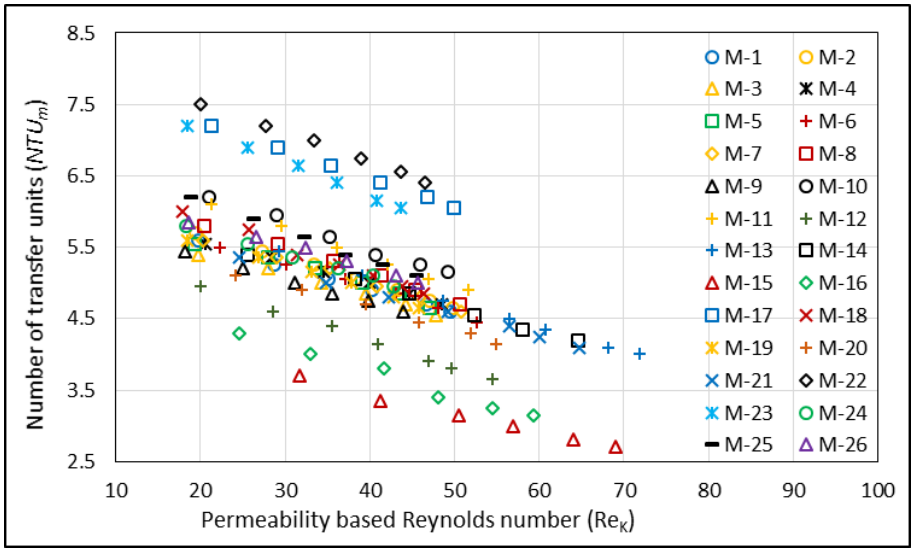

Figure 7-3 Medium samples NTUm against Reynolds number based Permeability

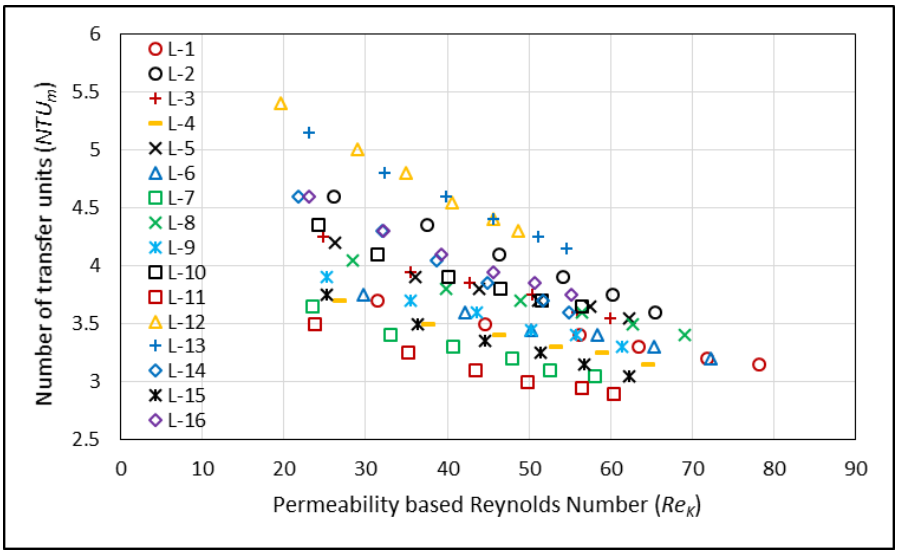

Figure 7-4 Large samples NTUm against Reynolds number based Permeability

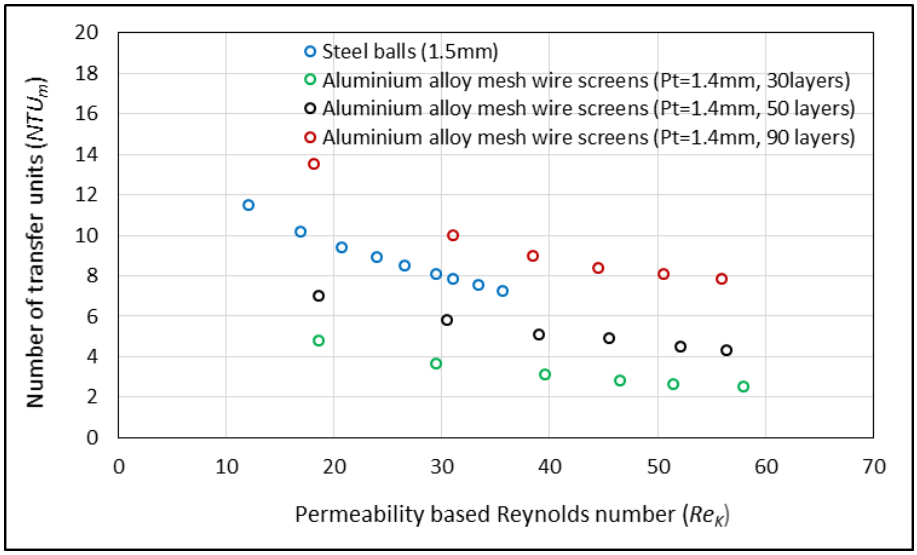

Figure 7-5 Steel balls and mesh wire screens samples NTUm against Reynolds number based Permeability

The NTU_m was found to decrease with Reynolds number [8, 194]. The NTU_m is an indicative measure of the amount of energy transferred from the fluid to the matrix or vice versa. As the flow rate increased so did the content energy but the heat transfer area of the core matrix remained constant so the relative heat transfer was lower.

It can be seen that NTU_m increased with decreasing of the pore size as the smallest pore size samples provided higher heat transfer area. Although the interstitial velocity also increased with the decreasing in pore size and this would also enhance the heat transfer. In the case of the packed bed of steel balls the total heat capacity was higher due to its higher density (lower porosity) compared to the other samples. For this reason it had a relatively high NTU_m as it was able to absorb more energy than the aluminium metal sponges. In the case of mesh wire screens, the NTU_m increased with number of layers as the result of increase in the total thermal capacity in terms of mass and heat transfer area.

7.2 Convective heat transfer coefficient

The thermal performance of porous media can be presented in terms of wall and volumetric convective heat transfer coefficients. In order to obtain the convective heat transfer coefficients the specific area per unit volume and the heat transfer area should be known. The area of replicated aluminium sponges is calculated based upon the average value of the preform salt diameter, porosity, and the dimensions of the sample. Once the specific area (area per unit volume) and heat transfer area are known the convective heat transfer coefficients can be obtained by Equations 2.16 and 2.17. Shown in Figures 7-6 to 7-10 are the volumetric heat transfer coefficients against the permeability based pore Reynolds number.

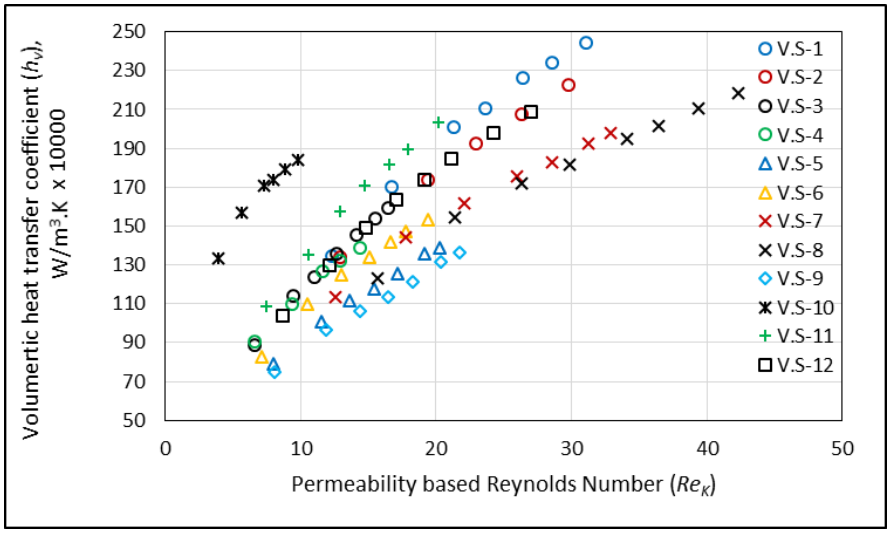

Figure 7-6 Volumetric heat transfer coefficient against permeability based Reynolds number (Very Small pore size samples)

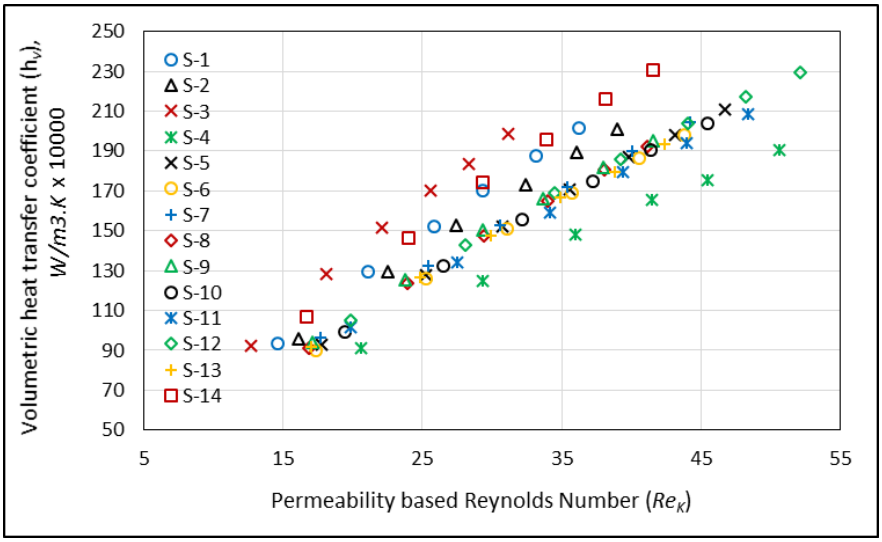

Figure 7-7 Volumetric heat transfer coefficient against permeability based Reynolds number (Small pore size samples)

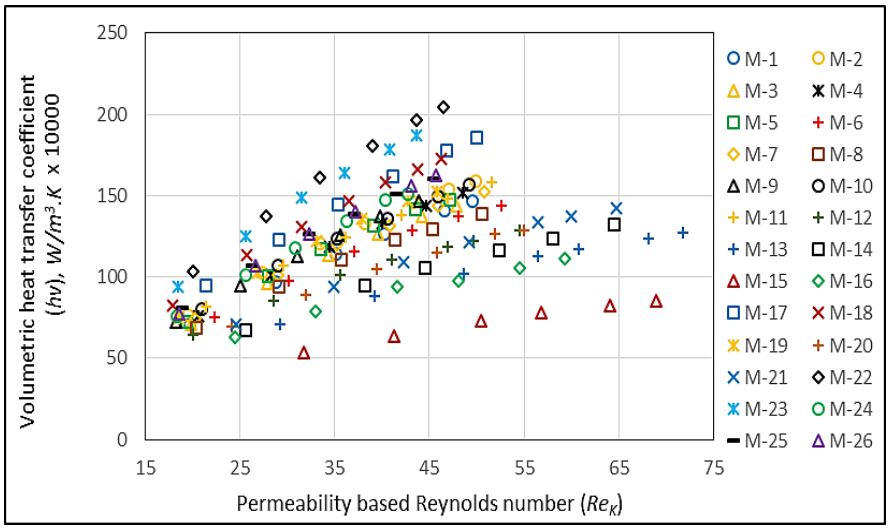

Figure 7-8 Volumetric heat transfer coefficient against permeability based Reynolds number (Medium pore size samples)

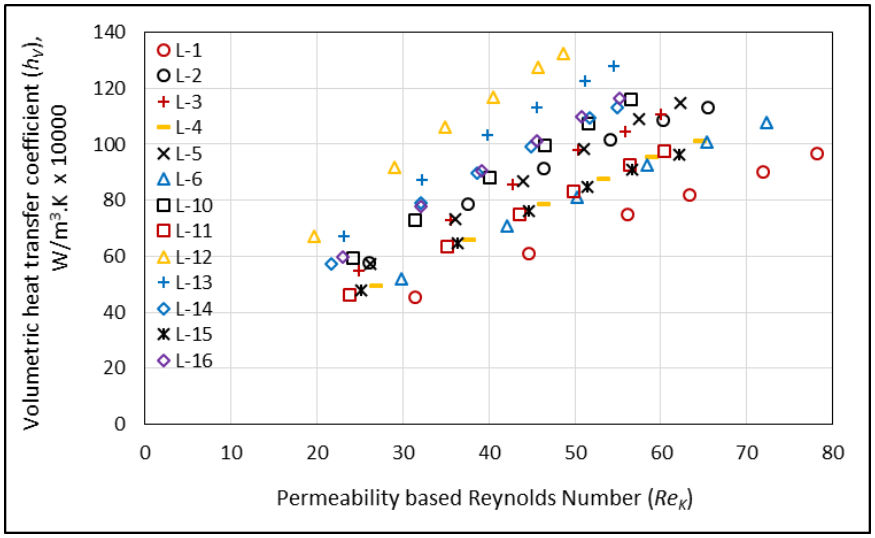

Figure 7-9 Volumetric heat transfer coefficient against permeability based Reynolds number (Large pore size samples)

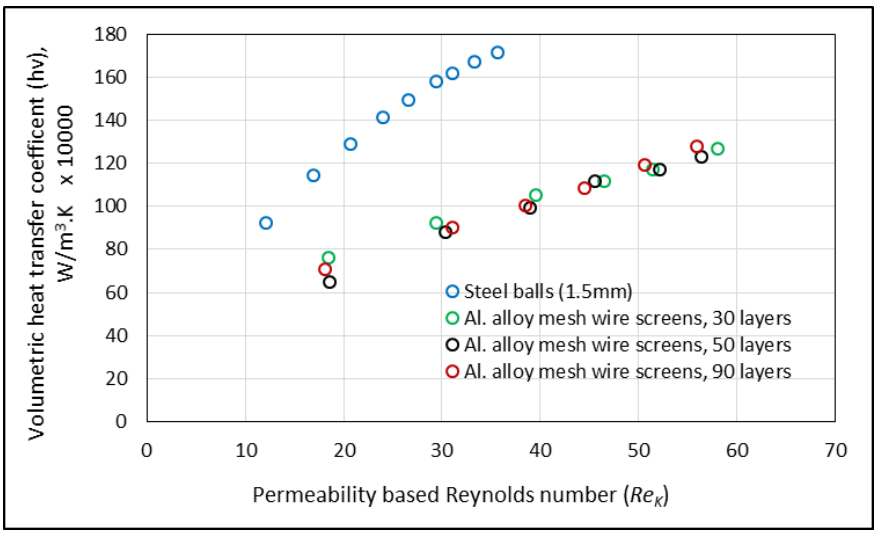

Figure 7-10 Volumetric heat transfer coefficient against permeability based Reynolds number (Steel balls and mesh wire screens samples)

As the Reynolds number increased the volumetric heat transfer coefficient increased. With increasing pore size the volumetric heat transfer coefficient decreased, although the values of h_v for the Small and Very Small samples were similar; hence, as the pore size decreased the h_v increased. The increase in volumetric heat transfer coefficient with decrease of pore size or particle diameter and porosity was also reported in open literature [5, 48]. For the mesh wire screens samples no effect of varying the number of layers on h_v was found as the specific area and the microstructure parameters were the same. At the same Reynolds number the steel ball sample had higher h_v due to its relatively high specific area.

The thermal performance of the porous materials can also be described by the wall convective heat transfer coefficient (*h*). This parameter is an indication of the heat transfer per unit area at certain temperature difference. Shown in Figures 7-11 to 7-15 is *h* as a function of permeability based Reynolds number.

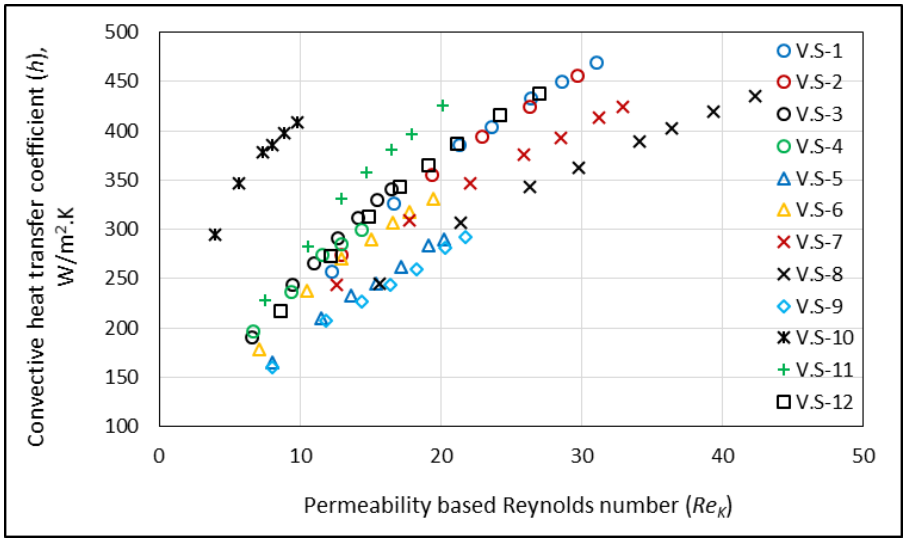

Figure 7-11 Heat transfer coefficient against permeability based Reynolds number (very small samples)

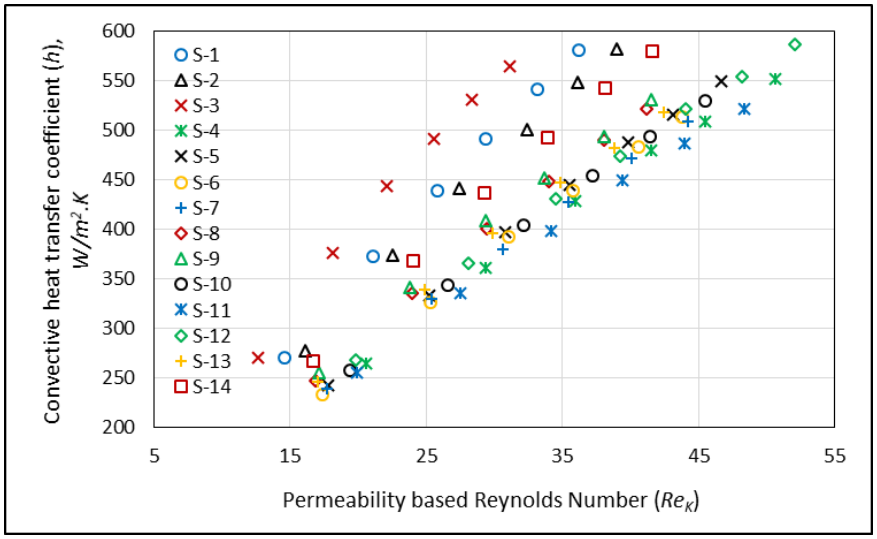

Figure 7-12 Heat transfer coefficient against permeability based Reynolds number (small samples)

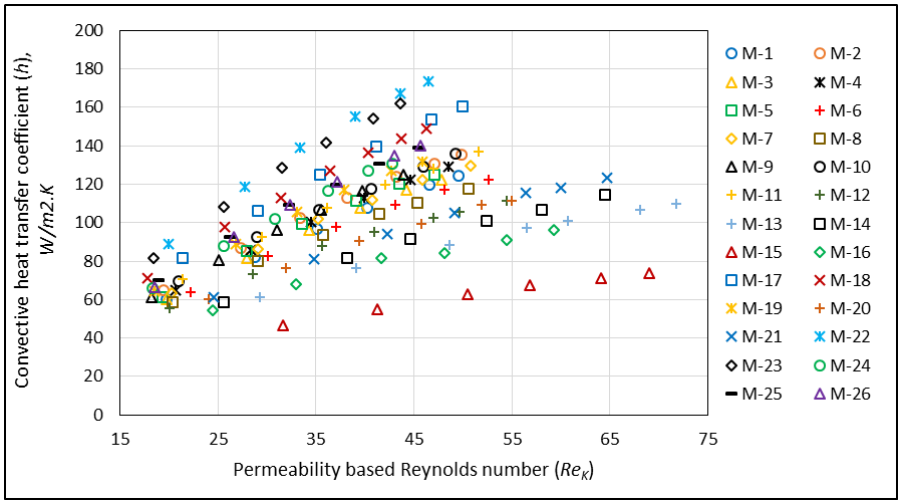

Figure 7-13 Heat transfer coefficient against permeability based Reynolds number (medium samples)

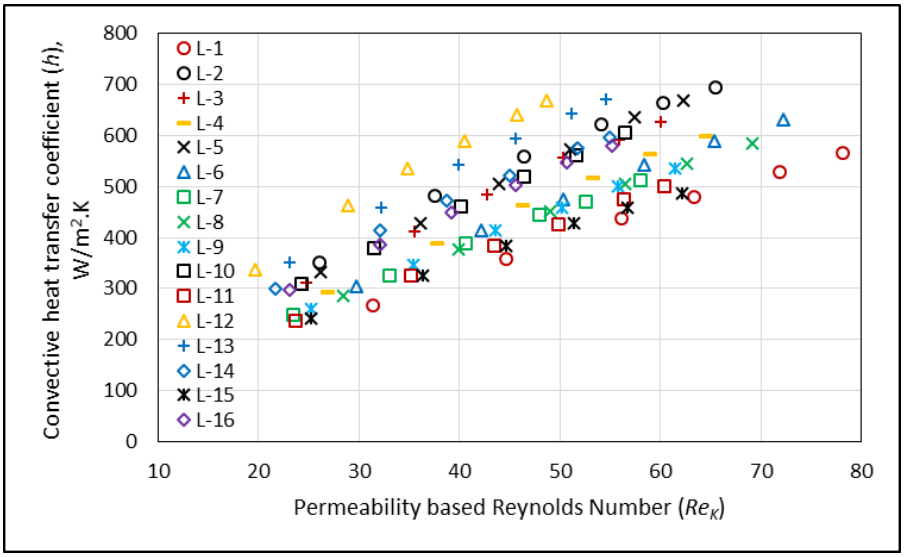

Figure 7-14 Heat transfer coefficient against permeability based Reynolds number (large samples)

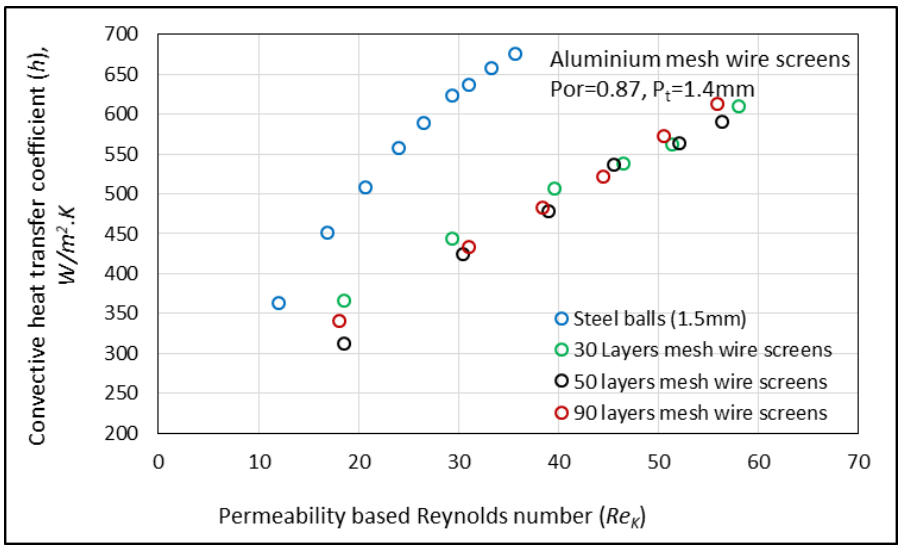

Figure 7-15 Heat transfer coefficient against permeability based Reynolds number (steel balls and mesh wire screens samples)

The same trend as for the volumetric heat transfer coefficient has been observed for convective heat transfer coefficient. And both volumetric and wall heat transfer coefficients increased with the decrease of porosity. Some scattered data were found in the pressure drop and will be discussed in the next chapter. These scattered data were the result of the manufacturing defects and differences in pore shape and porosity.

7.3 Effect of microstructure parameters on convective heat transfer coefficient

The microstructure parameters (porosity, pore size) were observed to play a measurable role in heat transfer phenomena in metal foams. An increase in the convective heat transfer coefficient with decreasing of porosity and increasing of PPI (decrease of pore size) has been reported by a number of authors [47, 64, 199, 202]. Shown in Figure 7-16 is the effect of porosity on the convective heat transfer coefficient at certain mass flow rate per unit area (G). This value of mass flow rate is 7.0 g/s in current experiments. Decreasing the porosity and pore diameter increases the specific area and thus the heat transfer area. Also the decrease of both these geometrical parameters increases the pore velocity. This increase of both heat transfer area and pore velocity resulted in increase of convective heat transfer coefficient.

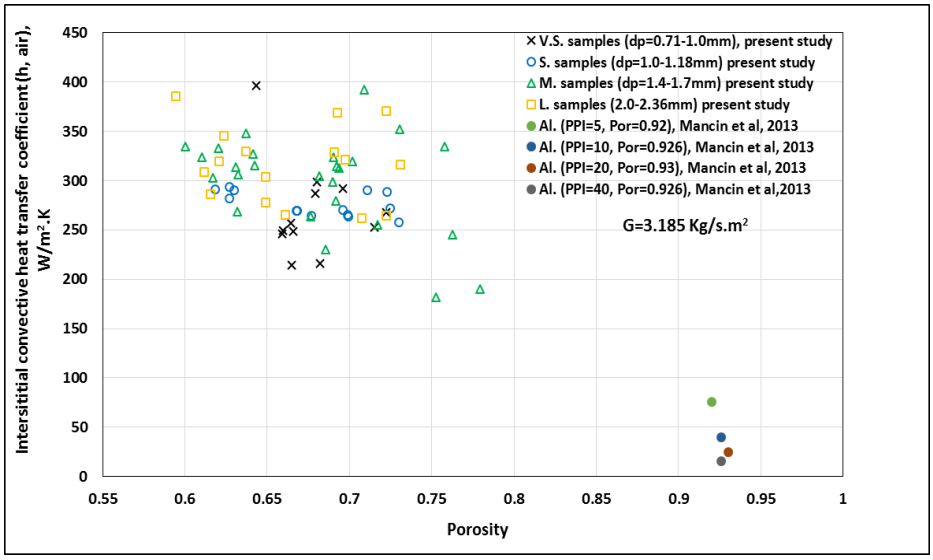

Figure 7-16 Effect of porosity on convective heat transfer coefficient

The scattering in the reported data in Figure 7-16 is the result of the pore diameter and shape differences and manufacturing defects.

The volumetric heat transfer coefficient (h_v) is widely used to assess the thermal performance of porous material. Shown in Figure 7-17 is volumetric heat transfer coefficient (h_v) against pore Reynolds number for all the current samples.

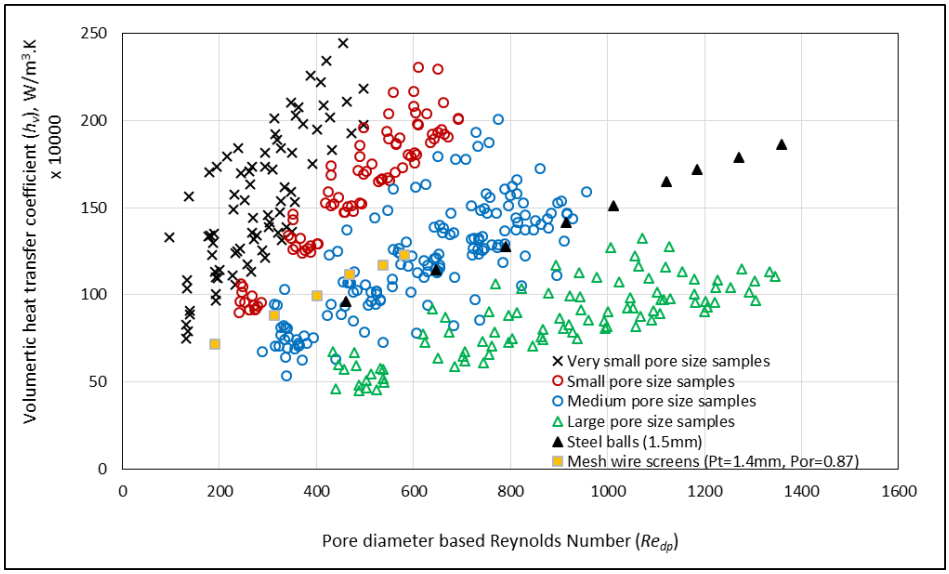

Figure 7-17 Volumetric heat transfer coefficient against pore Reynolds number for different classes of porous media

The characterization of convective heat transfer in reticulated materials is frequently reported in terms of volumetric heat transfer coefficient. This is because measuring the specific area of cellular reticulated porous material is difficult [11, 186]. The increase in h_v with the decrease of porosity and pore size as a result of the increase of pore velocity and specific area has been reported [48, 69, 122]. The samples with the highest value of h_v are the Very Small pore size (0.71-1.0mm) samples and they have a higher h_v four times that of the large pore size samples at the same a Re_{dp} ~ 400. At the same Re_{dp} they also provide h_v approximately two times higher than those provided by steel balls and mesh wire screens.

The comparison of h_v for the current samples with those in the literature is shown in Figure 7-18 in order to show the effect of pore density (or pore size) and porosity on h_v. It appears the samples from the current study have a higher h_v compared with more open metallic foams reported in the literature due to their higher porosity. The effect of porosity also can be noticed from the tested samples by Hwang et al. [122]. The increase in h_v with increase of PPI at fixed porosity is clear from examined samples of Fu et al. [186], Vijya et al.[203], Kamiuto et al.[198], Ando et al. [200] and Xia et al. [48].

Figure 7-18 Volumetric heat transfer coefficient versus frontal velocity

In contrast, the contradiction in the results of two samples with same porosity (0.87) and PPI (10) was reported by Younis et al. [199] and Vijay et al. [203]. This was explained as the difference in the thickness that resulted in an important entrance effect [122, 203]. They were also produced with different techniques and with different pore diameter [203]. Therefore, the effect of pore diameter is more predominant on the convective heat transfer than porosity [203]. This can be also concluded from the comparison of current tested samples (low porosity) with samples with high porosity, namely, those examined by Fu et al. [186] with pore diameter 1.25 mm and Calmidi et al. [69] with pore diameter 1.8mm.

The method of measuring the h_v whilst transient or steady state is the possible source of the contradiction in the reported results, due to transverse temperature distribution as stated by Fuller et al. [47], when the same samples of Calmidi et al. [69] and Hwang et al. [122] were compared. In the steady state technique the temperature in the centre of the samples is less than that of the substrate wall at the source of the heat. The effect of the base material type on h_v has been found not that substantial when the Ni, Sic and Cu foams were examined at the same conditions and with the same geometrical parameters [48].

Shown in Figure 7-19 is the effect of porosity on the volumetric heat transfer coefficient. Increasing the porosity and the pore size reduced the volumetric heat transfer coefficient. This is attributed to lower specific area and pore velocity and can also result in changes of the ligament shape and thickness. The effect of pore and fibre shape on the convective heat transfer has been reported in open literature in terms of cell inclination and ligament tapering [52, 245]. In the current study, the samples with spherical pore shape provide higher volumetric heat transfer coefficients than those of irregular pore shape. This can be attributed to the differences in fibre shapes and the irregular pore samples having less pore velocity due to higher window size. The heat transfer area provided by the spherical pores is higher than that provided by the irregular pores. For the same causes the samples with small pore size provide higher thermal performance.

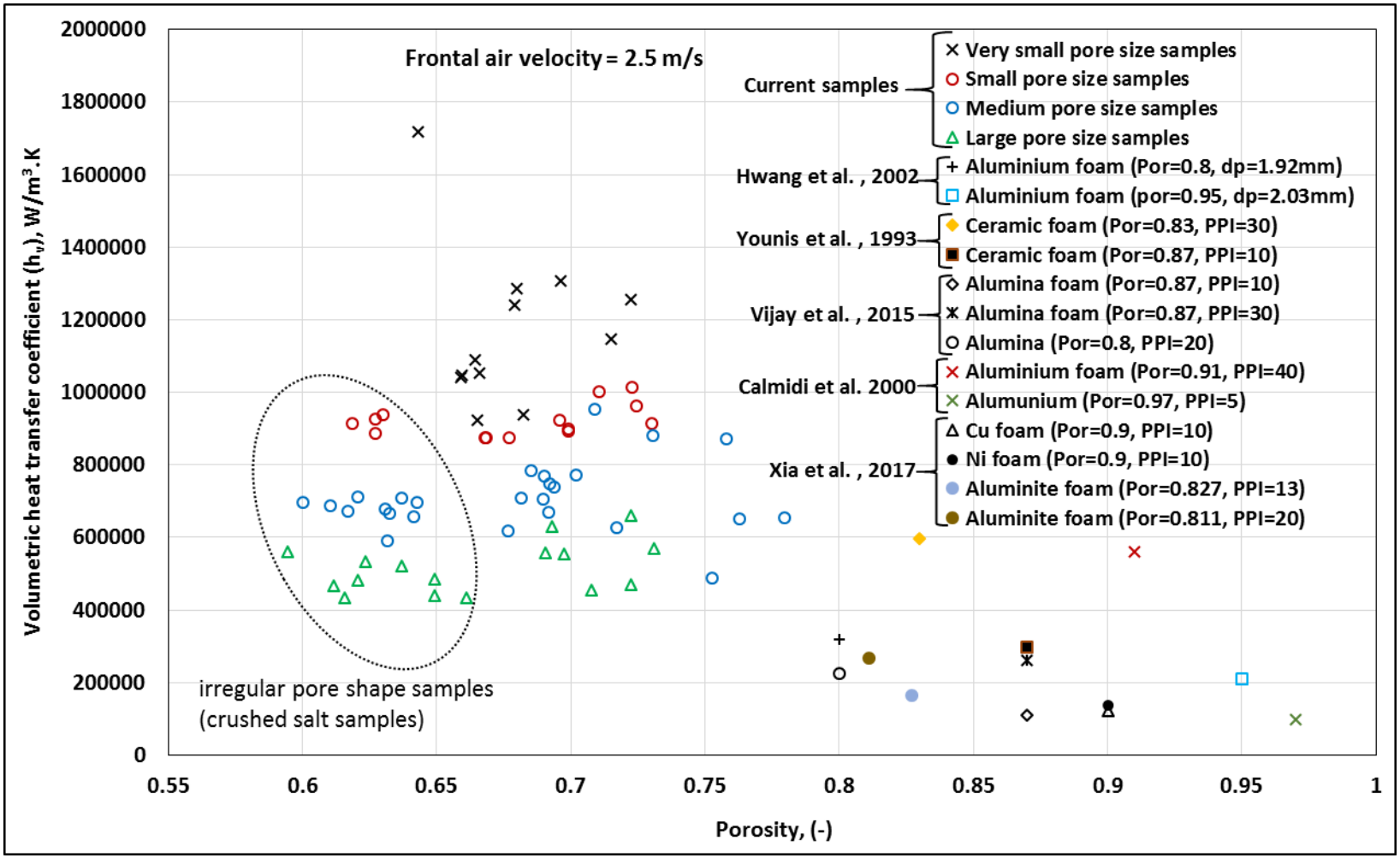

Figure 7-19 The volumetric heat transfer coefficient versus porosity

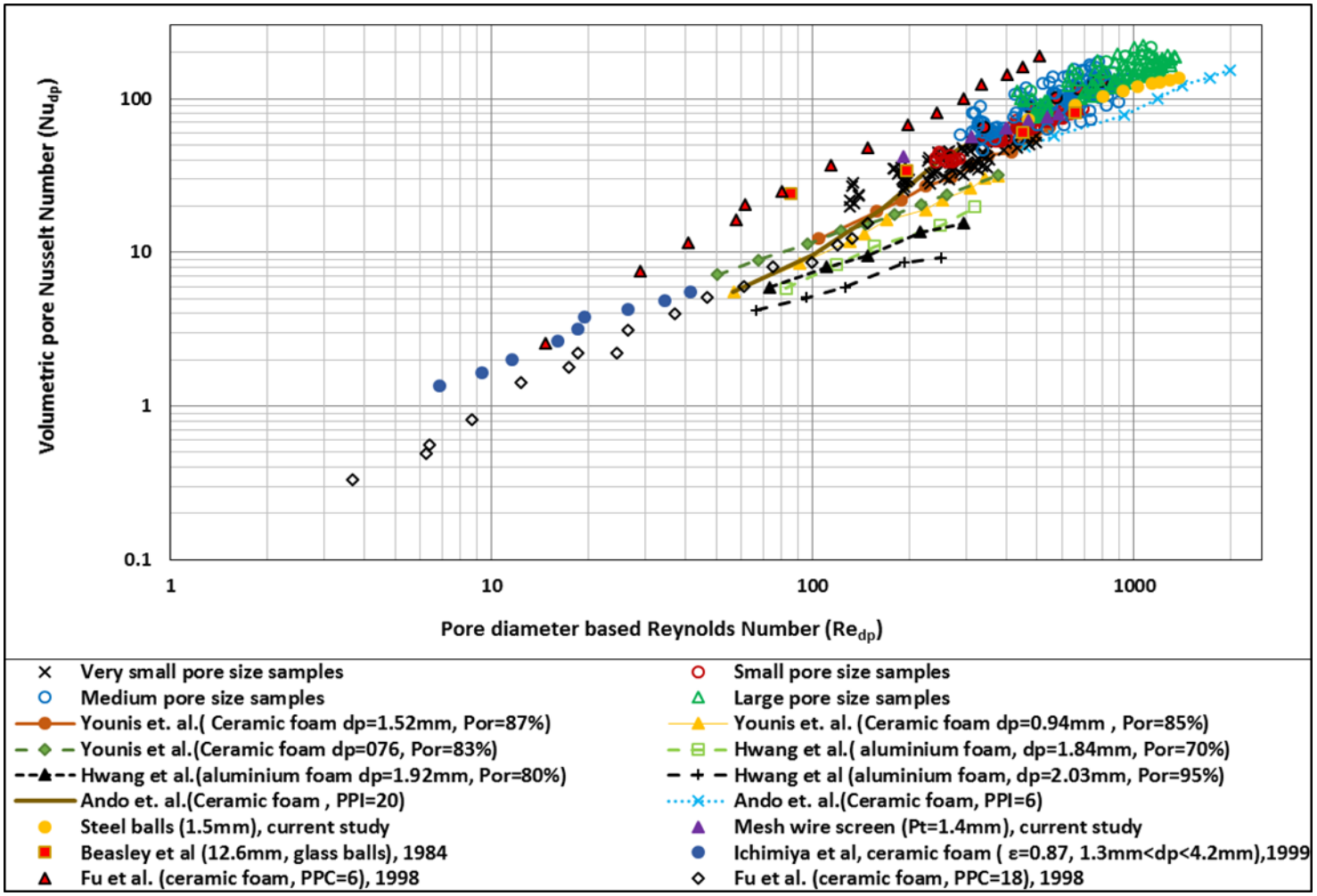

Figure 7-20 Volumetric Nusselt number against pore Reynolds number

The usual non-dimensional form to illustrate the volumetric convective heat transfer coefficient is pore volumetric Nusselt number (Nu_{vdp}) [5, 48, 122, 199, 203, 218]. Although a number of attempts have been made to generalise a relation of Nusselt number as function of pore Reynolds and Prandtl numbers, the differences in morphological structure due to different manufacturing methods prevented such efforts. Some of these correlations have been examined by Xia et al. [48] who found the deviation for some was as high as 100%, while the minimum deviation was found by Dietrich [201] to be about 30%. The Figure 7-20 shows the Nu_{vdp} against the pore Reynolds number.

The results show the agreement between the packed beds of balls, mesh wire screens packed beds and aluminium sponges over this range of Re_{dp} in this study. At low Reynolds number, agreement is not satisfactory between the metal foams and packed beds of balls regarding the Beasley et al. [9] results. A satisfactory validation can be observed between the current aluminium foams and the ceramic sponges examined by Ando et al. [200], Younis et al. [199] and Ichimiya et al. [218]. An unsatisfactory agreement was noticed with the aluminium sponges results studied by Hwang et al. [122]. This can be attributed to the fact that the ceramic sponges and aluminium sponges produced by replication resemble each other in structure. Whereas, the Hwang et al. [122] samples are Duocel and their cell shape and ligaments are different and produced with a different technique. Also the source of the contradiction in results is inconsistency of the characteristic length used in Nu_{vdp} and Re_{dp}. The pore mean diameter is used in some studies [122], while Fu et al. [186] used the pore diameter as function of porosity and PPI. There is also different interpretation in terms of considering pore diameter as actual pore diameter or window size [203].

7.4 Effective thermal conductivity impact on thermal characteristics and effectiveness

In the relatively low porosity materials manufactured in this study the thermal conductivity may have a significant impact on the heat transfer between fluid and solid. When the thermal conductivity of the solid material is high, the heat conduction through the solid matrix reduces the temperature difference between

the fluid and matrix. In order to reduce the effect of thermal conductivity, a low thermal conductivity solid material can be used such as steel or ceramic. This was not practical in this case as using the replication technique for different materials than aluminium was not feasible, therefore samples were cut into slices. The small air gap between the slices works as thermal resistance with very low thermal conductivity (K_f) but the surface area of the samples is maintained constant. Electrical discharge machining (EDM) was used to cut the samples without damaging the ligament of pores as shown in Figure 7-21.

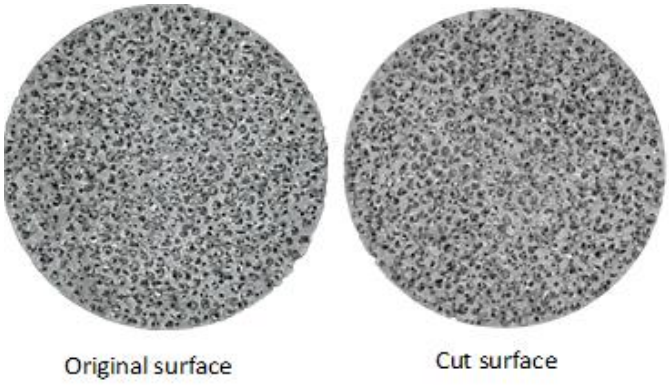

Figure 7-21 Surfaces of the cut samples

Three samples with different pore diameters were selected to study the effect of ETC on the NTU_m. The samples were cut into five equal slices with constant thickness of all slices. The thermal resistance due to the air gap can be described using an electrical resistance analogy as shown in Figure 7-22.

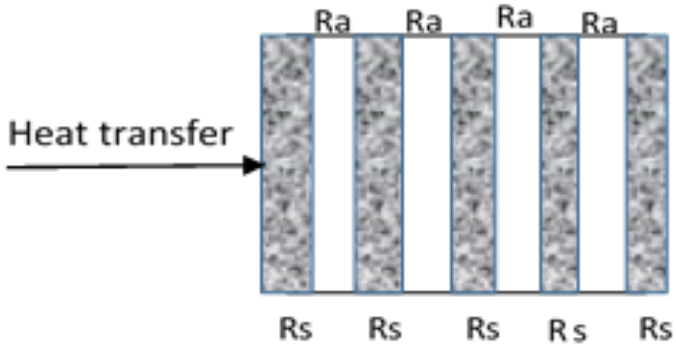

Figure 7-22 Electrical analogy of thermal resistances

The total thermal resistance (R_t) of the complex can be obtained by the summation of air gaps thermal resistance (R_a) and slice thermal resistance (R_s). The resistances R_s and R_a can be determined by the each slice thickness (t_s), the air gap thickness (t_f) and number of slices (N). The air gap was measured by measuring the

total length. If we assume the air gaps were of equal thickness and the slices were cut by equal length, the complex total thermal resistance can be obtained by the total of single resistances for air gap and slice sample as

$$R_a = \frac{t_f}{A_m K_f}, \qquad R_s = \frac{t_s}{A_m K_{eff}} \tag{7.5}$$

$$R_t = (N-1)\frac{t_a}{A_m K_a} + N\frac{t_s}{A_m K_{eff}} \tag{7.6}$$

Then the effective thermal conductivity of the complex (K_{effc}) can be obtained by R_t, cross section area of the sample (A_m) and total thickness of the complex (t_T) as

$$K_{effc} = \frac{t_T}{A_m R_t} \tag{7.7}$$

The number of slices plays a measurable role to reduce the effective thermal conductivity and to increase the overall thermal resistance. Hence, as the number of slices increased the number of the air layers increased and this resulted in lower effective thermal conductivity and higher thermal resistance. Shown in Figure 7-23 is the impact of number of slices on the effect thermal conductivity and thermal resistance of the complex (e.g. $K_{eff} = 26.37\frac{W}{m.K}$, t_T=*25.22mm*).

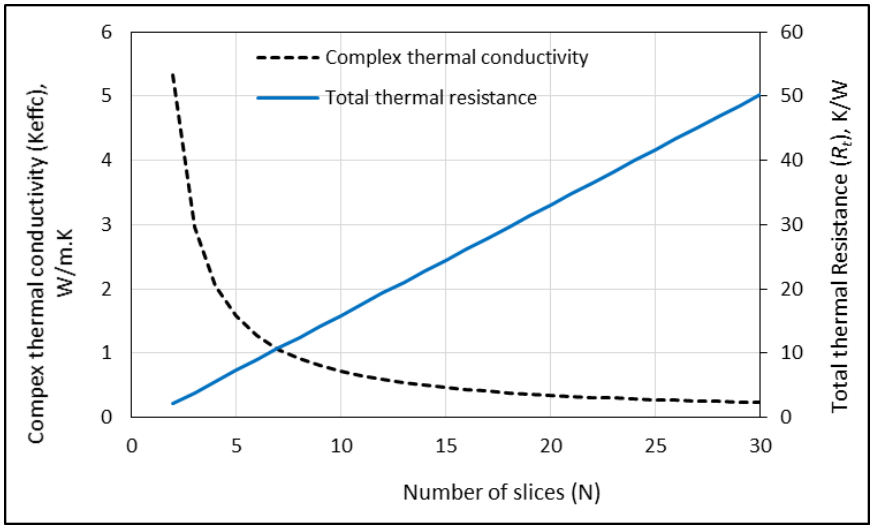

Figure 7-23 Effect of slices number on complex thermal conductivity

The effective thermal conductivity of the sliced samples was measured experimentally using the rig described in section 3.2. The results of the measured and calculated K_{effc} are shown in Table 7-1. From the results, the effective thermal

conductivity was reduced by 8 times for sample (V.S-1) and 15 times for sample (S-5) and sample (M-25).

Table 7-1 Geometrical and thermal conductivity values of porous material

Sample	Porosity	Pore diameter, mm	Original thermal conductivity	Sliced sample thermal conductivity, calculated	Sliced sample thermal conductivity, measured
V.S-1	0.723	0.71-1.0	21.45	1.69	2.6
S-5	0.696	1.0-1.18	26.37	1.57	1.7
M-25	0.702	1.4-1.7	28.20	1.67	1.8

Shown in Figure 7-24 and Figure 7-25 are the recorded exit fluid temperatures of an original and sliced sample.

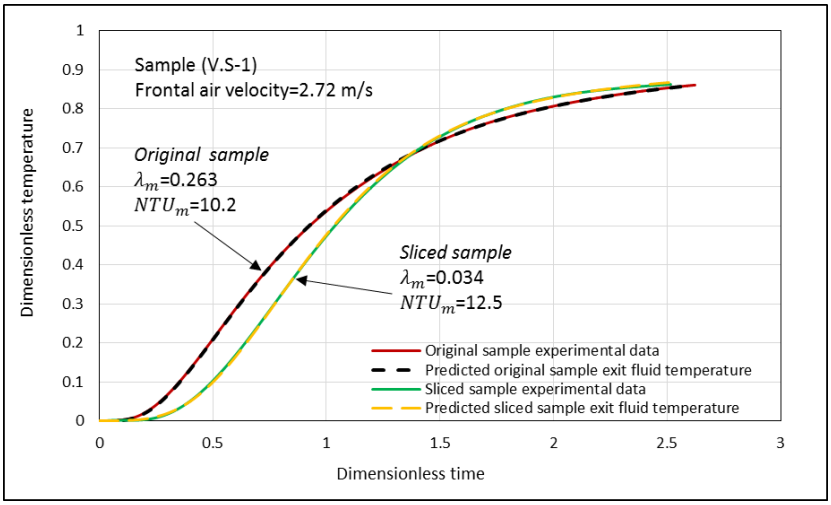

Figure 7-24 Dimensionless exit fluid temperature response (very small pore size sample)

As can be seen from both Figure 7-24 and Figure 7-25, the exit fluid temperature of the sliced samples increased sharply compared with that of lower thermal conductivity.

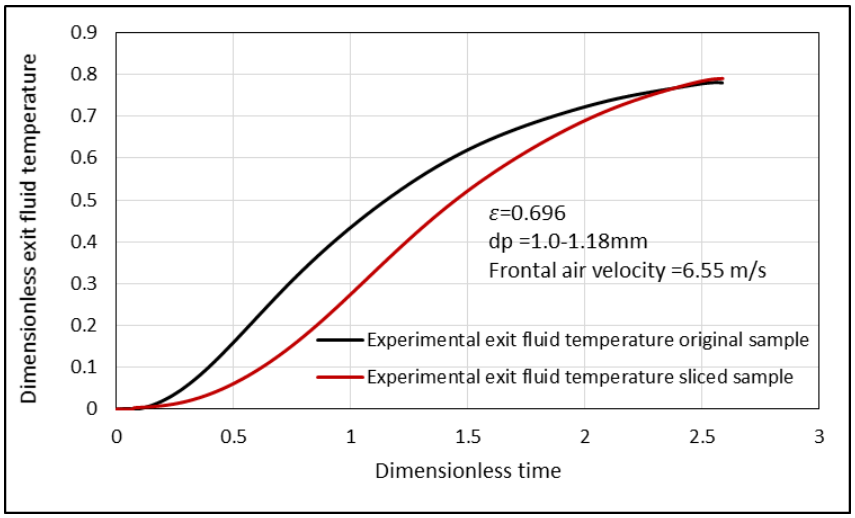

Figure 7-25 Dimensionless exit fluid temperature response small pore size sample)

In the case of the original samples a significant portion of the heat was transferred by conduction between the neighbouring elements. As the pathway for conduction was reduced by slicing the samples, the convective heat transfer increased, driven by an increase in temperature difference between the matrix and fluid. The significance of this effect will depend on the flow rate. Shown in Figure 7-26 are the recorded and predicted exit fluid temperatures at high flow rates. Comparing Figure 7-24 and Figure 7-26 for the same samples, the effect of slicing the samples and hence the effect of conduction can be seen to have less influence at high flow rates.

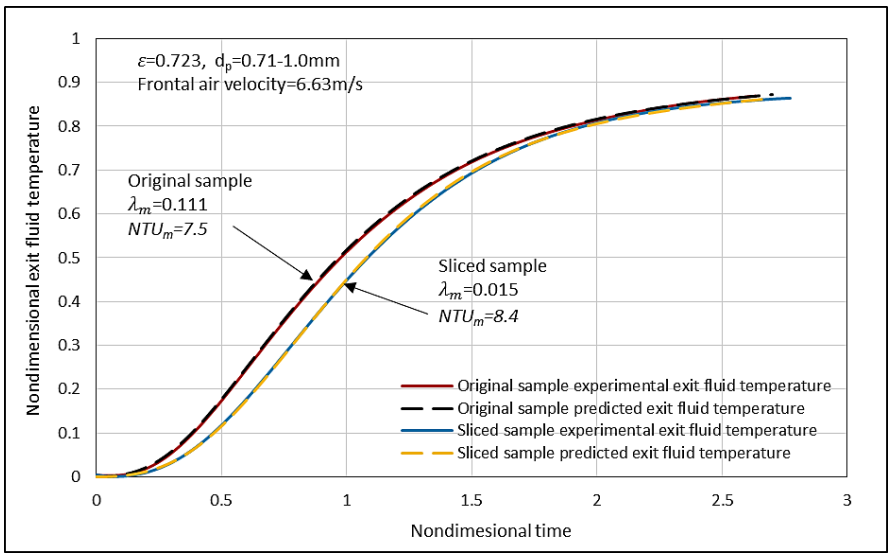

Figure 7-26 Dimensionless exit fluid temperature response

The number of transfer units of the three samples is presented against the Reynolds number based pore size in Figure 7-27, Figure 7-28 and Figure 7-29.

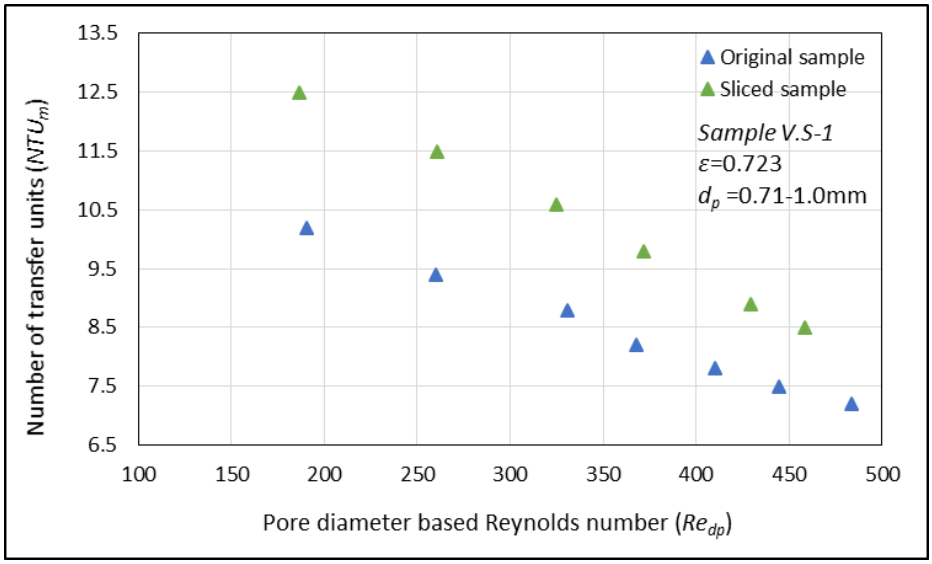

Figure 7-27 Effect of thermal conductivity on NTUm for sample V.S-1

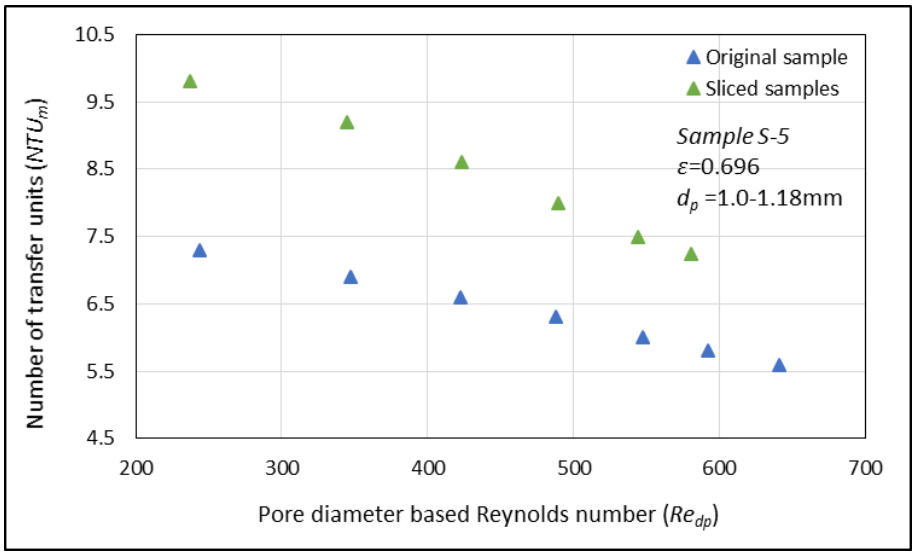

Figure 7-28 Effect of thermal conductivity on NTUm for sample S-5

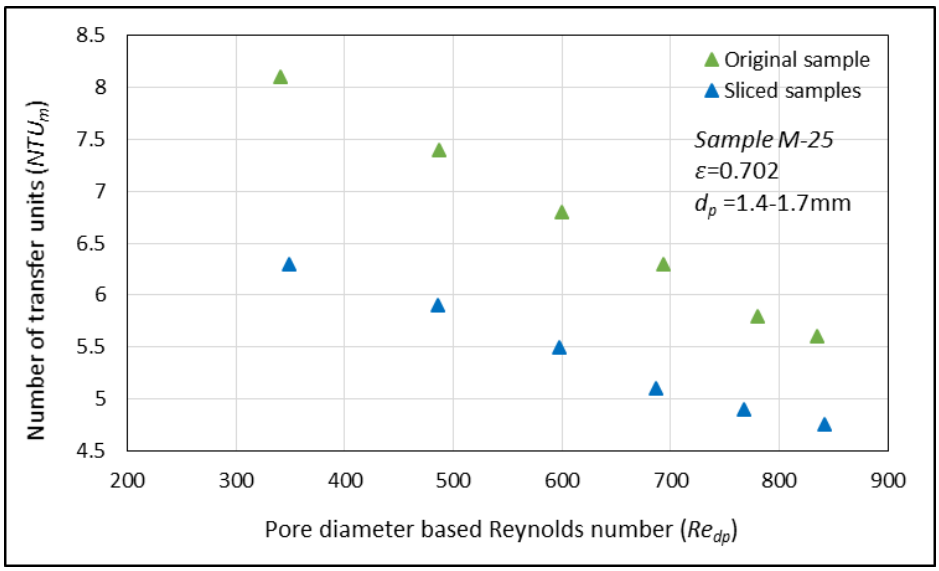

Figure 7-29 Effect of thermal conductivity on NTUm for sample M-25

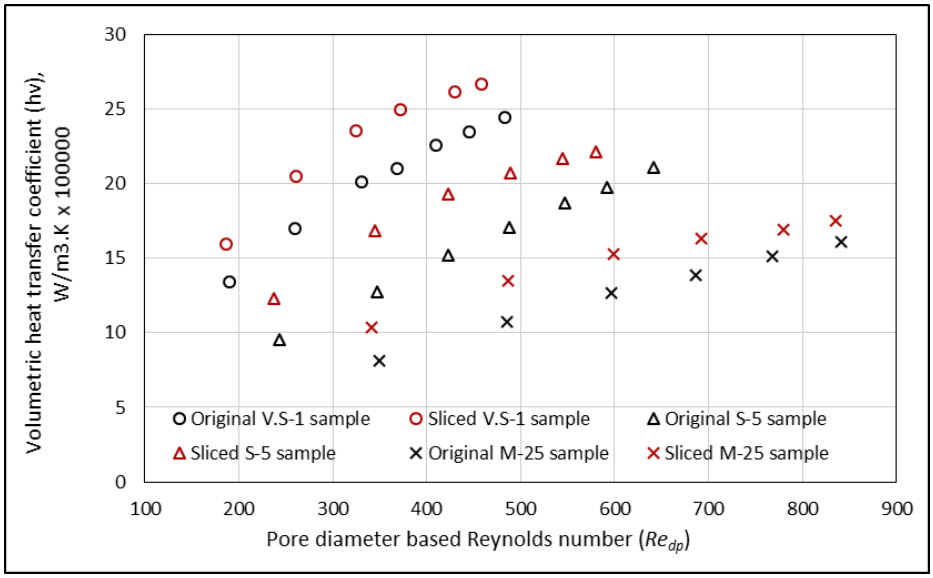

Figure 7-30 Effect of thermal conductivity on volumetric heat transfer coefficient

From Figure 7-27, for sample V.S-1, the NTU_m increased by 23% at a frontal air velocity of 2.72 m/s but increased by only 13% at 6.63 m/s. For sample S-5, shown in Figure 7-28, NTU_m increased by 34% at 2.64 m/s. Therefore the increase in convective heat transfer was most significant at lower flow rates. This is because the influence of thermal conductivity decreased with the increase of flow rate. The same scenario can be observed for the volumetric heat transfer coefficient as shown in Figure 7-29.

7.5 Convective heat transfer uncertainty analysis

The errors in number of transfer units and heat transfer coefficient are mainly from the deviation of the predicted and measured exit fluid temperatures. This difference can be found by considering the uncertainty of root-mean square (RMS). The maximum error (Rm) in RMS in temperature difference was found to be 8.5%. Starting with the number of transfer units uncertainty this can be summarised as

$$NTU_m = f(\dot{m}_f, \Delta T_f, K_{eff}, Rm) \qquad 7.8$$

The uncertainty of flow measured by the orifice plate was found to be 4.5% (see Chapter 4), the temperature uncertainty was <0.5% and for the thermal conductivity was found to be <6.1%. Therefore, the total uncertainty of $\mathrm{NTU_m}$ can be determined as

$$\frac{\delta NTU_m}{NTU_m} = \sqrt{\left(\frac{\delta \dot{m}_f}{\dot{m}_f}\right)^2 + \left(\frac{\delta \Delta T_f}{\Delta T_f}\right)^2 + \left(\frac{\delta K_{eff}}{K_{eff}}\right)^2 + (\delta Rm)^2} \qquad 7.9$$

By using the above known uncertainties, the $\frac{\delta NTU_m}{NTU_m}$ <11.4 %. The same procedure was followed to find the uncertainty of h_v.

$$h_V = f(NTU_m, V_S, C_f, \dot{m}_f) \qquad 7.10$$

Once the uncertainties of sample volume (V_S) and specific heat of the fluid were identified as 0.9% and 0.5% the uncertainty of h_V was found to be <11.45%.

Chapter 8

8. Microstructure and manufacturing defects effect on measured parameters

8.1 Introduction

For open cell metal foams the microstructure varies with porosity and manufacturing technique, with fibre thickness decreasing as the porosity increases [105]. The ligament cross section shape has been shown to change from circular at porosity 0.85 to an inner concave triangle at porosity 0.97 [18, 20, 32, 306]. Both the ligament shape and its cross section have a measurable impact on the pressure drop and heat transfer in metal foams [245, 306]. Both the inertia and drag form coefficients are sensitive to the roughness of the metal sponge. The roughness of foam is strongly based upon the shape of the fibre and cell size [105]. An increase in the ligament cross sectional area increases the conduction heat transfer.

There are three techniques to obtain material parameters in metallic foams [306]: experiments, numerical simulation based on the CT-Scan tomography of the real sample, and computational models based on the cell geometry. Due to the complexity and unrepeatability of the microstructure of foam cells, modelling based geometry is a challenging problem because of the inherent production defects in the microstructure of foams [38, 60, 307]. Evans et al. [308, 309] classified three kinds of defects in the microstructure as: lost or thin cell ligaments, bending cell struts, and the high relative density ranges due to inclusions. The main types of defects reported in the literature include: variation of strut thickness, irregularity in the cell size and shape, and wavy cell strut [60, 310-312]. Information is available about the effect of defects on the mechanical properties materials [60] but information is scarce about the impact on pressure drop and convective heat transfer [34, 172]. These defects might be the reason for the mismatch between the experimental results and the models [34, 313].

In the experimental results for this work significant scattering was noticed in the measured hydraulic and thermal parameters. In this chapter the detection of the manufacturing defects is discussed and their effect on microstructure, pressure drop, thermal conductivity and convective heat transfer coefficient determined. The

current replicated samples were produced using two types of infiltration salt: crushed and spherical, resulting in differences in cell and ligament shape. Image processing has been used to identify the defects and differences in microstructure parameters in terms of average window size and free flow area.

8.2 Defects identification and microstructure differences

Shown in Figure 8-1 are photographs of the faces of a sample demonstrating completely and semi closed cells. This defect was noticeable in low porosity spherical replicated metal foams infiltrated by spherical salt particles and is due to the high infiltration pressure that forced the melted aluminium to penetrate and close the contact point of spherical salt particles.

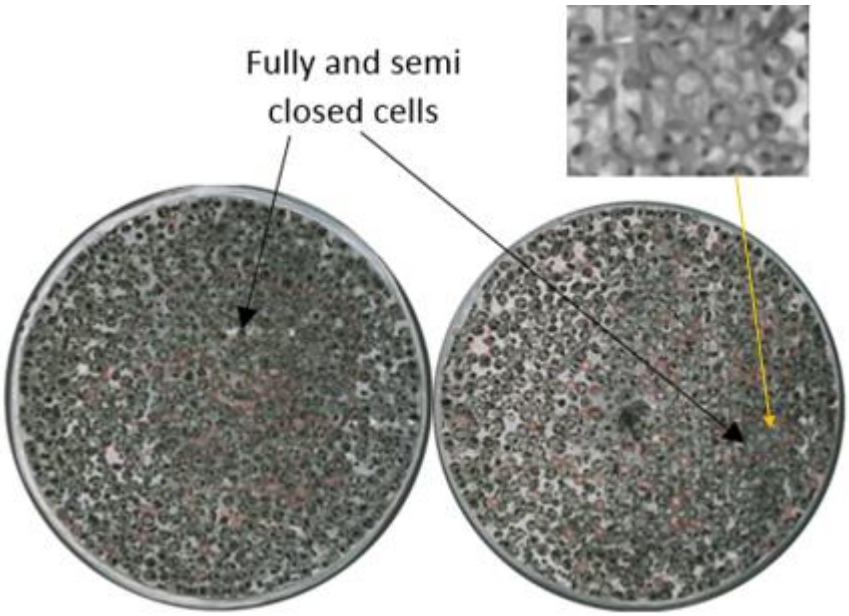

Figure 8-1 Scanned cross-sections for sample M-23

Another noticeable defect is the missing cells, an example of which can be seen in sample M-15, shown in Figure 8-2, which gave the lowest pressure drop in the medium group of samples. In the same figure sample M-21 is shown which has missing ligaments in some cells.

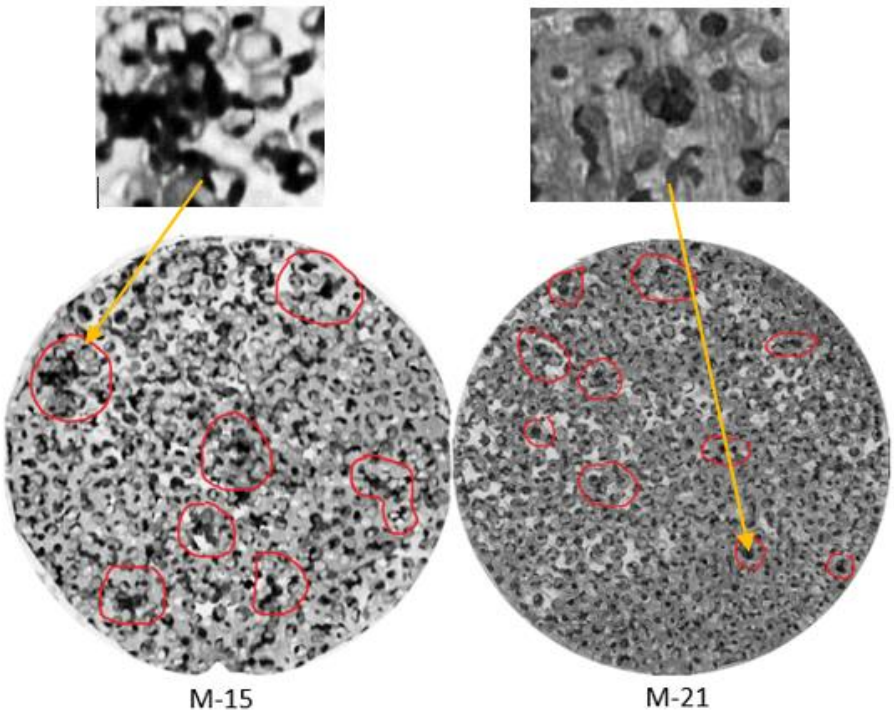

Figure 8-2 Missing cells and ligaments defects

The cell shape was found to impact on the presence of defects. Shown in Figure 8-3 are photographs of two large pore size samples with spherical (sample L-15) and crushed salt infiltration (sample L-2). The difference in pore shape can be clearly observed with L-2 exhibiting a more irregular structure.

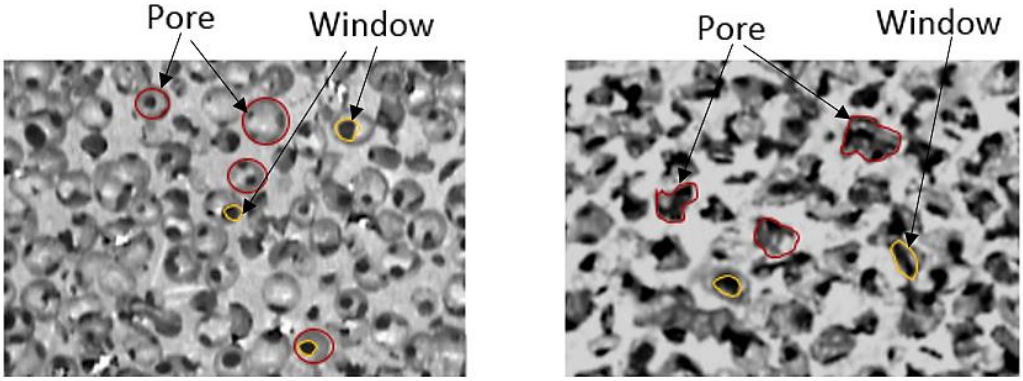

L-15 (Spherical pore shape) L-2 (Irregular pore shape)

Figure 8-3 Microstructure difference in samples

As the thickness and shape of the ligaments have been shown to have a measurable effect on the pressure drop it would be expected to observe differences in pressure drop even at the same porosity and pore diameter. As shown in Figure 8-4, the sample L-2 (Por=0.5943) induced the same pressure drop per unit length as sample L-10 (Por=0.6974) due to the pore shape effect.

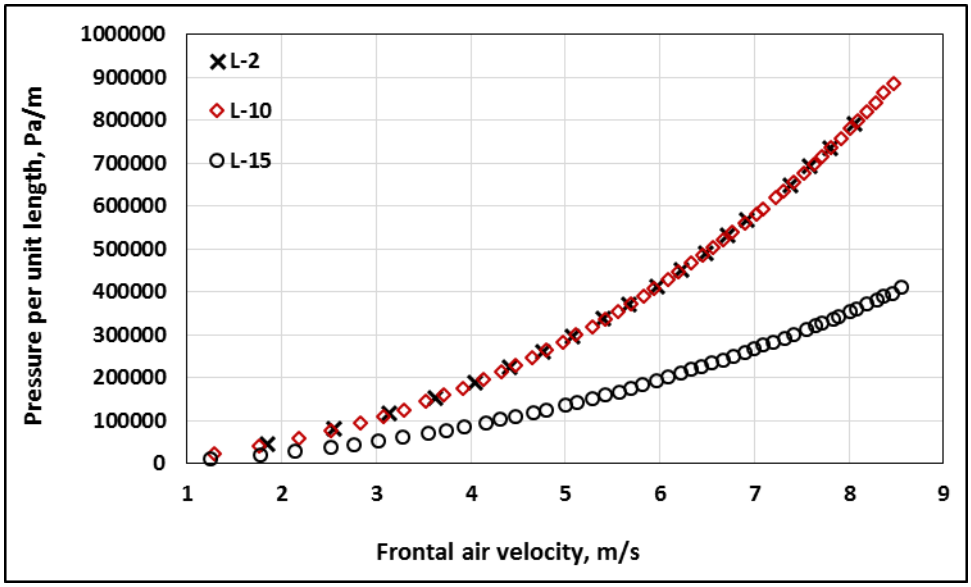

Figure 8-4 Pore shape effect on pressure drop

8.3 CT-Scan tomography and image processing

There are three non-destructive methods commonly used to achieve detailed information about the internal microstructure of porous media: optical analysis, X-ray computed micro tomography (micro-CT), and magnetic resonance imaging (MRI) [314]. X-ray tomography has been widely used to visualise and find such morphological parameters as free flow cross sectional area (Amin), ligament thickness (Df) and pore diameter (dp) [32, 52, 72, 130, 245, 315-317]. However, the large number of samples manufactured here means this technique was not practical. Image processing of photographs of the external surfaces can be used to identify manufacturing defects and to obtain surface microstructure parameters such as free flow area ratio (AR) and average window cell size (dw). This method was adopted in the current work by employing the ImageJ software which is widely used for X-ray tomography segmentation analysis [52, 315, 318].

Both faces of the samples were scanned by high resolution scanner (Sharp MX-5141). In order to differentiate between the aluminium and the pores, suitable threshold values were selected [32, 130, 319]. To identify the solid phase material over the cross section of the metal foam the intensity of the colour can be recognised by the histogram of foam cross section as shown in the Figure 8-5. The histogram shows the intensity of the colour with pixel values ranging from 0 for the black to 255 for the white [130, 314, 319]. An appropriate value of thresholding intensity for each

sample was found by taking the average value of two consecutive peaks on the left half of histogram as shown in Figure 8-5. This average value was applied in the ImageJ software for the threshold. The brightness and contrast quality of the image were improved by the ImageJ software filters.

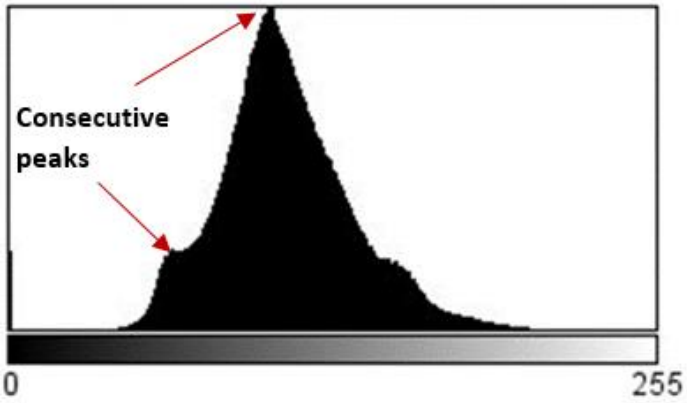

Figure 8-5 The histogram of the sample M-23

For one face of the sample M-23 the intensity average value was found to be 84. Shown in Figure 8-6 are the original and thresholded photos. Increasing the thresholding value by one increased the free area ratio by 6% and the average particle diameter by <5% and vice versa.

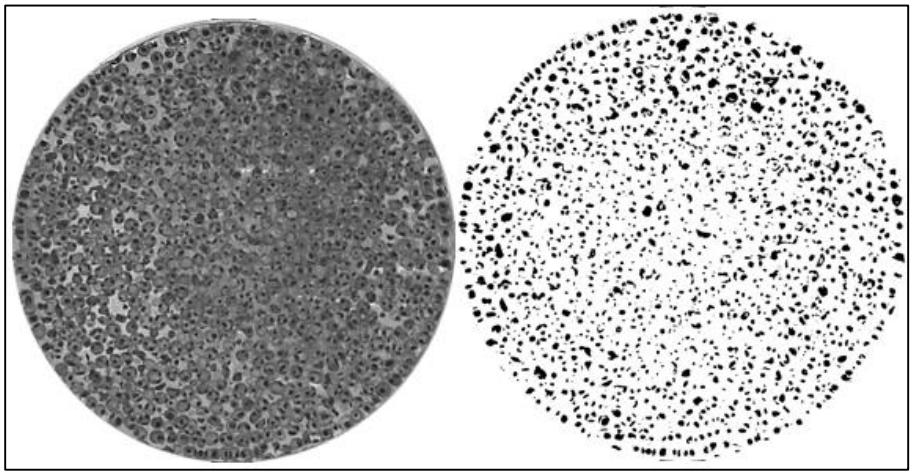

Figure 8-6 The original and thresholded photos of sample M-23

8.4 Microstructure and defects effect on pressure drop

In order to study the effect of closed pore defects on pressure drop, two samples from the same pore size group were selected: M-21 with porosity of 0.69 and M-23 with porosity of 0.73 and a measured pressure drop higher than that of M-21. Shown in Figure 8-7 are images of M-21 and M-23.

From these images it can be seen that the free flow area in sample M-23 is diminished by the closed cells. Whereas, in the sample M-21 there are no closed pores and some missing cells are apparent that increased the free flow area.

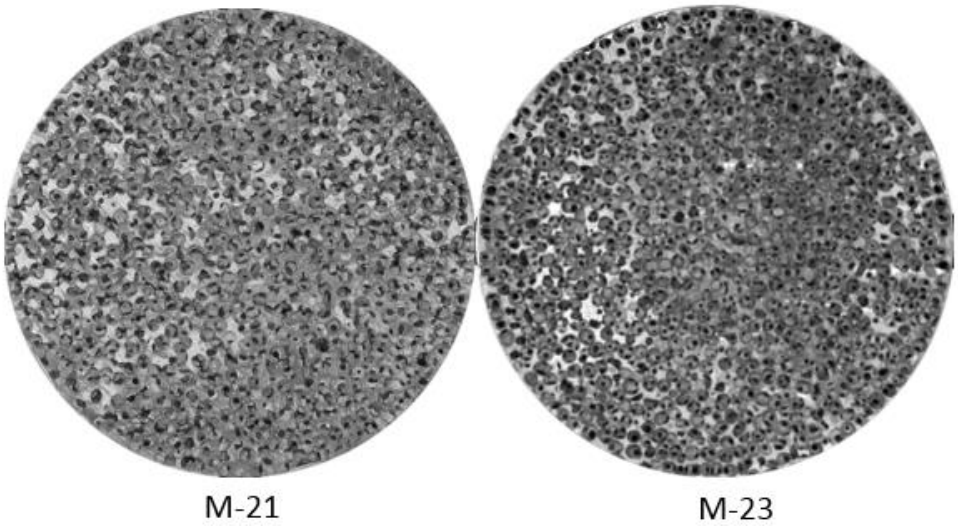

Figure 8-7 Scanned cross-sections of M-21 and M-23 samples

To determine the free flow area the images were analysed using the ImageJ software. Shown in Figure 8-8 are the thresholded images where white is the material and the black represents the pores.

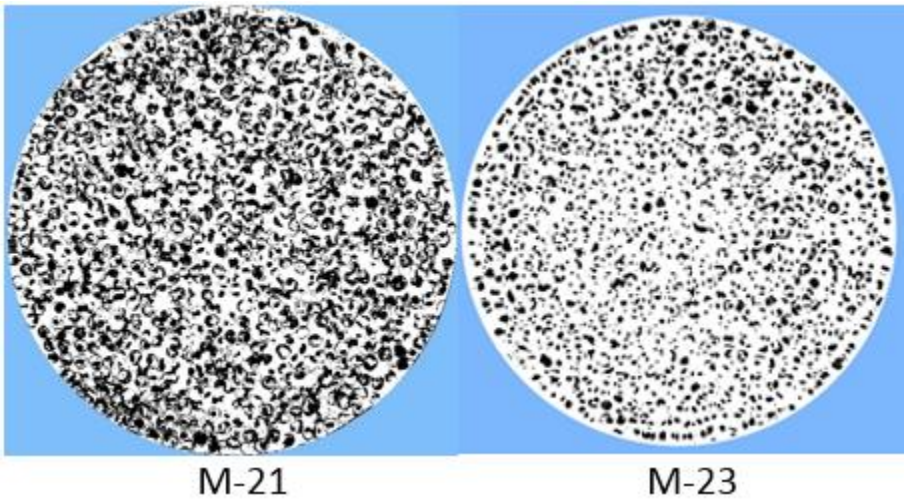

Figure 8-8 The pixel threshold of the samples

For the sample M-23, the average cell size (from both faces) was found to be 0.163 mm and the free area ratio was 16.76 %. In the case of M-21 the average cell size was found to be 0.252 mm and the free area ratio was 23.32%.

The effect of morphological parameters on hydraulic parameters such as, pressure drop and inertia coefficient is complex [103]. There are the multiple influences of free flow area ratio, average cells size, ligament shape and size, and cell shape. All have a measurable impact on the pressure drop and permeability [17, 74]. In the current samples the impact of cell shape in pressure measurements can be demonstrated by comparing crushed and spherical salt samples. For example, in the large pore size group samples the sample L-2 induced the same pressure as sample L-10 even though they have different porosities. The porosity of L-2 was 0.59 and for L-10 it was 0.70, while from image processing analysis the average cell sizes were 0.153 mm and 0.167 mm and the free flow area ratios were 21.57% and 21.50% respectively. In this case the values of average cell size and free area ratio of both samples were approximately the same.

The effect of the defects and imperfections on the pressure drop was noticed for all pore size groups . Shown in Figures 8-9 to 8-12 are measured pressure drop against frontal air velocity for selected samples, with their corresponding geometrical parameters given in Table 8-1.

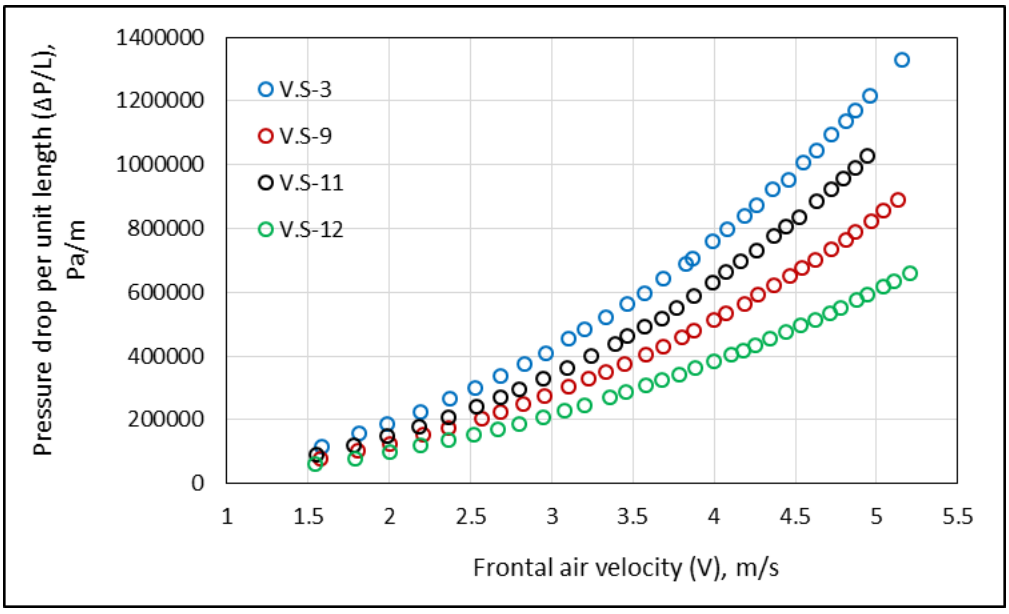

Figure 8-9 Pressure drop per unit length against frontal air velocity (very small pore size samples)

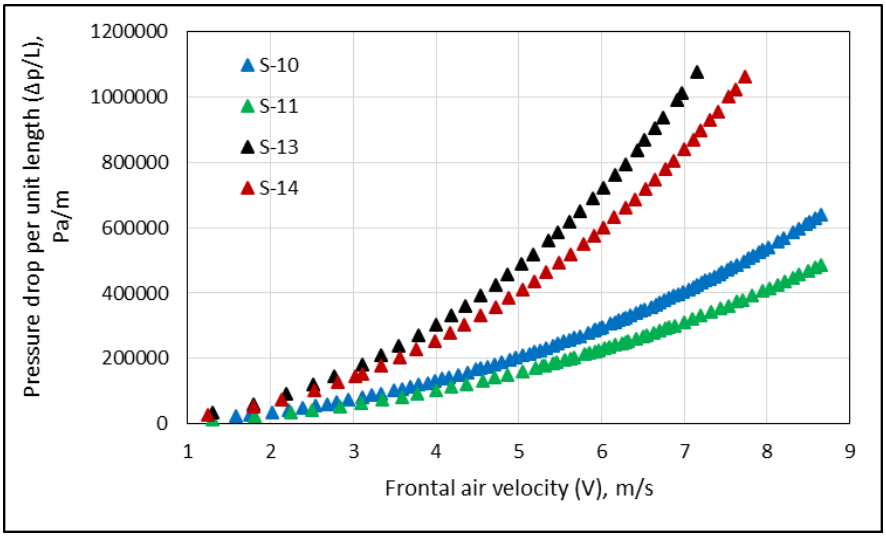

Figure 8-10 Pressure drop per unit length against frontal air velocity (small pore size samples)

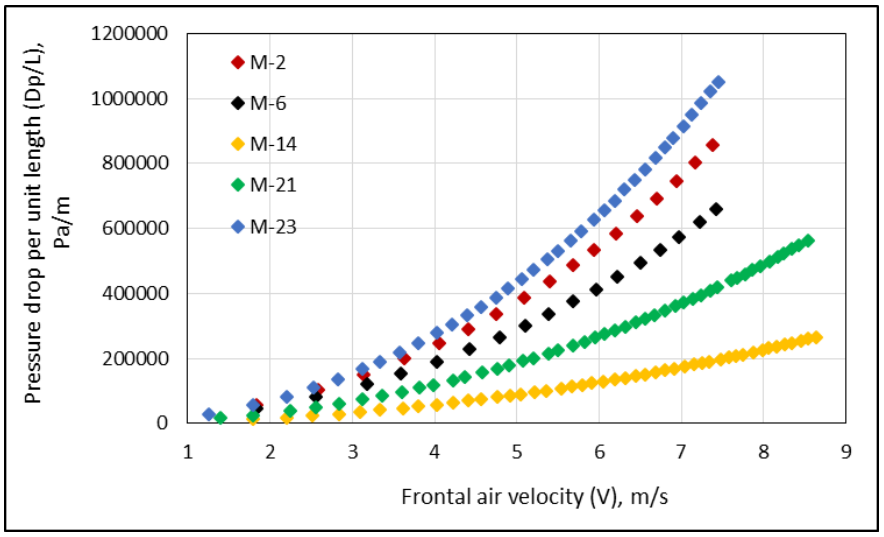

Figure 8-11 Pressure drop per unit length against frontal air velocity (Medium pore size samples)

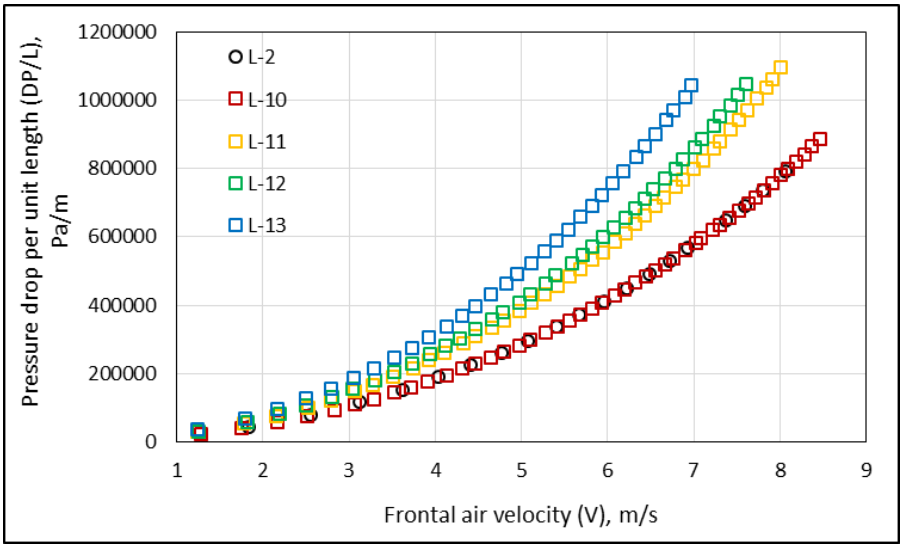

Figure 8-12 Pressure drop per unit length against frontal air velocity (Large pore size samples)

Missing pores or fibres were found to be the reason for the low pressure drop, such as in sample S-11. Whereas closed pores resulted in higher pressure drops than normal, as seen in S-14, M-2 and M-23. Samples S-10 and M-21 had the same pressure drop but the free area and the average window size were different, see Figure 8-13. These differences can be seen in terms of ligament thickness and window size and free flow area. In the sample M-21 it is clear that the cells were bigger and the fibre thicker compared with those for S-10, whereas the free flow area ratio in sample S-10 was higher than in M-21.

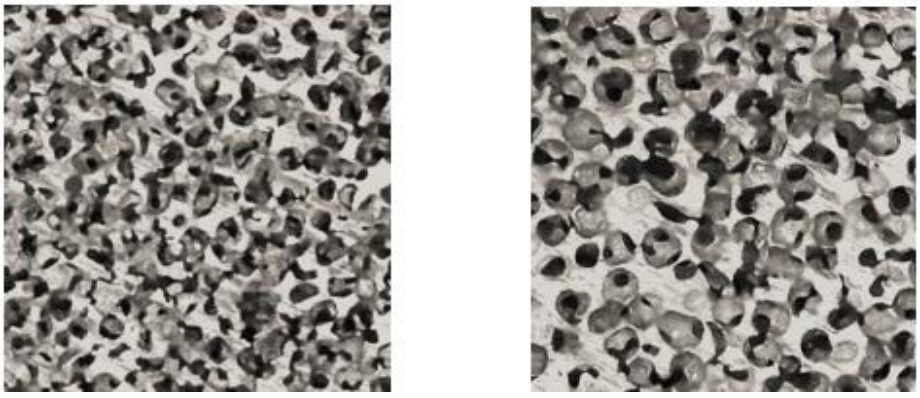

S-10 M-21

Figure 8-13 Difference in cell window size between samples S-10 and M-21

Table 8-1 The geometrical parameters of the samples and identified defects

Sample	Porosity, %	Free area ratio (A_R), %	d_w, *mm*	Defect	Effect
V.S-3	66.60	11.12	0.079	One face some closed pores	Higher pressure drop
V.S-9	66.50	14.52	0.119	Closed pores on one face	Higher pressure drop
V.S-11	68.0	13.57	0.105	One face semi closed pores	Higher pressure drop
V.S-12	67.92	14.74	0.135	No clear defects	Normal pressure drop
S-10	69.90	24.10	0.200	No clear defects	Normal pressure drop
S-11	72.46	28.84	0.355	Missing pores on one side	Lower pressure drop
S-13	67.70	16.10	0.10	No clear defects	Normal pressure drop
S-14	72.27	19.47	0.141	Closed pores on both faces	Higher pressure drop
M-2	62.05	19.71	0.352	No clear defects (crushed salt sample)	Normal pressure drop
M-6	60.0	20.68	0.373	No clear defect (crushed salt sample)	Normal pressure drop
M-14	77.96	28.77	0.410	No clear defects	Normal pressure drop
M-21	69.19	23.32	0.252	Missing pores on both faces	Normal pressure drop
M-23	73.06	16.76	0.163	Closed and semi closed pores on both faces	Higher pressure drop

L-2	59.43	21.57	0.153	No clear defect (crushed salt sample)	Normal pressure drop
L-10	69.74	21.50	0.167	No clear defects	Normal pressure drop
L-11	70.75	23.54	0.322	Closed pores more than missing pores	Non normal pressure drop
L-12	72.24	17.83	0.269	Closed pores on one face	Higher pressure drop
L-13	69.29	14.79	0.142	Closed pores on both faces	Higher pressure drop

8.5 Microstructure and defects effect on thermal conductivity

Lu et al. [172] studied the effect of the fraction of cell wall misalignments and the random distribution of the fractured cell walls on thermal conductivity. They found that whereas the former defect had a relatively small influence on the effective thermal conductivity, thermal conductivity can be reduced by the impact of the random distribution of the fractured cell walls. It was also noticed that solid inclusions lead to increase in the thermal conductivity [172].

The thermal conductivity depends on the solid phase cross section area and the thickness of the fibres. Therefore, the fraction of the material visible on the face of the samples was used to identify any impact from defects. The samples V.S-11 and V.S-12 had almost the same porosity but V.S-11 had a higher pressure drop due to the closed pores. However, the thermal conductivity of V.S-11 (31 *W/.m.K*) was only *10%* higher than that of V.S-12 (28 *W/m.K*). In the small pore size group samples, S-11 and S-14 had the same macroscopic void fraction but had thermal conductivities of *22.3 W/m.K* and *26.5 W/m.K* respectively. The sample S-11 was missing pores on one face and S-14 had a closed cells on both faces. Sample S-14 had a pressure drop of more three times that of S-11 but the thermal conductivity was bigger only by a factor of 1.2. The same scenario was noticed for the samples M-21 and M-23, where the increase in the pressure drop was *125%* but in the thermal conductivity just *3%*.

It can be concluded that the closed cells have a higher measurable effect on pressure drop than the thermal conductivity. Conduction heat transfer depends upon the solid phase cross sectional area and ligament thickness. Closed or missing cells will only add or remove a little heat transfer area. Therefore, their impact on the pressure drop is not the same. The thermal conductivity is more sensitive to the solid

phase void fraction than to the pore shape. This can be seen from the comparison of the samples L-2 and L-10 which had the same pressure drop. The thermal conductivity of sample L-2 was *1.6* times higher than that of L-10 due to the difference in macroscopic porosity. The sample V.S-9 provided high thermal conductivity (36 W/m.K) and the cause of this might be the closed cell inclusions enlarging the heat transfer area as shown in Figure 8-14.

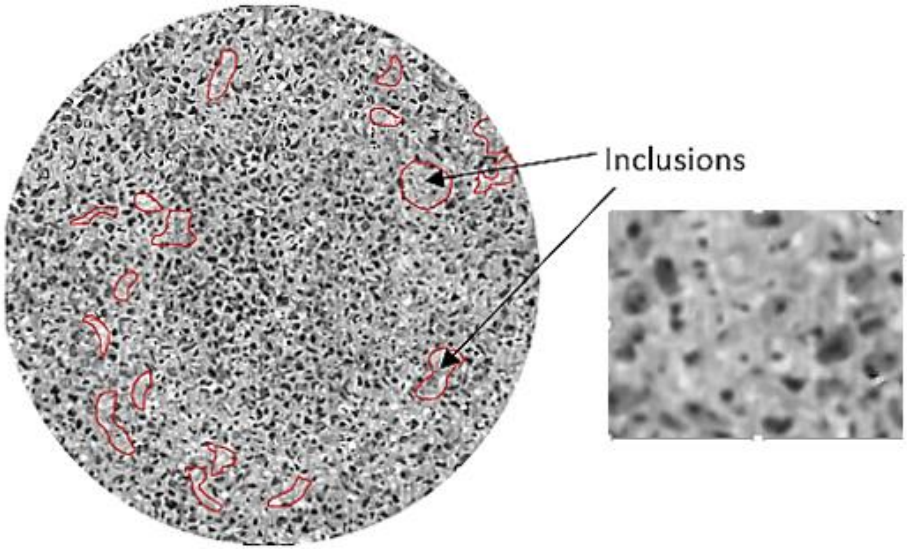

Figure 8-14 Inclusions on the view section of the sample

8.6 Microstructure and defects effect on convective heat transfer coefficient

The convective heat transport phenomenon between the solid phase and flowing fluid is based upon the heat transfer area, flow rate and temperature difference. As the current tests were performed at the same conditions, a comparison in terms of convective heat transfer coefficient (*h*) can be done. Shown in Figure 8-15 is the convective heat transfer coefficient versus permeability based Reynolds number for the very small pore size samples.

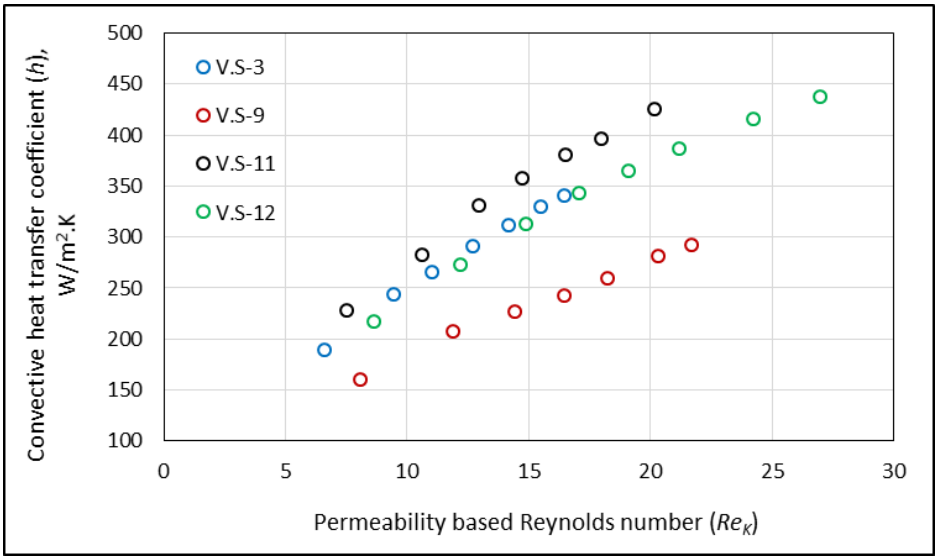

Figure 8-15 Convective heat transfer coefficient against permeability based Reynolds number (Very small pore size samples)

The sample V.S-11 had the highest *h,* while V.S-9 had the lowest. From Table 8-1, it can be seen that the average window size in V.S-11 was smaller, resulting in an increase of the interstitial velocity. The heat transfer area was also larger in V.S-11 due to the increased fibre thickness and solid phase material. Completely closed pores were observed on one face of the sample V.S-9 and these might be closed within the sample, thus reducing the convective heat transfer coefficient. The samples (V.S-3, V.S-12) had the same heat transfer coefficient.

Shown in Figure 8-16 are two small pore size samples, S-10 and S-13. Sample S-13 has a heat transfer coefficient higher than of S-10 due to its higher porosity and smaller average pore size. Missing pores resulted in lower heat transfer area such as in sample S-11, as evident in Figure 8-17.

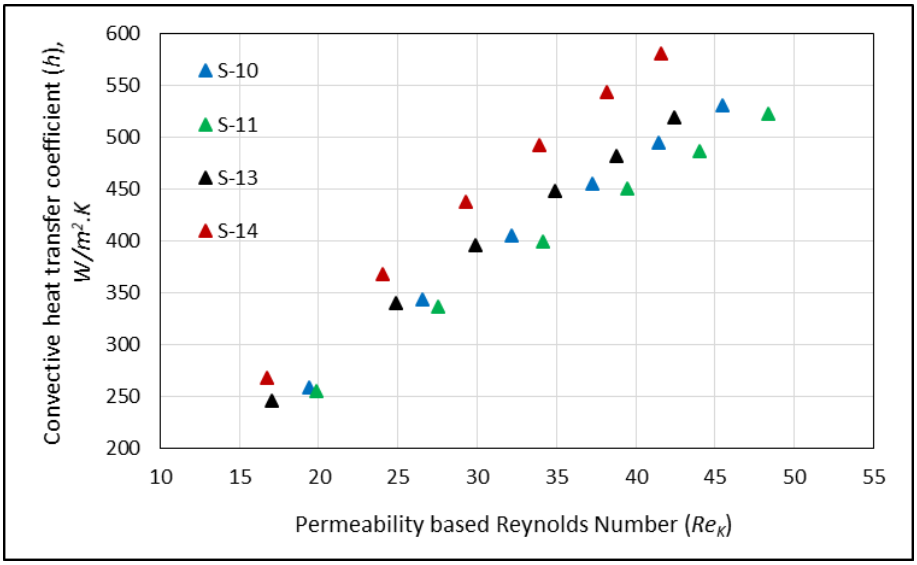

Figure 8-16 Convective heat transfer coefficient against permeability based Reynolds number (small pore size samples)

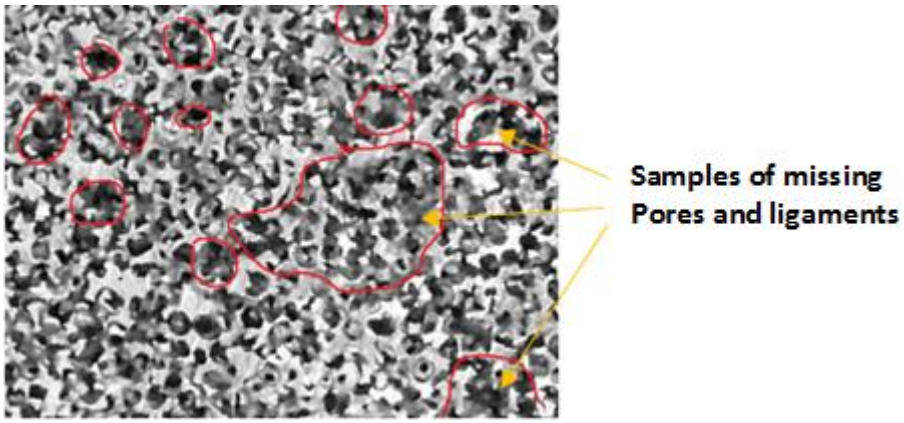

Figure 8-17 Samples of missing and damaged pores and ligaments (Sample S-11)

Missing and damaged pores can contribute to lower heat transport mechanism in terms of lower heat transfer area and lower pore velocity. Whereas, closed and semi closed pores lead to lower average window size, higher heat transfer area and high pore velocity, for example in S-14.

The convective heat transfer coefficient increases with a decrease of porosity. Therefore, M-14 has the lowest value of *h* in the medium group as shown in Figure 8-19. In this sample a small heat transfer area occurred due to the thinner ligaments as the result of its high porosity. On the other hand, the pore velocity was lower as the result of its wider cell windows. For the sample M-23, semi closed and closed cells were observed on the surface, resulting in higher surface area and inside pore

velocity. Samples M-14 and M-21 can be assumed 'normal' because the number of missing ligaments and cells was small compared with the total number of cells.

The typical behaviour of porous materials is that if the porosity increases the window size increases, while the heat transfer area and pore velocity are decreased. As a result, the pressure drop in sample M-14 is lower as well as the value of *h*. On the other hand, the semi closed cell windows result in high pressure drop but also give high thermal performance such as in sample M-23. Shown in Figure 8-18 is a photo of M-23 in which semi closed cells are evident and increase the flow velocity inside the cells.

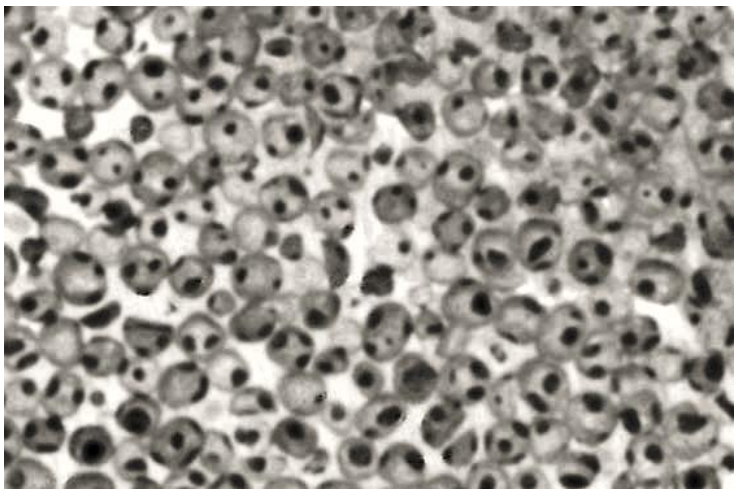

Figure 8-18 View of surface of sample M-23

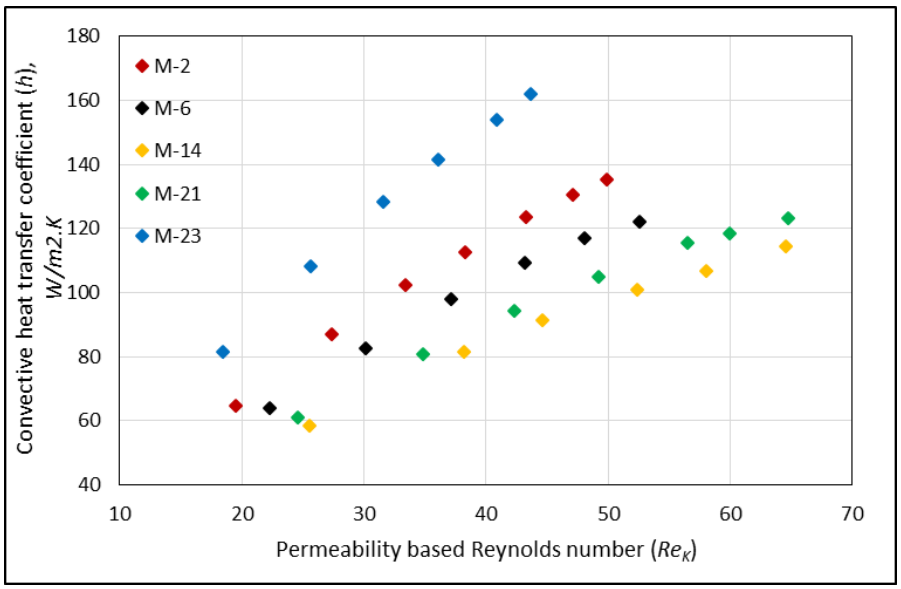

Figure 8-19 Convective heat transfer coefficient against permeability based Reynolds number (medium pore size samples)

Shown in Figure 8-20 are the convective heat transfer coefficient results of the selected samples from large group size samples. The best thermal performance in terms of *h* was provided by L-12; this is due to the same cause as in the medium pore samples, namely, semi closed cells and thicker fibres resulting in higher heat transfer area and interstitial high velocity due to the cells' small window size. The sample L-11 has both missing pores and closed pores, hence it cannot be determined which of these most influences its results.

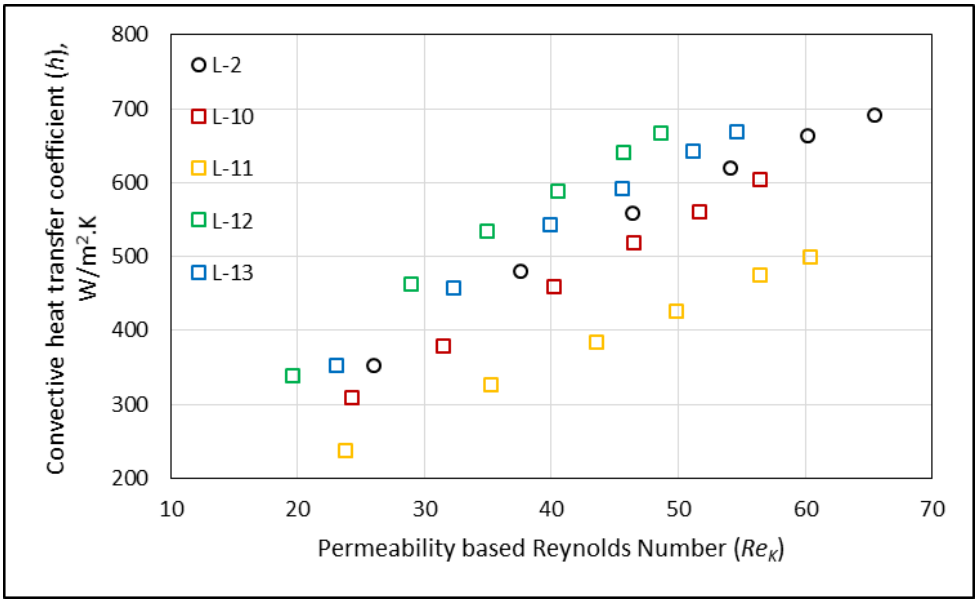

Figure 8-20 Convective heat transfer coefficient against permeability based Reynolds number (Large pore size samples)

This analysis showed the effect of the manufacturing defects on hydraulic and thermal results for porous material. The commonly reported defects are missing cells and ligaments, pore misalignment, curved fibres and inclusions. Due to the relatively low porosity in the current work the closed and semi closed cells were also identified. The cause of this defect was high infiltration gas pressure which was used to control the porosity of the sample. If too high a pressure is used the melted aluminium is forced to penetrate through the contact point of the spherical salt balls and the metal sponge's cells become closed. It also might be the case that not all the salt can be removed. In addition, the limited infiltration pressure varies depending on the average spherical salt diameter.

The solidification rate and uncontrolled production technique are demonstrated as direct causes of the missing and damaged cells, curved ligament

and inclusions [38, 60, 307]. The infiltration pressure in casting production methods can be considered the direct cause of the closed and semi closed defect.

The impact of the these defects on the measured hydraulic and thermal parameters can be summarised as

- Closed and semi closed cells are the cause of high pressure drop and high convective heat transfer coefficient, while a little effect on thermal conductivity has been noticed.
- Lost or damaged cells and ligaments are the source of lower pressure drop and convective heat transfer and the effect on thermal conductivity is not that measurable.
- The inclusions are the source of high thermal conductivity and pressure drop and lower heat transfer coefficient.
- The effect of all the above defects depends upon the fraction of the defected compared with non-defected cells.

Chapter 9

9. Conclusions and recommendations

9.1 Conclusions

Cellular metallic foams have become the potential choice for many engineering applications as a result of their morphological features. Knowledge of impact of geometrical parameters (porosity and pore size) on the thermal performance and pressure loss across the cellular materials is essential. The increase of thermal performance in terms of convective and volumetric heat transfer coefficients with decrease of porosity and pore size has been reported. The increase of pumping power in terms of pressure drop has been also observed with decreasing porosity and pore size.

In this project sixty eight samples with four different pore sizes and porosity varying from 0.57 to 0.77 have been examined. The pore diameter varied between 0.85 and 2.18 mm. These aluminium sponges were produced by the replication technique. These replicated foams were examined to obtain hydraulic and thermal characterisations, using air as the working fluid. The effective thermal conductivity was also measured. The results of this study are summarised in the following concluding remarks.

9.1.1 Steady state pressure drop measurements and hydraulic parameters

The steady state measurements of pressure drop results can be summarised in these points

1- The four flow regimes in porous media were observed; pre-Darcy, Darcy, Forchheimer and turbulent. These regimes were identified by the change in slope of the reduced pressure drop per unit length.
2- The effect of pore size and porosity on the transition points of flow regimes was investigated. With increasing the porosity or pore diameter the Reynolds number at the transition points of flow regimes increased.

3- The pressure drop increased with frontal air velocity. The typical linear and quadratic relationships between the pressure drop and frontal air velocity were observed in the Darcy and Forchheimer flow regimes respectively.

4- The pressure drop per unit length increased with decreasing of porosity and pore diameter of the metal foams. It also increased with the decrease of particle diameter and pitch size for packed beds of spheres and mesh wire screens respectively.

5- The inertia factor and drag form coefficient increased with the decrease of pore size and porosity. The relationship between porosity and pore diameter with pressure drop, permeability and inertia form drag coefficients was found to high interdependent. For instance, some samples with different pore size induced the same pressure drop due to the increase in porosity of the smallest pore diameter.

6- The permeability is key parameter of porous media and was found to increase with increase of both porosity and pore diameter. It was normalised by the pore diameter and correlated well with porosity of metal foams.

7- The friction factor is the common nondimensional relation to describe hydraulic loss in different fluid flow applications. The friction factor increased with decrease of pore diameter and porosity and decreased with increase of Reynolds number. The friction factor was found to equal $1/Re_k$ at Darcy flow regime. It was also correlated well with Reynolds number and inertia factor.

8- The replicated foams pore shape was found to have a significant effect on the pressure drop and hydraulic parameters in terms of inertia and drag coefficients. The spherical shape metal foams induced higher pressure drop than those of irregular shape. The inertia and drag coefficients for spherical pore shape samples were higher than those for irregular pore shape.

9- The effect of manufacturing defects in terms of fully or semi closed cells was resulted in scattering and increase in the pressure drop results.

9.1.2 Effective thermal conductivity

The comparative steady state method was used to measure the effective thermal conductivity.

1- The ETC increased with decrease of porosity and no measurable effect was noticed due to the pore size. These results showed good agreement with published results.
2- The closed celled metal foams provides higher thermal conductivity than those with open celled due to the differences in microstructure and thermal contact resistance.
3- There was no effect of pore shape on ETC.
4- The natural convection heat transport contribution in ETC was assessed by change the configuration of the rig and the source of heat source.
5- The contribution of natural convection increased with temperature and porosity and resulted in the increase in ETC.
6- Some of available correlations and models in previous studies for open celled metal foams were examined and it was found that they were not applicable for low range of porosities.
7- A new correlation to determine the ETC was demonstrated for range of porosity from 0.5 to 1.0.

9.1.3 Convective heat transfer

The convective heat transfer results were demonstrated for two types of applications: for thermal regenerators in terms of NTU_m and h_v and for extended heat transfer surfaces in terms of h and Nu_{vdp}. The effect of thermal conductivity on the thermal performance was also reported.

1- The single blow technique was used and the local thermal non equilibrium (LTNE) approach was applied to derive the mathematical model. In this model the axial conduction was included and the holder wall was assumed as non-adiabatic.
2- The effect of longitudinal conduction and the R_{tc} on the outlet fluid temperature and thermal performance were analysed.
3- The direct matching technique was implemented to match the predicted and measured outlet fluid temperatures and calibrated by the maximum gradient scheme in order to confirm the results.
4- The NTU_m decreased with the increase of Reynolds number or flow rate. It also increased with decrease of pore size and porosity.

5- The convective and volumetric heat transfer coefficients increased with Reynolds number. With decreasing porosity and pore size the both heat transfer coefficients increased. The convective heat transfer coefficient reached the maximum value at porosity around ~ 60%.

6- Nusselt number based on the average pore diameter was found to increase with Reynolds number. The very small pore size samples provided lower thermal performance in terms of Nu_{vdp}. In contrast, the medium and small pore diameters samples provided Nu_{vdp} in almost the same order.

7- The pore size effect was found more dominant in convective heat transfer when the volumetric heat transfer and Nu_{vdp} compared. The Nu_{vdp} was also found to increase with decrease of porosity.

8- In packed beds of mesh wire screens and spherical balls, the NTU_m increased with decreasing of both pitch size and spherical diameter. It also increased with the number of layers in mesh wire screens and decreased with increase of Reynolds number.

9- In mesh wire screens packed beds, there is no effect was noticed from the number of layers on convective and volumetric heat transfer coefficients and Nusselt number.

10- The thermal results in terms of volumetric heat transfer coefficient and Nusselt number are in the same order compared with reported values in literature.

11- The thermal performance of thermal regenerators can be improved by decreasing the thermal conductivity of the prism. This was done by using the metal foams in forms of slices to increase the thermal resistance. Where the NTU_m increased by 34% when the sample was sliced to five pieces.

9.1.4 Manufacturing defects

There are common manufacturing defects as a result of uncontrolled production techniques and conditions. These defects are demonstrated in types of missed or twisted fibre, missed cells, closed cells and inclusions. The closed cells are commonly found in low porosities and pore diameter samples. The missed cells and the fibres are also usually recognised at high porosities. A significant influence of these defects on the mechanical properties was reported in literature. In current samples the

defects were tracked by scanning the faces of the samples and their effect was also analysed by implementation of the image processing technique. The concluded notes are listed as

1- The closed cell and inclusion defects were identified in some current samples and they might be a result of high infiltration pressure and a high solidification rate. These defects increased the pressure drop significantly but the minor knocking up of ETC was observed due these defects.
2- The missed cell or fibre defect was resulted in lower pressure and lower thermal performance and the slight decrease in ETC was also noticed.
3- Imperfections impact in terms of semi or fully closed cells differ from parameter to others. For example, the effect on ETC was not that measurable because there was a slight increase in conductive heat transfer area. In contrast, the measurable influence was reported in pressure drop and convective heat transfer because these defects were resulted in blockage area of the flow.

9.2 Recommendations and future plan

Due to time limitation several points of research were out of scope and could not be covered and some were discovered and related to this topic of project. These opportunities can be expressed in the following list

1- The shape of the pore was found to have a measurable influence on the pressure drop and hydraulic parameters such as inertia and drag coefficients. The examined irregular pore shape samples in this study were with limited porosities < 0.65. Therefore, producing more samples with irregular shape with porosity higher than 0.65 and compared with current samples would be a great opportunity to investigate the pore shape.
2- In the replicated aluminium foams the pore diameter is usually expressed as the average value of lower and higher limitations. In this case the distribution of the preform salt particles is random and unknown. Producing samples with small range of preform salt diameter by closing the range of sieves size might be a possible solution to improve pore diameter effect.

3- There is a minimum porosity can be achieved with each spherical preform salt diameter with a certain infiltration pressure. In this case the pores will be closed and this pressure should be identified to avoid producing samples with closed cells.

4- The small and very small pore size samples provides the best thermal performance and induced higher pressure. Thereby, producing samples with different layers of preform salt diameters will be a possible technique to improve the performance. It could be also sliced to study the ETC effect.

5- Increasing the flow rate to cover the turbulent regime is a great opportunity to study the behaviour of the flow and how the hydraulic parameters is effected in this regime. It is also expected to influence by the compressibility.

6- Using the image processing to measure structural dimensions such as, fibre or ligament thickness and windows size is beneficial. This technique gives opportunity to apply the approaches which based on these parameters to predict pressure drop.

7- The ETC is the key parameter in the subject of heat transfer collaborating metal foams. In this study the ETC was measured at moderate temperatures. To include the contribution of radiative heat transfer and to express the ETC as function of temperature the ETC could be measured at relative high temperatures. These measurements can be conducted at vacuum container to exclude the natural convection effect.

8- The most common fluids used with metal foams in different applications are air and water. Therefore, measuring the effective thermal conductivity with water as a filler fluid and the contribution of the natural convection is essential to provide bank of data about these class of cellular materials.

9- There are still a number of opportunities of research in the topic of convective heat transfer in current class of metal foams. The priority is increasing the fluid velocity to study this phenomena at turbulent regime.

10- In the case of high flow rates, the effect of two more important factors could be examined and included to the single blow technique model. First is the Joule-Thomson coefficient because at high flow rates the pressure drop will be increased. Secondly, the dispersion effect is recommended to include at high velocities.

11- There are two kinds of single blow technique, one is to blow hot fluid and the other is to blow cold fluid to cool the sample. In the application of thermal storage knowledge about the two processes is essential to know for estimating the efficiency of the regenerator. Therefore, assessment the thermal characteristics in both processes is important.

12- The effect of ETC decreases with flow rate, then by increasing the flow rate can be identified at which flow rate the ETC influence might be excluded.

13- The effect R_{tc} (heat capacity ratio) was studied theoretically and was found to have a measurable effect on thermal characteristics of the thermal regenerators. So, this influence can be studied experimentally by changing the holder of the test section with different materials.

14- Increasing the number of slices gradually to reduce the thermal conductivity and to identify the number of slices effect on the thermal conductivity.

10. References

1. Pérez-Lombard, L., J. Ortiz, and C. Pout, A review on buildings energy consumption information. Energy and Buildings, 2008. 40(3): p. 394-398.

2. Yang, L., H. Yan, and J.C. Lam, Thermal comfort and building energy consumption implications – A review. Applied Energy, 2014. 115: p. 164-173.

3. Davis, S.J. and K. Caldeira, Consumption-based accounting of CO2 emissions. Proceedings of the National Academy of Sciences, 2010. 107(12): p. 5687-5692.

4. Zhou, H., Chen, Q., Li, G., Luo, S., Song, T.B., Duan, H.S., Hong, Z., You, J., Liu, Y. and Yang, Y., Interface engineering of highly efficient perovskite solar cells. Science, 2014. 345(6196): p. 542-546.

5. Halkarni, S.S., A. Sridharan, and S.V. Prabhu, Estimation of volumetric heat transfer coefficient in randomly packed beds of uniform sized spheres with water as working medium. International Journal of Thermal Sciences, 2016. 110: p. 340-355.

6. Sadrameli, S. and H. Ajdari, Mathematical modelling and simulation of thermal regenerators including solid radial conduction effects. Applied Thermal Engineering, 2015. 76: p. 441-448.

7. Lu, C., Wang, S., Chen, C. and Li, Y., Effects of heat enhancement for exhaust heat exchanger on the performance of thermoelectric generator. Applied Thermal Engineering, 2015. 89: p. 270-279.

8. Barari, F., Luna, E.M.E., Goodall, R. and Woolley, R., Metal foam regenerators; heat transfer and storage in porous metals. Journal of Materials Research, 2013. 28(17): p. 2474-2482.

9. Beasley, D.E. and J.A. Clark, Transient response of a packed bed for thermal energy storage. International Journal of Heat and Mass Transfer, 1984. 27(9): p. 1659-1669.

10. Abduljalil, A.S., Z. Yu, and A.J. Jaworski, Selection and experimental evaluation of low-cost porous materials for regenerator applications in thermoacoustic engines. Materials & Design, 2011. 32(1): p. 217-228.

11. Wu, Z., Caliot, C., Flamant, G. and Wang, Z., Numerical simulation of convective heat transfer between air flow and ceramic foams to optimise volumetric solar air receiver performances. International Journal of Heat and Mass Transfer, 2011. 54(7): p. 1527-1537.

12. Kamath, P.M., C. Balaji, and S.P. Venkateshan, Convection heat transfer from aluminium and copper foams in a vertical channel – An experimental study. International Journal of Thermal Sciences, 2013. 64: p. 1-10.

13. PING, L.-h., J.-y. QIAN, and D.-h. XU, A Review of the Thermal Control Technologies for Electronic Systems: Part I [J]. Electro-Mechanical Engineering, 2008. 1: p. 002.

14. Xu, Z.G. and C.Y. Zhao, Experimental study on pool boiling heat transfer in gradient metal foams. International Journal of Heat and Mass Transfer, 2015. 85: p. 824-829.

15. Peng, W., Xu, M., Huai, X., Liu, Z. and Lü, X., Performance evaluation of oscillating flow regenerators filled with particles, wire screens and high porosity open-cell foams. Applied Thermal Engineering, 2017. 112: p. 1612-1625.

16. Yang, J., Wang, J., Bu, S., Zeng, M., Wang, Q. and Nakayama, A., Experimental analysis of forced convective heat transfer in novel structured packed beds of particles. Chemical Engineering Science, 2012. 71: p. 126-137.

17. Edouard, D., Lacroix, M., Huu, C.P. and Luck, F., Pressure drop modelling on SOLID foam: State-of-the art correlation. Chemical Engineering Journal, 2008. 144(2): p. 299-311.

18. Bhattacharya, A., V.V. Calmidi, and R.L. Mahajan, Thermophysical properties of high porosity metal foams. International Journal of Heat and Mass Transfer, 2002. 45(5): p. 1017-1031.

19. Paek, J.W., Kang, B.H., Kim, S.Y. and Hyun, J.M., Effective thermal conductivity and permeability of aluminium foam materials. International Journal of Thermophysics, 2000. 21(2): p. 453-464.

20. Kumar, P., F. Topin, and J. Vicente, Determination of effective thermal conductivity from geometrical properties: Application to open cell foams. International Journal of Thermal Sciences, 2014. 81(0): p. 13-28.

21. Chang, Z.C., Hung, M.S., Ding, P.P. and Chen, P.H., Experimental evaluation of thermal performance of Gifford–McMahon regenerator using an improved single-blow model with radial conduction. International Journal of Heat and Mass Transfer, 1999. 42(3): p. 405-413.

22. Chen, P. and Z. Chang, Measurements of thermal performance of the regenerator of a cryocooler with a high number of transfer units value. Proceedings of the Institution of Mechanical Engineers, Part C: Journal of Mechanical Engineering Science, 1996. 210(4): p. 341-352.

23. Geb, D., F. Zhou, and I. Catton, Internal heat transfer coefficient determination in a packed bed from the transient response due to solid phase induction heating. Journal of Heat Transfer, 2012. 134(4).

24. Heggs, P. and D. Burns, Single-blow experimental prediction of heat transfer coefficients: A comparison of four commonly used techniques. Experimental Thermal and Fluid Science, 1988. 1(3): p. 243-251.

25. Lu, W., C.Y. Zhao, and S.A. Tassou, Thermal analysis on metal-foam filled heat exchangers. Part I: Metal-foam filled pipes. International Journal of Heat and Mass Transfer, 2006. 49(15–16): p. 2751-2761.

26. Cha, J.S., S.M. Ghiaasiaan, and C.S. Kirkconnell, Oscillatory flow in microporous media applied in pulse – tube and Stirling – cycle cryocooler regenerators. Experimental Thermal and Fluid Science, 2008. 32(6): p. 1264-1278.

27. Luna, E.M.E., Barari, F., Woolley, R. and Goodall, R., Casting protocols for the production of open cell aluminium foams by the replication technique and the effect on porosity. Journal of visualized experiments: JoVE, 2014(94).

28. Barari, F., Metal foam regenerators; heat transfer and pressure drop in porous metals. 2014, University of Sheffield.

29. Abadi, G.B. and K.C. Kim, Experimental heat transfer and pressure drop in a metal-foam-filled tube heat exchanger. Experimental Thermal and Fluid Science, 2017. 82: p. 42-49.

30. Bhattacharya, A. and R.L. Mahajan, Finned metal foam heat sinks for electronics cooling in forced convection. Journal of Electronic Packaging, Transactions of the ASME, 2002. 124(3): p. 155-163.

31. De Schampheleire, S., De Jaeger, P., Huisseune, H., Ameel, B., T'Joen, C., De Kerpel, K. and De Paepe, M., Thermal hydraulic performance of 10 PPI aluminium foam as alternative for louvered fins in an HVAC heat exchanger. Applied Thermal Engineering, 2013. 51(1–2): p. 371-382.

32. Ranut, P., E. Nobile, and L. Mancini, High resolution microtomography-based CFD simulation of flow and heat transfer in aluminium metal foams. Applied Thermal Engineering, 2014. 69(1–2): p. 230-240.

33. Paul, A. and U. Ramamurty, Strain rate sensitivity of a closed-cell aluminium foam. Materials Science and Engineering: A, 2000. 281(1–2): p. 1-7.

34. Solórzano, E., Reglero, J.A., Rodríguez-Pérez, M.A., Lehmhus, D., Wichmann, M. and De Saja, J.A., An experimental study on the thermal conductivity of aluminium foams by using the transient plane source method. International Journal of Heat and Mass Transfer, 2008. 51(25-26): p. 6259-6267.

35. Kopanidis, A., Theodorakakos, A., Gavaises, E. and Bouris, D., 3D numerical simulation of flow and conjugate heat transfer through a pore scale model of high porosity open cell metal foam. International Journal of Heat and Mass Transfer, 2010. 53(11): p. 2539-2550.

36. Mendes, M.A., Skibina, V., Talukdar, P., Wulf, R., Gross, U., Trimis, D. and Ray, S., Experimental validation of simplified conduction-radiation models for evaluation of Effective Thermal Conductivity of open-cell metal foams at high temperatures. International Journal of Heat and Mass Transfer, 2014. 78: p. 112-120.

37. Inayat, A., Klumpp, M., Lämmermann, M., Freund, H. and Schwieger, W., Development of a new pressure drop correlation for open-cell foams based completely on theoretical grounds: Taking into account strut shape and geometric tortuosity. Chemical Engineering Journal, 2016. 287: p. 704-719.

38. Banhart, J., Manufacture, characterisation and application of cellular metals and metal foams. Progress in materials science, 2001. 46(6): p. 559-632.

39. Mancin, S., Zilio, C., Cavallini, A. and Rossetto, L., Pressure drop during air flow in aluminium foams. International Journal of Heat and Mass Transfer, 2010. 53(15-16): p. 3121-3130.

40. Jacobi, A., K. Nawaz, and J. Bock, Novel Materials for Heat Exchangers. 2013, AHRTI: Air-Conditioning, Heating and Refrigeration Technology Institute, INC 2111 Wilson Boulevard, Suite 500, Arlington, Virginia 22201-3001.

41. Miwa, S. and S.T. Revankar, Hydrodynamic characterization of nickel metal foam, part 1: Single-phase permeability. Transport in Porous Media, 2009. 80(2): p. 269-279.

42. Kramberger, J., M. Šraml, and S. Glodež, Computational study of low-cycle fatigue behaviour of lotus-type porous material. International Journal of Fatigue, 2016. 92, Part 2: p. 623-632.

43. Hamadouche, A., Nebbali, R., Benahmed, H., Kouidri, A. and Bousri, A., Experimental investigation of convective heat transfer in an open-cell aluminium foams. Experimental Thermal and Fluid Science, 2016. 71: p. 86-94.

44. Alhusseny, A. and A. Turan, An effective engineering computational procedure to analyse and design rotary regenerators using a porous media approach. International Journal of Heat and Mass Transfer, 2016. 95: p. 593-605.

45. Goodall, R. and A. Mortensen, 24 - Porous Metals A2 - Laughlin, David E, in Physical Metallurgy (Fifth Edition), K. Hono, Editor. 2014, Elsevier: Oxford. p. 2399-2595.

46. Index A2 - Laughlin, David E, in Physical Metallurgy (Fifth Edition), K. Hono, Editor. 2014, Elsevier: Oxford. p. 2837-2899.

47. Fuller, A.J., Kim, T., Hodson, H.P. and Lu, T.J., Measurement and interpretation of the heat transfer coefficients of metal foams. Proceedings of the Institution of Mechanical Engineers, Part C: Journal of Mechanical Engineering Science, 2005. 219(2): p. 183-191.

48. Xia, X.L., Chen, X., Sun, C., Li, Z.H. and Liu, B., Experiment on the convective heat transfer from airflow to skeleton in open-cell porous foams. International Journal of Heat and Mass Transfer, 2017. 106: p. 83-90.

49. Chen, X., F. Tavakkoli, and K. Vafai, Analysis and characterization of metal foam-filled double-pipe heat exchangers. Numerical Heat Transfer; Part A: Applications, 2015. 68(10): p. 1031-1049.

50. Mortensen, R.G.A., Porous Metals, in Physical Metallurgy. 2014, Elsevier. p. 2399-2595.

51. Mancin, S., L. Rossetto, and Iop. An assessment on forced convection in metal foams. in 6th European Thermal Sciences Conference (Eurotherm). 2012. Poitiers, FRANCE: Iop Publishing Ltd.

52. Ambrosio, G., Bianco, N., Chiu, W.K., Iasiello, M., Naso, V. and Oliviero, M., The effect of open-cell metal foams strut shape on convection heat transfer and pressure drop. Applied Thermal Engineering, 2016. 103: p. 333-343.

53. Iasiello, M., Cunsolo, S., Oliviero, M., Harris, W.M., Bianco, N., Chiu, W.K. and Naso, V., Numerical Analysis of Heat Transfer and Pressure Drop in Metal Foams for Different Morphological Models. Journal of Heat Transfer, 2014. 136(11): p. 112601.

54. Park, S.-H., T.H. Kim, and J.H. Jeong, Experimental investigation of the convective heat transfer coefficient for open-cell porous metal fins at low Reynolds numbers. International Journal of Heat and Mass Transfer, 2016. 100: p. 608-614.

55. Dixit, T. and I. Ghosh, An experimental study on open cell metal foam as extended heat transfer surface. Experimental Thermal and Fluid Science, 2016. 77: p. 28-37.

56. Hu, H., Weng, X., Zhuang, D., Ding, G., Lai, Z. and Xu, X., Heat transfer and pressure drop characteristics of wet air flow in metal foam under dehumidifying conditions. Applied Thermal Engineering, 2016. 93: p. 1124-1134.

57. Xiao, Z. and Y. Zhao, Heat transfer coefficient of porous copper with homogeneous and hybrid structures in active cooling. J. Materials Research, 2013. 28(17): p. 2545-2553.

58. Zhang, L., Mullen, D., Lynn, K. and Zhao, Y., Heat transfer performance of porous copper fabricated by lost carbonate sintering process. In MRS Proceedings. 2009. Cambridge University Press.

59. Mancin, S., Zilio, C., Diani, A. and Rossetto, L., Air forced convection through metal foams: Experimental results and modelling. International Journal of Heat and Mass Transfer, 2013. 62(1): p. 112-123.

60. Lu, Z.-X., Q. Liu, and J.-X. Huang, Analysis of defects on the compressive behaviours of open-cell metal foams through models using the FEM. Materials Science and Engineering: A, 2011. 530: p. 285-296.

61. Gan, Y., C. Chen, and Y. Shen, Three-dimensional modelling of the mechanical property of linearly elastic open cell foams. International Journal of Solids and Structures, 2005. 42(26): p. 6628-6642.

62. Mukherjee, M., F. Garcia-Moreno, and J. Banhart, Defect generation during solidification of aluminium foams. Scripta Materialia, 2010. 63(2): p. 235-238.

63. Zhao, C.Y., Review on thermal transport in high porosity cellular metal foams with open cells. International Journal of Heat and Mass Transfer, 2012. 55(13–14): p. 3618-3632.

64. Mancin, S., Zilio, C., Cavallini, A. and Rossetto, L., Heat transfer during air flow in aluminium foams. International Journal of Heat and Mass Transfer, 2010. 53(21–22): p. 4976-4984.

65. Ghosh, I., How good is open-cell metal foam as heat transfer surface?. Journal of Heat Transfer, 2009. 131(10): p. 101004.

66. Dukhan, N., Ö. Bağcı, and M. Özdemir, Experimental Flow in Various Porous Media and Reconciliation of Forchheimer and Ergun Relations. Experimental Thermal and Fluid Science, 2014.

67. Dukhan, N. and C.A. Minjeur Ii, A two-permeability approach for assessing flow properties in metal foam. Journal of Porous Materials, 2011. 18(4): p. 417-424.

68. Dukhan, N., Correlations for the pressure drop for flow through metal foam. Experiments in Fluids, 2006. 41(4): p. 665-672.

69. Calmidi, V. and R. Mahajan, Forced convection in high porosity metal foams. Journal of Heat Transfer, 2000. 122(3): p. 557-565.

70. Calmidi, V.V. and R.L. Mahajan, The effective thermal conductivity of high porosity fibrous metal foams. Journal of Heat Transfer-Transactions of the ASME, 1999. 121(2): p. 466-471.

71. Mendes, M.A., Goetze, P., Talukdar, P., Werzner, E., Demuth, C., Rössger, P., Wulf, R., Gross, U., Trimis, D. and Ray, S., Measurement and simplified numerical prediction of effective thermal conductivity of open-cell ceramic foams at high temperature. International Journal of Heat and Mass Transfer, 2016. 102: p. 396-406.

72. Zafari, M., Panjepour, M., Emami, M.D. and Meratian, M., Microtomography-based numerical simulation of fluid flow and heat transfer in open cell metal foams. Applied Thermal Engineering, 2015. 80: p. 347-354.

73. Dul'nev, G.N. and B.L. Muratova, Thermal conductivity of fibrous systems. Journal of Engineering Physics, 1972. 14(1): p. 15-18.

74. Ahmed, J., C. Pham-Huu, and D. Edouard, A predictive model based on tortuosity for pressure drop estimation in ‘ slim’ and ‘ fat’ foams. Chemical Engineering Science, 2011. 66(20): p. 4771-4779.

75. G. Fourie, J. and J. P. Du Plessis, Pressure drop modelling in cellular metallic foams. Chemical Engineering Science, 2002. 57(14): p. 2781-2789.

76. Bear, J., Dynamics of Fluids in Porous Media. Environmental Science, Ed. ISBN-13:978-0486-65675-5. 1972, New York: Dover Publications, INC. 122-130.

77. Bağcı, Ö., N. Dukhan, and M. Özdemir, Flow regimes in packed beds of spheres from Pre-Darcy to turbulent. Transport in Porous Media, 2014. 104(3): p. 501-520.

78. Boomsma, K. and D. Poulikakos, The effects of compression and pore size variations on the liquid flow characteristics in metal foams. Journal of Fluids Engineering-Transactions of the ASME, 2002. 124(1): p. 263-272.

79. Darcy, H., Les fontaines publiques de la ville de Dijon. Paris: Dalmont, 1856.

80. Lage, J.L. and B.V. Antohe, Darcy's experiments and the deviation to nonlinear flow regime. Journal of Fluids Engineering-Transactions of the ASME, 2000. 122(3): p. 619-625.

81. Carman, P.C., Fluid flow through granular beds. Transactions-Institution of Chemical Engineers, 1937. 15: p. 150-166.

82. Kundu, P., V. Kumar, and I.M. Mishra, Experimental and numerical investigation of fluid flow hydrodynamics in porous media: Characterization of pre-Darcy, Darcy and non-Darcy flow regimes. Powder Technology, 2016. 303: p. 278-291.

83. Choi, Y.S., S.J. Kim, and D. Kim, A semi- empirical correlation for pressure drop in packed beds of spherical particles. Transport in Porous Media, 2008. 75(2): p. 133-149.

84. Ergun, S., Fluid Flow Through Packed Columns. Chemical Engineering Prog., 1952. 48 (2): p. 89-94.

85. Comiti, J. and M. Renaud, A new model for determining mean structure parameters of fixed beds from pressure drop measurements: application to beds packed with parallelepipedal particles. Chemical Engineering Science, 1989. 44(7): p. 1539-1545.

86. Kececioglu, I. and Y.X. Jiang, Flow in Porous Media of Packed Spheres Saturated with Water. Journal of Fluids Engineering-Transactions of the ASME, 1994. 116(1): p. 164-170.

87. Fand, R.M., Kim, B.Y.K., Lam, A.C.C. and Phan, R.T., Resistance to the Flow of Fluids through Simple and Complex Porous Media Whose Matrices are Composed of Randomly Packed Spheres. Journal of Fluids Engineering-Transactions of the ASME, 1987. 109(3): p. 268-274.

88. Macdonald, I.F., El-Sayed, M.S., Mow, K. and Dullien, F.A.L., Flow through porous media-the Ergun equation revisited. Industrial & Engineering Chemistry Fundamentals, 1979. 18(3): p. 199-208.

89. Li, L., S. Gong, and W. Ma, Experimental Study of Two Phase Flow regime and Pressure Drop in a Particulate Bed Packed with Multidiameter Particles. Nuclear Technology, 2012. 177(1): p. 107-118.

90. Bağcı, Ö. and N. Dukhan, Experimental hydrodynamics of high-porosity metal foam: Effect of pore density. International Journal of Heat and Mass Transfer, 2016. 103: p. 879-885.

91. Dukhan, N. and M. Ali, On Various Flow Regimes in Open-Cell Metal Foam. International Journal of Transport Phenomena, 2012. 13(2).

92. Beavers, G.S. and E.M. Sparrow, Non- Darcy Flow through Fibrous Porous Media. Journal of Applied Mechanics, 1969. 36(4): p. 711.

93. Bağci, Ö., N. Dukhan, and M. Özdemir, Flow Regimes in Packed Beds of Spheres from Pre-Darcy to Turbulent. Transport in Porous Media, 2014. 104(3): p. 501-520.

94. Dukhan, N., Ö. Bağci, and M. Özdemir, Metal foam hydrodynamics: Flow regimes from pre-Darcy to turbulent. International Journal of Heat and Mass Transfer, 2014. 77: p. 114-123.

95. Kececioglu, I. and Y. Jiang, Flow through porous media of packed spheres saturated with water. Journal of Fluids Engineering, Transactions of the ASME, 1994. 116(1): p. 164-170.

96. Antohe, B.V., Lage, J.L., Price, D.C. and Weber, R.M., Experimental determination of permeability and inertia coefficients of mechanically compressed aluminum porous matrices. Journal of Fluids Engineering-Transactions of the ASME, 1997. 119(2): p. 404-412.

97. Kouidri, A. and B. Madani, Experimental hydrodynamic study of flow through metallic foams: Flow regime transitions and surface roughness influence. Mechanics of Materials, 2016. 99: p. 79-87.

98. Sedghi-Asl, M., H. Rahimi, and R. Salehi, Non-Darcy Flow of Water Through a Packed Column Test. Transport in Porous Media, 2014. 101(2): p. 215-227.

99. Li, Z., Wan, J., Huang, K., Chang, W. and He, Y., Effects of particle diameter on flow characteristics in sand columns. International Journal of Heat and Mass Transfer, 2017. 104: p. 533-536.

100. Huang, K., Wan, J.W., Chen, C.X., He, L.Q., Mei, W.B. and Zhang, M.Y., Experimental investigation on water flow in cubic arrays of spheres. Journal of Hydrology, 2013. 492: p. 61-68.

101. Ribeiro, A., P. Neto, and C. Pinho, Mean porosity and pressure drop measurements in packed beds of monosized spheres: side wall effects. International Review of Chemical Engineering, 2010. 2(1): p. 40-46.

102. Montillet, A., J. Comiti, and J. Legrand, Determination of Structural Parameters of Metallic Foams from Permeametry Measurements. Journal of Materials Science, 1992. 27(16): p. 4460-4464.

103. Liu, J.F., Wu, W.T., Chiu, W.C. and Hsieh, W.H., Measurement and correlation of friction characteristic of flow through foam matrixes. Experimental Thermal and Fluid Science, 2006. 30(4).

104. Dukhan, N., O. Bagci, and M. Ozdemir, Metal foam hydrodynamics: Flow regimes from pre-Darcy to turbulent. International Journal of Heat and Mass Transfer, 2014. 77: p. 114-123.

105. Paek, J.W., Kang, B.H., Kim, S.Y. and Hyun, J.M., Effective thermal conductivity and permeability of aluminium foam materials1. International Journal of Thermophysics, 2000. 21(2): p. 453-464.

106. Dybbs, A. and R.V. Edwards. New Look at Porous Media Fluid Mechanics - Darcy to Turbulent. In NATO ASI Series, Series E: Applied Sciences. 1984.

107. Lage, J.L., B.V. Antohe, and D.A. Nield, Two types of nonlinear pressure-drop versus flow-rate relation observed for saturated porous media. Journal of Fluids Engineering-Transactions of the ASME, 1997. 119(3): p. 700-706.

108. Oun, H. and A. Kennedy, Tailoring the pressure-drop in multi-layered open-cell porous Inconel structures. Journal of Porous Materials, 2015. 22(6): p. 1627-1633.

109. Dukhan, N. and P. Patel, Equivalent particle diameter and length scale for pressure drop in porous metals. Experimental Thermal and Fluid Science, 2008. 32(5): p. 1059-1067.

110. Kamath, P.M., C. Balaji, and S. Venkateshan, A simple thermal resistance model for open cell metal foams. Journal of Heat Transfer, 2013. 135(3): p. 032601.

111. Kumar, P. and F. Topin, Investigation of fluid flow properties in open cell foams: Darcy and weak inertia regimes. Chemical Engineering Science, 2014. 116: p. 793-805.

112. Kumar, P. and F. Topin, Micro-structural Impact of Different Strut Shapes and Porosity on Hydraulic Properties of Kelvin-Like Metal Foams. Transport in Porous Media, 2014. 105(1): p. 57-81.

113. Ou, X., Zhang, X., Lowe, T., Blanc, R., Rad, M.N., Wang, Y., Batail, N., Pham, C., Shokri, N., Garforth, A. and Withers, P., X-ray micro computed tomography characterization

of cellular SiC foams for their applications in chemical engineering. Materials Characterization, 2017. 123: p. 20-28.

114. Ranut, P., E. Nobile, and L. Mancini, High resolution X-ray microtomography-based CFD simulation for the characterization of flow permeability and effective thermal conductivity of aluminium metal foams. Experimental Thermal and Fluid Science, 2015. 67: p. 30-36.

115. Vafai, K. and C.L. Tien, Boundary and inertia effects on convective mass transfer in porous media. International Journal of Heat and Mass Transfer, 1982. 25(8): p. 1183-1190.

116. Du Plessis, P., Montillet, A., Comiti, J. and Legrand, J., Pressure Drop Prediction for Flow through High Porosity Metallic Foams. Chemical Engineering Science, 1994. 49(21): p. 3545-3553.

117. Lacroix, M., Nguyen, P., Schweich, D., Huu, C.P., Savin-Poncet, S. and Edouard, D., Pressure drop measurements and modelling on SiC foams. Chemical Engineering Science, 2007. 62(12): p. 3259-3267.

118. Richardson, J.T., Y. Peng, and D. Remue, Properties of ceramic foam catalyst supports: pressure drop. Applied Catalysis A: General, 2000. 204(1): p. 19-32.

119. Crosnier, S., Rivam, R., Bador, B. and Blet, V., Modelling of gas flow through metallic foams. In 1st European Hydrogen Energy Conference. 2003.

120. Topin, F., Bonnet, J.P., Madani, B. and Tadrist, L., Experimental Analysis of Multiphase Flow in Metallic foam: Flow Laws, Heat Transfer and Convective Boiling. Advanced Engineering Materials, 2006. 8(9): p. 890-899.

121. Mancin, S., Zilio, C., Diani, A. and Rossetto, L., Experimental air heat transfer and pressure drop through copper foams. Experimental Thermal and Fluid Science, 2012. 36: p. 224-232.

122. Hwang, J.J., Hwang, G.J., Yeh, R.H. and Chao, C.H., Measurement of interstitial convective heat transfer and frictional drag for flow across metal foams. Journal of Heat Transfer-Transactions of the ASME, 2002. 124(1): p. 120-129.

123. Wu, Z., Caliot, C., Bai, F., Flamant, G., Wang, Z., Zhang, J. and Tian, C., Experimental and numerical studies of the pressure drop in ceramic foams for volumetric solar receiver applications. Applied Energy, 2010. 87(2): p. 504-513.

124. Medraj, M., Baril, E., Loya, V. and Lefebvre, L.P., The effect of microstructure on the permeability of metallic foams. Journal of Materials Science, 2007. 42(12): p. 4372-4383.

125. Reutter, O., Smirnova, E., Sauerhering, J., Angel, S., Fend, T. and Pitz-Paal, R., Characterization of air flow through sintered metal foams. Journal of Fluids Engineering, 2008. 130(5): p. 051201.

126. Khayargoli, P., Loya, V., Lefebvre, L.P. and Medraj, M., The impact of microstructure on the permeability of metal foams. 2004, CSME 2004 Forum: Canada.

127. Wang, H. and L. Guo, Experimental investigation on pressure drop and heat transfer in metal foam filled tubes under convective boundary condition. Chemical Engineering Science, 2016. 155: p. 438-448.

128. Dukhan, N. and M. Ali, Strong wall and transverse size effects on pressure drop of flow through open-cell metal foam. International Journal of Thermal Sciences, 2012. 57(0): p. 85-91.

129. Inayat, A., Schwerdtfeger, J., Freund, H., Körner, C., Singer, R.F. and Schwieger, W., Periodic open-cell foams: Pressure drop measurements and modelling of an ideal tetrakaidecahedra packing. Chemical Engineering Science, 2011. 66(12): p. 2758-2763.

130. Nawaz, K., Bock, J. and Jacobi, A.M., Thermal-Hydraulic Performance of Metal Foam Heat Exchangers. 2012, International Refrigeration and Air Conditioning Conference at Purdue.

131. Kim, S.Y., J.W. Paek, and B.H. Kang, Flow and Heat Transfer Correlations for Porous Fin in a Plate-Fin Heat Exchanger. Journal of Heat Transfer, 2000. 122(3): p. 572-578.

132. Despois, J.F. and A. Mortensen, Permeability of open-pore microcellular materials. Acta Materialia, 2005. 53(5): p. 1381-1388.

133. Goodall, R., Marmottant, A., Salvo, L. and Mortensen, A., Spherical pore replicated microcellular aluminium: Processing and influence on properties. Materials Science and Engineering: A, 2007. 465(1): p. 124-135.

134. Zhong, W., Li, X., Liu, F., Tao, G., Lu, B. and Kagawa, T., Measurement and Correlation of Pressure Drop Characteristics for Air Flow Through Sintered Metal Porous Media. Transport in Porous Media, 2014. 101(1): p. 53-67.

135. Zhong, W., Li, X., Tao, G. and Kagawa, T., Measurement and Determination of Friction Characteristic of Air Flow through Porous Media. Metals, 2015. 5(1): p. 336-349.

136. Amiri, A. and K. Vafai, Analysis of dispersion effects and non-thermal equilibrium, non-Darcian, variable porosity incompressible flow through porous media. International Journal of Heat and Mass Transfer, 1994. 37(6): p. 939-954.

137. Zhao, C.Y., Kim, T., Lu, T.J. and Hodson, H.P., Thermal transport phenomena in Porvair metal foams and sintered beds. University of Cambridge, Final Report, 2001.

138. Tzeng, S.-C. and T.-M. Jeng, Interstitial Heat Transfer Coefficient and Dispersion Conductivity in Compressed Metal Foam Heat Sinks. Journal of Electronic Packaging, 2006. 129(2): p. 113-119.

139. Dukhan, N., R. Picon-Feliciano, and A.R. Alvarez-Hernandez, Air flow through compressed and uncompressed aluminium foam: Measurements and correlations. Journal of Fluids Engineering-Transactions of the ASME, 2006. 128(5): p. 1004-1012.

140. Hamaguchi, K., S. Takahashi, and H. Miyabe, Flow friction and heat transfer characteristics of a regenerator matrix (case of foamed metal). Transactions of the Japan Society of Mechanical Engineering, 1983. 49: p. 1991-2000.

141. Takegoshi, E., Hirasawa, Y., Matsuo, J. and Okui, K., A study on effective thermal conductivity of porous metals. Transactions of the Japan Society of Mechanical Engineering, Series A, 1992. 58(547): p. 237-242.

142. Bonnet, J.-P., F. Topin, and L. Tadrist, Flow Laws in Metal Foams: Compressibility and Pore Size Effects. Transport in Porous Media, 2008. 73(2): p. 233-254.

143. Dukhan, N. and K. Patel, Effect of sample's length on flow properties of open-cell metal foam and pressure-drop correlations. Journal of Porous Materials, 2011. 18(6): p. 655-665.

144. Moreira, E., M. Innocentini, and J. Coury, Permeability of ceramic foams to compressible and incompressible flow. Journal of the European Ceramic Society, 2004. 24(10): p. 3209-3218.

145. Du Plessis, J.P. and J.H. Masliyah, Mathematical modelling of flow through consolidated isotropic porous media. Transport in Porous Media, 1988. 3(2): p. 145-161.

146. Huu, T.T., et al., Towards a more realistic modelling of solid foam: Use of the pentagonal dodecahedron geometry. Chemical Engineering Science, 2009. 64(24): p. 5131-5142.

147. Boomsma, K., D. Poulikakos, and Y. Ventikos, Simulations of flow through open cell metal foams using an idealized periodic cell structure. International Journal of Heat and Fluid Flow, 2003. 24(6): p. 825-834.

148. Lu, T.J., H.A. Stone, and M.F. Ashby, Heat transfer in open-cell metal foams. Acta Materialia, 1998. 46(10): p. 3619-3635.

149. Scheidegger, A.E., The physics of flow through porous media. Revised ed. 1960, Toronto: Toronto: University of Toronto Press, 1960.

150. Mahjoob, S. and K. Vafai, A synthesis of fluid and thermal transport models for metal foam heat exchangers. International Journal of Heat and Mass Transfer, 2008. 51(15–16): p. 3701-3711.

151. Zhao, C.Y., Kim, T., Lu, T.J. and Hodson, H.P., Thermal transport in high porosity cellular metal foams. Journal of Thermophysics and Heat Transfer, 2004. 18(3): p. 309-317.

152. Dukhan, N. and C.A. Minjeur Ii. Minimum thickness for open-cell metal foam to behave as a porous medium. 2010. In *40th Fluid Dynamics Conference and Exhibit* (p. 4618).

153. Kamath, P.M., C. Balaji, and S.P. Venkateshan, Convection heat transfer from aluminium and copper foams in a vertical channel - An experimental study. International Journal of Thermal Sciences, 2013. 64: p. 1-10.

154. Oliviero, M., Cunsolo, S., Harris, W.M., Iasiello, M., Chiu, W.K.S., Naso, V. and Bianco, Microtomography-based analysis of pressure drop and heat transfer through open cell metal foams. In ASME 2013 Heat Transfer Summer Conference collocated with the ASME 2013 7th International Conference on Energy Sustainability and the ASME 2013 11th International Conference on Fuel Cell Science, Engineering and Technology. 2013. American Society of Mechanical Engineers.

155. Bodla, K.K., J.Y. Murthy, and S.V. Garimella, Microtomography-based simulation of transport through open-cell metal foams. Numerical Heat Transfer, Part A: Applications, 2010. 58(7): p. 527-544.

156. Mendes, M.A.A., S. Ray, and D. Trimis, An improved model for the effective thermal conductivity of open-cell porous foams. International Journal of Heat and Mass Transfer, 2014. 75: p. 224-230.

157. Xiao, X., P. Zhang, and M. Li, Effective thermal conductivity of open-cell metal foams impregnated with pure paraffin for latent heat storage. International Journal of Thermal Sciences, 2014. 81(1): p. 94-105.

158. Dyga, R. and Witczak, S., 2012. Investigation of effective thermal conductivity aluminium foams. *Procedia Engineering*, *42*, pp.1088-1099.

159. Zhao, C.Y., Lu, T.J., Hodson, H.P. and Jackson, J.D., The temperature dependence of effective thermal conductivity of open-celled steel alloy foams. Materials Science and Engineering: A, 2004. 367(1–2): p. 123-131.

160. Ranut, P. and E. Nobile, On the effective thermal conductivity of metal foams. Journal of Physics: Conference Series, 2014. 547(1).

161. Maxwell, J.C., A treatise on electricity and magnetism. 3rd ed. / unabridged. ed. 1954, New York: New York: Dover, 1954.

162. Hsu, C., P. Cheng, and K. Wong, Modified Zehner-Schlunder models for stagnant thermal conductivity of porous media. International Journal of Heat and Mass Transfer, 1994. 37(17): p. 2751-2759.

163. Leach, A., The thermal conductivity of foams. I. Models for heat conduction. Journal of Physics D: Applied Physics, 1993. 26(5): p. 733.

164. Boomsma, K. and D. Poulikakos, On the effective thermal conductivity of a three-dimensionally structured fluid-saturated metal foam. International Journal of Heat and Mass Transfer, 2001. 44(4): p. 827-836.

165. Singh, R. and H.S. Kasana, Computational aspects of effective thermal conductivity of highly porous metal foams. Applied Thermal Engineering, 2004. 24(13): p. 1841-1849.

166. Mendes, M.A.A., S. Ray, and D. Trimis, A simple and efficient method for the evaluation of effective thermal conductivity of open-cell foam-like structures. International Journal of Heat and Mass Transfer, 2013. 66: p. 412-422.

167. Coquard, R., D. Rochais, and D. Baillis, Conductive and Radiative Heat Transfer in Ceramic and Metal Foams at Fire Temperatures. Fire Technology, 2012. 48(3): p. 699-732.

168. Ranut, P., On the effective thermal conductivity of aluminium metal foams: Review and improvement of the available empirical and analytical models. Applied Thermal Engineering, 2016. 101: p. 496-524.

169. Yang, X.H., Kuang, J.J., Lu, T.J., Han, F.S. and Kim, T., A simplistic analytical unit cell based model for the effective thermal conductivity of high porosity open-cell metal foams. J. Phys. D-Appl. Phys., 2013. 46(25).

170. Kirkpatrick, S., Percolation and Conduction. Reviews of Modern Physics, 1973. 45(4): p. 574-588.

171. Abuserwal, A.F., Luna, E.M.E., Goodall, R. and Woolley, R., The effective thermal conductivity of open cell replicated aluminium metal sponges. International Journal of Heat and Mass Transfer, 2017. 108, Part B: p. 1439-1448.

172. Lu, T.J. and C. Chen, Thermal transport and fire retardance properties of cellular aluminium alloys. Acta Materialia, 1999. 47(5): p. 1469-1485.

173. Coquard, R., D. Rochais, and D. Baillis, Experimental investigations of the coupled conductive and radiative heat transfer in metallic/ceramic foams. International Journal of Heat and Mass Transfer, 2009. 52(21): p. 4907-4918.

174. Laschet, G., Sauerhering, J., Reutter, O., Fend, T. and Scheele, J., Effective permeability and thermal conductivity of open-cell metallic foams via homogenization on a microstructure model. Computational Materials Science, 2009. 45(3): p. 597-603.

175. Wulf, R., Mendes, M.A., Skibina, V., Al-Zoubi, A., Trimis, D., Ray, S. and Gross, U., Experimental and numerical determination of effective thermal conductivity of open cell FeCrAl-alloy metal foams. International Journal of Thermal Sciences, 2014. 86: p. 95-103.

176. Gustafsson, S.E., Transient plane source techniques for thermal conductivity and thermal diffusivity measurements of solid materials. Review of Scientific Instruments, 1991. 62(3): p. 797-804.

177. Gustafsson, S., A device for measuring thermal properties of a sample of a substance. 1989, Google Patents.

178. Thewsey, D. and Y. Zhao, Thermal conductivity of porous copper manufactured by the lost carbonate sintering process. Phyisca Status Solidi (A) Applications and Materials Science, 2008. 205(5): p. 1126.

179. Babcsán, N., I. Mészáros, and N. Hegman, Thermal and electrical conductivity measurements on aluminium foams. Materialwissenschaft und Werkstofftechnik, 2003. 34(4): p. 391-394.

180. Ye, H., M. Ma, and Q. Ni, An experimental study on mid-high temperature effective thermal conductivity of the closed-cell aluminium foam. Applied Thermal Engineering, 2015. 77: p. 127-133.

181. Sadeghi, E., S. Hsieh, and M. Bahrami. Thermal contact resistance at a metal foam-solid surface interface. In ASME/JSME 2011 8th Thermal Engineering Joint Conference, AJTEC 2011. 2011.

182. Dias, R.P., Fernandes, C.S., Mota, M., Teixeira, J.A. and Yelshin, A., Permeability and effective thermal conductivity of bisized porous media. International Journal of Heat and Mass Transfer, 2007. 50(7-8): p. 1295-1301.

183. Fischedick, T., M. Kind, and B. Dietrich, High temperature two-phase thermal conductivity of ceramic sponges with stagnant fluid – Experimental results and correlation including thermal radiation. International Journal of Thermal Sciences, 2015. 96: p. 1-11.

184. Skochdopole, R.E., The Thermal Conductivity of Foamed Plastics. Chemical Engineering Progress, 1961(55:57): p. 10.

185. Copyright of Volume I A2 - Laughlin, David E, in Physical Metallurgy (Fifth Edition), K. Hono, Editor. 2014, Elsevier: Oxford. p. iv.

186. Fu, X., R. Viskanta, and J.P. Gore, Measurement and correlation of volumetric heat transfer coefficients of cellular ceramics. Experimental Thermal and Fluid Science, 1998. 17(4): p. 285-293.

187. Dukhan, N., R. Picón-Feliciano, and Á.R. Álvarez-Hernández, Heat Transfer Analysis in Metal Foams with Low-Conductivity Fluids. Journal of Heat Transfer, 2006. 128(8): p. 784-792.

188. Dukhan, N., Ö. Bağcı, and M. Özdemir, Thermal development in open-cell metal foam: An experiment with constant wall heat flux. International Journal of Heat and Mass Transfer, 2015. 85: p. 852-859.

189. Lee, D.-Y. and K. Vafai, Analytical characterization and conceptual assessment of solid and fluid temperature differentials in porous media. International Journal of Heat and Mass Transfer, 1999. 42(3): p. 423-435.

190. Chen, P.H. and Z.C. Chang, An improved model for the single-blow measurement including the non-adiabatic side wall effect. International Communications in Heat and Mass Transfer, 1996. 23(1): p. 55-68.

191. Ranganayakulu, C., X. Luo, and S. Kabelac, The single-blow transient testing technique for offset and wavy fins of compact plate-fin heat exchangers. Applied Thermal Engineering, 2016.

192. Guo-Yan, Z., T. Shan-Tung, and M. Hu-Gen, Numerical and Experimental Study on the Heat Transfer and Pressure Drop of Compact Cross-Corrugated Recuperators. Journal of Heat Transfer, 2014. 136(7): p. 071801.

193. Chen, P.H., Z.C. Chang, and B.J. Huang, Effect of oversize in wire-screen matrix to the matrix-holding tube on regenerator thermal performance. Cryogenics, 1996. 36(5): p. 365-372.

194. Chen, P.H. and Z.C. Chang, Measurements of thermal performance of cryocooler regenerators using an improved single-blow method. International Journal of Heat and Mass Transfer, 1997. 40(10): p. 2341-2349.

195. Nielsen, K.K., K. Engelbrecht, and C.R. Bahl, The influence of flow maldistribution on the performance of inhomogeneous parallel plate heat exchangers. International Journal of Heat and Mass Transfer, 2013. 60: p. 432-439.

196. Nielsen, K.K., G.F. Nellis, and S.A. Klein, Numerical modelling of the impact of regenerator housing on the determination of Nusselt numbers. International Journal of Heat and Mass Transfer, 2013. 65: p. 552-560.

197. Elizondo Luna, E.M., Investigation of Porous Metals as Improved Efficiency Regenerators. 2016, University of Sheffield.

198. Kamiuto, K., Heat transfer correlations for open-cellular porous materials. International Communications in Heat and Mass Transfer, 2005. 32(7): p. 947-953.

199. Younis, L.B. and R. Viskanta, Experimental determination of volumetric heat transfer coefficient between streams of air and ceramic foam. International Journal of Heat and Mass Transfer, 1993. 36(6): p. 1425-1434.

200. Ando, K., Hirai, H. and Sano, Y., An Accurate Experimental Determination of Interstitial Heat Transfer Coefficients of Ceramic Foams Using the Single Blow Method, The Open Transport Phenomena Journal, 2013. **5**, pp. 7-12

201. Dietrich, B., Heat transfer coefficients for solid ceramic sponges–experimental results and correlation. International Journal of Heat and Mass Transfer, 2013. 61: p. 627-637.

202. Vijay, D., Goetze, P., Wulf, R. and Gross, U., Forced convection through open cell foams based on homogenization approach: Steady state analysis. International Journal of Thermal Sciences, 2015. 98: p. 381-394.

203. Vijay, D., Goetze, P., Wulf, R. and Gross, U., Forced convection through open cell foams based on homogenization approach: Transient analysis. International Journal of Thermal Sciences, 2015. 98: p. 395-408.

204. Moon, C., Kim, D., Abadi, G.B., Yoon, S.Y. and Kim, K.C., Effect of ligament hollowness on heat transfer characteristics of open-cell metal foam. International Journal of Heat and Mass Transfer, 2016. 102: p. 911-918.

205. Renken, K. and D. Poulikakos, Forced convection in channel filled with porous medium, including the effects of flow inertia, variable porosity, and Brinkman friction. ASME Journal of Heat transfer, 1987. 109: p. 880-888.

206. Geb, D., K. Sbutega, and I. Catton. A New Technique for Measuring Convective Heat Transfer Coefficients in Solid Matrices for Compact Heat Exchanger Design. in ASME 2012 Heat Transfer Summer Conference collocated with the ASME 2012 Fluids Engineering Division Summer Meeting and the ASME 2012 10th International Conference on Nanochannels, Microchannels, and Minichannels. 2012. American Society of Mechanical Engineers.

207. Xu, H., Gong, L., Huang, S. and Xu, M., Flow and heat transfer characteristics of nanofluid flowing through metal foams. International Journal of Heat and Mass Transfer, 2015. 83: p. 399-407.

208. Salas, K.I. and A.M. Waas, Convective heat transfer in open cell metal foams. Journal of Heat Transfer-Transactions of the ASME, 2007. 129(9): p. 1217-1229.

209. Sim, Y.S. and Y. Wen-Jei, New performance-evaluation analyses on heat transfer surfaces by single-blow technique. International journal of heat and mass transfer, 1987. 30(8): p. 1587-1594.

210. Hunt, M.L. and C.L. Tien, Effects of thermal dispersion on forced convection in fibrous media. International Journal of Heat and Mass Transfer, 1988. 31(2): p. 301-309.

211. Achenbach, E., Heat and flow characteristics of packed beds. Experimental Thermal and Fluid Science, 1993. 7(2): p. 129.

212. Kim, S.Y., B.H. Kang, and J.-H. Kim, Forced convection from aluminium foam materials in an asymmetrically heated channel. International Journal of Heat and Mass Transfer, 2001. 44(7): p. 1451-1454.

213. Hsieh, W.H., Wu, J.Y., Shih, W.H. and Chiu, W.C., Experimental investigation of heat-transfer characteristics of aluminium-foam heat sinks. International Journal of Heat and Mass Transfer, 2004. 47(23): p. 5149-5157.

214. DeGroot, C.T., A.G. Straatman, and L.J. Betchen, Modelling Forced Convection in Finned Metal Foam Heat Sinks. Journal of Electronic Packaging, 2009. 131(2): p. 021001-021001-10.

215. Zhang, H., Chen, L., Liu, Y. and Li, Y., Experimental study on heat transfer performance of lotus-type porous copper heat sink. International Journal of Heat and Mass Transfer, 2013. 56(1–2): p. 172-180.

216. Kim, S.Y., J.W. Paek, and B.H. Kang, Thermal performance of aluminium-foam heat sinks by forced air cooling. IEEE Transactions on components and packaging technologies, 2003. 26(1): p. 262-267.

217. Shih, W.-H., C.-C. Liu, and W.-H. Hsieh, Heat-transfer characteristics of aluminium-foam heat sinks with a solid aluminium core. International Journal of Heat and Mass Transfer, 2016. 97: p. 742-750.

218. Ichimiya, K., A New Method for Evaluation of Heat Transfer between Solid Material and Fluid in a Porous Medium. Journal of Heat Transfer, 1999. 121(4): p. 978-983.

219. Karlekar, B.V. and R.M. Desmond, Engineering heat transfer. 1977: West publishing company.

220. Yang, K. and K. Vafai, Transient Aspects of Heat Flux Bifurcation in Porous Media: An Exact Solution. Journal of Heat Transfer, 2011. 133(5): p. 052602-052602-12.

221. Mahmoudi, Y., Effect of thermal radiation on temperature differential in a porous medium under local thermal non-equilibrium condition. International Journal of Heat and Mass Transfer, 2014. 76: p. 105-121.

222. Dukhan, N., Quinones-Ramos, P.D., Cruz-Ruiz, E., Velez-Reyes, M. and Scott, E.P., One-dimensional heat transfer analysis in open-cell 10-ppi metal foam. International Journal of Heat and Mass Transfer, 2005. 48(25–26): p. 5112-5120.

223. Ghosh, I., Heat-Transfer Analysis of High Porosity Open-Cell Metal Foam. Journal of Heat Transfer, 2008. 130(3): p. 034501-034501.

224. Lu, W., T. Zhang, and M. Yang, Analytical solution of forced convective heat transfer in parallel-plate channel partially filled with metallic foams. International Journal of Heat and Mass Transfer, 2016. 100: p. 718-727.

225. Guarino, S., Rubino, G., Tagliaferri, V. and Ucciardello, N., Thermal behaviour of open cell aluminium foams in forced air: experimental analysis. Measurement, 2015. 60: p. 97-103.

226. Nie, X., Evitts, R., Besant, R. and Bolster, J., A New Technique to Determine Convection Coefficients with Flow through Particle Beds. Journal of Heat Transfer, 2011. 133(4): p. 041601.

227. Lerro, A., Geb, D., Sbutega, K. and Catton, I., A Single Blow Transient Test Technique With Volume Averaging Theory Modelling for Random Fibre Matrices. in ASME 2012 Heat Transfer Summer Conference collocated with the ASME 2012 Fluids Engineering Division Summer Meeting and the ASME 2012 10th International Conference on Nanochannels, Microchannels, and Minichannels. 2012. American Society of Mechanical Engineers.

228. Prasad, S.B., J.S. Saini, and K.M. Singh, Investigation of heat transfer and friction characteristics of packed bed solar air heater using wire mesh as packing material. Solar Energy, 2009. 83(5): p. 773-783.

229. Thakur, N., J. Saini, and S. Solanki, Heat transfer and friction factor correlations for packed bed solar air heater for a low porosity system. Solar Energy, 2003. 74(4): p. 319-329.

230. Kamiuto, K. and S.S. Yee, Heat transfer correlations for open-cellular porous materials. International Communications in Heat and Mass Transfer, 2005. 32(7): p. 947-953.

231. Xiao, Z. and Y. Zhao, Heat transfer coefficient of porous copper with homogeneous and hybrid structures in active cooling. Journal of Materials Research, 2013. 28(17): p. 2545-2553.

232. Wen, D. and Y. Ding, Heat transfer of gas flow through a packed bed. Chemical Engineering Science, 2006. 61(11): p. 3532-3542.

233. Nakayama, A., Ando, K., Yang, C., Sano, Y., Kuwahara, F. and Liu, J., A study on interstitial heat transfer in consolidated and unconsolidated porous media. Heat and Mass Transfer, 2009. 45(11): p. 1365-1372.

234. Kurtbas, I. and N. Celik, Experimental investigation of forced and mixed convection heat transfer in a foam-filled horizontal rectangular channel. International Journal of Heat and Mass Transfer, 2009. 52(5–6): p. 1313-1325.

235. Fedorov, A. and R. Viskanta, A numerical simulation of conjugate heat transfer in an electronic package formed by embedded discrete heat sources in contact with a porous heat sink. Journal of Electronic Packaging, 1997. 119(1): p. 8-16.

236. Xu, Z.G. and C.Y. Zhao, Enhanced boiling heat transfer by gradient porous metals in saturated pure water and surfactant solutions. Applied Thermal Engineering, 2016. 100: p. 68-77.

237. Odabaee, M., K. Hooman, and H. Gurgenci, Metal Foam Heat Exchangers for Heat Transfer Augmentation from a Cylinder in Cross-Flow. Transport in Porous Media, 2011. 86(3): p. 911-923.

238. Chen, X., F. Tavakkoli, and K. Vafai, Analysis and Characterization of Metal Foam-Filled Double-Pipe Heat Exchangers. Numerical Heat Transfer, Part A: Applications, 2015. 68(10): p. 1031-1049.

239. Ströhle, S., Haselbacher, A., Jovanovic, Z.R. and Steinfeld, A., Transient discrete-granule packed-bed reactor model for thermochemical energy storage. Chemical Engineering Science, 2014. 117: p. 465-478.

240. Costa, S.C., Tutar, M., Barreno, I., Esnaola, J.A., Barrutia, H., García, D., González, M.A. and Prieto, J.I., Experimental and numerical flow investigation of Stirling engine regenerator. Energy, 2014. 72: p. 800-812.

241. Duprat, F. and G. Lopez Lopez, Comparison of performance of heat regenerators: relation between heat transfer efficiency and pressure drop. International Journal of Energy Research, 2001. 25(4): p. 319-329.

242. Ehsani, M., S. Movahedirad, and S. Shahhosseini, The effect of particle properties on the heat transfer characteristics of a liquid–solid fluidized bed heat exchanger. International Journal of Thermal Sciences, 2016. 102: p. 111-121.

243. Kuwahara, F., M. Shirota, and A. Nakayama, A numerical study of interfacial convective heat transfer coefficient in two-energy equation model for convection in porous media. International Journal of Heat and Mass Transfer, 2001. 44(6): p. 1153-1159.

244. Sir Thomson, W., On the division of space with minimum partitional area. Acta Mathematica, 1887. 11(1): p. 121-134.

245. Pusterla, S., Barbato, M., Ortona, A. and D'Angelo, C., Numerical study of cell morphology effects on convective heat transfer in reticulated ceramics. International Journal of Heat and Mass Transfer, 2012. 55(25-26): p. 7902-7910.

246. Noh, J.S., K.B. Lee, and C.G. Lee, Pressure loss and forced convective heat transfer in an annulus filled with aluminium foam. International Communications in Heat and Mass Transfer, 2006. 33(4): p. 434-444.

247. Hlushkou, D. and U. Tallarek, Transition from creeping via viscous-inertial to turbulent flow in fixed beds. Journal of Chromatography A, 2006. 1126(1–2): p. 70-85.

248. Weber, L., Ingram, D., Guardia, S., Athanasiou-Ioannou, A. and Mortensen, A., Fluid flow through replicated microcellular materials in the Darcy-Forchheimer regime. Acta Materialia, 2017.

249. Hamagutci, K., S. Takahashi, and H. Miyabe, Flow Friction and Heat Transfer Characteristics of a Regenerator Matrix: Case of Foamed Metal. Transactions of the Japan Society of Mechanical Engineers Series B, 1983. 49(445): p. 1991-2000.

250. White, F.M., Fluid Mechanics. 2003, Mc GROW-HILL.

251. Standard, B., Measurement of fluid flow by means of pressure differential devices inserted in circular cross-section conduits running full, in Part 2: Orifice plates. 2003, BSI 389 Chiswick High Road London W4 4AL: London.

252. Standard, B., Measurement of fluid flow by means of pressure differential devices. Part 1: Orifice plates, nozzles and Venturi tubes inserted in circular cross-section conduits running full. BS EN ISO, 1997: p. 5167-1.

253. Gustafsson, S.E., E. Karawacki, and M.N. Khan, Transient hot-strip method for simultaneously measuring thermal conductivity and thermal diffusivity of solids and fluids. Journal of Physics D: Applied Physics, 1979. 12(9): p. 1411.

254. Holman, J.P., Heat transfer. 10th ed. ed. 2010, Boston: Boston: McGraw Hill Higher Education, c2010.

255. Sadeghi, E., S. Hsieh, and M. Bahrami, Thermal conductivity and contact resistance of metal foams. Journal of Physics D: Applied Physics, 2011. 44(12): p. 125406.

256. Liang, C.Y. and W.J. Yang, Modified single blow technique for performance evaluation on heat transfer. Journal of Heat Transfer-Transactions of the ASME, 1975. 97(1): p. 16-21.

257. Leong, K.C. and H.C. Toh, An experimental investigation of heat transfer and flow friction characteristics of louvered fin surfaces by the modified single blow technique. Heat and Mass Transfer, 1999. 35(1): p. 53-63.

258. Kays, W.M., Compact heat exchangers. 3rd ed., A.L. London. 1997, Malabar, FL: Malabar, FL: Krieger Pub, 1997.

259. Mahood, H.B., A.O. Sharif, and R.B. Thorpe, Transient volumetric heat transfer coefficient prediction of a three-phase direct contact condenser. Heat and Mass Transfer, 2015. 51(2): p. 165-170.

260. Pucci, P., C. Howard, and C. Piersall, The single-blow transient testing technique for compact heat exchanger surfaces. Journal of Engineering for Power, 1967. 89(1): p. 29-38.

261. Kays, W.M. and A.L. London, Compact heat exchangers. 1984: McGraw-Hill,New York, NY; None. Medium: X; Size: Pages: 335.

262. Loehrke, R., Evaluating the results of the single-blow transient heat exchanger test. Experimental Thermal and Fluid Science, 1990. 3(6): p. 574-580.

263. Luo, X., W. Roetzel, and U. Lüdersen, The single-blow transient testing technique considering longitudinal core conduction and fluid dispersion. International Journal of Heat and Mass Transfer, 2001. 44(1): p. 121-129.

264. Stang, J. and J. Bush, The Periodic Method for Testing Compact Heat Exchanger Surfaces. Journal of Engineering for Power, 1974. 96(2): p. 87-94.

265. Schumann, T.E.W., Heat transfer: A liquid flowing through a porous prism. Journal of the Franklin Institute, 1929. 208(3): p. 405-416.

266. Howard, C. The single-blow problem including the effects of longitudinal conduction. In ASME 1964 Gas Turbine Conference and Products Show. 1964. American Society of Mechanical Engineers.

267. Mondt, J. and D. Siegla, Performance of perforated heat exchanger surfaces. Journal of Engineering for Power, 1974. 96(2): p. 81-86.

268. Schmidt, F.W. and A.J. Willmott, Thermal Energy Storage and Regeneration. 1981, McGraw-Hill Book Company: New York.

269. Furnas, C., Heat transfer from a gas stream to bed of broken solids. Industrial & Engineering Chemistry, 1930. 22(1): p. 26-31.

270. Creswick, F., A digital computer solution of the equations for transient heating of a porous solid including the effects of longitudinal conduction. Industrial Mathematics, 1957. 8: p. 61-69.

271. Cai, Z.H., Li, M.L., Wu, Y.W. and Ren, H.S., A modified selected point matching technique for testing compact heat exchanger surfaces. International Journal of Heat and Mass Transfer, 1984. 27(7): p. 971-978.

272. Causon, D. and C. Mingham, Introductory finite difference methods for PDEs. 2010: Bookboon.

273. Chapra, S.C. and R.P. Canale, Numerical methods for engineers. Vol. 2. 2012: McGraw-Hill New York.

274. Mullisen, R.S. and R.I. Loehrke, A Transient Heat Exchanger Evaluation Test for Arbitrary Fluid Inlet Temperature Variation and Longitudinal Core Conduction. Journal of Heat Transfer, 1986. 108(2): p. 370-376.

275. Iwai, H., Kawakami, S., Suzuki, K., Tsujii, J. and Abiko, T., Performance evaluation of wire spring fin for compact plate-fin heat exchangers. 2005.

276. Locke, G., Heat transfer and flow friction characteristics of porous. Technical Report No. 10. 1950, Stanford University.

277. Kohlmayr, G.F., Exact maximum slopes for transient matrix heat-transfer testing. International Journal of Heat and Mass Transfer, 1966. 9(7): p. 671-680.

278. Tong, L.-S. and A. London, Heat-transfer and flow-friction characteristics of woven-screen and crossed-rod matrices. 1956, DTIC Document.

279. Barari, F., Metal foam regenerators heat transfer and pressure drop in porous metals. 2014, University of Sheffield.

280. Kohlmayr, G.F., Implementation of direct curve matching methods for transient matrix heat transfer testing. Applied Scientific Research, 1971. 24(1): p. 127-148.

281. British Standards, I., Measurement of fluid flow by means of pressure differential devices. Pt.1, Orifice plates, nozzles, and Venturi tubes inserted in circular cross-section conduits running full. 1997, London: London: BSI, 1997.

282. Savitzky, A. and M.J. Golay, Smoothing and differentiation of data by simplified least squares procedures. Analytical chemistry, 1964. 36(8): p. 1627-1639.

283. Math Works, I., Curve fitting toolbox: for use with MATLAB®: user's guide. 2002: Math Works.

284. Božidar Šarler, P.N.M., P. Professor P. Nithiarasu, and R. Chennu, Steady state and transient analysis of compact plate-fin heat exchanger fins for generation of design data using CFD. International Journal of Numerical Methods for Heat & Fluid Flow, 2016. 26(2): p. 440-460.

285. Luo, G., Xue, P., Li, L. and Lu, G., Metal Foams: A Design Guide. Applied Mechanics Reviews, 2001. 54(6): p. B105.

286. Furman, E.L., A.B. Finkelstein, and M.L. Cherny, Permeability of aluminium foams produced by replication casting. Metals, 2012. 3(1): p. 49-57.

287. Despois, J.F., Marmottant, A., Salvo, L. and Mortensen, A., Influence of the infiltration pressure on the structure and properties of replicated aluminium foams. Materials Science and Engineering: A, 2007. 462(1): p. 68-75.

288. Conde, Y., Despois, J.F., Goodall, R., Marmottant, A., Salvo, L., San Marchi, C. and Mortensen, A., Replication Processing of Highly Porous Materials. Advanced Engineering Materials, 2006. 8(9): p. 795-803.

289. Goodall, R. and Mortensen, A., Microcellular Aluminium?–Child's Play! Advanced Engineering Materials, 2007. 9(11): p. 951-954.

290. Jinnapat, A. and A. Kennedy, The manufacture and characterisation of aluminium foams made by investment casting using dissolvable spherical sodium chloride bead preforms. Metals, 2011. 1(1): p. 49-64.

291. Goodall, R., Despois, J.F., Marmottant, A., Salvo, L. and Mortensen, A., The effect of preform processing on replicated aluminium foam structure and mechanical properties. Scripta Materialia, 2006. 54(12): p. 2069-2073.

292. Chang, W.S., Porosity and Effective Thermal Conductivity of Wire Screens. Journal of Heat Transfer, 1990. 112(1): p. 5-9.

293. Seguin, D., A. Montillet, and J. Comiti, Experimental characterisation of flow regimes in various porous media - I: Limit of laminar flow regime. Chemical Engineering Science, 1998. 53(21): p. 3751-3761.

294. Seguin, D., Montillet, A., Comiti, J. and Huet, F., Experimental characterization of flow regimes in various porous media—II: Transition to turbulent regime. Chemical Engineering Science, 1998. 53(22): p. 3897-3909.

295. Kim, T.H., W. Lee, and J.H. Jeong, Thermo-fluidic characteristics of open cell metal foam as an anodes for DCFC, part I: Head loss coefficient of metal foam. International Journal of Hydrogen Energy, 2014. 39(23): p. 12369-12376.

296. Altheimer, M., Becker, D., D'Aleo, F.P. and von Rohr, P.R., Flow regime and liquid–solid mass transfer investigation in a designed porous structure using electrochemical micro-probes. Chemical Engineering Science, 2016. 152: p. 699-708.

297. Seguin, D., A. Montillet, and J. Comiti, Experimental characterisation of flow regimes in various porous media—I: Limit of laminar flow regime. Chemical engineering science, 1998. 53(21): p. 3751-3761.

298. Hirech, K., A. Arhaliass, and J. Legrand, Experimental investigation of flow regimes in an SMX Sulzer static mixer. Industrial & Engineering Chemistry Research, 2003. 42(7): p. 1478-1484.

299. Comiti, J., N. Sabiri, and A. Montillet, Experimental characterization of flow regimes in various porous media—III: limit of Darcy's or creeping flow regime for Newtonian and

purely viscous non-Newtonian fluids. Chemical Engineering Science, 2000. 55(15): p. 3057-3061.

300. Morancais, P., Hirech, K., Carnelle, G. and Legrand, J., Friction factor in static mixer and determination of geometric parameters of SMX Sulzer mixers. Chemical Engineering Communications, 1999. 171(1): p. 77-93.

301. John, R.T., An introduction to error analysis: the study of uncertainties in physical measurements. 2nd ed. ed. 1997, Sausalito, Calif.: Sausalito, Calif.: University Science Books, c1997.

302. Argento, C. and D. Bouvard, Modelling the effective thermal conductivity of random packing of spheres through densification. International Journal of Heat and Mass Transfer, 1996. 39(7): p. 1343-1350.

303. Goodall, R. and A. Mortensen, Microcellular Aluminium? – Child's Play! Advanced Engineering Materials, 2007. 9(11): p. 951-954.

304. Progelhof, R.C. and J.L. Throne, Cooling of structural foams. Journal of Cellular Plastics, 1975. 11(3): p. 152-163.

305. Wang, W., Yang, X., Han, B., Zhang, Q., Wang, X. and Lu, T., Analytical design of effective thermal conductivity for fluid-saturated prismatic cellular metal honeycombs. 2016. p. 69-75.

306. Ambrosio, G., Bianco, N., Chiu, W.K., Iasiello, M., Naso, V. and Oliviero, M., The effect of open-cell metal foams strut shape on convection heat transfer and pressure drop. Applied Thermal Engineering, 2016. 103: p. 333-343.

307. Boschetto, A., Bottini, L., Campana, F., Consorti, L. and Pilone, D., Morphological characteristics of aluminium foams produced by replication casting. In CONVEGNO IGF XXII ROMA 2013. 2013.

308. Evans, A.G., Hutchinson, J.W., Fleck, N.A., Ashby, M.F. and Wadley, H.N.G., The topological design of multifunctional cellular metals. Progress in Materials Science, 2001. 46(3–4): p. 309-327.

309. Evans, A.G., J.W. Hutchinson, and M. Ashby, Multifunctionality of cellular metal systems, in Prog. Mater. Sci. 1998. p. 171-221.

310. Roberts, A. and E. Garboczi, Roberts, AP. Acta Materialia, 2001. 49(2): p. 189-197.

311. Grenestedt, J.L., Influence of wavy imperfections in cell walls on elastic stiffness of cellular solids. Journal of the Mechanics and Physics of Solids, 1998. 46(1): p. 29-50.

312. Silva, M. and L. Gibson, Modelling the mechanical behaviour of vertebral trabecular bone: effects of age-related changes in microstructure. Bone, 1997. 21(2): p. 191-199.

313. Braginsky, L., Shklover, V., Witz, G. and Bossmann, H.P., Thermal conductivity of porous structures. Physical Review B, 2007. 75(9): p. 094301.

314. Leszczyński, B., Gancarczyk, A., Wróbel, A., Piątek, M., Łojewska, J., Kołodziej, A. and Pędrys, R., Global and Local Thresholding Methods Applied to X-ray Micro

tomographic Analysis of Metallic Foams. Journal of Non-destructive Evaluation, 2016. 35(2): p. 1-9.

315. Baker, D.R., Mancini, L., Polacci, M., Higgins, M.D., Gualda, G.A.R., Hill, R.J. and Rivers, M.L., An introduction to the application of X-ray micro tomography to the three-dimensional study of igneous rocks. Lithos, 2012. 148: p. 262-276.

316. Lambert, J., Cantat, I., Delannay, R., Renault, A., Graner, F., Glazier, J.A., Veretennikov, I. and Cloetens, P., Extraction of relevant physical parameters from 3D images of foams obtained by X-ray tomography. Colloids and Surfaces A: Physicochemical and Engineering Aspects, 2005. 263(1): p. 295-302.

317. Landis, E.N. and D.T. Keane, X-ray micro tomography. Materials Characterization, 2010. 61(12): p. 1305-1316.

318. Abràmoff, M.D., P.J. Magalhães, and S.J. Ram, Image processing with ImageJ. Biophotonics international, 2004. 11(7): p. 36-42.

319. Nawaz, K., J. Bock, and A.M. Jacobi, Thermal-hydraulic performance of metal foam heat exchangers under dry operating conditions. Applied Thermal Engineering, 2017. 119: p. 222-232.

Appendix A

1- Flow rate devices calibration

In order to perform measurements at low flow rates (creeping flow) at ranges of (0.5 L/m – 50 L/M), the Roxspur air mass flowmeter (FFLM0035) with accuracy of (0.8% of reading + 0.2% FS) was used. At the moderate flow rates (50 L/M – 300 L/M) were also measured by the Omega air mass flow meter (FMA-LP1600A) with the range of 2.5 LPM to 500 LPM with accuracy of (0.8% of reading + 0.2% FS). These mass flow meters were calibrated by the manufactured companies. The calibration certificates are shown in Figures A-1 and A-2 respectively.

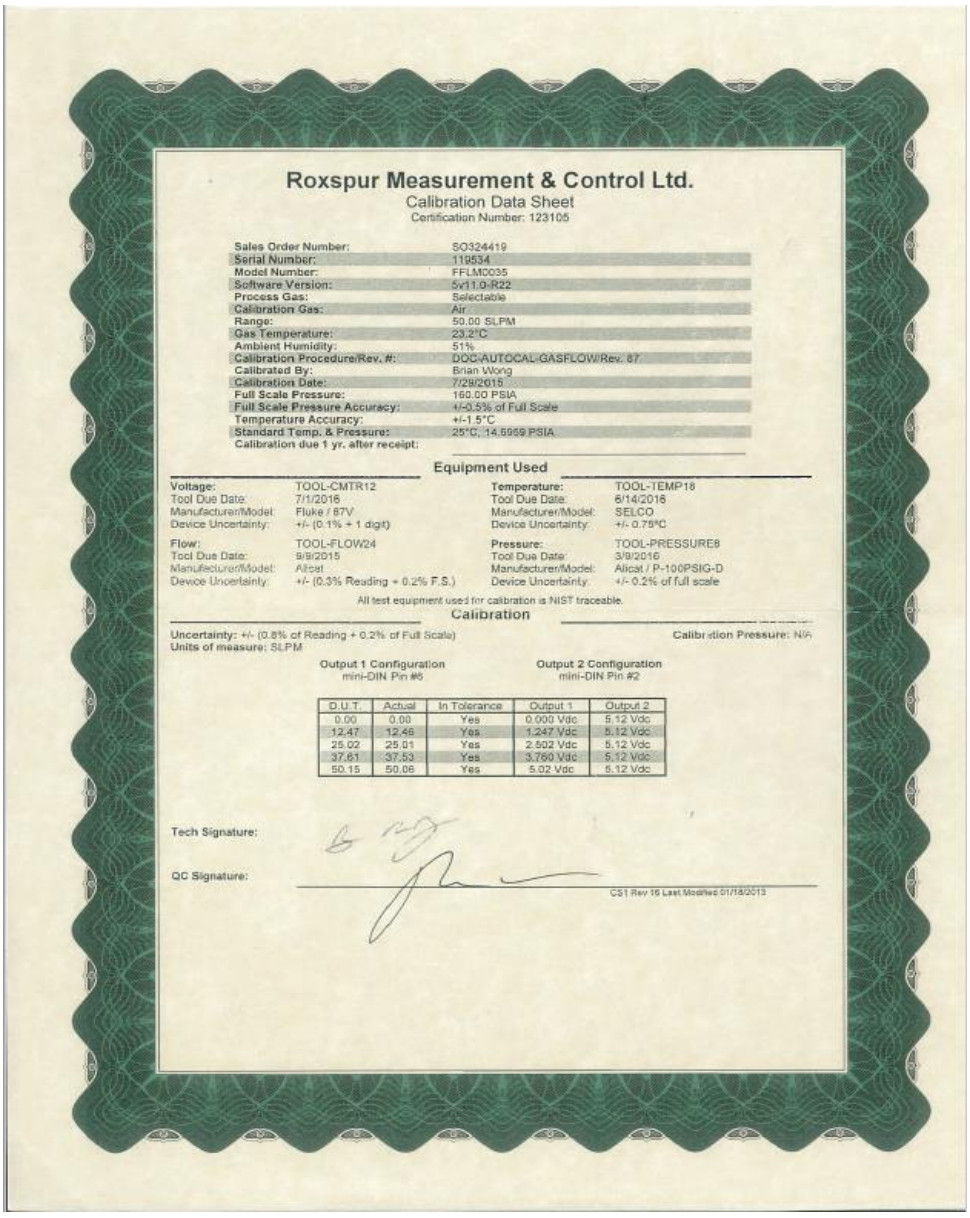

Roxspur Measurement & Control Ltd.

Calibration Data Sheet

Certification Number: 123105

Sales Order Number:	SO324419
Serial Number:	119534
Model Number:	FFLM0035
Software Version:	5v11.0-R22
Process Gas:	Selectable
Calibration Gas:	Air
Range:	50.00 SLPM
Gas Temperature:	23.2°C
Ambient Humidity:	51%
Calibration Procedure/Rev. #:	DOC-AUTOCAL-GASFLOW/Rev. 67
Calibrated By:	Brian Wong
Calibration Date:	7/28/2016
Full Scale Pressure:	160.00 PSIA
Full Scale Pressure Accuracy:	+/-0.5% of Full Scale
Temperature Accuracy:	+/-1.5°C
Standard Temp. & Pressure:	25°C, 14.6959 PSIA
Calibration due 1 yr. after receipt:	

Equipment Used

Voltage:	TOOL-CMTR12	Temperature:	TOOL-TEMP18
Tool Due Date:	7/1/2016	Tool Due Date:	6/14/2016
Manufacturer/Model:	Fluke / 87V	Manufacturer/Model:	SELCO
Device Uncertainty:	+/- (0.1% + 1 digit)	Device Uncertainty:	+/- 0.75°C
Flow:	TOOL-FLOW24	Pressure:	TOOL-PRESSURE8
Tool Due Date:	9/9/2015	Tool Due Date:	3/9/2016
Manufacturer/Model:	Alicat	Manufacturer/Model:	Alicat / P-100PSIG-D
Device Uncertainty:	+/- (0.3% Reading + 0.2% F.S.)	Device Uncertainty:	+/- 0.2% of full scale

All test equipment used for calibration is NIST traceable.

Calibration

Uncertainty: +/- (0.8% of Reading + 0.2% of Full Scale) Calibration Pressure: N/A

Units of measure: SLPM

Output 1 Configuration mini-DIN Pin #6				Output 2 Configuration mini-DIN Pin #2
D.U.T.	Actual	In Tolerance	Output 1	Output 2
0.00	0.00	Yes	0.000 Vdc	5.12 Vdc
12.47	12.46	Yes	1.247 Vdc	5.12 Vdc
25.02	25.01	Yes	2.502 Vdc	5.12 Vdc
37.61	37.53	Yes	3.760 Vdc	5.12 Vdc
50.15	50.06	Yes	5.02 Vdc	5.12 Vdc

Tech Signature:

QC Signature:

CS1 Rev 16 Last Modified 01/18/2013

Figure A-1 Calibration certificate of the Mass flow meter (0.5 L/M - 50 L/M)

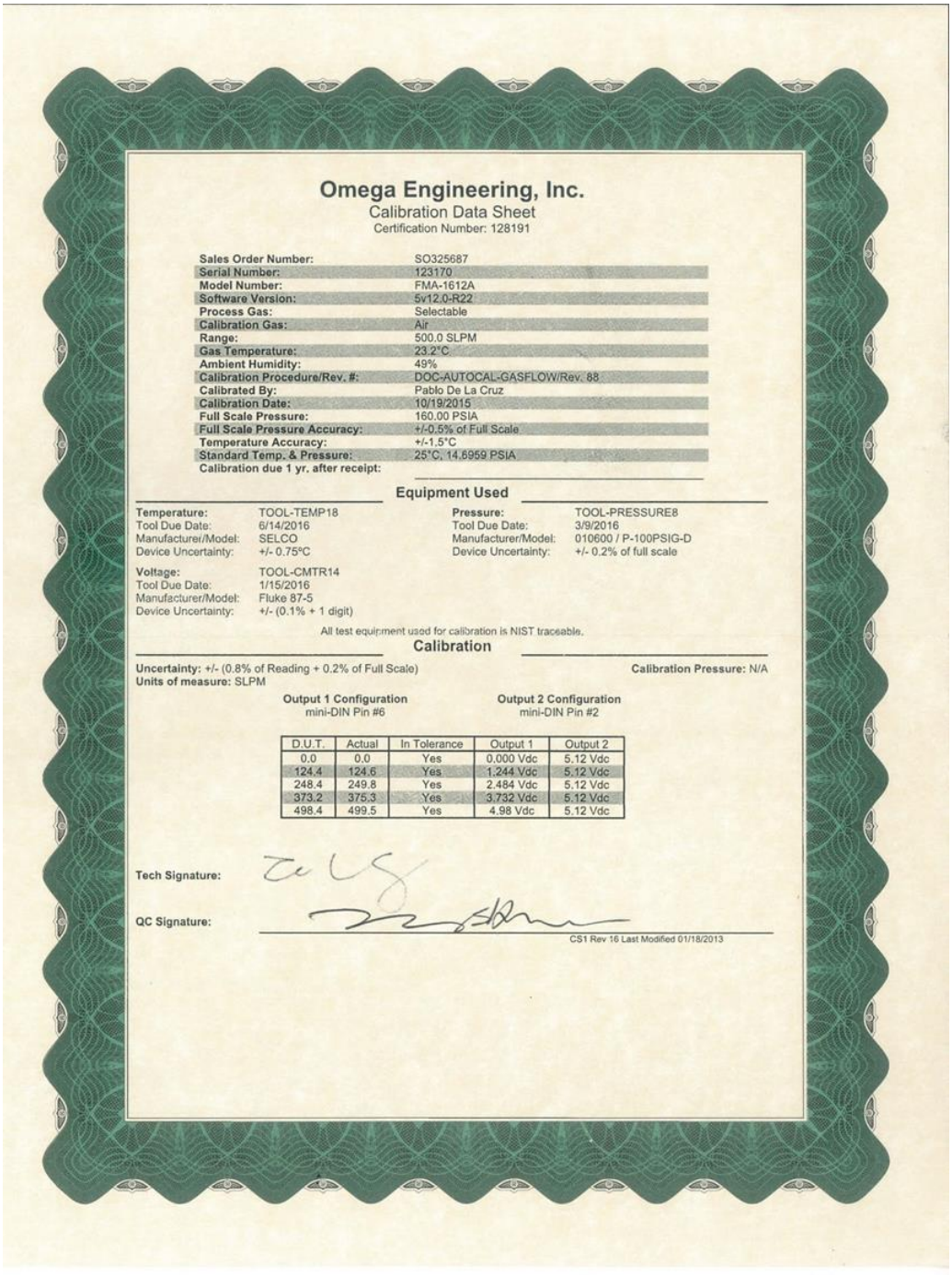

Omega Engineering, Inc.

Calibration Data Sheet

Certification Number: 128191

Sales Order Number:	SO325687
Serial Number:	123170
Model Number:	FMA-1612A
Software Version:	5v12.0-R22
Process Gas:	Selectable
Calibration Gas:	Air
Range:	500.0 SLPM
Gas Temperature:	23.2°C
Ambient Humidity:	49%
Calibration Procedure/Rev. #:	DOC-AUTOCAL-GASFLOW/Rev. 88
Calibrated By:	Pablo De La Cruz
Calibration Date:	10/19/2015
Full Scale Pressure:	160.00 PSIA
Full Scale Pressure Accuracy:	+/-0.5% of Full Scale
Temperature Accuracy:	+/-1.5°C
Standard Temp. & Pressure:	25°C, 14.6959 PSIA
Calibration due 1 yr. after receipt:	

Equipment Used

Temperature:	TOOL-TEMP18	**Pressure:**	TOOL-PRESSURE8
Tool Due Date:	6/14/2016	Tool Due Date:	3/9/2016
Manufacturer/Model:	SELCO	Manufacturer/Model:	010600 / P-100PSIG-D
Device Uncertainty:	+/- 0.75°C	Device Uncertainty:	+/- 0.2% of full scale
Voltage:	TOOL-CMTR14		
Tool Due Date:	1/15/2016		
Manufacturer/Model:	Fluke 87-5		
Device Uncertainty:	+/- (0.1% + 1 digit)		

All test equipment used for calibration is NIST traceable.

Calibration

Uncertainty: +/- (0.8% of Reading + 0.2% of Full Scale) **Calibration Pressure:** N/A

Units of measure: SLPM

	Output 1 Configuration mini-DIN Pin #6	**Output 2 Configuration** mini-DIN Pin #2			
D.U.T.	Actual	In Tolerance	Output 1	Output 2
0.0	0.0	Yes	0.000 Vdc	5.12 Vdc
124.4	124.6	Yes	1.244 Vdc	5.12 Vdc
248.4	249.8	Yes	2.484 Vdc	5.12 Vdc
373.2	375.3	Yes	3.732 Vdc	5.12 Vdc
498.4	499.5	Yes	4.98 Vdc	5.12 Vdc

Tech Signature:

QC Signature:

CS1 Rev 16 Last Modified 01/18/2013

Figure A-2 Calibration certificate of the Mass flow meter (2.5 L/M - 500 L/M)

Appendix B

1- Thermocouples calibration

Sixteen thermocouples were used for effective thermal conductivity measurements. These thermocouples were calibrated against mercury thermometer at the ice melting point and water boiling point individually. Both the thermocouples and thermometer were put in thermal insulated vessel with ice for the first point. As shown in Figure B-1 is the typical calibration technique against the ice melting point.

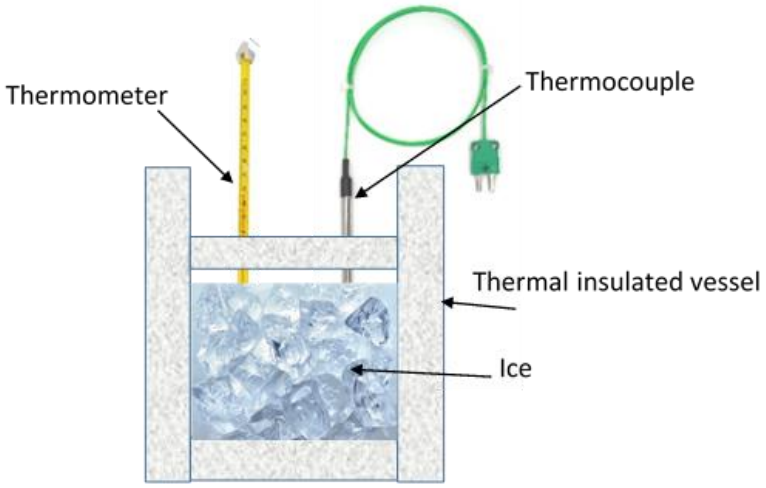

Figure B-1 Thermocouples calibration equipment arrangement

The second point is against the water boiling point at atmosphere, the calibration against this point was performed by using the container and heater. The thermometer and thermocouples were held at the same level in the boiling point at the container. During all calibration procedures the thermocouples were connected with USB TC-08 Thermocouple Data Loggers during the calibration in order to include the errors of the loggers and connections.

In order to improve the calibration precision the water in the container left to cool and the data collected from the thermocouples and the mercury thermometer in the same time. Shown in Figure B-2 is the sample of typical calibration data collected. The same procedure was done for the all thermocouples. The typical linear relation used for the fitting data is

$$Y = a\,X + b \qquad \text{B.1}$$

Where Y is the calibrated temperature (thermometer reading) and the X is the thermocouple reading. The fitting factors (a and b) are tabulated in Table B-1.

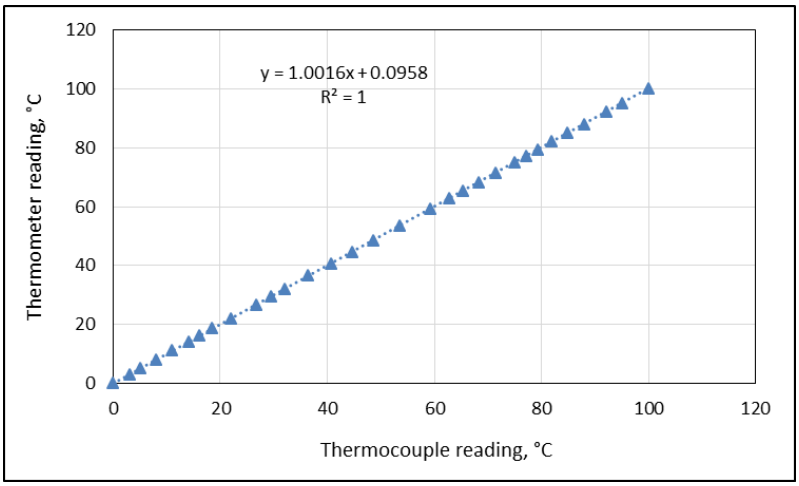

Figure B-2 The typical thermocouple calibration data fitting

Table B-1 the fitting coefficients of the thermocouples

Thermocouple	a	b	R^2
1	0.9987	-02908	1
2	1.0009	-0.2485	1
3	1.0011	-0.365	1
4	0.9916	0.6889	1
5	0.9996	0.4021	0.9999
6	0.9993	0.0643	0.9999
7	1.0022	-0.4487	1
8	1.0015	-0.5347	0.9999
9	1.0014	-0.417	1
10	0.9979	-0.1997	1
11	1.0024	-0.2447	1
12	1.0016	0.0958	1
13	0.9919	.04752	1
14	1.0013	-0.2142	0.9999
15	1.0011	-0.1954	1
16	0.9996	0.1304	1